FINAL PROJECT REPORT

THE UNIVERSITY OF QUEENSLAND AUSTRALIA

Centre for Natural Gas

Converting tight contingent CSG resources: Application of graded particle injection in CSG stimulation

Project

This document is the final report of the *Converting tight contingent CSG resources: Application of graded particle injection in CSG stimulation* project.

Research team

Prof Ray Johnson[1], Dr Christopher Leonardi[2], Dr Zhenjiang You[3], Dr Ayrton Ribeiro[1], Mr Nathan Di Vaira[2]

[1]Centre for Natural Gas, [2]School of Mechanical and Mining, [3]School of Chemical Engineering, Engineering
The University of Queensland

Acknowledgments

Citation

Publication details

Project Report Release Date: 4 May 2022

Disclosure

The UQ Centre for Natural Gas is currently funded by the University of Queensland and the Industry members (Arrow Energy, APLNG, and Santos). The Centre conducts research across Water, Geoscience, Petroleum Engineering, and Social Performance themes.

For more information about the Centre's activities and governance see natural-gas.centre.uq.edu.au

Disclaimer

The information, opinions, and views expressed in this report do not necessarily represent those of The University of Queensland, the Centre for Natural Gas, or its constituent members or associated companies. Researchers within or working with the Centre for Natural Gas are bound by the same policies and procedures as other researchers within The University of Queensland, which are designed to ensure the integrity of research. You can view these policies at: http://ppl.app.uq.edu.au/content/4.-research-and-research-training

The Australian Code for the Responsible Conduct of Research outlines the expectations and responsibilities of researchers to further ensure independent and rigorous investigations.

This report has not yet been independently peer-reviewed.

Document control sheet

Version #	Reviewed by	Revision Date	Brief description of changes
1	R Johnson	14 February 2022	Final Draft for CNG Review
4	R Johnson, J Lane	23 February 2022	Minor edits for submission to CNG member companies
5	R Johnson, A Garnett, J Lane	4 May 2022	Modified initial summary; minor edits through document
6	R Johnson	20 June 2022	Minor edits and recent additions, finalisation

Table of Contents

List of Figures

List of Tables

1 Project overview

In September 2020, the Australian government announced a "Gas-fired recovery" suite of policies with the intention of getting more gas to market. This included the intent to unlock "*… five key gas basins starting with the Beetaloo Basin in the NT and the North Bowen and Galilee Basin in Queensland …*".

For the purposes of this NERA project, "unlocking" means developing extraction and predictive modelling technologies which can increase production from known currently sub-economic coal seam gas accumulations *(Contingent Resources)* mainly in existing development areas. The specific focus for technology development is for such accumulations from where gas cannot flow at commercial rates due to low very permeabilities (aka "tight").

A number of AEMO Gas Statements of Opportunity (GSOOs) e.g. from 2018 to 2022 have consistently forecast a domestic gas shortfall in the mid-2020s. According to the latest GSOO (2022) there are over 40 PJ of coal seam gas which is classed as *Contingent Resource (2C)* in Queensland alone. A significant proportion of this is due to low permeabilities. Improvements in extraction technology that overcome this low permeability barrier could deliver national-scale benefits in terms of domestic supply and potentially export revenues.

Recent laboratory analysis showed that the Graded Particle Injection (GPI) technique could potentially (i) increase the permeability of CSG formations; and (ii) retain that permeability as the field produces or depletes (loss of permeability with production is common problem in "tight coals"). For this to be deployed, two hurdles need first to be overcome. First, additional confidence in permeability enhancement and retention is needs from additional lab trials to guide field applications. Second, new and complex GPI predictive modelling needs to be developed support decisions to employ this new technology.

The aim of this project is to undertake this critical work required to monetise this resource.

- Chapters 2-3 summarise prior work in this field through a review of previous modelling and experimental studies, identifying current knowledge gaps and research priorities, and informing design of the experimental work in this project.
- Chapters 4-5 summarise the development and application of new particle-scale and fracture-scale modelling tools, addressing a crucial gap in the industry's ability to assess various extraction techniques at scale.
- Chapters 6-7 also provide new insights on the prospects for the GPI technique, through laboratory testing of commercially available micro proppants, and reservoir simulation of field-scale response to the application of GPI using a range of assumed micro-proppant specifications.
- Finally, Chapters 8-9 recommend the workflow and diagnostics needed to design and evaluate programs to improve recovery from CSG wells using GPI.

This new research delivered three key findings of relevance to industry and government stakeholders.

- There is a strong case for larger-scale field trials, with the modelling work demonstrating the potential for valuable resource yield improvements. The recommended assessment framework and workflows establish the criteria against which to assess the feasibility of individual field-scale project proposals.
- Laboratory testing with the commercially available product was inconclusive, with the modelling analysis suggesting that modified product specifications would likely be more successful. The next stage of work would therefore benefit from R&D that integrates across field trials and product development.
- The fit-for-purpose models developed through this project improve the suite of tools available to guide industry assessment and optimization of prospective extraction enhancement techniques.

Establishing a successful approach for low-risk enhancement of localised production rates would substantially de-risk the investment required to consolidate production from existing CSG fields and/or progress development from formations that are currently deemed uneconomic. The research findings from this project suggest that the GPI technique would be particularly suited to the types of formations found in the Bowen, Galilee and deep Cooper Basins, the former two being flagged as priority targets of current national government policy.

2 Technical Summary

A review of past modelling of the GPI process at The University of Adelaide shows that laboratory-based mathematical models have demonstrated promising results. That study found that using 10 and 20 µm diameter, hollow sphere, graded particles in injection and drawdown leads to a three-fold improvement in permeability due to the propping of cleats. Our modelling indicates that using GPI, either as a standalone treatment or in conjunction with hydraulic fracturing treatments, may improve productivity and reduce costs. This could improve productivity and convert many contingent, low-permeability coal resources to reserves in both the Bowen and Surat Basins. This project research expands the earlier modelling techniques to design and evaluate the potential benefits from the radial application (Ribeiro, et al., 2019) or co-application with hydraulic fracturing (Santiago, et al., 2021).

Next, the current models for understanding the injection behaviour of graded particles available in the literature are based on several assumptions, which over-simplify the real process and limit their application in the field. These assumptions include isotropic one-dimensional Darcy flow, smooth cleats of constant thickness, equidistant packing of particles in a single monolayer, constant suspension viscosity, and geometric particle straining. Our project developed new models to understand the transport, bridging, and embedment behaviour of micro proppants to advance the technology and better modelling in more complex fully 3D hydraulic fracture models.

In the late 1990's, an experimental study by the US laboratory, Stim-Lab, presented key findings regarding coalbed methane (CBM) stimulation in two areas, namely coal-fluid interactions and rheology and proppant transport. The coal-fluid interactions study showed that common gelled fracturing fluids can be extremely damaging to the fragile cleat permeability of CSG reservoirs. The damage of permeability can range from 50 to 99% of initial permeability. Formation damage associated with coal cleat permeability can be extended to reservoirs with natural fracture production mechanisms. The rheology and proppant transport study indicated that the addition of low concentration gel does not significantly improve proppant transport in horizontal fractures. Thus, the most efficient and cost-effective way to transport proppant is with water at velocities of at least 3 ft/s. However, the use of an enzymatic breaker with guar yielded greater than 97% returned conductivity.

Finally, the use of hollow sphere, graded particles limit the applications to low closure stress regions, where closure, embedment, and fines generation are not critical. An experimental study on fracture conductivity in Cooper Basin deep coals discovered that coal rank has a significant effect on fracture conductivity (Fraser & Johnson Jr, 2018). Increased vitrinite reflectance (VR_o) was found to yield increased fracture conductivity. This was a result of increased proppant embedment and coal fines generation in lower rank coals. There were also significant learnings concerning proppant type and coal sample selection (e.g., preserved core, thermal maturity, etc.). More sophisticated models were developed in this project that describe the effects of embedment – as with the Cooper Basin study, the results are dependent on coal strength models that typically correlate with coal rank (You, et al., 2019). These models can inform the practitioner on the application of harder, man-made ceramic micro proppants (e.g., Deeprop® 600) that will be affected by the closure and embedment effects.

Modelling of CSG production enhancement using GPI is based on finite element modelling (FEM) of particle embedment, and lattice Boltzmann modelling (LBM) of fracture conductivity. In combination, these models provide predictions of fracture conductivity under varying coal types, particle packing, closure stress, and fluid flow. This represents an improvement over analytical solutions based on prior studies using the Hertz elastic contact theory, which has previously been applied to characterise the deformation of the fracture surface. The LBM simulations for a range of particle embedment patterns reveal the nonlinear relationship between fracture conductivity and particle concentration, under different stress conditions. The results agree well with previous computational fluid dynamics (CFD) results. These new results represent one component of the large-scale fracture flow modelling that will be developed in the associated PhD work accompanying the project.

Modelling of suspension flow in coal fractures using the LBM-DEM method accounts for particle transport and straining in fractures with leak-off cleats. Model validation has been performed using a benchmark particle-settling problem. Preliminary simulation results of particle distribution in a model, representing a single fracture with leak-off into a cleat, characterise the behaviour of microparticles, including interactions between particles, the fracture walls, and the fluid. Systematic investigation on the effects of particle properties, carrier fluid rheology and fracture geometry on particle transport is possible based on the advances in particle transport modelling completed in this research. Further the understanding of particle bridging or jamming and 'screen-out' could be investigated using this methodology with a probabilistic model used to contrast the previous deterministic methods of estimating the likelihood of screen-out. This would contribute to improved modelling of the GPI process with models capable of incorporating these effects at field scale, thereby enhancing the planning of field implementations.

To date, the laboratory experimentation has used a slurried, commercially available product mixture composed of the proppant, fluid, and enzyme 'breaker' additive that can be physically managed and pumped in the field by the ratio of mixing into a treated or produced water stream (see Appendix H). To test the slurry mixing and pumping in the experimental apparatus, a test 40/70 mesh sand pack was injected with the proppant to understand the effects of inter-mixing of proppants and the effect on conductivity. As expected, the proppant was selectively bridging at the face or early into the pack with a more significant reduction in permeability than expected with the guar and enzyme combination. The experiments focussed on reproducing the retained conductivity that is known to be achieved with the selected guar and enzyme. The core flooding was repeated with a 20/40 sand that exhibited straining and loss of permeability, with some passthrough of the injected microparticles. The final testing showed a loss in permeability in cleated coal cores, but were pressure limited so as to fully assess their ability to show permeability under fracturing-pressure conditions.

With regards to candidate selection, a significant amount of research has been made on fracture modelling, fluid/particle dynamics, reservoir performance prediction, and slurry development. The research has provided workflows within a framework of modelling evaluations to allow performance evaluation of the proposed implementation. This report develops at a high level the reservoir, operational, and diagnostic workflows that need to be considered as part of this implementation strategy. The use of diagnostic fracture injection testing along with integrated reservoir and hydraulic fracture modelling field data have identified methods to identify and characterise pressure-dependent permeability (PDP) in a case study from the Surat Basin (Johnson Jr., et al., 2020). By constraining the key factors in pressure-dependent permeability, the ability to better design and ascertain the benefits of GPI in both radial and co-applications with hydraulic fracturing models are possible.

In summary, a framework of required inputs, outputs and expected outcomes has been produced for varying conditions based on actual field cases. This provides operators with an overall framework to evaluate the application and potential of microparticle injection in pressure-dependent permeability coals. The integrated reservoir and hydraulic fracturing modelling provide simulated outputs for field

implementation. Finally, insight and observations regarding field implementation are suggested by experimental results of laboratory studies on the placement of particles in coal and 3D-printed naturally fractured core material using the proposed carrier fluids. In conclusion, the published modelling and laboratory results from this research provide the basis to design, execute, and evaluate treatments using commercially available micro proppants to improve low permeability coal productivity.

3 Introduction

Negative responses in well productivity, based on drawdown, have been observed in Bowen and Surat basin coal measures. Such production responses are often described as a function of drawdown rate and are often observed post-stimulation of the coals or in areas with higher permeability anisotropy. To address hydraulic fracturing for these areas, the current project focuses on the determination of stimulation effectiveness and improved methods in geomechanical definition to improve hydraulic fracturing modelling and effectiveness. Coupled with improved modelling, better understanding and implementation of graded particle injection (GPI, or proppants <50 µm) hydraulic fracturing treatments can improve productivity in low-permeability coal intervals.

GPI was first proposed as a technology to improve the poor production index observed in naturally fractured unconventional reservoirs such as coal seams (Keshavarz, et al., 2015; Keshavarz, et al., 2016; Alireza Keshavarz, et al., 2014; Khanna, et al., 2013). The underlying premise of GPI is the injection of micron-scale particles to essentially prop the narrow aperture of cleats and fractures in coals, preventing closure and the associated reduction in permeability due to an increase in net effective stress. By sequencing an increasing size of injected particles (e.g., from 10 to 50 µm in diameter), the smallest particles can be placed deep within the seam, with the near-wellbore region being supported by larger, standard-sized proppants (Figure 1). In parallel, Halliburton Energy Services has been investigating the use of micro proppants (<200 mesh) for injection and propping of natural fractures for clastic and coal stimulation, with a patent awarded in 2014 (Saini, et al., 2015).
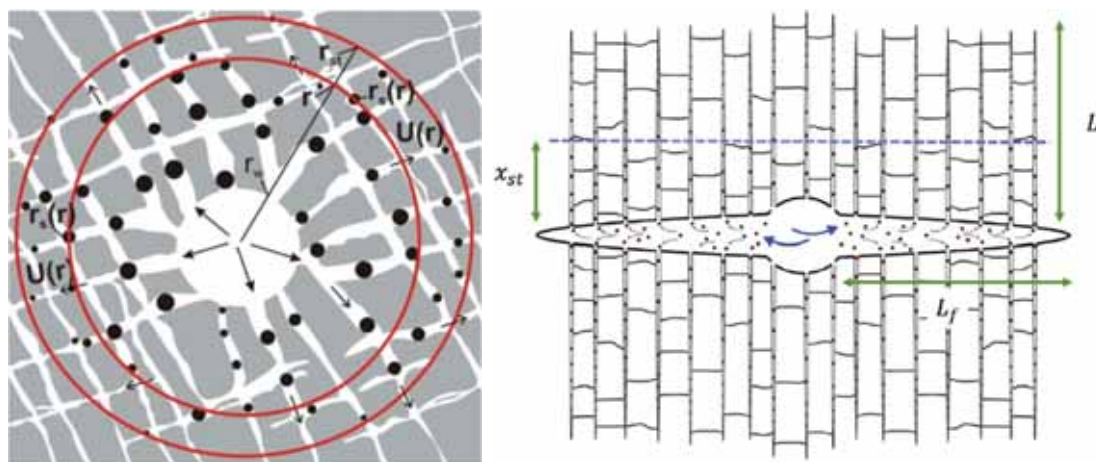
Figure 1: Schematic representations of graded particle injection, showing (left) the relative movement of particles of increasing *size (reproduced from Keshavarz et al., 2014) and (right) its application in conjunction with hydraulic fracturing (reproduced from Keshavarz et al., 2016).*

3.1 Aims and Objectives

This project aims to demonstrate the improvement in the productivity index that can be achieved by

the application of GPI in Queensland CSG wells. The objectives which support this aim are as follows:

1. Quantify the particle embedment likely to be observed in both Permian and Walloon coal measures in the presence of time-dependent processes such as creep, and then calculate its influence on the long-term permeability of cleats and fractures.
2. Determine the particle (e.g., size distribution, concentration, compressive strength) and fluid (e.g. pH, salinity) properties, as well as injection sequencing, which are most suited to GPI application in both Permian and Walloon coal measures.
3. Identify candidate locations that are well-suited to field application of GPI based on the in-situ stress state, natural fracture network, and coal properties.
4. Undertake field trials of GPI to quantify the change in permeability and productivity, as well as the material (i.e., fluid, particles) required to achieve the design pressures.
5. Develop advanced modelling techniques that can be employed as part of the engineering workflow in the future design and application of GPI at scale.
6. Develop an additional tool for hydraulic fracturing treatments or an alternative stimulation strategy to address stimulation of low-permeability coals using graded particle injection treatments.

3.2 Project Schedule

The activities of this project will include a review of previous work including modelling and experimental study, model development and validation, and finally application of the developed workflow. The project team will be comprised of specialists from a range of backgrounds, and some tasks will be able to be performed concurrently. Three stages and associated checkpoints have been defined as a means of periodically reviewing the future directions and resources for the project, and the tasks for each of these are defined as follows.

3.2.1 Stage I: Insight and tool development (0 -12 months from start)
- Review prior work at ASP for particle/fluid interactions and behaviour and verification of most recent mathematical models with new parameters (completed).
- Determine the relationship between proppant packing, embedment and fracture permeability in coals including:
  - perform elastoplastic finite element modelling (FEM), incorporating findings from the Centre for Natural Gas (formerly Centre for Coal Seam Gas) Pressure Dependent Permeability project, to characterise the embedment of a micron-scale particle in Permian and Walloon coals for a range of pack configurations and particle size distributions;
  - validate embedment modelling via a subset of experimental studies;
  - use the embedment findings to predict the relationship between particle packing concentration, effective stress and cleat/fracture permeability via computational fluid dynamics (CFD); and
  - define a new relationship between particle packing/spacing and fracture permeability at varying effective stress.
- Characterise the transport and straining of micron-sized particles in coal fractures including:

- o perform direct numerical simulation (DNS) of suspension transport in a single fracture with leak-off cleats to determine the conditions under which bridging and agglomeration will occur;
- o use DNS modelling to explore the preferential flow of suspensions in an orthogonal fracture/cleat network under anisotropic stress conditions; and
- o estimate improved jamming ratios for micron-sized particles in coals based on DNS results, having also considered the influence of electrostatic interactions.
- All Stage 1 proposed objectives achieved.

3.2.2 Stage II: Design and implementation (12 - 18 months from start)

- Develop an improved mathematical model of fracture pressure, aperture width and proppant concentration/placement at the field scale, using existing models as a basis to:
  - o incorporate the new relationship between fracture packing and permeability;
  - o include a new understanding of particle jamming/straining in fractures; and
  - o adjust fluid rheology based on suspension concentration.
- Determine the criteria for selecting candidate wells for field trials;
- Hold workshops with collaborators, proponents and subject matter experts to identify GPI trial sites and set a commercial strategy for any field trials.
- All Stage 2 proposed objectives achieved.

3.2.3 Stage III: Further development and future applications (18-24 months from start)

- Proposed to integrate GPI into hydraulic fracture treatment designs based on optimized Advanced Simulation Technology (AST) modelling/processes, using models to define:
  - o histogram of natural fracture activation based on bottom-hole pressure history-matched response;
  - o particle ranges and potential implementation strategy, based on complementary mathematical and DNS models of GPI; and
  - o the range of application required to show short-term benefit basic reservoir modelling productivity index vs time.
  - o These goals were completed by published research studies and case history analysis as no actual well cases were forthcoming for trials (Johnson et al., 2020, Ribeiro et al., 2019, Santiago et al., 2021)
- Proposed to design staged field experiments (including success criteria) to calibrate application models including diagnostic plans (i.e., what should it look like) incorporating:
  - o diagnostic fracture injection testing (DFIT);
  - o pressure transient analysis (PTA);
  - o rate transient analysis methods (RTA); and
  - o coupled reservoir geomechanical modelling to illustrate what success looks like based on input parameters.
  - o These goals were completed by published case history analysis and proposed design implementations no actual well cases were forthcoming for trials (Johnson et al., 2020, Johnson et al., 2021).
- Support the implementation and evaluation of staged experiments in the field to calibrate models using the tools previously described.

- Unfortunately, no actual wells were available for implementation except the application of Silica Flour in deep coal stimulation (Camac et al., 2018); however,
- laboratory testing of a commercial micro proppant included coal core and synthetic 3D printed fractured media to evaluate performance and inform future testing.
- Final report and completion of the project.

3.3 Report Structure

This report communicates the overall findings of this project. Section 4 reviews progress related to the development of hydraulic fracturing models capable of providing insight and guidance for the candidate selection and implementation process. Section 5 reviews research related to coal-fluid interactions, as well as rheology and proppant transport studies. Section 6 presents a study of modelling results of production enhancement using GPI for a Surat Basin case. Section 7 summarises laboratory work to date on the injection of commercially available polymer, breaker and micro proppants in a sand pack, Permian coal, and 3D printed natural fracture core. Section 8 outlines the findings of an integrated case study of pressure-dependent permeability and implementation in fracture modelling that supports the application workflow to implement GPI as outlined in Section 9. Finally, Section 10 outlines the conclusions and Section 11 the recommendations for future research or implementation. The Appendices provide the cover pages of key papers and laboratory findings generated in the course of this research.

4 Hydraulic Fracture Modelling in Coal Measures

The prediction of hydraulic fracture growth in coal measures using two-dimensional models in a one-dimensional stress state is motivated by several factors. Generally, these models are numerically robust, which facilitates a wide parameter range when undertaking sensitivity studies. For example, improbable or nonphysical values of leak-off coefficients or fracture toughness can be chosen to help match pressure histories. In addition, simulation times are relatively short, meaning that multiple runs to history-match production data can be accommodated in industrial workflows.

4.1 Hydraulic Fracture Model Calibration

Most hydraulic fracture modelling calibration in the past has focused on history-matching net pressure generated within the propagating fracture, which leads to a high degree of uncertainty between models. Early attempts to ascertain the uncertainty in modelling outputs from given calibrated data showed the high degree of variability that could be observed between several models all based on sound physics but using different parameters to 'tweak' to an appropriate pressure history-match in clastic reservoirs (Warpinski, et al., 1994). Early attempts to match out-of-interval fracture growth to radioactive (RA) tracers, temperature diagnostics, and early microseismic studies using pseudo-3D and planar-3D models showed the benefit of planar-3D models in matching hydraulic fractures where the fracture dimensions may propagate away from the injection point or may involve complex behaviour at bounding layers (Barree & Winterfeld, 1998; Johnson Jr & Woodroof, 1996). However, complex layer behaviours and elevated net pressures are common to coal stimulation treatments and lead to uncertainties in geometry in North American coals using pseudo-3D and planar-3D models (Conway, et al., 1997; Johnson Jr, 1995).

4.2 Modelling Coal Hydraulic Fracturing Treatments in Australia

As the specific stress conditions of eastern Australia deviate significantly from generic assumptions of a normal stress regime ($S_v > S_H > S_h$), the one-dimensional conceptualisation of stress is the input that constrains most pseudo-3D and planar-3D hydraulic fracture simulators (Tavener, et al., 2017). Early attempts at history-matching coal stimulations in Australia focused on characterising and managing the manifestations of non-planar and pressure-dependent effects to place more effective well treatments (Badri, et al., 2000; Johnson Jr, et al., 2002; Morales & Davidson, 1993). However, data from coal mine back studies of hydraulic fractures in Queensland and New South Wales (Jeffrey, et al., 1992; Jeffrey & Settari, 1995, 1998; Jeffrey, et al., 1998), showed that non-planar components observed in early North American coal stimulations (Diamond, 1987) were more widespread in the Australian stress environment and represent a significant volume of the hydraulic fracture pumped within a coal stimulation treatment.

Several cases have been presented from the Surat Basin, where developing a thorough understanding of the stress state and employing multiple diagnostics and more advanced modelling methods were used to improve understanding and management of non-planar effects. These studies included: one-dimensional stress profiling; varying well azimuth and inclination; characterising natural fracture azimuth and leak-off interaction through extensive multilayer diagnostic fracture injection testing (DFIT) data; and employing multiple diagnostics (i.e., pre- and post-sonic anisotropy logging, surface deformation tiltmeters, downhole microseismic monitoring, and radioactive tracers) to assess dimensions and progression of treatments, and often used a planar-3D model (Thomas Flottman, et al., 2013; Johnson Jr, Glassborow, et al., 2010; Johnson Jr, Scott, et al., 2010; Megorden, et al., 2013; Scott, et al., 2010). However, the non-planar components could not be adequately described by these studies and the secondary benefits of non-planar fractures cannot be estimated to guide decisions regarding future treatment strategies.

Recently, the work of Pandey et al. (2017) used several case studies from the Surat Basin to compare the fracture predictions of various two-dimensional fracture simulators, contrast the differences in fracture geometries observed between modelling and field measurements, and highlight the areas where a significant improvement in fracture modelling is required. One of the major findings of this study was that the simulated fracture height was greater than the observed values for the majority of well stages, irrespective of the modelling assumptions. This was in part attributed to the simulators' inability to capture shear slip at weak interfaces, which is well documented, including the differences in fracture crossing from low to high Young's modulus and vice versa (Gu & Siebrits, 2006). In one case from Vibhas J. Pandey, et al. (2017), the simulated fracture height was double the observed value, yet the simulated half lengths were quite similar to observations.

This implies a significant mismatch in the distribution of fracture volume and highlights the need to capture the vertical termination and horizontal growth of fractures as they contact the various interfaces between coals and interburden. This horizontal growth was clearly observed in tiltmeter surveys of some of the well stages and has also been documented following mine-back operations in coals (Jeffrey, et al., 1992). Other findings by Jeffrey (1992) included the difficulty to pressure match water (as opposed to gel) treatments and model their resultant fracture geometries and predict the higher fracture gradients that were frequently observed in shallower regions (close to 400 mRT). The former was attributed to the fracture complexity that could not be captured by the tested simulators, while the latter meant that modelling results were unreliable when the fracture gradient approached

and or exceeded the overburden pressure gradient.

4.3   Unique Aspects of Modelling GPI in Hydraulic Fracture Models

The modelling of GPI in a hydraulic fracture will be innovative in several ways. Foremost, it requires the development of a model of microparticle suspensions which simultaneously bridges the scales at which colloidal and non-Brownian behaviours exist. This will provide a unified modelling framework in which the viscous, mechanical, inertial, electrostatic, and thermodynamic forces relevant to transport in porous and fractured media can be compared, and the dominant mechanisms identified. To the best of the team's knowledge, a direct numerical simulation strategy of this kind has not yet been presented in the literature. The combination of numerical and potential experimental data will then be used in defining new, large-scale analytical models of micro-suspension transport in porous and fractured media.

In the context of rheology, this project comprises innovation in both fundamental and applied scientific contexts. At the fundamental level, the direct numerical simulation will be employed to predict the rheology of microparticle suspensions in inertial, non-Newtonian flows and at high solid volume fractions. A review of the state of the art (Bedrikovetsky, et al., 2011; Ness & Sun, 2015; Trulsson, et al., 2012) shows that this has not been done to date. At the applied level, the successful development of this model will result in a procedure for numerical rheometry, which will facilitate the virtual exploration of new and or novel suspension formulations.

In the area of colloid transport, attachment and detachment this project is innovative in its development of a direct numerical simulation approach that captures all of the forces acting on a particle. This will provide insight that reduces the dependence of large-scale transport models on parameters and experimental tuning. The modelling will also elucidate the relative influence of the prevailing forces and their dependence on environmental conditions (e.g., fluid salinity).

4.4   Go Forward Strategy

To summarise, there exists a need to explore the potential benefits of propping non-planar and secondary fractures and better strategise treatments in complex stress environments using fully three-dimensional modelling. This approach could allow the ability to track the progression and potential width characteristics of any non-planar elements to enhance the effectiveness of hydraulic fracture stimulations. This will require a more thorough description of the full stress tensor as well as a good description of the natural fracturing that will interact with the propagating hydraulic fracture. After an extensive review of several potential models (Aghighi, et al., 2019), studies have commenced on modelling fracture behaviour with Elfen TGR, the most applicable commercial three-dimensional finite element-discrete code for GPI application.

A companion project being undertaken at the UQ Centre for Natural Gas has completed the first iteration of three-dimensional modelling of hydraulic fracture growth in coal measures representative of the Surat Basin. It aims to demonstrate the influence of stress regimes that vary from normal, to strike-slip ($S_H > S_v > S_h$), to reverse faulting ($S_H > S_h > S_v$) on the vertical and horizontal growths in a simplified, homogenous medium that is representative of the conditions of interest. These results have clearly shown the changes in fracture propagation (i.e., preferential growth direction, non-planar fracture turning) that occur as a result of relative changes in the three principal stress magnitudes. The next step in this work is to enhance the model with stratigraphic heterogeneities that manifest as

planes of weakness, stress barriers, and preferential fracture and damage paths. This will be supported by models of varying discrete fracture networks to ascertain the optimal sizing of GPI and introduce flow mechanics derived from small-scale modelling of GPI flow, straining and embedment behaviour. Finally, once a created fracture dimension is defined, reservoir simulation of the resulting stimulated reservoir volume can be evaluated in a reservoir simulation framework incorporating uncertainty in parameters to determine the likely distribution of outcomes.

5 Transport, Straining and Embedment Behaviour in GPI

It is important to understand and model the particle transport and embedment behaviour in GPI, as it significantly affects the fracture conductivity, the performance of the hydraulic fracturing stimulation and overall improvement of well productivity. This section consists of two parts. The first subsection summarises the main findings from the modelling of production enhancement accounting for particle embedment, using typical coal samples from the Bowen and Surat Basins in Queensland. In the second subsection, modelling of particle transport and leak-off in coal fractures intersecting with a cleat demonstrates the effects of particle and cleat sizes, particle concentration and sedimentation on the leak-off process. Both of these investigations contribute information necessary to the planning of GPI implementation.

5.1 Modelling of embedment, fracture conductivity, and productivity

5.1.1 Methodology

The modelling of proppant embedment, fracture conductivity, and production enhancement consists of three sub-models (You et al., 2019; Wang et al., 2021):

1. The first stage is the modelling of fracture surface deformation due to particle embedment. As an improvement from the previous linear elastic deformation model, the current study implements an elastoplastic finite element model to calculate the embedment depth and fracture deformation under varying particle packing density, effective stress and material parameters.
2. In the second stage, the modelling of fracture permeability under the influence of embedded particles is undertaken using the coupled lattice Boltzmann-discrete element model (LBM-DEM). The 3D fluid domain is discretised using a D3Q27 lattice, and a two-relaxation-time (TRT) collision operator is adopted for better simulation accuracy and stability than the conventional BGK operator (Wang et al., 2021).
3. In the third and final stage, the modelling of the productivity index after well stimulation by microparticle injection is performed using a mathematical model for radial flow from the reservoir towards the wellbore.

5.1.2 Modelling results

The material properties of the proppant particles include the Young's modulus (E), E = 70 GPa, Poisson's ratio (v), v = 0.17, and density (ρ), ρ = 2410 kg/m^3. The representative coal samples from

the Bowen and Surat Basins, Queensland (Australia) are modelled as a Mohr-Coulomb material with properties listed in Table 1 below, which include E, ρ, ν, cohesion (c) and friction angle (ϕ). A vertical closure stress is applied downwards on the top of the upper half of coal sample. The bottom of the lower half of coal is restrained with no vertical displacement. The fracture surface profile after deformation in the presence of the embedded particle is calculated using an axisymmetric formulation of the finite element method.

Table 1: Material properties of the representative coal samples

Sample No.	Place of origin	E	ρ	ν	c	ϕ
1	Bowen Basin	3GPa	1500kg/m^3	0.25	1.27 MPa	30°
2	Surat Basin	3.123GPa	1500kg/m^3	0.43	5MPa	41.8°

Under the confining stress, the upper and lower parts of coal rock near the particle surface protrude downward and upward, respectively (Figure 2). It results in a decreased fracture aperture and associated permeability. Further increase of stress will lead to the significant protrusion of coal into the fracture, causing its ultimate closure. Consequently, the permeability will drop to zero at a high level of stress. Figures 2 (c) and (f) demonstrate that coal sample 1 experienced significantly greater embedment than that of sample 2. This indicates that sample 2 can better sustain the same level of effective stress than sample 1. Simulations on a higher particle packing result in a similar displacement trend, despite a lower magnitude of embedment.

(a) Sample: $\sigma_e = 10^{-5}$ (b) Sample 1: $\sigma_e = 10^{-4}$ (c) Sample 1: $\sigma_e = 10^{-3}$

(d) Sample 2: $\sigma_e = 10^{-5}$ (e) Sample 2: $\sigma_e = 10^{-4}$ (f) Sample 2: $\sigma_e = 10^{-3}$
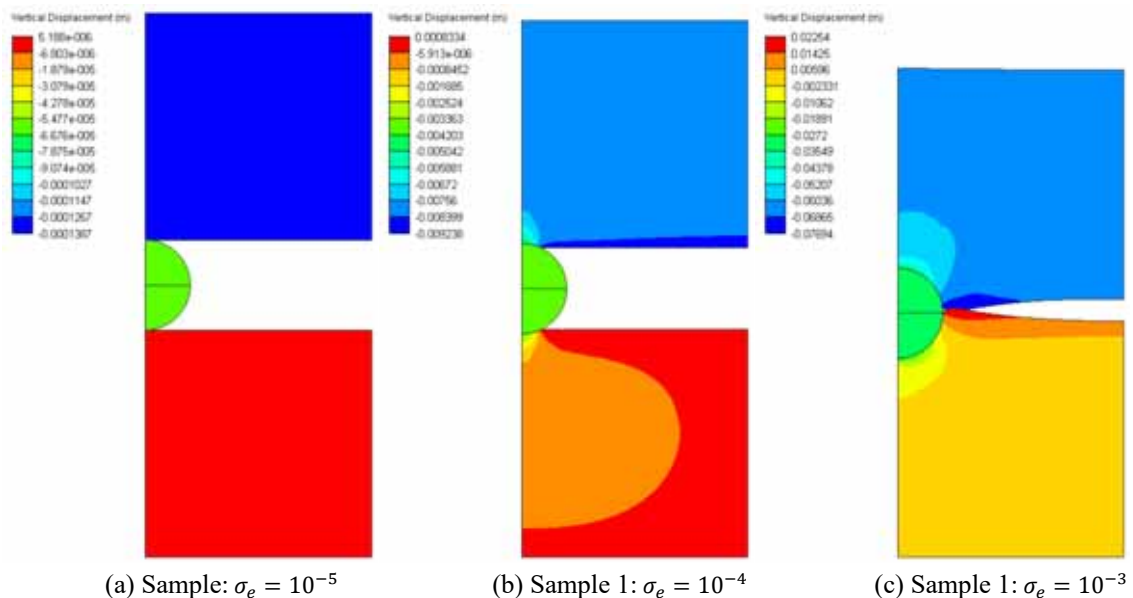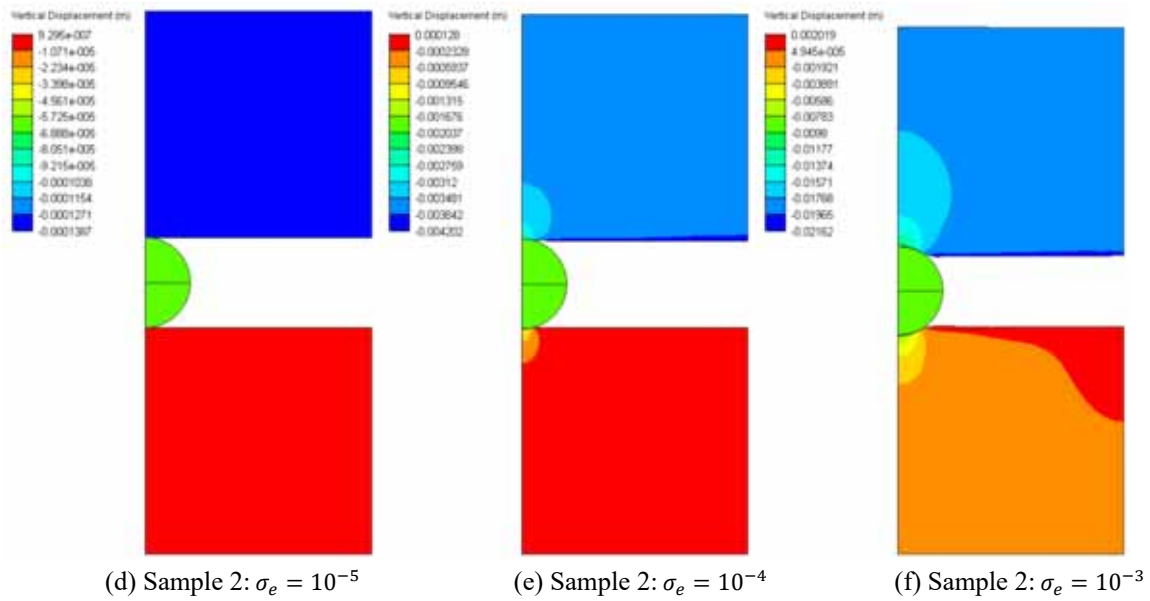
Figure 2: Elastoplastic finite element modelling results of particle embedment in coal, showing the vertical displacement (m) under increasing effective stress σ_e for ρ_p=0.2: (a-c) Sample 1 and (d-f) Sample 2

The embedment and permeability analyses can be summarised simultaneously. The resulting fracture permeability reduction factor, f, as a function of particle packing ratio, ρ_p, are presented in Figure 3 for a range of effective stress values, σ_e. Solid and dashed curves show the results of elastoplastic and linear elastic deformation models, respectively. For the fixed values of ρ_p and σ_e, an elastoplastic model yields a lower fracture permeability than a linear elastic model. The non-monotonic function $f(\rho_p)$ indicates an optimal ρ_p can achieve the maximum permeability under each effective stress condition.

(a)   (b)
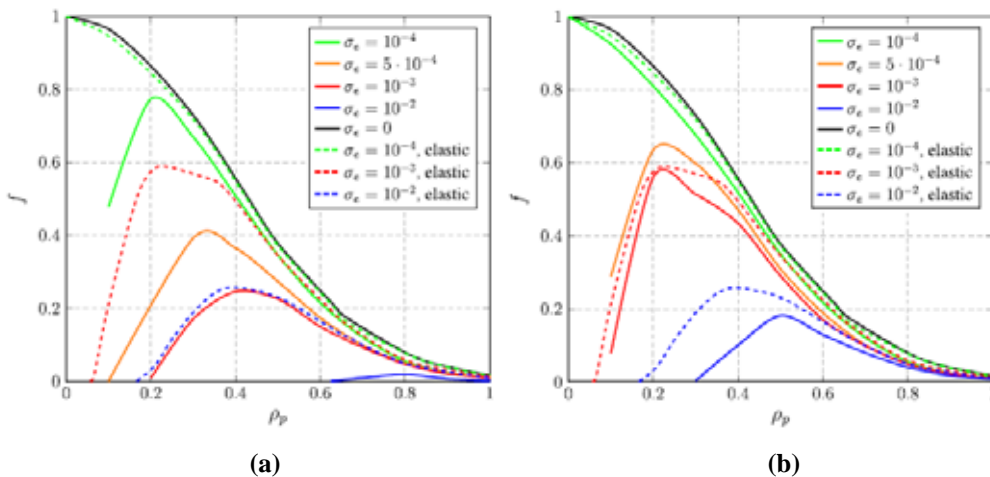
Figure 3: Permeability reduction factor versus particle packing ratio for different values of effective stress, showing reduced fracture conductivity when elastoplastic proppant embedment is considered (under the same closure stress): (a) Sample 1 and (b) Sample 2

The effect of injection pressure on the well productivity index (PI) is shown in Figure 4. The PI value increased with the stimulation radius and injection pressure. With the same injection pressure, a larger permeability enhancement of Sample 2 led to a higher PI than Sample 1. Meanwhile, the elastoplastic model yielded a smaller PI value if compared to the elastic model, which was a result of

smaller permeability enhancement under the same effective stress.

(a)   **(b)**
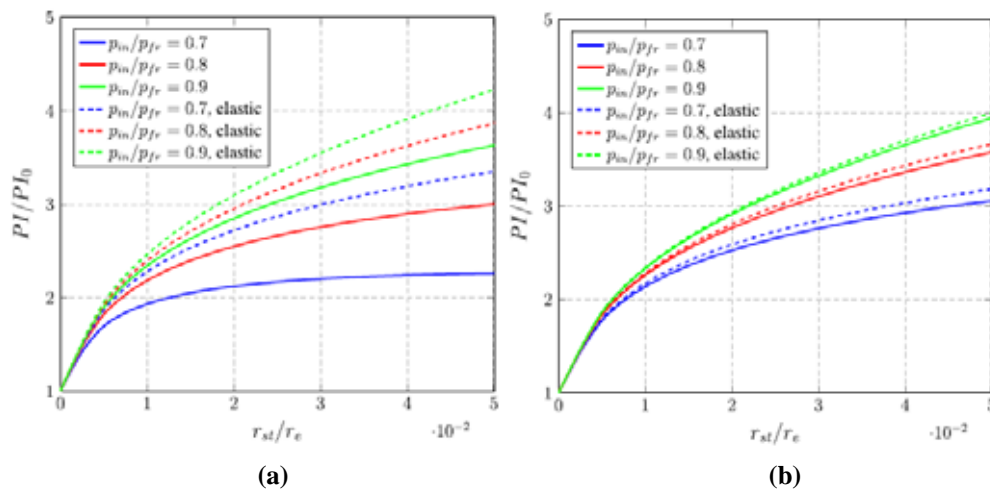
Figure 4: Productivity index versus stimulation radius under varying injection pressure for (a) Sample 1 and (b) Sample 2

The effect of fracture compressibility on the PI is presented in Figure 5. A higher value of fracture compressibility generally allows larger proppants to be injected into the formation. Consequently, the PI value increased with the fracture compressibility. Under the same fracture compressibility, the elastoplastic model yielded a smaller production enhancement increase than the elastic model.

(a)   **(b)**
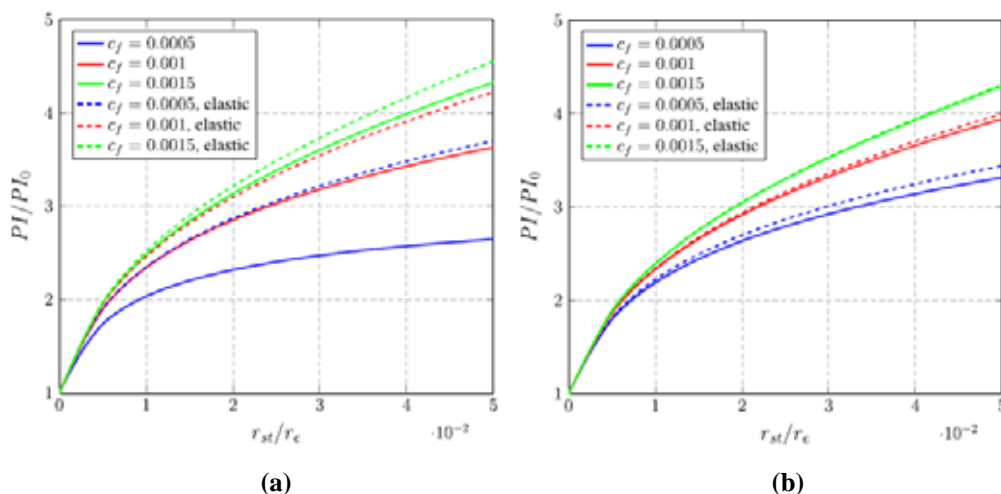
Figure 5: Productivity index versus stimulation radius at varying fracture compressibility for (a) Sample 1 and (b) Sample 2

5.1.3   Summary

A combined predictive model is developed and presented in this section, using elastoplastic FE modelling for proppant embedment prediction, the LBM for permeability evaluations, and a mathematical model for resultant well productivity calculation. Modelling of production enhancement using microparticle injection in naturally fractured reservoirs predicts that compared to linear elastic deformation of the coal fracture, the elastoplastic deformation is less significant outside the contact area between the particle and fracture surface. However, the particle embeds more deeply into the rock under elastoplastic deformation. It leads to smaller fracture width and lowers fracture permeability under the same effective stress conditions. For each effective stress value, an optimum particle aspect ratio yields the maximum fracture permeability. The developed methodology in the present work can be used for designing and evaluating stimulation outcomes with microparticle

injection for a range of uncertain reservoir parameters and a range of coal types.

5.2 Particle transport modelling

Three key problems arise in the transport of proppant particles to the coal cleat network. Firstly, the control of the particle size distribution becomes expensive and intractable at the micron scale, resulting in large particle size ratios which allows segregation by particle size in the primary hydraulic fracture. Secondly, for small cleat and fracture widths the entire proppant suspension can jam. This behaviour, commonly termed screen-out, significantly reduces the effectiveness of hydraulic fracturing treatments. Thirdly, proppant leak-off from the hydraulic fracture into the intersecting cleats is required to stimulate the far-field network, but can be inhibited depending on the physical parameters. In this work, the LBM-DEM has been applied to elucidate unique behaviours pertaining to each of these problems. Section 5.2.1 summarises size segregation results from a manuscript under consideration for publication in the Journal of Fluid Mechanics (Di Vaira et al., 2021a); Section 5.2.2 summarises key elements of a paper recently presented at SPE URTeC (Di Vaira et al., 2021b); and Section 5.2.3 presents the proppant transport modelling results of the paper presented at SPE URTeC 2019 (You et al., 2019). The significance of these results to reservoir stimulation are summarised in 5.2.4. Overall, the result presented here are now at a point where they can be scaled to field-scale design of GPI implementation.

5.2.1 Size segregation

Hydraulic fracturing simulators and studies of fracture flows typically idealise the primary hydraulic fracture as a straight channel. The same approach is taken here for the test cell pictured in Figure 6, which is periodic in the flow (x) and vertical (z) directions. For these types of particle-laden channel flows, the accumulation of particle interactions cause a bulk migration of the particles to the channel centre. In general particles of larger size will also preferentially migrate to the channel (Lyon & Leal 1998). Thus far, however, suspensions have only been modelled with particles of one (monodisperse) size or two (bidisperse) different sizes, which does not reflect the continuously distributed (polydisperse) sizes of actual proppant.
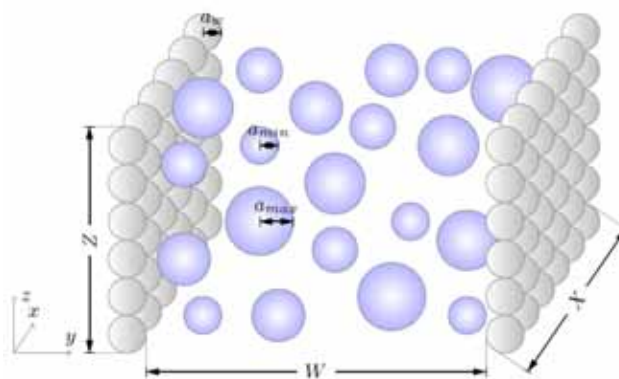
Figure 6: Schematic of the numerical channel used to study the bulk migration and size segregation of polydisperse suspensions.

The five distinct polydisperse and bidipserse distributions in Table 2 are implemented as the basis for investigating the effect of polydispersity on bulk migration and size segregation. The size distribution functions for the polydisperse suspensions are also depicted in Figure 7a, along with a comparison of

P_2 and B_2 in Figure 7b. The distributions are characterised by their first three statistical moments (mean, variance, skewness) since the rheologies of bidisperse and polydisperse suspensions are completely described by their first three statistical moments (Pednekar et al., 2018). P_1, P_2 and P_3 are designed to have widely varying mean, while P_2, $P_{2,1}$ and $P_{2,2}$ have matching mean but widely varying variance and skewness.

Table 2: The first three statistical moments of the corresponding polydisperse and bidisperse suspensions implemented in this work, demonstrating statistical equivalence.

Distribution	Mean	Variance	Skewness
P_1, B_1	1.58	0.35	1.5
P_2, B_2	1.88	0.34	0.92
P_3, B_3	2.47	0.28	0.17
$P_{2,1}, B_{2,1}$	1.89	0.4	0.9
$P_{2,2}, B_{2,2}$	1.89	0.28	0.78

(a)	(b)
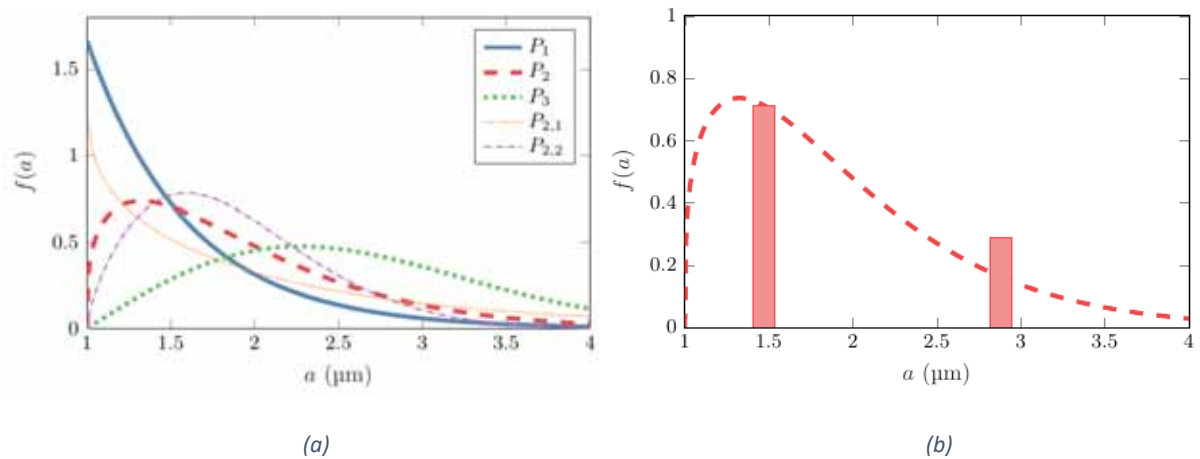
Figure 7: (a) Probability density functions, f(a), by particle radius, a, of the five distinct polydisperse size distributions. (b) Comparison of a continuous polydisperse distribution, P_2, and its equivalent bidisperse suspension, B_2.

Firstly, Figure 8 shows a plot of the scalar bulk migration, C, as the suspensions flow along the channel length (normalised by the width), L/W. A lower C indicates that the channel-averaged particle mass is closer to the channel mid-plane. Graphical representations of P_2 and B_2 are depicted in Figure 8 to aid in interpreting the migration and size segregation. Remarkably, the polydisperse (Figure 7a) and bidisperse (Figure 7b) bulk migrations match very closely, suggesting that the cross-channel migration of a suspension with two or more particle sizes can be completely characterised by its first three statistical moments. Fundamentally, this dependence on the moments is due to a dual dependence of migration on particle size and the suspension rheology on solid volume fraction and particle size distribution. A graphical representation of a polydisperse suspension, P_2 (Figure 9a), and its statistically equivalent bidisperse suspension (Figure 9b), each captured at L/W≈1800.
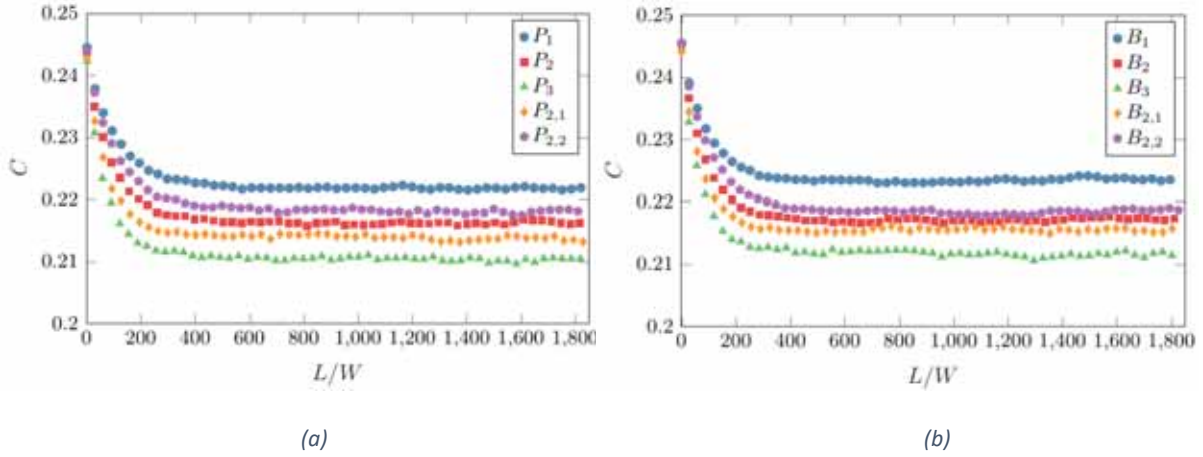
Figure 8: Development of bulk scalar dispersion function, C, along normalised channel length, L/W, demonstrating excellent agreement between (a) polydisperse suspensions and (b) bidisperse suspensions. A lower C indicates that the channel-averaged particle mass is closer to the channel mid-plane.
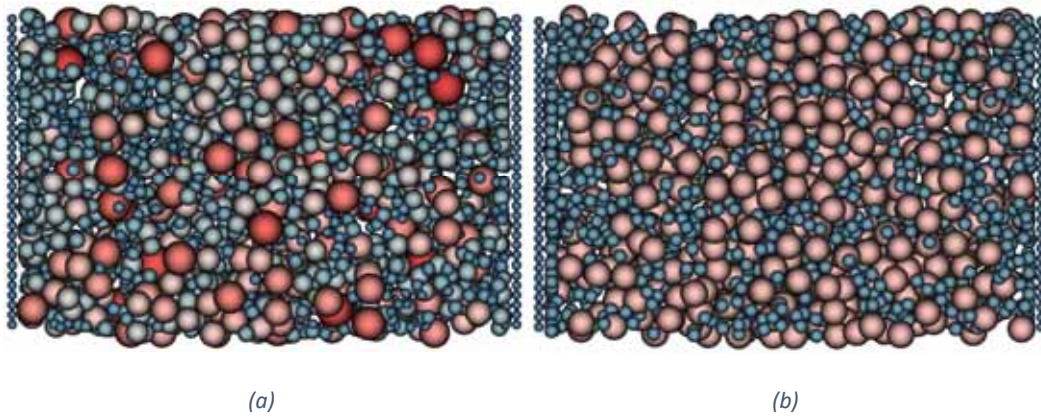
Figure 9: Graphical representation of (a) a polydisperse suspension, P_2, and (b) its statistically equivalent bidisperse suspension, B_2, each captured at $L/W \approx 1800$.

When the bulk solid volume fraction, ϕ, reaches a value of approximately $\phi = 0.4$, the number of particles which migrate to the channel centre becomes so high that a solid plug forms, and the suspension around the channel mid-plane moves as a single unyielded solid. Here, four increasing solid volume fractions, $\phi \in [0.2, 0.3, 0.4, 0.5]$, are simulated for P_2. Figure 10 depicts the cross-channel velocity profiles of each ϕ, which are all blunted compared to the pure fluid case due to the particle migration. For $\phi = 0.4$ and 0.5, complete flattening of the velocity profile indicates the region where a plug has formed, with the plug becoming larger as ϕ increases. A graphical illustration for $\phi = 0.5$ is shown in Figure 11, where the smallest particles compose the plugs. This contrasts with the previous results with no plugging, where the largest particles preferentially migrated to the channel centre. This result has not been observed in the literature hitherto.
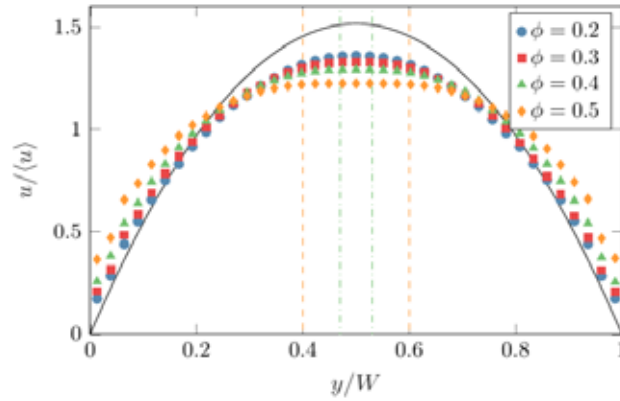
Figure 10: Comparison of velocity profiles for increasing ϕ for P_2, measured at $L/W \approx 1800$. Black solid line indicates pure fluid velocity profile, demonstrating blunting of suspension velocity profiles, and vertical dotted lines indicate the plugged regions for $\phi = 0.4$ and 0.5.
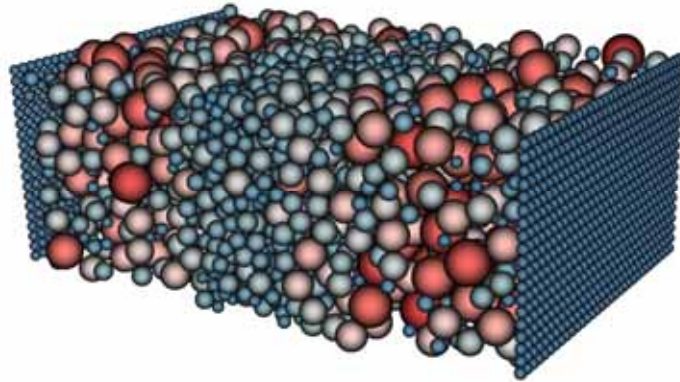
Figure 11: Graphical representation of P_2 for $\phi = 0.5$, captured at $L/W \approx 1800$, demonstrating formation of plug with small particles.

5.2.2   Screenout

Screenout is a symptom of the fracture channel and cleat morphology of coal reservoirs. Near the wellbore the cleat network is well connected by the primary hydraulic fracture. With increasing distance from the wellbore, however, the mean hydraulic fracture width decreases, turns and sharp discontinuities become more frequent, while the apertures of the cleats decrease in size. In these regions of reduced channel width static bridges of proppant form across the channel, which are held in place by the contact forces between proppant particles and fracture walls, as well as the hydrodynamic forcing of the fluid. This bridging phenomenon is the cause of screen-out. Currently, however, hydraulic fracturing simulators use a fracture width to proppant diameter ratio of 2.5 to indicate screen-out, which is an industry-wide standard. In the subsequent results this is shown to be inadequate, and a new methodology is proposed.

The screen-out data in this work is obtained using the numerical test cell depicted in Figure 12 (Di Vaira, et al., 2022.) The key feature of this test cell is the ridges of the channel walls, which are included to induce the short-range transverse particle motion required to cause bridging, as well as provide surface asperities to which particles can attach via particle-wall electrostatic attraction. The ridge height and spacing yields reasonable bridging and electrostatics results, however a sensitivity analysis of these parameters should be conducted in future work when considering rough fracture surfaces.

The channel width, w, is defined as the average distance between surfaces in the z-direction.
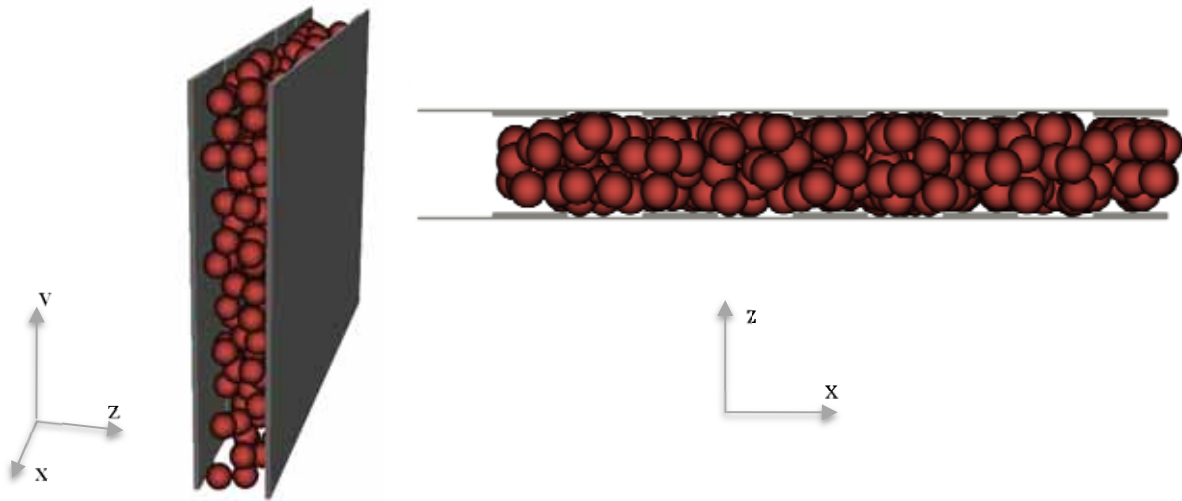
Figure 12: Isometric view (left) and 2-d top view (right) of numerical test cell used to measure screen-out probabilities.

Fluid flow is modelled with a constant pressure gradient of 4 MPa.m^{-1} in the x-direction. Proppant is injected at the inlet of the channel at constant ϕ and leaves the simulation when it exists the domain, however the fluid boundary is periodic in the x-direction. Both the fluid and solid boundaries are periodic in the y-direction, representing a fracture of infinite vertical height. The fluid is Newtonian with constant viscosity and density matching water and the proppant has a density of 3500 kg.m^{-3}, however no gravity is implemented in the vertical direction. The proppant particles have constant diameter $d = 5$ μm. The simulation is terminated once the proppant travels an equivalent of ten channel lengths.

For several separate simulations using the test cell in Figure 13 at an identical combination of parameters, some may screen-out and some may not. Consequently, there exists a probability of screen-out, P, which is the number of simulations in which screen-out occurs divided by the total number of simulations (within the finite test time). P depends on the likelihood of particles coming into contact and then maintaining a stable bridge, both of which increase with ϕ (Sharp & Adrian, 2005). In these tests w/d and ϕ are varied as the key parameters to elucidate the fundamental dependence of P on each. Figure 13a shows the results obtained for $w/d = 1.8$, where each marker is the P obtained from ten parametrically identical simulations. As expected, P increases with ϕ, and there exists a lower limit of ϕ below which screen-out never occurs ($P = 0$) and a higher ϕ above which bridging always occurs ($P = 1$).
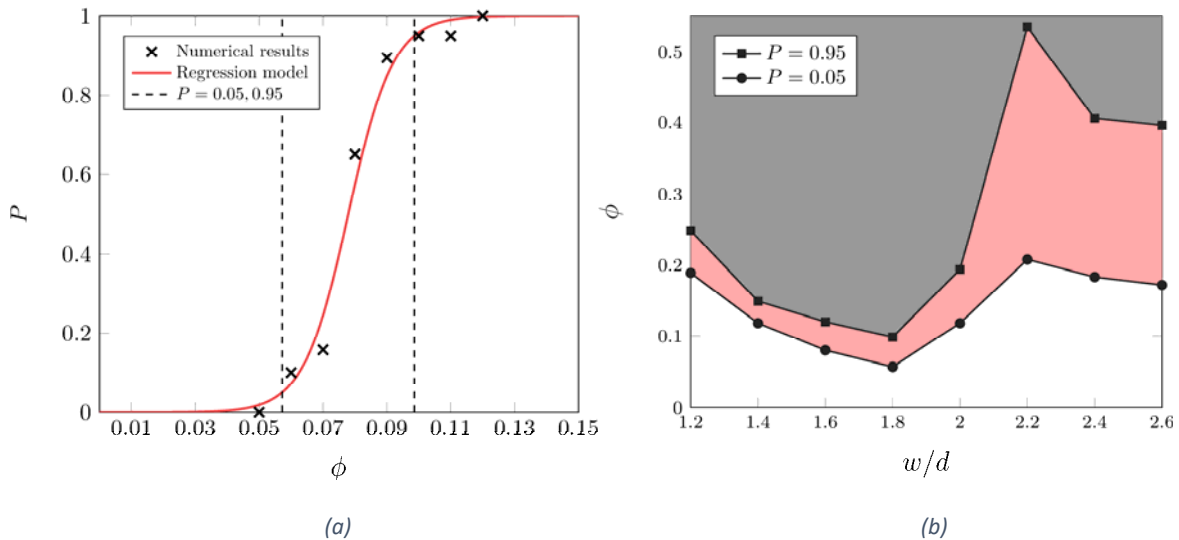
Figure 13: (a) Probability of screen-out, P, obtained at discrete φ with the numerical test cell at w/d=1.8. The discrete φ are predicted with a continuous binomial regression model, from which predicted φ at P = 0.05 and 0.95 are obtained. (b) Plotting of P = 0.05 and 0.95 points for a range of w/d. The grey and white regions represent where screen-out will and will not occur, respectively, for 5% of cases.

The red line in Figure 13a is a continuous prediction of the discrete simulation results using a binomial regression model. From this the predicted values of ϕ at which $P = 0.05$ and 0.95 are obtained (vertical dashed lines). These values are plotted in Figure 13b, and by repeating for many values of w/d the interval where $0.05 < P < 0.95$ is obtained as the red region. In other words, above and below the red region are the combinations of w/d and ϕ for which screen-out will and will not occur for 5% of cases. Dependence on w/d is evident, while two distinct regimes can be identified for $w/d \leq 2$ and $w/d > 2$, aligning with two different types of bridge configurations. For $w/d \leq 2$, ϕ decreases to a minimum at $w/d = 1.8$ because the contact angles of the bridges increase the likelihood of maintaining a stable bridge compared to other w/d.

In terms of scaling these results to a reservoir-scale model, Figure 13b can be incorporated into a discrete fracture network (DFN) model coupled with suspension flow. The DFN can be obtained via the type of integrated pressure dependent permeability testing subsequently presented in Section 8, which gives a transient prediction of the cleat network apertures. The w/d and ϕ dependent data of Figure 13b would therefore inform a much more accurate map of where proppant blockage would occur, compared to using the current industry-wide standard of $w/d = 2.5$.

5.2.2.1   Electrostatics

For micro-proppants, which are on the order of 1-50 µm (compared to 210-400 µm for conventional 40/70 mesh proppant), electrostatic forces become significant relative to the hydrodynamic forcing of the fluid. These electrostatic forces, which cause proppant aggregation and surface deposition, greatly affect the onset of bridging. Particles which attach to the fracture wall at a surface asperity (deposition) effectively reduce the channel width and increase the likelihood of collisions, consequently accelerating the bridging process (Kang et al., 2018). However, hydraulic fracturing simulators currently have no way of factoring in electrostatics.

Here, electrostatics is incorporated into the screen-out framework presented above. To do so, the complete DLVO forces have been integrated into the existing LBM-DEM numerical model and rigorously verified. For a full description of the individual forces and their implementation please

refer to Di Vaira et al. (2021b). The key DLVO parameter investigated here is the system Hamaker constant, A_{132}, which represents the attractive potential between particles and walls. Two wall and two particle materials are modelled (with water as the fluid), resulting in the four material combinations shown in Table 3. The profiles of the total electrostatic force, F_e, with separation distance between a particle-particle and particle-wall, h, are depicted in Figure 14. Generally, the large attractive minimum causes surface attachment, with increasing A_{132} resulting in a higher attractive force. At a large separation distance there also exists a repulsive force barrier for most of the cases, which the particles must overcome to reach the attractive minimum. This is shown to have an appreciable effect on screen-out.

Table 3: *The particle and wall materials investigated here, with their resulting Hamaker constants, A_{132}, representing the attractive potential. Units are in zJ.*

Materials (1-3-2)	A_{132}
quartz-water-coal	2
proppant-water-coal	4.5
quartz-water-shale	8.4
proppant-water-shale	18.7
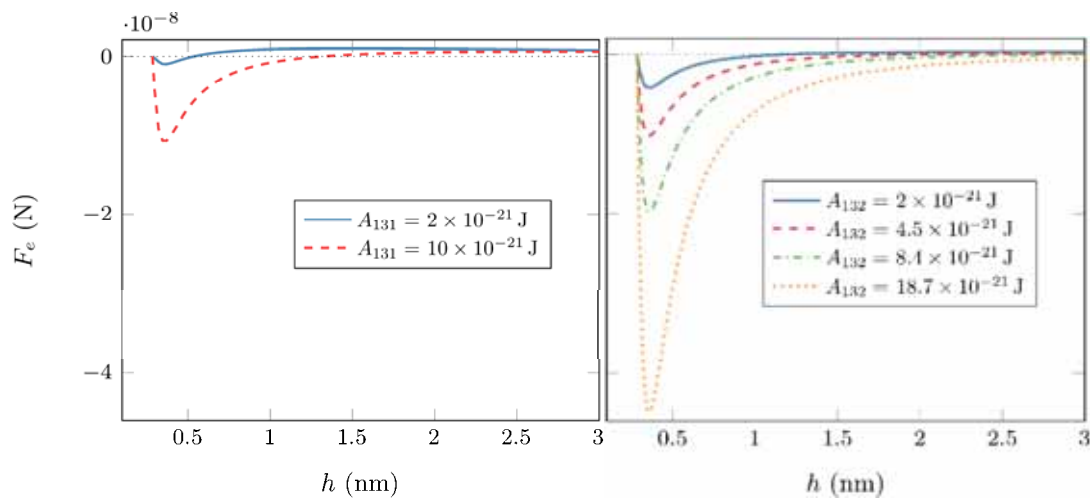
Figure 14: *Profiles of total electrostatic force, F_e, vs separation distance, h, for particle-particle (left) and particle-wall (right) interactions.*

Attachment of micro-proppant to surface asperities due to electrostatic attraction has a large influence on P seeing as it increases the likelihood of both particles contacting and forming a stable bridge. Attachment will only occur, however, below a critical pressure gradient, G^*. These values are obtained here for the four A_{132} implemented in this work via detachment tests of a single particle and plotted in Figure 15. G^* is below the implemented pressure gradient of $G = 4$ MPa.m^{-1} for $A_{132} = 2 \times 10^{-21}$ only.
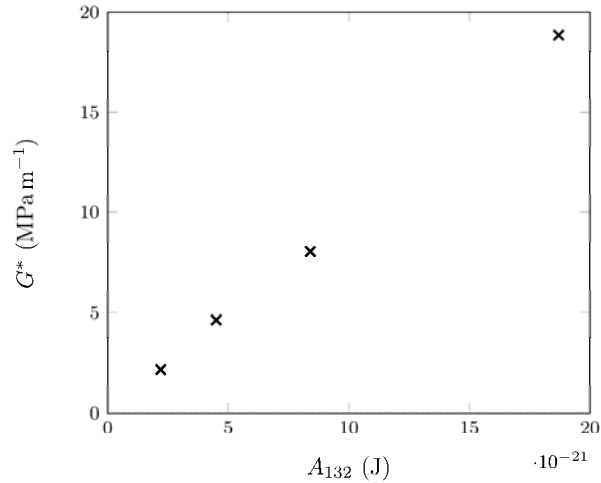
Figure 15: Critical pressure gradient, G^*, for the four A_{132} implemented in this work.

Figure 16 reproduces the screen-out regions of Figure 13b in terms of A_{132}, rather than w/d, at $w/d = 1.8$ and 2.4. Regarding $w/d = 1.8$, the ϕ at which screen-out occurs has decreased significantly for the three largest A_{132}. Indeed, $P > 0$ even at $\phi = 0.01$ for the three largest A_{132}, meaning that at least some screen-out always occurs. This shows that increased screen-out occurs due to surface attachment. For $A_{132} = 2 \times 10^{-21}$, however, the ϕ at which screen-out occurs increases, suggesting that when there is no surface attachment the presence of electrostatics in fact decreases the probability of screen-out. This must be due to the repulsive barrier at $h > 0.5$ nm. For the wider channel of $w/d = 2.4$, however, screen-out never occurs for the two lower A_{132}, even with surface attachment for $A_{132} = 4.5 \times 10^{-21}$. The values plotted are for a theoretical maximum flowing $\phi \approx 0.585$. This is further evidence that the repulsive barrier significantly influences bridging. The size of the repulsive barrier is dependent on not only on A_{132}, but also the fluid salinity, which can increase at later frac stages as the fracturing fluid is recycled. Further investigation is therefore required to quantify the impact of salinity.
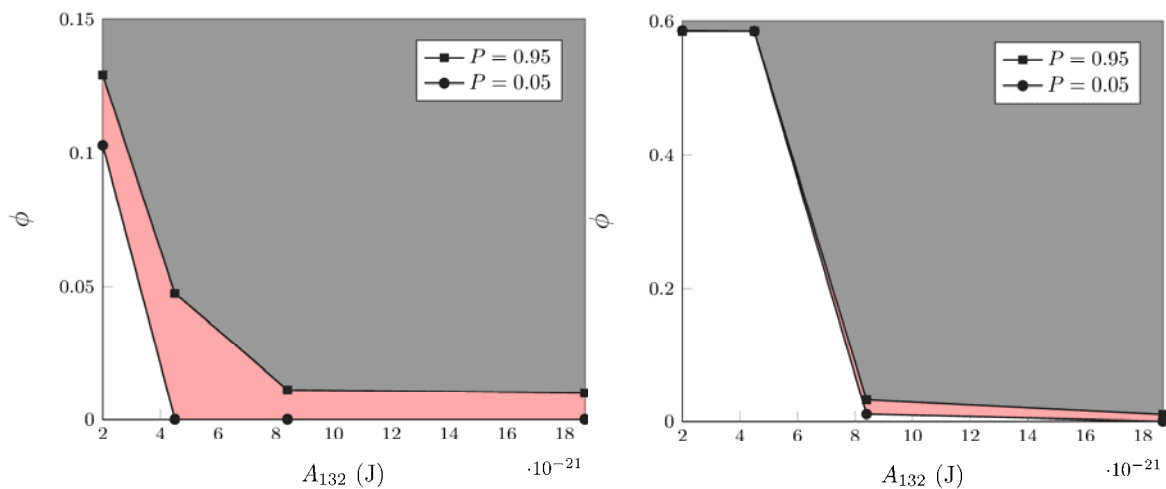
Figure 16: Dependence of the ϕ at which screen-out occurs on A_{132}, for $w/d = 1.8$ (left) and $w/d = 2.4$ (right).

5.2.3 Particle Leak-off

To analyse the effects of particle size, concentration, and sedimentation on leak-off into cleats, the bifurcation geometry shown in Figure 17 is used. The particle suspension is injected at the fracture

inlet at a constant rate and flows through the main fracture channel to the junction, where the total flux is split between the leak-off cleat and the main fracture. The inlet of the fracture, the outlet of the main channel and the leak-off channel are denoted by the subscripts 0, 1 and 2, respectively. The key measure of particle leak-off is the particle leak-off coefficient, γ, defined as the ratio of particles exiting through the cleat, n_2, to the total number of particles entering the main fracture, n_0, i.e., $\gamma = n_2/n_0$.
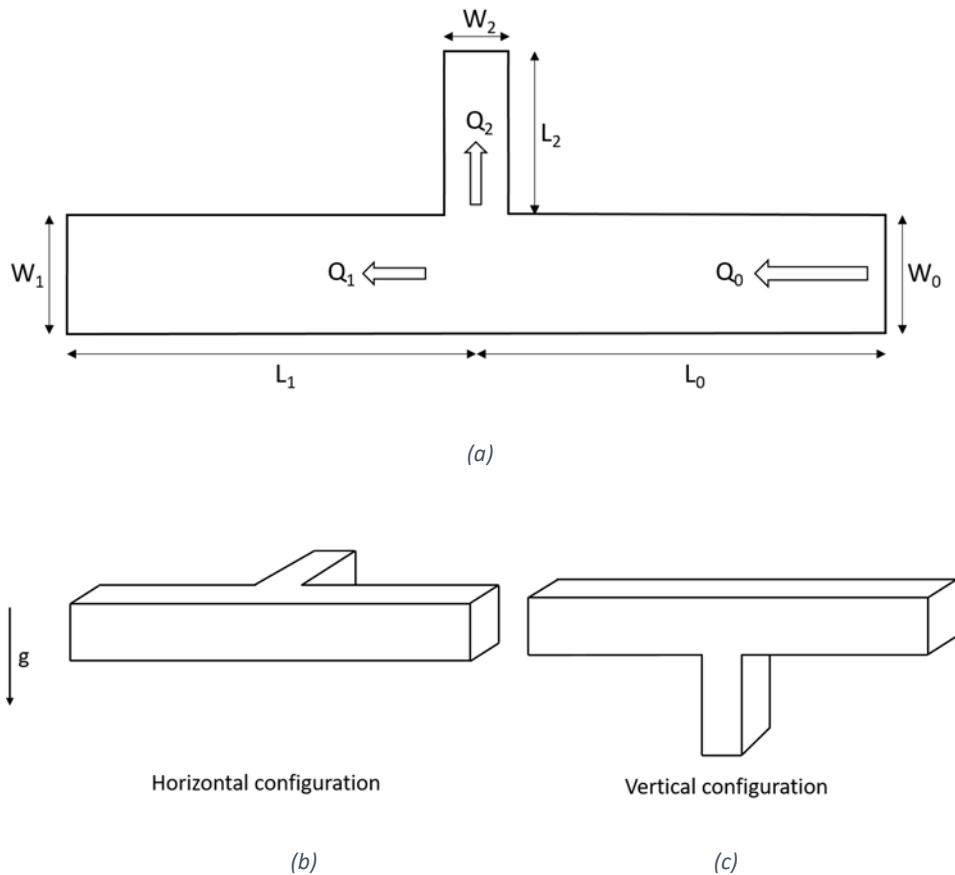
Figure 17: Schematic of the computational domain used for the leak-off problem: (a) cross section; (b) horizontal configuration; (c) vertical configuration

The dimensions of the main fracture are held constant, with $L_0 = L_1 = 5W_0 = 5W_1$. The cross section of the fracture is a square. The aperture ratio between the fracture and cleat has three different values, $W_0/W_2 = 2,3,5$, and the cleat length is $L_2 = 5W_2$. A constant flow rate Q_0 at the fracture inlet is split at the junction such that $Q_0 = Q_1 + Q_2$ and $W_1/W_2 = Q_1/Q_2$. Both horizontal and vertical configurations are implemented to investigate the effects of particle sedimentation. The channel walls are smooth, with no friction between the walls and particles.

Suspensions of mono-sized particles are injected at a volumetric particle concentration of $\phi = 0.25$, over a range of particle sizes, such that $0.2 < d/W_2 < 1$. Results show a clear decrease in particle leak-off, γ, as the cleat size, W_2, decreases (Figure 18). For particle sizes much smaller than the cleat aperture, $0.2 < d/W_2 < 0.5$, the variation of γ is insignificant. However, as the ratio d/W_2 approaches unity, a substantial decrease in γ is observed.
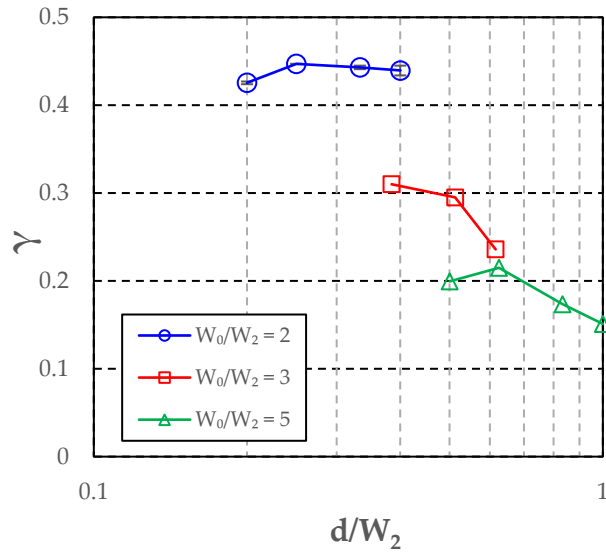
Figure 18: Variation of particle leak-off for different particle and cleat sizes

Particle distributions during the steady state flow for $d/W_2 = 0.25, 0.4, 0.5$ are shown in Figure 19. In all the cases, the fracture-cleat size ratio remains as $W_0/W_2 = 2$. Figure 19 shows particles stagnate in the fracture near the cleat entrance. This stagnation is more prevalent for larger particles. As the particle size becomes large enough (d/W_2=0.5), the junction is completely blocked, and both the suspension flow in the fracture and the leak-off into the cleat decrease to zero, as depicted in Figure 19.

(b)

(c)
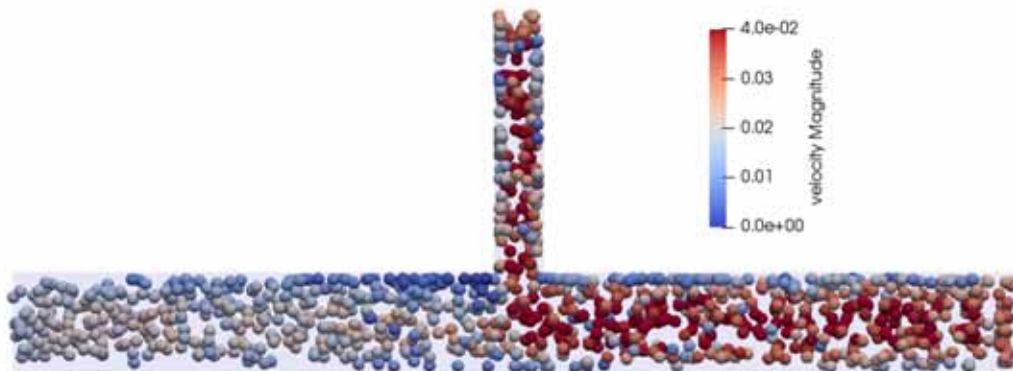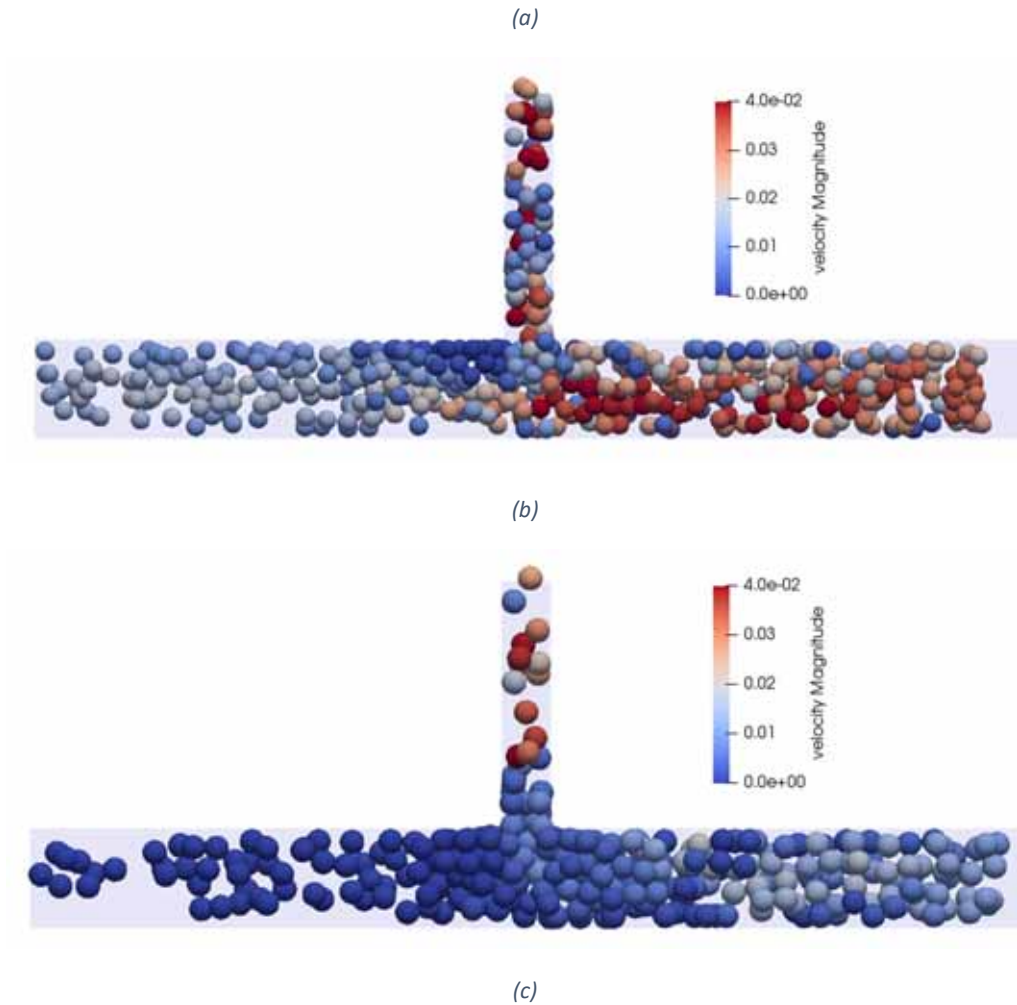
Figure 19: Particle distributions during the steady state flow for $W_0/W_2=2$: (a) $d/W_2=0.25$; (b) $d/W_2=0.4$; (c) $d/W_2=0.5$. Colours of particles denote the magnitudes of their total velocities.

The effect of particle concentration on leak-off is investigated by simulations performed for three particle sizes. Results indicate that a decrease in particle concentration yields slightly lower leak-off for all sized particles (Figure 20). This may be attributed to a reduction in particle accumulation at the junction, as well as reduced transverse particle motion due to reduced particle interactions.
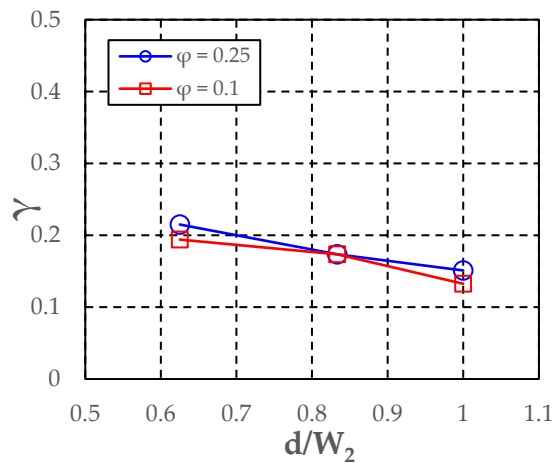
Figure 20: Effect of particle concentration on leak-off into cleats.

Finally, the effect of particle density on the leak-off is analysed. The density ratio between particles and fluid varies in the range of $1 < \rho_s/\rho_f < 2.5$ for a single particle size ($d/W_0 = 0.17$), where ρ_s and ρ_f are the particle and fluid densities, respectively. For the horizontal configuration, in which the gravity is perpendicular to the direction of flow, particle sedimentation has no effect on leak-off, i.e., γ remains constant. For the vertical configuration, however, in which the gravity is in the direction of flow through the cleat, γ increases approximately linearly with particle density, as shown in Figure 20. Particle sedimentation along the fracture leads to an increase in particle concentration at the fracture bottom, which corresponds to a higher leak-off. This trend is similar for different cleat apertures.

5.2.4 Summary

Several novel contributions have been made to the study of proppant transport in natural and induced fractures. The first regards the flow of a suspension containing two or more different particle sizes through an idealised fracture channel, where it has been demonstrated that the cross-channel migration is completely characterised by the first three statistical moments of the particle size distribution. For high proppant concentrations, smaller particles segregate to the channel centre instead of large particles, which has several implications for field application of GPI: as the proppant suspension travels through the hydraulic fracture, the smallest particles will be too far from the fracture walls to divert into the cleats, while cleats near the wellbore may be blocked by the largest particles. Consequently, it is desirable to inject proppant at a low to moderate concentration.

Next, a modelling framework has been presented which predicts screen-out based on parameters such as the solid volume fraction and channel width. This represents a significant improvement to the industry-wide standard of a single screen-out factor of 2.5, and can be incorporated into a DFN description of the complete reservoir to obtain an improved prediction of proppant straining in the cleat network. The addition of electrostatics demonstrates that, for microproppants, screen-out is strongly dependent on the material types (fines vs. proppant, coal vs. shale). Possible dependence on the fluid salinity, which can increase at later frac stages as the fracturing fluid is recycled, is also shown, which requires further investigation.

Finally, simulations of a single leak-off cleat reveal the effect of particle size. Particle build-up at the cleat entrance becomes more significant with increasing particle size, until complete blockage of the junction at $d/W_2 = 0.5$. Particle sedimentation significantly increases leak-off into a vertical cleat, yet has no effect on horizontal cleats perpendicular to the direction of gravity. Suspensions of higher concentration result in higher leak-off.

6 Reservoir Simulation of GPI Applications

In this section, we detail the results of a reservoir simulation study to investigate the effects of GPI on the gas recovery factor (RF) and productivity index (PI) under field conditions. The results contribute to the delineation of the application of GPI technology based on a given length of penetration into a coal matrix. This section summarises key aspects relevant to GPI of a larger documented and presented at the 2019 Asia Pacific URTeC meeting in Brisbane (Ribeiro, et al., 2019) and further elaborated and presented at the Brisbane 2021 Asia Pacific URTeC meeting (Santiago, et al., 2021). Once a hydraulic fracture can be defined a more complex reservoir model can be created including

the hydraulic fracture, the area and dimensioning of the stimulated reservoir volume (SRV) enhanced by GPI and the effect on overall drainage and shrinkage.

6.1 Methodology

The initially developed reservoir simulation model (Ribeiro, et al., 2019) consisted of three steps to model the stimulation benefit of graded particle injection to a radially represented volume :

Step 0 simulates the gas and water production without stimulation. During production, the well is constrained with the maximum water rate of 5 m^3/d and the minimum bottom-hole pressure (BHP) of 150 kPa. The values of PI and RF are calculated for comparison purposes.

Step 1 simulates water injection into the reservoir for GPI stimulation. The permeability reduction due to particle retention is calculated by applying the permeability reduction function (A. Keshavarz, Y. Yang, et al., 2014; You, et al., 2019). During injection, the well is constrained with a maximum water rate of 750 m^3/d.

Step 2 simulates the production after stimulation. The reservoir is divided into two zones: In the stimulated zone near the wellbore, the residual permeability after GPI application is taken from the Step 1 result. In the unstimulated zone away from the wellbore, the permeability profile is dependent on pore pressure during depressurisation, but not affected by GPI. The post-stimulation porosity varies according to the porosity-permeability cubic law. The well constraint is the same as in Step 0.

This methodology of Ribeiro et al. was extended to accommodate the hydraulic fracture and stimulated reservoir volumes as discrete cartesian volumes allowing evaluation of the effects of stimulation of graded particle injection in conjunction with hydraulic fracture (Santiago, et al., 2021). A comparison of the modelling methods for both radial injection and application with hydraulic fracturing are noted in Table 4.

Table 4: Comparison of the methodologies developed to simulate fluid production after GPI

This Paper	Ribeiro et al 2019
Cartesian Grids	Radial Grids
Contain hydraulic fracture in addition to natural fractures	Only natural fractures are present
Water injection is simulated up to a time where the desired stimulated region reaches a residual permeability higher or equal to initial permeability (i.e., kstep2 ≥ k0);	Water injection is simulated up to a time where permeability values stabilise.
Compressibility of stimulated region is cFst = 0.1cFo	The compressibility of stimulated region is nearly zero (i.e., cFst≈ 0)

6.2 Model Validation

To validate the radial model, we can evaluate a single-layer, radial flow of water with a constant pressure boundary (aquifer attached). The analytical solution of PI enhancement after GPI stimulation (A. Keshavarz, A. Badalyan, et al., 2014; A. Keshavarz, Y. Yang, et al., 2014) is used for comparison with our modelling results. Figure 21 shows that PI enhancement as a function of stimulation radius agrees well with that from the analytical solution. The trivial deviation (within 4%) validates the reservoir simulation model developed in this project.
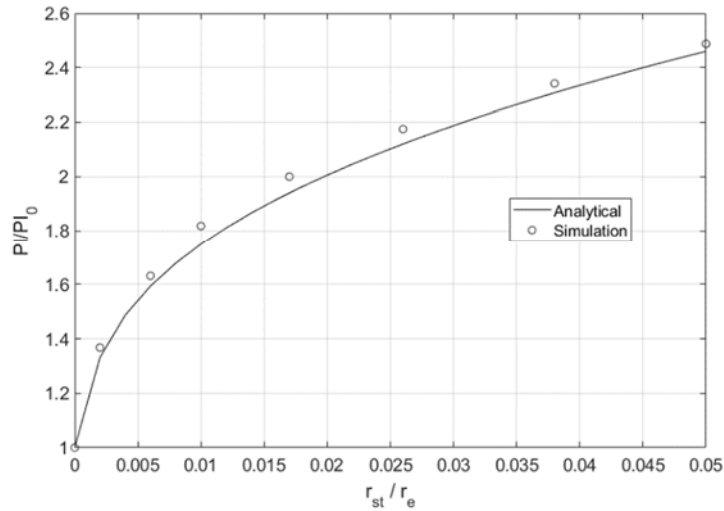
Figure 21: PI enhancement after well stimulation by GPI: comparison between the analytical solution (solid line) and simulation model (circular points).

6.2.1   Reservoir simulations with gas desorption effect

After validation, we apply the model to more general scenarios of production, by accounting for gas-water two-phase flow with gas desorption during depressurisation. The attached aquifer is removed from the reservoir model.

The geomechanical properties of the reservoir are listed in Table 5. To investigate the effect of stimulation radius on the production, the stimulation radius r_{st} is taken in the range of zero to 5% of the reservoir radius r_e in this study. The larger r_{st} results from the injection of smaller particles during GPI stimulation. The maximum r_{st} of $0.05r_e$ corresponds to the injected particle radius of 55μm. The gas and water production histories, bottom-hole pressure and profiles of gas content in the reservoir are obtained from reservoir simulation. Modelling results reveal that GPI stimulation leads to (a) slower decrease of the well BHP to maintain the constant water rate at the initial stage; (b) higher pressure drawdown thus enhancing gas desorption near-wellbore; and (c) more efficient depressurisation of the reservoir, with stronger desorption in areas far from the well (Figures 22 and 23).

Table 5: Geomechanical properties of the reservoir

Property	Value
Confining stress (σ)	13.1 MPa
Pore pressure (P)	6.945 MPa
Biot's constant (α)	1
Poisson's ratio (ν)	0.3
Young's modulus (E)	3,000 MPa
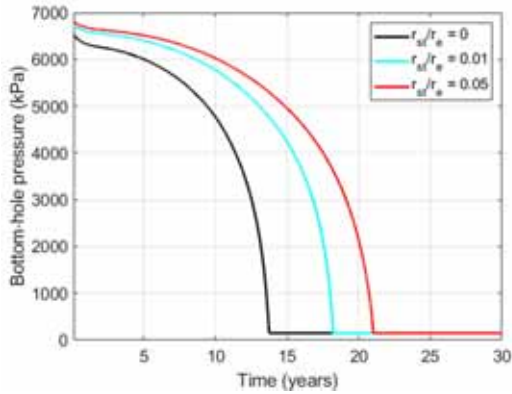
Figure 22: Variation of bottom-hole pressure with time for differing radii of stimulation.
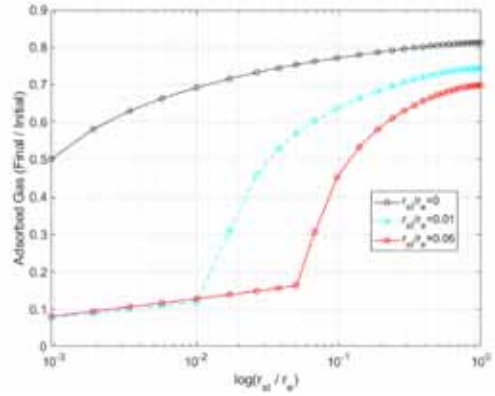
Figure 23: Profiles of gas content after 30 years of production for differing radii of stimulation. GPI (blue and red curves) enhances gas desorption in the whole reservoir.

The effects of GPI stimulation on gas production rate and recovery factor are presented in Figure 24. After the minimum BHP is reached, higher peak gas rates and RFs are consistently obtained from larger stimulated zones (Figure 24). We calculated the PIs for gas and water phases separately. At the beginning of production, the PI enhancements after GPI stimulation of 5% of the reservoir are around 2.6 times of PI without stimulation, for both gas and water (Figure 25). PI enhancements for both phases during production increase to the maximum of 7.6 after 14 years, then decrease continuously. PI for water decreases faster compared to PI for gas.
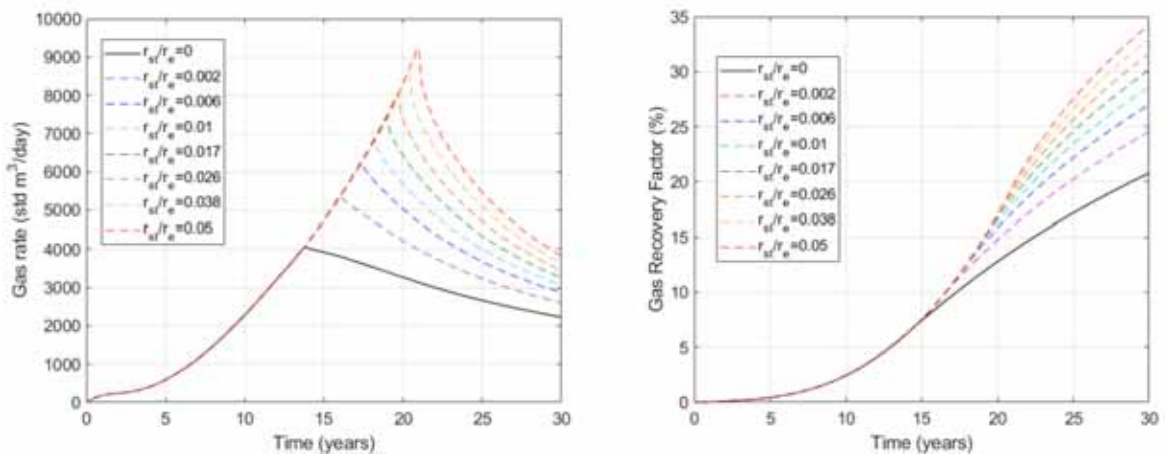
Figure 24: Gas production rates and recovery factors for different radii of stimulation. GPI delays the peak of gas production by allowing a higher gas recovery rate through a longer depressurisation period.
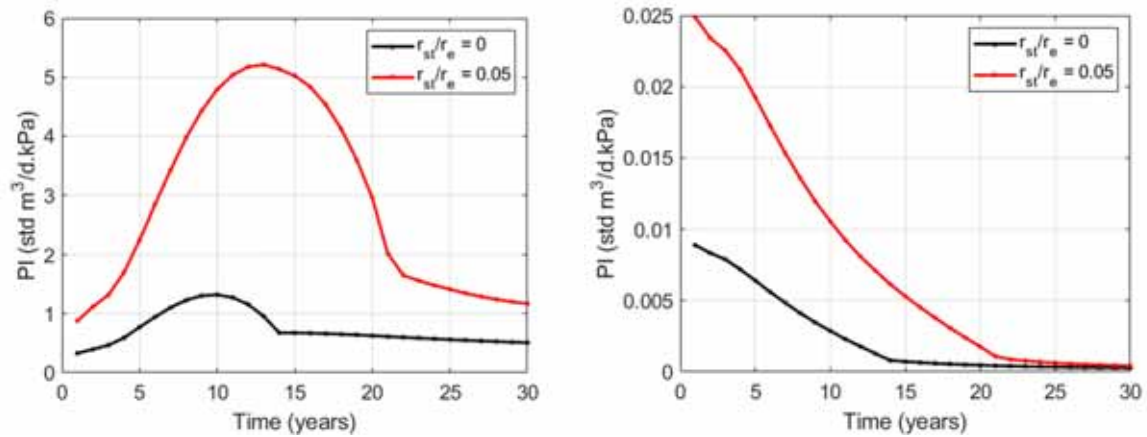
Figure 25: PI for gas (left) and water phases (right), with and without stimulation. The PI for gas starts to decrease before gas peak production is achieved.

6.2.2   Effect of matrix shrinkage

The permeability reduction far from the wellbore becomes larger after GPI stimulation, due to the lower pressure values at the end of the production. However, this reduction is offset by the permeability increase in the stimulated zone. If matrix shrinkage is significant, stronger depressurisation yields smaller permeability reduction in the far-field and a larger increase of the RF (Table 6 and Figure 26)

Table 6: Gas recovery factors (RF) with and without matrix shrinkage, for different radii of stimulation (r_{st}/r_e)

r_{st}/r_e	0	0.002	0.006	0.01	0.017	0.026	0.038	0.05
RF (%) without matrix shrinkage	20.8	24.5	27.0	28.6	30.1	31.6	33.0	34.3
RF (%) with matrix shrinkage	30.1	35.1	38.4	40.5	42.5	44.3	46.0	47.4
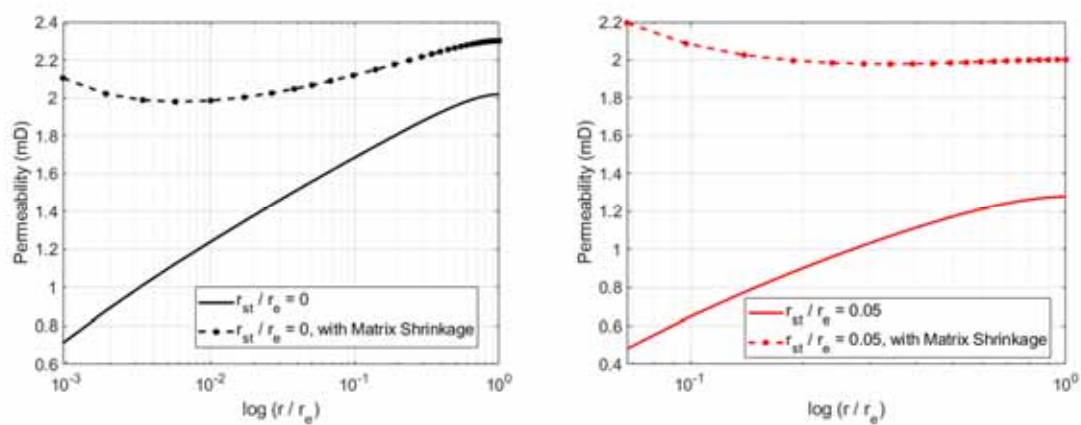
Figure 26: Permeability profiles after 30 years in the unstimulated zones with (dashed lines) and without matrix shrinkage (solid lines). Lower permeability reduction results from matrix shrinkage.

6.2.3 Effect of vertical heterogeneity

To investigate the effect of reservoir heterogeneity on GPI stimulation, we analysed scenarios with a stack of multiple seams of different porosities and permeabilities. The radius of stimulation is the maximum distance that the injected proppants have travelled along before being captured by the narrow cleats. This radius depends on the ratio between cleat aperture and proppant size, which must be higher than three to allow the particles to enter the porous media (Bedrikovetsky, 2008). Assuming the smallest proppant diameter is 20 µm, the maximum travelling distance during injection is determined by the location where the cleat aperture is 60 µm. In our simulations, the cleat spacing is set to 15 mm, which results in an aperture of 60 µm, equivalent to the porosity of 0.80%. Therefore, for heterogeneous models, the stimulation zone in each model layer is determined by the local porosity values obtained during injection (Step 1), which has to reach at least 0.80% to enable proppants to enter the cleats (Ribeiro, et al., 2019). In this sense, the most permeable layer is the best stimulated, while the least permeable layer may not be stimulated at all (Figure 27). Reservoirs with strong porosity and permeability contrast may not benefit from GPI stimulation if there is no vertical communication between layers, as significant sections of the perforated interval will not exhibit a permeability increase (Table 7).
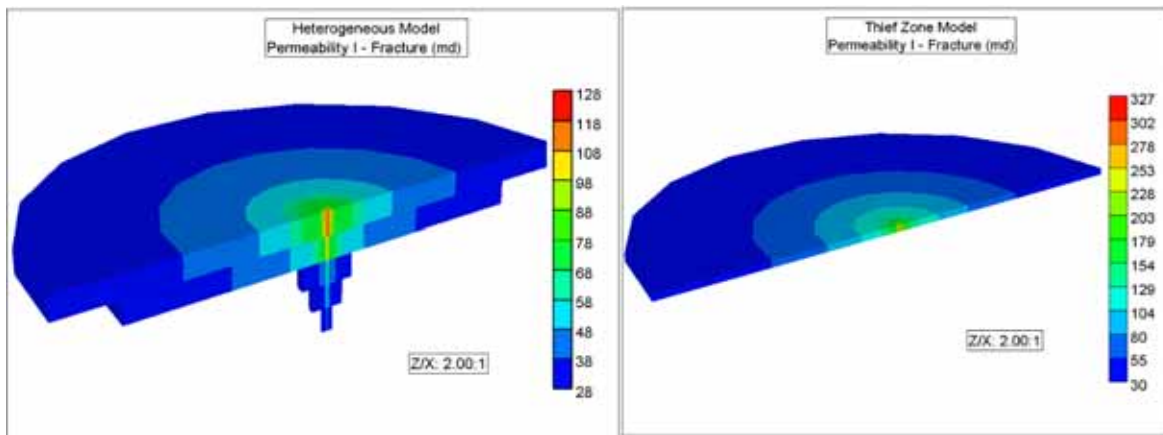
Figure 27: Permeability in the stimulated zones for models with different permeability contrasts: 3 times (left) and 25 times (right). Only the grid blocks for the stimulated zones are shown. If the contrast is too high, not all the layers can be stimulated.

Table 7: Increase in gas-water-ratio (GWR) and Recovery Factor (RF) after GPI for different permeability contrasts (no cross-flow between layers)

	GWR		RF
k_1/k_5	High k layer	Whole Reservoir	Whole Reservoir
25	+61%	+48%	+77%
3	+59%	+43%	+72%
1	+39%	+39%	+65%

6.3 Go-forward Implementation: economic analyses

After designing a reservoir simulation methodology to predict gas recovery from the co-application of GPI with hydraulic fracturing, the final step for field implementation requires an economic evaluation for different SRVs and initial reservoir properties. In this sub-section, the results of an economic analysis of incremental net present value were prepared for varying permeability values and stimulated reservoir volumes, based on a ratio of fracture half-length using the cartesian model of a hydraulic fractured well with co-application of GPI (Santiago, et al., 2021).

A coal seam layer of 5 m (17.4 ft) thickness with a hydraulic fracture of half-length of 100 m (350 ft) matches the pressure profile and gas rates in the early production time of a Surat Basin well (Johnson et al. 2020). In this study, history-matched reservoir parameters (Table 8), constrained by the integration of reservoir characterization tools and production data analysis, are used as input to simulate fluid production with and without GPI.

Table 8: Reservoir parameters used for reservoir simulation (base case).

Reservoir Parameter	Symbol	Value
Coal Thickness (ft)	h	17.4
Fracture Porosity (%)	φ	2.0
Fracture Permeability (mD)	k	1.0
Coal Compressibility (psi^{-1})	c_F	0.00128
Fracture Spacing (ft)	a	0.033
Sorption Time (days)	t_d	10.0
Coal Density (lb/ft^3)	ρ_c	93.6
Langmuir Pressure (psi)	P_L	920.0
Langmuir Volume (g mole CH_4/ lb rock)	V_L	0.26
Poisson's Ratio (fraction)	v	0.3
Young's Modulus (psi)	E	500,000
Strain at Infinite Pressure (fraction)	ε_L	0.01
Hydraulic Fracture Height (ft)	h_f	17.4
Hydraulic Fracture Conductivity (mDft)	F_{cd}	17,750
Hydraulic Fracture Half-length (ft)	x_f	350.0
Pore Pressure (psi)	P_p	1330.0
Depth (ft)	H	2224.0

Net Cash Flow (NCF) is the method used to analyse the economic feasibility of GPI treatment in hydraulic fractured CSG reservoirs under different stimulation scenarios. This method is widely adopted in the oil and gas industry to estimate the net present value (NPV) of a project. The value of money over time is accounted for by using a discount factor per period.

Instead of calculating all costs and expected income of a typical CSG hydraulic fracture well operation, only the additional costs and profits due to GPI are considered to estimate the increment in NPV, i.e., ΔNPV. Cash outflow represents the investment made to inject water and proppants into the formation at time zero. Cash inflows are the revenues due to additional gas production based on the gas price of the Australian market. If ΔNPV > 0.0 GPI treatment is economically viable.

Gas price and costs are based on typical values found in the Australian market. The parameters used for economic analysis are presented in Table 9:

Table 9: Basic data for economic analysis.

Parameter	Value
Water Price	$0.10/gal injected
Micro Proppant Price	$0.40/lb
Gas Price	$0.01/SCF
Discount Rate	10% p.a.
The density of Proppant (ρ_{prop})	22.05 lb/gal

*$ in $AUD

Since the coal thickness is constant, the stimulated area is used instead of SRV. The cases selected for evaluating the benefit of SRV ranged for permeability values (k_0) of 0.1, 1 and 10 mD and from 6.35 to 95% of fracture half-length (x_f) in opposite direction (e.g., $A_{st} = 0.0625x_f^2$).

Figure 28 shows the ΔNPV versus time for different stimulated areas and varying initial permeabilities. More permeable seams exhibit higher cumulative gas production because greater areas of the reservoir are depleted. As a consequence, ΔNPV is higher for more permeable seams. On the other hand, stimulating tighter coals leads to larger increments in gas production with a lower, but still positive, ΔNPV.
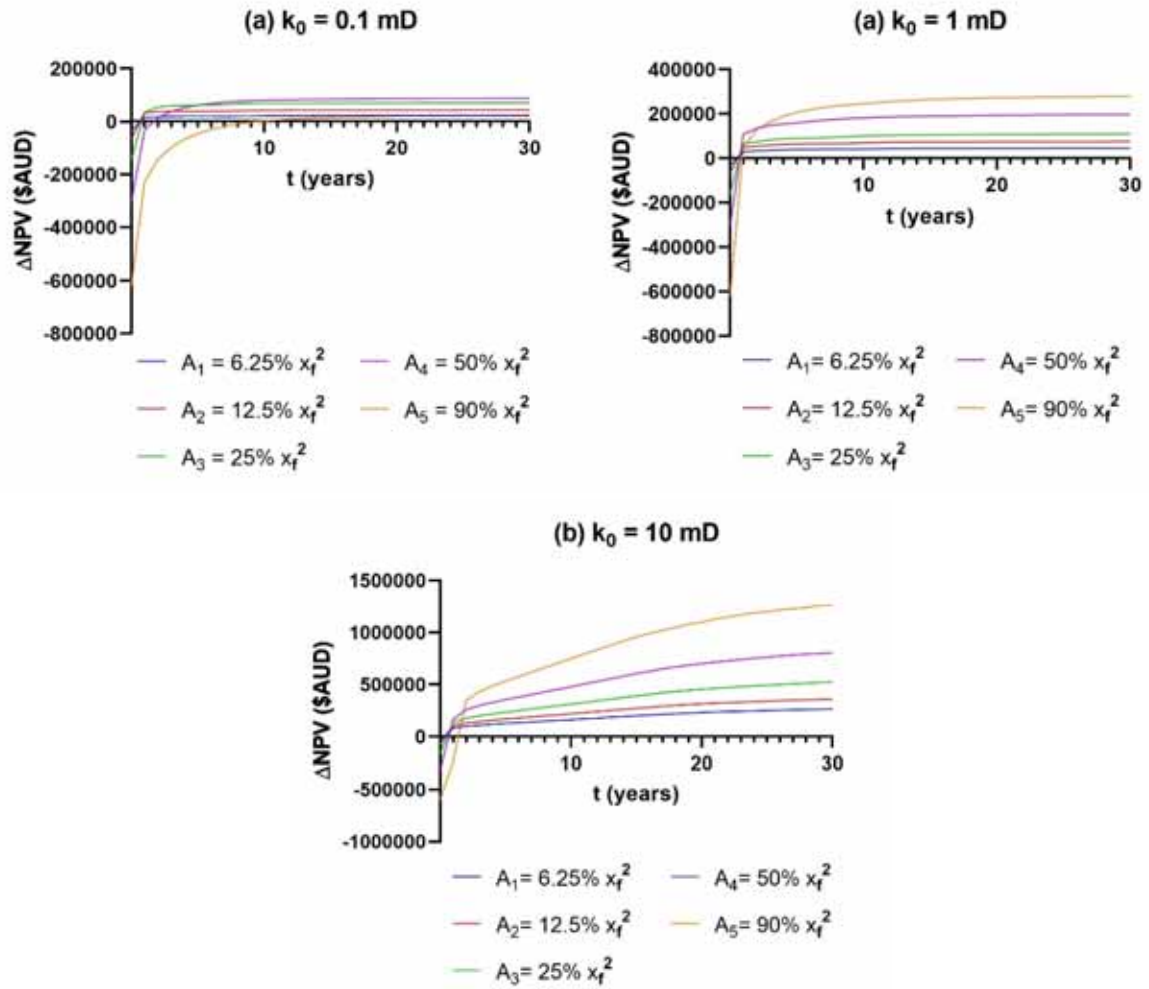
Figure 28: Effect of stimulated reservoir area by GPI on ΔNPV of a hydraulically fractured CSG well (a) ΔNPV versus time (b) ΔNPV versus % of the stimulated area.

7 Testing of Candidate Fluids and Particles

Past laboratory investigations of GPI in coal have employed glass micro-balloons (GMB) as the particulate medium. These have the advantage of being neutrally buoyant in water, meaning that they can be suspended and injected without requiring an elevated fluid viscosity. However, GMB have little prospect for field application as they will be prone to crushing under closure stresses and expensive to deploy (as a non-standard product).

Ceramic microparticles, namely Deeprop® 600, have been identified as a practical alternative to GMB as they possess a track record of application in unconventional fields. The 50th, 90th, and 95th percentile diameters of these particles are 10 μm, 25 μm, and 35 μm, respectively. With a specific gravity of approximately 2.3, these particles will, however, settle out of suspension and thus require elevated viscosity to aid storage and injection. A guar polymer (FWG150D) has been selected for this purpose and paired with the enzyme concentrate, ASP®FWB605E, which is used for clean-up post-injection. There exists a large body of literature reporting on the effectiveness of this enzyme in reversing permeability loss associated with the use of guar polymers (H. D. Brannon & R. M. Tjon-Joe-Pin, 1995; H.D. Brannon & R. M. Tjon-Joe-Pin, 1995; Brannon, et al., 2003). Initially developed as a damage removal solution, guar linkage specific enzymes (GLSE) became the primary means to gain higher later conductivities in conjunction with faster active oxidative breakers to lower crosslinked gel pH and viscosity. The key indicator for breaker efficiency is molecular weight distributions post-break, not viscosity. The GLSE and guar were also found to have the highest retained conductivity and least impact on coal desorption of any products testing in the StimLab work on coal damage (Penny & Conway, 1995).

7.1 University of Adelaide Testing

An experimental campaign within the project was commissioned with the University of Adelaide to determine the collective performance of the chosen particles (Deeprop® 600), fluid polymer (FWG150D), and breaker (ASP®FWB605E) in scenarios that can be extrapolated to GPI implementation (Appendix I, Section 20.1-19.3). In particular, these experiments focus on (i) the straining of the microparticles in a sand pack representative of a propped fracture (i.e., 40/70 and 20/40 mesh packs) and (ii) the injection of microparticles into a coal core sample. To create the sand pack, washed dry sand was sieved using 210 μm (70 US mesh) and 425 μm (40 US mesh) stainless-steel sieves. This sand (85 g) was used to prepare an unconsolidated porous medium with length of 4.5 cm and a diameter of 3.81 cm. The mean pore-throat half-size for this porous medium was estimated to be approximately 27 μm. The coal core samples have been sourced from Walloon coals of the Surat Basin.

7.1.1 40/70 and 20/40 Sand Pack Testing

The first report from this testing campaign was performed with a 40/70 and 20/40 sand pack to evaluate straining and to test the guar carrier capabilities. The findings, in Appendix I are summarised as follows:

1. The guar polymer was successfully employed to formulate a carrier fluid that could prevent the ceramic microparticles from settling out of suspension;
2. The injection of the guar solution into a sand pack leads to significant formation damage,

manifested as an irrecoverable reduction in permeability. Testing of the enzyme solution as an effective breaker in benchtop testing shows effective viscosity reduction; ongoing testing including testing at room temperature and representative reservoir conditions (50° C) is being planned for the core testing (See Appendix I, Sections 19.1-19.3).

3. The combination of mean pore size and the microparticle size distribution resulted in significant straining, which was measured as decreased pack permeability and observed as the accumulation of particles on the inlet face of the sand pack. This proved that the candidate particles would not flow back to the well through a fracture packed with 40/70 proppant (an industry standard) and cause associated problems downstream (See Appendix I, Section 19.4).

4. Similar testing with a 20/40 sand pack did show a significant reduction of permeability to 335 ± 2 mD (6% retained permeability) from the initial pack permeability of 6045 ± 33 mD (See Appendix I, Sections 19.5). Further, the effluent contained a significant amount of particles indicating that the candidate particles would flow back to the well through a fracture packed with 20/40 proppant.

Therefore, the use of 100 mesh and 40/70 sand is recommended immediately behind the application of micro proppants to retain the particles in formation as much as is practical.

7.1.2   Core Preparation

Several attempts were made to use the provided Walloon coal samples for testing; however, the samples appeared to be unstable during the preparation of cylindrical plugs. Dr Badalyan noted "We have problems in regards to the integrity of coal during plug cutting. Out of two pieces of coal, we were unable to produce an acceptable cylindrical plug. The second piece disintegrated once the saw started getting through the core. Coal disintegrates during drilling through it and during trimming its ends." Thus, the decision was made to abandon the use of Walloon coal samples and evaluate using plugs from Permian coal remaining from the experimentation of Keshavarz, et al. Two Permian coal samples were prepared and micro-CT scans were performed to evaluate the best candidate for testing and comparison to post-injection Micro-CT scanning (See Appendix I, Section 19.6).

7.1.3   Core Injection Results

After establishing an injection of enzyme solution, an injection of guar gel with enzyme was injected in Coal Core 4 to assure injectability of 90% guar and 10% enzyme proppant carrier. This resulted in blockage of the core and cessation of the initial test (See Appendix I, Section 19.7); permeability was partially recovered using backflushes of enzyme solution (Appendix I, Section 19.7, Figure 96). Next, an attempt was made to test injectability of a 50% guar and 50% enzyme proppant carrier solution, which indicated less damage; however, even with post-flushes of enzyme solutions, the permeability did not fully recover.

After reestablishing adequate injection of enzyme solution, an injection of 20% guar and 80% enzyme proppant was trialled as a potential carrier in the already damaged Coal Core 4. Following injections of enzyme solution, the core was able to recover at an injection pressure 50% higher than initially observed (Appendix I, Section 19.7, Figure 99). Based on this testing, it was decided to alter the injection solution on the proppant-laden trial to 10% guar and 90% enzyme proppant carrier with Deeprop® 600 mixed at 2 ppg in the guar solution. As most of the damage was a result of unbroken

guar, it was also decided after removing hysteresis with tap water to precondition the core with enzyme solution and raise the operating temperature to that of a typical CSG well, or 50° C.

Following review of the Micro-CT scanning data (Appendix I, Section 20.7, Table 19), Coal Core 3 was chosen over Coal Core 1 based on a 10-fold calculated average pore volume and more physical evidence of cleating/fracturing (Appendix I, Section 20.7, Figure 102). Hysteresis in core permeability versus net effective stress were removed by repeated injection and relaxation cycles resulting in permeability ranges up to >10 versus initial permeability (Figure 29).
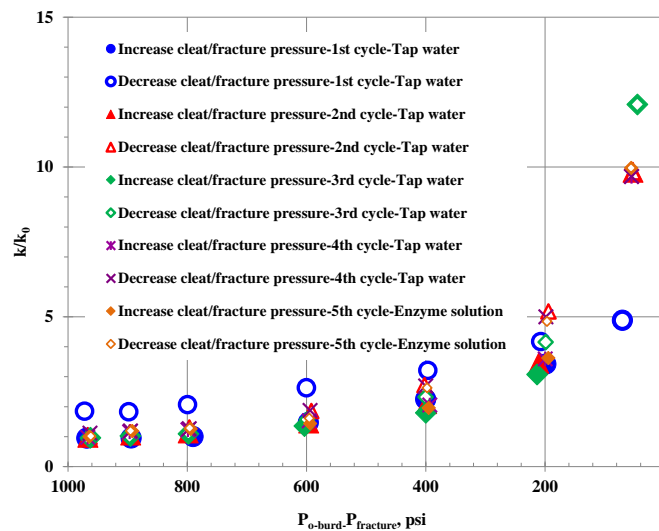
Figure 29. Graphs showing removal of hysteresis in reduced core permeability as function of effective stress at 22 ℃.

Following this procedure, preconditioning with the enzyme solution was performed then the 10% guar and 90% enzyme proppant carrier with Deeprop® 600 mixed at 2 ppg in the guar solution was injected to an effective stress value of 217.6 psi. At this point, the k/k_o had dropped from 5.14 to 0.023 resulting in proppant bridging within the coal core. Effectively the permeability had decreased from an initial value of 18.558 to 1.649. Then, after backflushing with enzyme solution, the permeability eventually increased to 2.063 then declined thereafter, likely as a result of fines and fracture closures. After the test, the inlet area was examined and it was observed that some inlet fractures have reduced their widths, and some fractures have disappeared/collapsed.

The post micro-CT scan (Figure 30) indicated that: (1) new fractures were generated in this coal core during hysteresis removal procedure; (2) fractures on the inlet cross-section of the core are filled with proppant; (3) some fractures in the middle of the core are also filled with proppant, suggesting that backflush with enzyme solution hasn't removed all deposited proppant; (4) outlet cross-section of the core has also fractures filled with proppant.
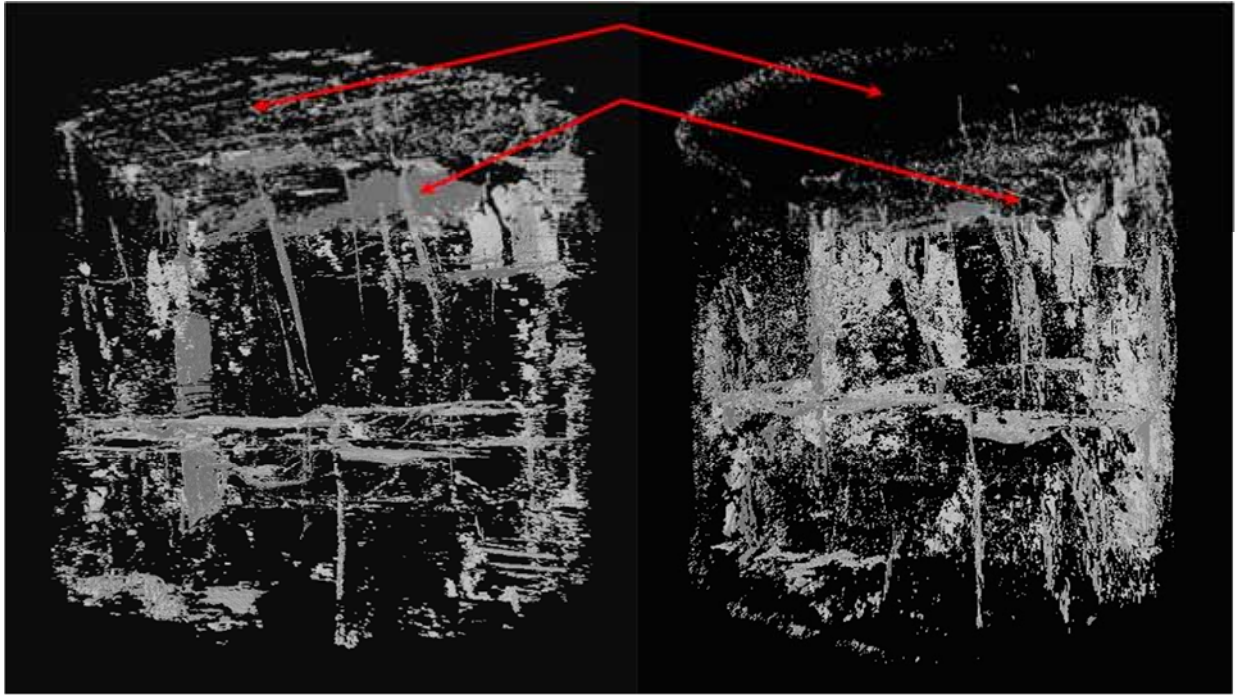
Before   After
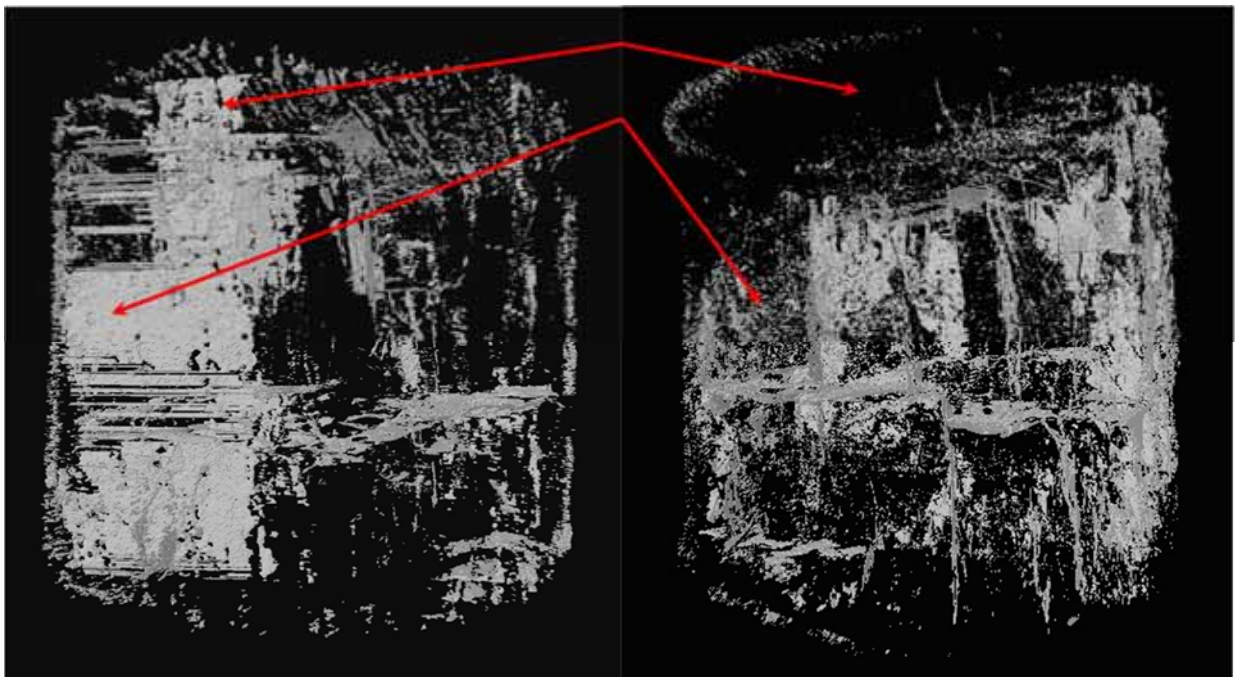
Before   After
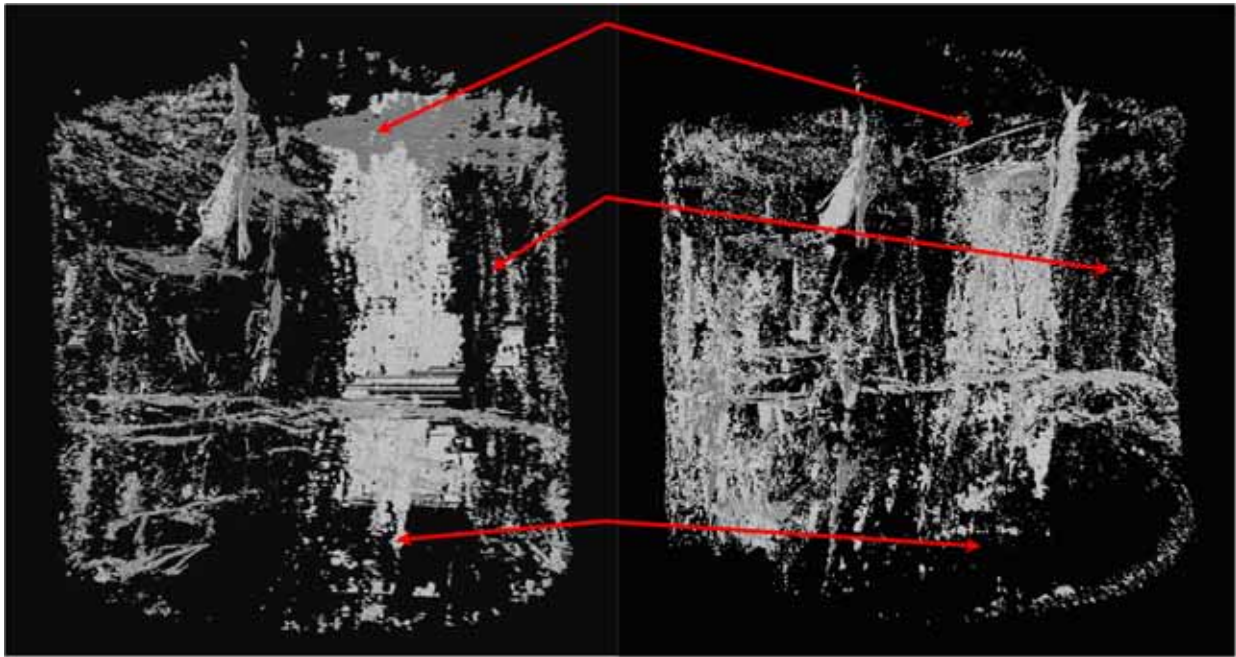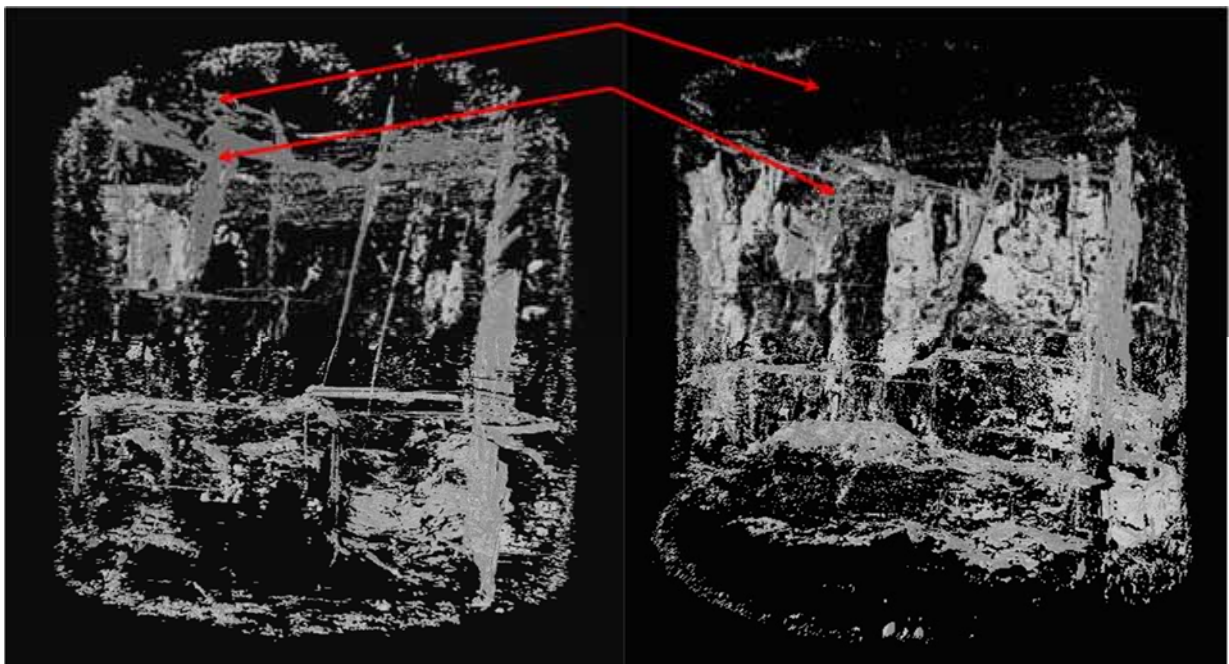
Before   After

Before   After

Figure 30. 3D images of pore spaces rotated by 90° for coal core-3 before after proppant deposition. (Red arrows show some parts of the coal core with deposited proppant).

Whilst this testing does not conclusively support or disprove the use of Deeprop® 600, it provides some insight into the mechanisms of stimulation and damage that may be occurring with micro proppant injection. First, the fractures were not done at expected fracturing pressure conditions, so the width and damage to created or extended natural fracturing is not likely to be occurring in a similar manner to this testing. However, at some point in the fracture a transition exists in the natural fracture system from extension to leak off; this is where there may be some localized permeability reduction by jamming of micro-proppants. This testing did show the importance of gellant carriers

with effective breakers as being essential in limiting collateral damage from fluids. Finally, as indicated by fluid flow studies, some damage may be mitigated by the self-sorting nature that will occur while pumping these distributions of particles over a large area. In short, these particles may be good at controlling leadoff and extending the fracture over a larger area, thus mitigating any potentially negative effects by the larger SRV achieved by their inclusion.

Unfortunately, this experimentation has not conclusively answered the questions on applicability of commercial micro proppants as did the studies by Keshavarz et al. (2014, 2015, 2016) using 10 and 20 µm diameter, hollow sphere, graded particles. It has increased our understanding on the necessity to correctly match the distribution of particles to the width distribution of cleats and fractures and under fracturing conditions. Therefore, further testing would require the use of further technology, such as 3D printed naturally fractured rock with rock mechanical properties of coal and morphologies of expected fracture patterns, based on core or image log analyses. These types of materials are under development and may give more insight on particle distributions to optimise stimulation benefits from micro proppants.

7.2 University of Alberta Testing

An ad hoc test programme was undertaken at the University of Alberta to test the potential benefit of micro proppants using 3D printed naturally fractured material with fracture patterns (Appendix J). The synthetic core material used mimics coal material properties and had a layered series of fractures creating fracture dominated flow (Appendix J, Slide 12). Based on the higher permeability of the samples a 'heavy' loading of guar and Deeprop® 600 could be developed and injected into the samples. The permeability in Tests 1-3 all indicated significant jamming and with permeability damage being reduced as the concentration of micro proppant was also reduced. Finally, on Test 4, a concentration was injected that preserved permeability under increased net effective stress conditions versus unpropped core measurements (Figure 31).
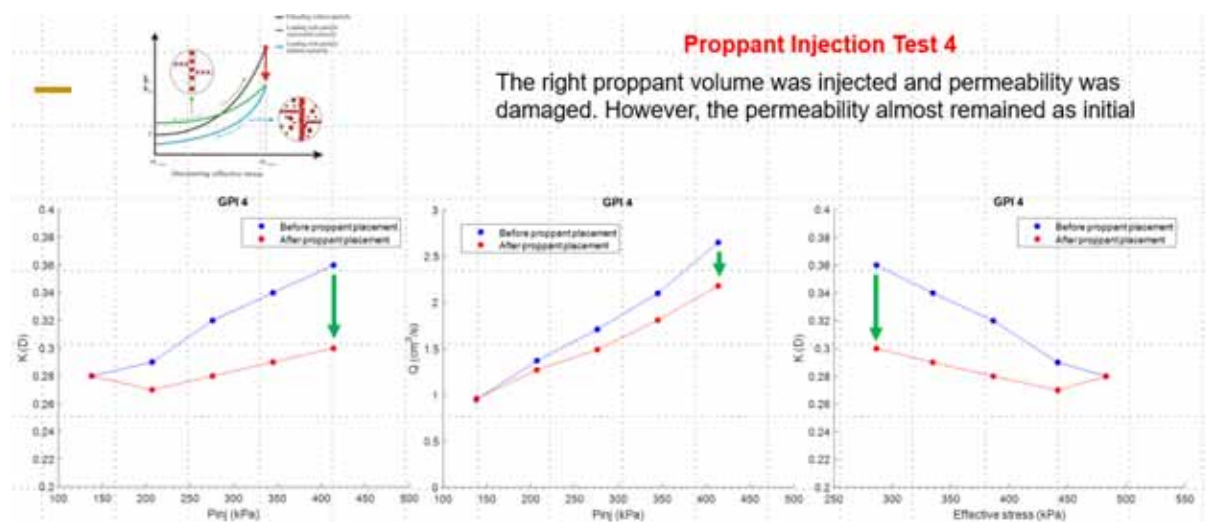
Figure 31. Proppant Injection Test 4 proved that the correct proppant volume could preserve permeability under higher net effective stress conditions

Whilst the core permeability was unrepresentative of low permeability coals (i.e., 300-360 mD), it gives promise that a lower permeability coal-like material may be developed and demonstrate optimal loadings for varying natural fracture morphologies.

8 Characterising pressure-dependent permeability behaviour in coal using an integrated approach

Pressure dependent permeability (PDP) is a special feature of CSG reservoirs. Characterising PDP behaviour in coal is critical to the field development and planning process. An integrated approach, involving reservoir characterisation, diagnostic fracture injection testing, hydraulic fracturing and post-frac well production data analysis, is developed for this purpose (Johnson et al., 2020).

8.1 Methodology

The newly developed integrated approach utilises the following data: fracture fabric and porosity reasonably defined from image log and areal core studies; DFIT data acquired under initial saturation conditions; hydraulic fracturing data; and long-term production data. The implementation workflow is briefly presented as follows:

1. Develop a reservoir geological description of the fracture fabric, permeability anisotropy and porosity reasonably defined from image log and areal core studies.

2. Review DFIT data acquired under initial saturation conditions and exhibiting PDL behaviour using multiple methods.

3. Pressure and volume history-match of the DFIT treatment data using a planar 3D model, a reservoir simulator capable of history-matching PDP effects and a 2D PKN hydraulic fracturing model incorporating a mathematical model for DFIT accounting for PDL and PDP.

4. Pressure and rate history-matching of hydraulic fracturing data using a planar 3D model and parameters derived by DFIT volume and pressure history-matching.

5. Pressure and history-matching of medium-term post-frac well production data and compare fracture dimensions with history-matched dimensions from the hydraulic fracture modelling.

The above workflow can be implemented in combination with early rate and pressure production history-matching, to provide a more detailed data pool to base predictive reservoir modelling on earlier in the field appraisal stage and better reduce uncertainty. Further, this analysis framework may allow better scenario modelling for hydraulic fracture optimisation or incorporation of emerging completion or micro-proppant technologies.

8.2 Mathematical modelling of DFIT data accounting for PDL and PDP

Since the commonly used hydraulic fracturing models do not adequately account for PDL and PDP behaviour, in this project we developed an underlying mathematical model for PDL and PDP effects for application in future models and to compare with the 3D models that include these effects. As coal DFIT treatments are likely to remain in the coal, based on stress contrasts and weak interfaces with respect to the surrounding boundaries, a PKN frac geometry is a reasonable framework to trial this new mathematical model for PDL and PDP.

The model describes the transient processes of fracture propagation during fluid injection, fluid leak-

off into formation, fracture closing up after shut-in, and pressure diffusion after fracture closure. The following assumptions are made during model derivation:

1. The fracture cross-section is elliptical, and the height is constant.

2. The fluid is injected from the wellbore into the fracture with a constant volumetric rate.

3. The fluid flow in the fracture is incompressible Newtonian laminar flow with negligible gravity effect.

4. The formation is homogeneous and contains single-phase fluid.

5. The porosity, fluid viscosity and total compressibility of the formation are pressure independent.

The mathematical model, including a complete system of governing equations and associated initial and boundary conditions, are presented in our paper Johnson et al. (2020). The equation system can be solved numerically using the finite difference method. The obtained transient pressure data can be applied to the history-matching with field DFIT data.

We have applied this model to a well case study with DFIT data. The inputs into this model were derived from the planar 3D fracture modelling, including reservoir porosity ϕ=1%, permeability k_0=20 md, reservoir pressure p_0=978.65 psi, fluid viscosity μ=0.466 cp, total compressibility $c_t = 5.14 \times 10^{-4}$ psi^{-1}, Young's modulus E=1.14 GPa, Poisson's ratio v=0.31, injection rate Q=4.85 bpm, and pumping time 5.08 min.

The treating pressure measured during the DFIT test is shown as the blue curve in Figure 32a. At the beginning of the injection, pressure increases rapidly until the breakdown pressure. After the fracture initiation, the pressure reduces and stabilises during fracture propagation. After shut-in, the fracture starts to close up and the pressure decreases further towards reservoir pressure. The black curve in Figure 32a shows the best match of the modelled result by tuning the two parameters in the pressure-dependent permeability function. The optimised parameter values are a=0.27 and b=0.007 psi^{-1}. The value of b is comparable to 0.01 psi^{-1} that is obtained from DFIT analysis. It is worth noting that the pressure response from the model at the initial stage does not match that from the field test. This is because the model does not account for the complexities present at fracture initiation.

The corresponding fracture width variation with time obtained from the model is shown in Figure 32b. During fluid injection at the early stage, the fracture propagation and fluid leak-off occur simultaneously. The variation of fracture width is insignificant. After shut-in, the fracture width decreases rapidly due to fracture closure. As soon as the fracture closes, the model predicts a minimum fracture width during the after-closure period.

(a)   (b)
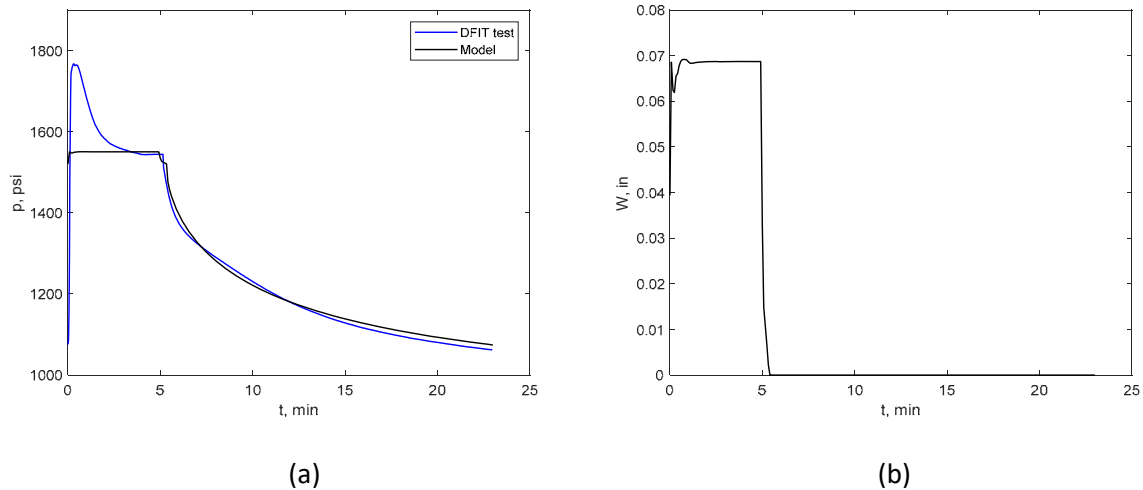
Figure 32: (a) History-match of pressure data from DFIT in target interval using the new mathematical model incorporating PDL and PDP; (b) Fracture width versus time

The two parameters (the coefficient *a* and exponent index *b*) in the pressure-dependent permeability function characterise the pressure decline behaviour after the fracture closure. Figures 33a and 33b demonstrate the effects of these two parameters a and b, respectively. The optimised values a=0.27 and b=0.007 psi^{-1} correspond to the black curves in Figs. 33 a and 33b, showing the minimal difference with the DFIT data (blue curves). In Figure 33a, the red and green curves correspond to the coefficient a=0.35 and 0.19, respectively. In Figure 33b, the red and green curves correspond to the index b=0.009 psi^{-1} and 0.005 psi^{-1}, respectively. The higher coefficient and index indicate the greater effect of pressure on the permeability, leading to faster pressure decline during the after-closure stage.

(a)   (b)
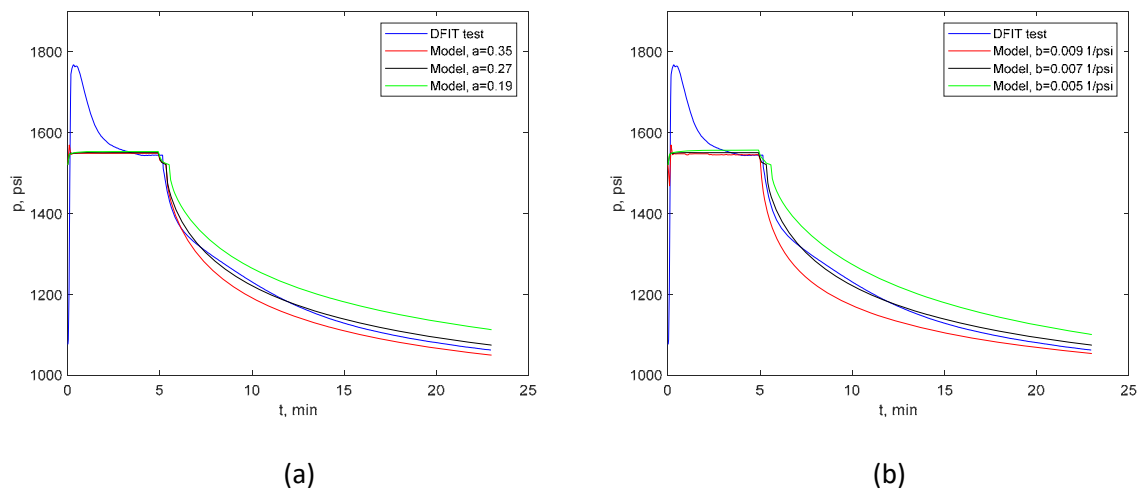
Figure 33: Effects of PDP parameters on the pressure decline behaviour: (a) Effect of the coefficient a; (b) Effect of the exponent index b.

9 Development of well selection criteria for GPI implementation

GPI technology is beneficial to reservoirs with substantial matrix shrinkage effects. However, it still

can be applied to coal seams that do not exhibit significant matrix shrinkage effects to improve the average permeability of the field. Reservoirs that exhibit permeability rebound after sufficient depressurisation require less stimulation. A significant amount of research has been made on fracture modelling, fluid/particle dynamics, reservoir performance prediction, and slurry development. The final stage of the NERA project will be based on the workflows presented in this section and evaluated within a framework of modelling evaluations to allow performance evaluation of the proposed implementation.

Firstly, the candidate selection process is defined based on our current understanding of the capabilities and likely results of implementing GPI technology as well as the results of laboratory testing to date. As the reservoir understanding is the first step in the design process, we will summarise key considerations for implementation as follows. Firstly, GPI technology is recommended to be applied to the reservoirs without strong vertical heterogeneity. There is little benefit to applying GPI stimulation to the interval with high permeability contrast between seams since the fluxes will tend to converge to the most permeable layers and the proppants will not penetrate in the least permeable layers. As a result, improvements in both the gas-water-ratio and recovery factor are very low. GPI should be applied to the intervals with limited vertical heterogeneity to stimulate the majority of the perforated interval more uniformly and enhance the overall productivity.

Next, based on the production history, **a** reservoir with characteristics indicating pressure-dependent permeability (PDP) is likely to be a key indicator for potential success as studies have shown that conventional fracturing technologies fail to deliver a stimulated reservoir volume adequate to sustain commercial production (T. Flottman, et al., 2013; Johnson Jr, Glassborow, et al., 2010; Johnson Jr. & Mazumder, 2014; R. L. Johnson, Jr., et al., 2002; Leonardi, et al., 2019; V.J. Pandey & Flottmann, 2015). The past Centre PDP project did identify potential cases with potential PDP effects and poor stimulation benefits in the past.

Further, site selection should target intervals in the coal where prior hydraulic fracturing diagnostics have indicated the propensity for predominantly vertical fracture development based on prior microseismic, surface tiltmeter, sonic anisotropy logs, or radioactive/non-radioactive tracer surveys. Complex fracturing such as natural fracture activation and multiple fractures are complexities that may enhance the overall treatment and can be well described by the DFIT. However, horizontal fractures tend to align with bedding planes and provide little benefit based on low vertical permeability values in coals. Again, prior literature describes the types of stress regimes and diagnostic responses that delineate positive complex vertical fracture behaviour as opposed to less effective horizontal hydraulic fracturing (T. Flottman, et al., 2013; Johnson Jr, Glassborow, et al., 2010; Johnson Jr. & Mazumder, 2014; R. L. Johnson, Jr., et al., 2002; Leonardi, et al., 2019; V.J. Pandey & Flottmann, 2015).

Finally, the operational logistics and planning that will be required are still to be developed following the completion of testing and verification of a final commercially available product. At this time, the high-level considerations are available and can be outlined for consideration by operators and service companies interested in applying micro proppant applications in the field in advance of final product testing. Notwithstanding, the identification of BTEX free products and a commercially available proppant will allow rapid deployment once the lab testing is completed.

The results of lab testing are envisaged to provide operators and service providers more confidence

in the process to risk capital investment in the approvals and equipment requirements to deploy the technology in Australia. At this stage, the results of silica flour deployment in deep coal treatments of the Cooper Basin provides some understanding of the risks, considerations and anecdotal benefits in micro proppant deployment in the field (Camac, et al., 2018).

The attached figures outline the design workflow considerations (Figure 34) and operational risks and considerations (Figure 35) associated with micro proppant deployment. These workflows will be reviewed and workshopped with the Centre for Natural Gas proponents at the earliest available time (e.g., December or January). Modelling (based on selected data from the PDP project) will commence on the integration of diagnostics and will provide a detailed workflow for implementation in the final report along with any changes based on operator input on workflows for design and operational risks and considerations. An example workflow for onsite diagnostics and post-treatment evaluation is presented in Figure 36 and will become more developed following further modelling.
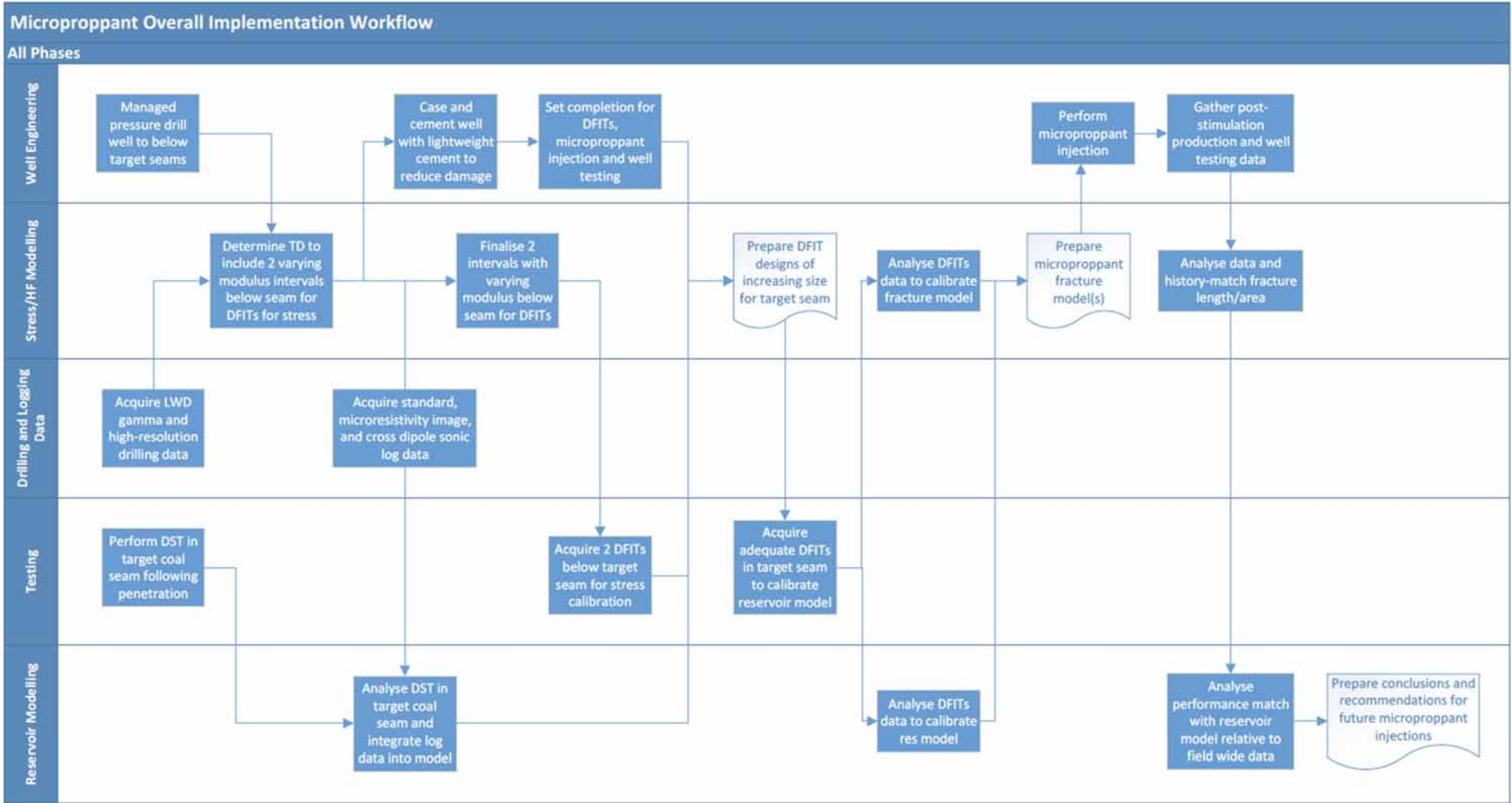
Figure 34: Micro proppant overall implementation workflow
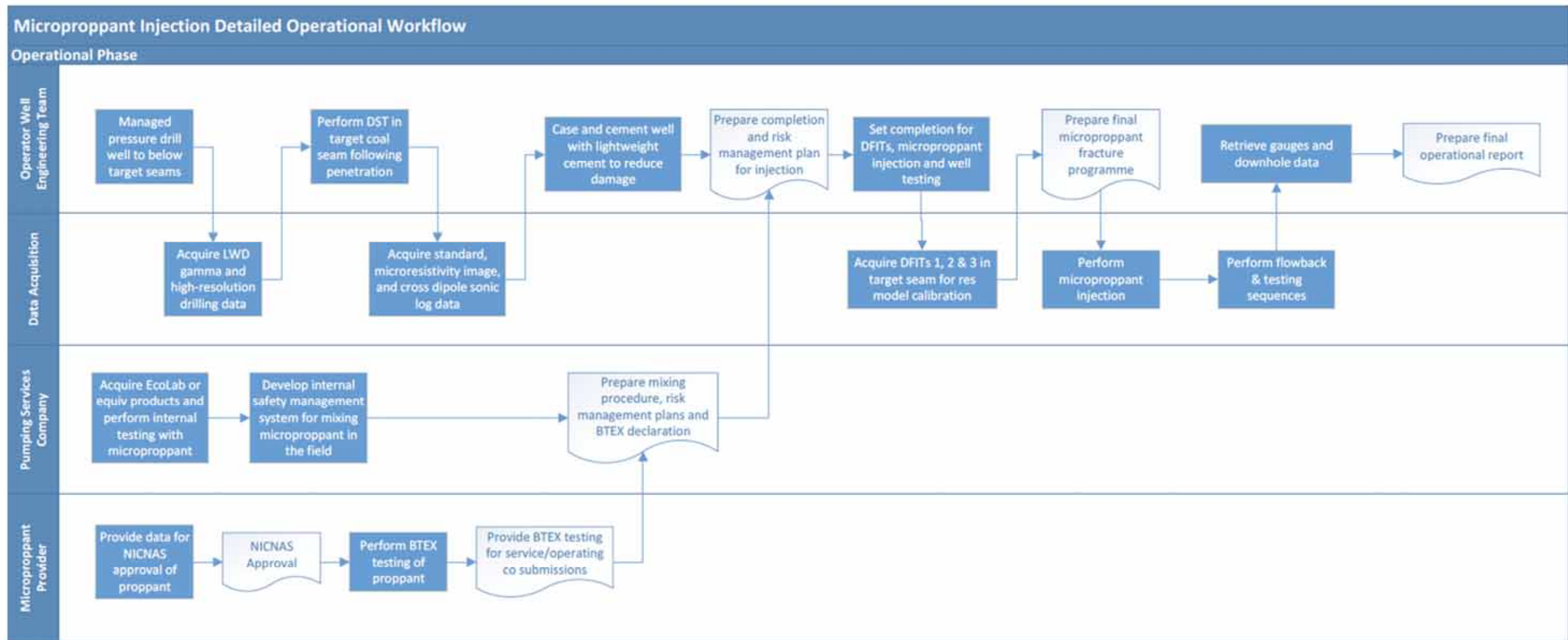
Figure 35: Micro proppant injection detailed operational workflow

Microproppant Injection Detailed Modelling Design/Evaluation Workflow

Modelling/Design Evaluation Process
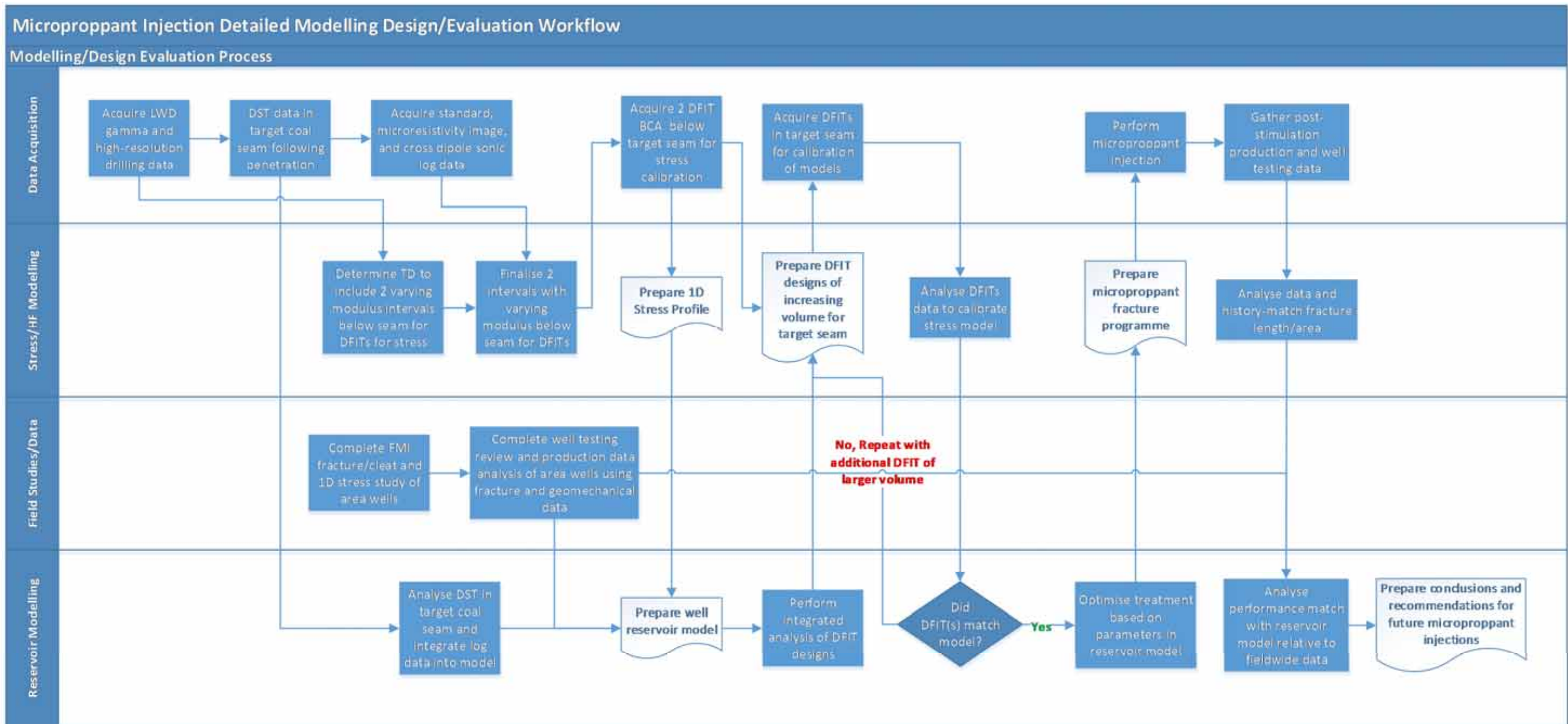
Figure 36: Micro proppant Injection Detailed Modelling Design/Evaluation workflow

10 Conclusions

This project aimed to better define the process of stimulation with graded particles or micro-proppants and further develop hydraulic and reservoir modelling tools. These tools should aid practitioners in properly designing and assessing the application of GPI in the field and performing laboratory studies on coal fracture conductivity using actual field core materials. Building on previous theoretical and experimental work, new developments in this project focussed on the extension and characterisation of mathematical models, and fracture-scale suspension transport simulation.

A previous Stim-Lab experimental study characterised common and potential fracturing fluids in terms of coal-fluid interactions to identify reasons for less than satisfactory performance and to devise alternative fluids and treatment procedures to optimise production following hydraulic fracturing. The coal-fluid interactions analysis indicates common gelled fracturing fluids may cause 50 to 99% damage of cleat permeability. The rheology and proppant transport study (Appendix I, Section 20.1-20.3) developed a slurried, commercially available product mixture composed of the micro proppant, fluid, and enzyme 'breaker' additive that can be physically managed and pumped in the field by the ratio of mixing into a treated or produced water stream.

Beyond mixing, our modelling of transport, using the coupled LBM-DEM method, indicates that the micro proppants can be transported deep into formation with a velocity above 3 ft/s. The developed model is validated by the benchmark problem of sphere settling with high accuracy (R^2 = 0.999). Simulation of suspension flow in a single fracture with a leak-off cleat predicts particle transport behaviour precisely and generates the particle distribution profile inside the fracture and cleat. Further investigation on the effects of particle properties, carrier fluid rheology and fracture geometry on suspension transport were used to improve modelling of well production enhancement using GPI.

Laboratory analysis (Appendix I, Section 20.7) indicates that a commercial product such as Deeprop® 600 (D50 30 micron) does penetrate coal cleats and maintains conductivity under closure and backflushing under the limitations of injection and post-injection net stress application. Further, laboratory testing with 3D printed, natural fractured materials with high permeability (Appendix I, "Proppant Injection 4") indicated that a crossover in permeability stabilisation was approaching at the limitations of the equipment's ability to apply post-injection net stress. Previously, StimLab GRI funded studies (Penny & Conway, 1995) show that proppants $\geq$100 mesh would not enter fractures less than 250μm and that 100 mesh mounds under these conditions at the fracture face. Project laboratory studies show that Deeprop® 600 was prevented from entering a sand pack of 40/70 mesh sand (Appendix I, Section 20.4) and partially passed through a 20/40 sand pack with damage (Appendix I, Section 20.5). Together, these findings guide the planning and design of frac treatments using micro proppant - a series of injected proppants should be used in all fracturing fluids from micro proppants in the pad; 100 mesh and 40/70 mesh in early pad stages to control fissure leak off; then 20/40 or larger proppant in the main body of the fracture at a concentration between 1 and 2 lbs/ft^2, to maximise fracture conductivity post-embedment.

An experimental study on fracture conductivity in Cooper Basin deep coals (Fraser and Johnson, 2018) identified that fracture conductivity increases with vitrinite reflectance (VRo) value. The minimum proppant concentration in anthracitic coal is 0.5 lb/ft^2 to avoid substantial conductivity reduction at

high closure stress. Cheaper sand proppant is ineffective on coals under high stresses (>4000 psi), due to lower conductivity and fines generation. 20/40 LWP ceramic proppant retains better conductivity than 30/50, but 30/50 proppant helps control fines. To achieve reasonable conductivity, the recommended range of proppant concentration is between 1 and 2 lbs/ft^2 in coal and smaller proppants experienced less embedment and associated fines generation.

Commercial micro proppant (i.e., Deeprop® 600) testing at The University of Adelaide provides some insight into the mechanisms of stimulation and damage that may be occurring with micro proppant injection (Appendix I, Section 20.7). First, the fractures were not done at expected fracturing pressure conditions, so the width and damage to created or extended natural fracturing is not likely to be evidenced in a similar manner to this testing. Notwithstanding, at some point in the fracture it is transitioning from extension to leadoff where there may be some localized permeability reduction by jamming of micro-proppants and an associated reduction in leadoff. Further, in some cases this reduced permeability may be mitigated by the self-sorting nature that will occur while pumping these distributions of particles over a large fracture region. Next, this research identified that gellant carriers with effective breakers are essential in limiting collateral damage from fluids. In conclusion, this testing indicates that the particles may be good at controlling leadoff and extending the fracture over a larger area, thus mitigating any potentially negative effects by the larger SRV achieved by their inclusion.

Modelling of production enhancement using GPI predicts that compared to elastic deformation of the coal fracture surface, elastoplastic deformation is less significant outside the contact zone with the particle and the coal surface. However, the particle embeds more deeply into the coal. This results in reduced fracture width and a decrease in fracture permeability under certain effective stress conditions. For each effective stress, an optimal value of particle aspect ratio yields the maximum fracture permeability. The developed methodology in the present work can be used for designing and evaluating stimulation outcomes with GPI for a range of uncertain reservoir parameters.

A review of the recent development of mathematical models for the GPI process shows that using 10 and 20 µm diameter graded particles in injection and drawdown may lead to a three-fold improvement in permeability and CSG productivity. The previously used models in the literature over-simplified the real process and limit their application in the field. This project overcame some of the shortcomings of previous models and develop new predictive tools for the GPI process. For example, post-stimulation gas production was modelled using a pressure-dependent permeability simulator. The predicted benefits of stimulation are larger and longer growth of the gas production rate given by a slower decrease of the applied bottom-hole pressure to maintain a constant production rate of water. Moreover, gas desorbs faster from the coal matrix, especially in the stimulated region. Investigation of the economic benefits to-date indicate that stimulation benefits of GPI in conjunction with hydraulic fracturing are achievable at bulk permeability applications > 0.1 mD (Santiago, et al., 2022).

With regards to the design process, a newly developed integrated approach using DFIT data, as well as image log, core analysis, hydraulic fracturing data and production data, can be implemented to reduce uncertainty in the production data analysis and history-matching by consistently incorporating pressure-dependent parameters (Johnson et al., 2020). Whilst the tools and methods can differ within the workflow, the correct accounting of pressure-dependent effects in modelling leak-off and

permeability is necessary to constrain the modelling and reduce the uncertainty in dimensions predicted in such environments between the hydraulic fracture and reservoir simulation outputs. By design, this study was completed by separate analysts on a single pass workflow to evaluate the effectiveness of the process. Despite this isolation in data processing, the PDP and PDL coefficients were within the same order of magnitude and the PDP coefficients used in the new 2D PDP frac model and PDRS are closer, considering differences in pressure, permeability, and total compressibility. Whilst the divergence between the hydraulic fracture and reservoir simulation outputs were not fully resolved or optimised as envisioned in applying the proposed workflow by this project, this example did substantiate a high conductivity fracture was effectively placed in a high permeability coal. Once a model is calibrated, then further optimisations are possible based on the application of micro proppants and as described by Santiago et al. (2021).

Given there were more similarities than differences in conclusions across the varying analyses, we hypothesise that developing a consistent approach in defining pressure-dependent variables using DFIT data across a field or play can result in reduced uncertainty and improve identification of key variables needed for successful completion strategies and well spacing determinations earlier in the development planning process. The results of this study guide high-level design and operational workflows for micro proppant deployment. These workflows were reviewed and workshopped with the Centre for Natural Gas industry partners and the earliest available time (e.g., December or January). Following that, modelling with integrated reservoir and hydraulic fracturing models (Santiago et al., 2021, Johnson et al., 2021) use known PDP examples to provide example simulated outputs for implementation of micro proppants in conjunction with hydraulic fracturing. These examples provide operators with design and field implementation guidelines that factored in their input to the workshops.

The benefit of using this process in combination with early rate and pressure production history-matching is that a more detailed data pool can be developed as a base for predictive reservoir modelling earlier in the field appraisal stage where DFIT data is more readily available. Further, this analysis framework may allow better scenario modelling for hydraulic fracture optimisation or incorporation of emerging completion or micro-proppant technologies as the field becomes more developed and the production data can be matched to layers by other diagnostics.

11 Recommendations

Ultimately, this technology needs to be implemented in suitable field trials. While UQ CNG can assist, this will be the purview of the operating and service companies. Building on this NERA project, there are additional opportunities to improve predictive modelling (and thereby confidence in business cases).

11.1 Reservoir Modelling

To better capture the dynamics of flow subjected to pressure-dependent permeability, further discretisation of the coal layer must be pursued. Heterogeneous distributions of porosity and permeability could be attributed to the model based on data such as vertical profiles of temperature change during production, or core analysis (when technically possible). The inclusion of more conductive zones within the coal layer into reservoir modelling could change how the pressure drops

with production and permeability. Moreover, if vertical flow is present (i.e., coal cleats are connected vertically), desorbed gas will tend to accumulate at the top of the layer. This will favour faster dewatering around the shallower perforations, while providing gas flow rates limited by the maximum relative permeability to gas. The opposite scenario is less sensitive to relative permeability curves since water saturation decreases more uniformly and more slowly.

Another opportunity for modelling improvement would be to consider non-Darcy effects. These could be either inertia effects (Forcheimer flow), which is relevant where flow rates are high (i.e., inside fractures), or slip flow (Klinkenberg flow), which is relevant at low-pressure conditions. Although difficult to directly identify non-Darcy effects using field data, they could be used to history match the gas rates and pressure. It has been shown that Klinkenberg effects on coal seams could represent the effects of permeability rebound due to matrix shrinkage (Gensterblum, et al., 2014; Zhang, et al., 2015) and dynamic relative permeability curves (Shaw, et al., 2019).

11.2 Fluid, Particle Flow and Transport Modelling

The laboratory testing at The University of Adelaide increased our understanding on the importance of correctly matching the distribution of particles to the width distribution of cleats and fractures and their dimensions under fracturing conditions (e.g., low net effective stresses). However, it has not definitively answered the questions on applicability of commercial micro proppants as did the studies by Keshavarz et al. (2014, 2015, 2016) using 10 and 20 µm diameter, hollow sphere, graded particles. Therefore, further testing, like that started at the University of Alberta (continuing after this NERA project), may increase our understanding by testing with 3D printed naturally fractured rock with similar rock properties to coal and based on morphologies of expected fracture patterns, derived from core or image log analyses.

The laboratory testing at The University of Alberta (Appendix J), using the guar-enzyme carrier formulation and Deeprop® 600, indicates that more focused studies with 3D printed, natural fractured materials with similar rock mechanical properties to coals and lower permeability should be able to determine the optimal loading of micro proppants to achieve a crossover in permeability stabilisation at post-injection net stress values. As these samples are complex fractures and can be applicable to naturally fractured rocks, this data has relevance for both coal seam gas and shale fracture stimulation depending on the base material used in the 3D printing.

Recent unpublished research by Di Vaira using the dimensions of flow cells used in the StimLab testing (Penny & Conway, 1995), reproduced the results of proppant mounding at fractures perpendicular to the modelled flow channel of varying degrees, based on proppant sizes. This research in conjunction with recent screen out modelling criteria (Di Vaira, et al., 2021) may be able to better define better micro and standard proppant application and reduce screen-out incidence.

11.3 Fracture Design, Modelling, and Implementation

The developed integrated approach using DFIT, image log, core analysis, hydraulic fracturing and short-term production data, can reduce uncertainty in early production data analysis, providing more confident long-term forecasts where pressure dependent parameters are present (Ramanandraibe, et al., 2021). This should provide operators with greater confidence earlier in the field appraisal process by identifying where micro proppants should yield higher productivity in conjunction with hydraulic fracturing treatments. Finally, recent research in indirect hydraulic fracturing has indicated

simpler fracture propagation and the potential to better control hydraulic fracturing, particularly from horizontal wellbores (R. L. Johnson, et al., 2021).

12 Appendix A: You, Z., Wang, D., Leonardi, C.R., Johnson Jr., R.L., & Bedrikovetsky, P. (2019). Influence of elastoplastic embedment on CSG production enhancement using graded particle injection. The APPEA Journal, 59(1), 9.

Influence of elastoplastic embedment on CSG production enhancement using graded particle injection

Zhenjiang You[A], *Duo Wang*[B], *Christopher Leonardi*[B,D], *Raymond Johnson* Jr[A] and *Pavel Bedrikovetsky*[C]

[A]School of Chemical Engineering, The University of Queensland, Brisbane, Qld 4072, Australia.
[B]School of Mechanical and Mining Engineering, The University of Queensland, Brisbane, Qld 4072, Australia.
[C]Australian School of Petroleum, The University of Adelaide, Adelaide, SA 5005, Australia.
[D]Corresponding author. Email: c.leonardi@uq.edu.au

Abstract. A large percentage of coal seam gas (CSG) reservoirs exhibit low permeability and require stimulation to achieve economic production rates. Graded particle injection (GPI) into the natural fracture and cleat system around hydraulically-induced fractures has been proposed and demonstrated by prior laboratory studies as an effective method of enhancing CSG production. However, pore pressure and fracture width decrease with the distance from the wellbore and hydraulic fractures. Previous modelling determined that staging the injected particles with increasing size may sequentially fill the propped cleats and keep them open during production. GPI results in an increase in permeability above the initial value, expands the stimulated zone, and consequently, increases the productivity index.

The present work aims to improve our understanding of the GPI process for production enhancement by developing a generalised modelling methodology for GPI into the fracture network. The new model accounts for elastoplastic deformation of fracture surface during particle embedment. This is based on elastoplastic finite element modelling of fracture deformation and flow modelling by the lattice Boltzmann method (LBM). Effects of packing densities, effective stress and material properties are incorporated in the modelling. Results of fracture permeability reduction factor due to particle embedment are then applied to the mathematical model for well productivity prediction. Modelling results indicate that elastoplastic fracture deformation leads to lower permeability and production enhancement using GPI, as compared with linear elastic deformation applied in traditional models.

The developed model is applicable to the assessment of potential stimulation outcomes for a range of uncertain reservoir parameters. Better understanding and implementation of GPI schemes can potentially improve post-fracturing results in low-permeability coal intervals substantially.

Keywords: coal seam gas, elastoplastic deformation, finite element method, graded particle injection, lattice Boltzmann method, particle embedment, production enhancement.

13 Appendix B: Ribeiro, A., Santiago, V., Z. You, R. Johnson Jr, S. Hurter, Evaluating Performance of Graded Proppant Injection Into CSG Reservoir: A Reservoir Simulation Study, URTEC-198324-MS, Asia Pacific Unconventional Resources Technology Conference, 18 – 19 November 2019, Brisbane, Australia

URTEC-198324-MS

Evaluating Performance of Graded Proppant Injection into CSG Reservoir: A Reservoir Simulation Study

Ayrton Ribeiro, The University of Queensland Centre for Natural Gas Energi Simulation Research Fellow, The University of Queensland; Vanessa Santiago and Zhenjiang You, School of Chemical Engineering, The University of Queensland; Raymond Johnson Jr, School of Chemical Engineering, The University of Queensland The University of Queensland Centre for Natural Gas; Suzanne Hurter, The University of Queensland Centre for Natural Gas

Abstract

Stress-dependent permeability in coal seam gas (CSG) reservoirs can challenge the development of coal fields with lower initial permeabilities. Thus, advanced well stimulation techniques become essential. This work evaluates the performance of novel graded proppant injection (GPI) technique for CSG reservoir stimulation using reservoir simulation models. A simplified model for steady-state incompressible fluid flow during the early dewatering stage of production is validated by the analytical model results. A general model is then developed for GPI process during unsteady-state compressible two-phase flow in coal, accounting for gas desorption, matrix shrinkage, heterogeneous permeability distribution, and cross-flow. Fractured porous medium is modelled by a dual-porosity radial model. Stress-dependent permeability and matrix shrinkage effects are modelled using the Palmer-Mansoori equation. Under the incompressible fluid flow condition, the productivity index after well stimulation using GPI technique increases by 1.3~2.3 times. Moreover, simulation of compressible gas-water flow coupled with gas desorption from matrix yields 4~13% increment on recovery factor (RF) during production for 30 years. Stimulation accounting for matrix shrinkage enhances RF by 9~13%. For heterogeneous permeability distribution, more permeable layers exhibit deeper penetration of particles. The enhanced permeability owing to GPI yields higher production of both gas and water. Cross-flow between the coal layers influence the effectiveness of the depressurisation process and hence gas desorption post-stimulation. It allows dewatering of deeper layers and additional desorption of gas.

Keywords: Coal Seam Gas, Graded Particle Injection, Reservoir Simulation, Dual-porosity, Productivity Index, Recovery Factor

14 Appendix C: Z. You, D. Wang, N. Di Vaira, R. Johnson Jr, P. Bedrikovetsky, C. Leonardi, Development of Predictive Models in Support of Micro-particle Injection in Naturally Fractured Reservoirs, URTEC-198276-MS, Asia Pacific Unconventional Resources Technology Conference, 18 – 19 November 2019, Brisbane, Australia

URTEC-198276-MS

Development of Predictive Models in Support of Micro-Particle Injection in Naturally Fractured Reservoirs

Zhenjiang You, School of Chemical Engineering, The University of Queensland; Duo Wang and Nathan Di Vaira, School of Mechanical and Mining Engineering, The University of Queensland; Raymond Johnson, Jr, School of Chemical Engineering, The University of Queensland The University of Queensland Centre for Natural Gas; Pavel Bedrikovetsky, Australian School of Petroleum, The University of Adelaide; Christopher Leonardi, School of Mechanical and Mining Engineering, The University of Queensland The University of Queensland Centre for Natural Gas

Abstract

New models for particle embedment during micro-particle injection into naturally fractured reservoirs are developed. The proposed models aim to predict production benefit from the application of micro-particle injection during coal seam gas (CSG) stimulation with broader applications to other naturally fractured reservoirs. The elastoplastic finite element modelling is applied to coal sample from Surat basin (Australia), to predict micro-particle embedment and fracture deformation under various packing densities and closure stresses. The coupled lattice Boltzmann-discrete element model (LBM-DEM) is then used for permeability prediction. These results are combined in a radial Darcy flow analytical solution to predict the productivity index of CSG wells. Modelling results indicate that considering elastoplastic fracture surface deformation leads to smaller permeability increase and less production enhancement, if compared with the linear elastic deformation of fracture implemented in traditional models. Although focused on Australian coals, the developed workflow is more broadly applicable in other unconventional resources. Modelling of particle transport and leak-off in coal fracture intersected with a cleat using LBM-DEM approach demonstrates the effects of particle and cleat sizes, particle concentration and sedimentation on the leak-off process. The leak-off is significantly affected if the particle-cleat size ratio is higher than 0.5. Particle sedimentation increases leak-off into vertical cleat substantially, but has no effect on horizontal cleat. Suspensions of higher concentration result in higher leak-off for cleats with different apertures.

15 Appendix D: R. Johnson Jr, Z. You, A. Ribeiro, S. Mukherjee, V. Santiago, C. Leonardi, Integrating reservoir characterisation, diagnostic fracture injection testing, hydraulic fracturing and post-frac well production data to define pressure dependent permeability behavior in coal. SPE-202281, SPE Asia Pacific Oil & Gas Conference and Exhibition, 17 –19 November 2020

SPE-202281-MS

Integrating Reservoir Characterisation, Diagnostic Fracture Injection Testing, Hydraulic Fracturing and Post-Frac Well Production Data to Define Pressure Dependent Permeability Behavior in Coal

Raymond L. Johnson, Jr., Zhenjiang You, Ayrton Ribeiro, Saswata Mukherjee, Vanessa Salomao de Santiago, and Christopher Leonardi, University of Queensland

Abstract

Defining pressure dependent permeability (PDP) behaviour in coalbed methane (CBM) or coal seam gas (CSG) reservoirs using reservoir simulation is non-unique based on the uncertainty in coal properties and input parameters. A diagnostic fracture injection test (DFIT) can be used to investigate bulk permeability at a reservoir level and at lowered net effective stress conditions. As coal has minimal matrix porosity and under DFIT conditions cleat porosity is fluid saturated with reasonably definable total compressibility values, the DFIT data can provide insight into PDP parameters. At pressures above the fissure opening pressure, pressure dependent leak off (PDL) behaviour increases exponentially with increasing pressure. Many authors have noted that with decreasing pressure PDP declines exponentially with increasing net effective stress. Thus, PDP behaviour can be defined by PDL.

In this paper, we show how combined analyses, using typically collected field data, can be used to better define and constrain the modelling of PDP. We illustrate this process based on a well case study that includes the following data: fracture fabric and porosity reasonably defined from image log and areal core studies; DFIT data acquired under initial saturation conditions; hydraulic fracturing data; and longer term production data. These analyses will be integrated and used to constrain the parameters required to obtain a rate and pressure history-match from the post-frac well production data.

This workflow has application in other coal seam gas cases by identifying key variables where hydraulic fracturing performance has been unable to overcome limitations based on pressure or stress dependent behaviours and often accompanied by low reservoir permeability values. While this is purposely targeting areas where only typically collected field data is available, this workflow can include coal testing data for matrix swelling/shrinkage properties or other production data analysis techniques.

16 Appendix E: D. Wang, Z. You, R. Johnson Jr, L. Wu, P. Bedrikovetsky, S.M. Aminossadati, C. Leonardi, Numerical investigation of the effects of proppant embedment on fracture permeability and well production in Queensland coal seam gas reservoirs. International Journal of Coal Geology (2021) (in press), https://doi.org/10.1016/j.coal.2021.103689

Numerical investigation of the effects of proppant embedment on fracture permeability and well production in Queensland coal seam gas reservoirs

Duo Wang [a,b], Zhenjiang You [c], Raymond L. Johnson Jr. [c,d], Lei Wu [b], Pavel Bedrikovetsky [e], Saiied M. Aminossadati [a], Christopher R. Leonardi [a,d,*]

[a] School of Mechanical and Mining Engineering, The University of Queensland, Brisbane, QLD, 4072, Australia
[b] Department of Mechanics and Aerospace Engineering, Southern University of Science and Technology, Shenzhen, 518055, China
[c] School of Chemical Engineering, The University of Queensland, Brisbane, QLD 4072, Australia
[d] Centre for Natural Gas, The University of Queensland, Brisbane, QLD 4072, Australia
[e] Australian School of Petroleum & Energy Resources, The University of Adelaide, Adelaide, SA 5005, Australia

ARTICLE INFO

ABSTRACT

This paper introduces the development of a new predictive model in support of proppant injection in naturally fractured coal seam gas (CSG) reservoirs. In the proposed model, the finite element method (FEM) is used for the prediction of proppant embedment and elastoplastic deformation of the coal. The lattice Boltzmann method (LBM) is applied to the modelling of fluid flow through propped fractures, in which the modified partially saturated method (MPSM) is implemented to characterise the fluid–solid interactions. Permeability diagrams of the fractures are then generated as functions of particle packing ratio and effective stress. Finally, these results are incorporated into a radial Darcy flow analytical solution to predict the productivity index of the CSG wells under various proppant injection pressures and cleat compressibilities. The developed model is applied to selected coal samples from the Bowen and Surat Basins in Queensland, Australia. Modelling results indicate that proppant injection leads to increased fracture permeabilities and enhanced well productivity indexes. The elastoplastic deformation results in smaller permeability increase and less production enhancement when compared to the traditional linear elastic models. Although focused on Australian coals, the developed workflow can be broadly applicable to the assessment of potential stimulation efficacy in other unconventional reservoirs. In addition, a better understanding and implementation of the proppant injection scheme can effectively improve the post-fracturing performance, particularly in low-permeability coal intervals, which benefits the CSG industry.

17 Appendix F: Santiago, Vanessa, Ribeiro, Ayrton, Johnson, Raymond, Hurter, Suzanne, and Zhenjiang You. "Modelling and Economic Analyses of Graded Particle Injections in Conjunction with Hydraulically Fracturing of Coal Seam Gas Reservoirs." Paper presented at the SPE/AAPG/SEG Asia Pacific Unconventional Resources Technology Conference, Virtual, November 2021

Modelling and Economic Analyses of Graded Particle Injections in Conjunction with Hydraulically Fracturing of Coal Seam Gas Reservoirs

Vanessa Santiago, Ayrton Ribeiro, Raymond Johnson, Jr, and Suzanne Hurter, The University of Queensland, Australia; Zhenjiang You, Edith Cowan University, Australia; The University of Queensland, Australia

Abstract

Hydraulic fractures can enhance well productivity from stress sensitive naturally fractured reservoirs such as coalbed methane or coal seam gas (CSG) reservoirs. Graded proppant injection (GPI) has been proposed to enhance long-term, far-field interconnectivity between the created hydraulic and short-term, enhanced natural fracture permeability, resulting from fracture fluid leakoff and lowered net effective stress. This novel study shows how applying GPI with hydraulic fracturing treatments resulting in an increased stimulated reservoir volume (SRV) can enhance well productivity and improve CSG well economics.

A commercially available reservoir model and history-matched hydraulically fractured coal seam case is used to evaluate well performance differences between a hydraulic fractured reservoir and one including GPI application. A dual-porosity system and Palmer and Mansoori model are used to simulate initial and long-term permeability accounting for reservoir depletion (i.e., increased net effective stress, matrix shrinkage). A previously validated case study is used to describe the post-embedment benefits of GPI based on the porosity model and history-matched reservoir properties. A net present value (NPV) can then be calculated for each scenario, based on the production differences and typical Australian CSG costs.

Our results show that permeability enhancement is achieved beyond the hydraulically fractured region for all post-GPI stimulation cases. An optimal SRV can be found relative to permeability that maximises the incremental NPV from GPI application. The next most significant parameters after permeability that influence the economic outcomes are fracture porosity and coal compressibility. A larger SRV yields higher cumulative gas production over 30 years with up to 7.2 times increase over gas production without GPI. This study substantially increases our understanding on how to model and understand the benefit of GPI application along with hydraulic fracturing to increase the SRV in CSG wells.

keywords: Coal Seam Gas, Coalbed Methane, Graded Proppant Injection, Hydraulic Fracturing, Economic Benefits

18 Appendix G: Di Vaira, Nathan J., Laniewski-Wollk, Lukasz, Johnson Jr., Raymond L., Aminossadati, Saiied M., and Christopher R. Leonardi. "A Novel Methodology for Predicting Micro-Proppant Screenout in Hydraulic Fracturing Treatments." Paper URTEC-208342-MS presented at the SPE/AAPG/SEG Asia Pacific Unconventional Resources Technology Conference, Virtual, November 2021.

A Novel Methodology for Predicting Micro-Proppant Screenout in Hydraulic Fracturing Treatments

Nathan J. Di Vaira, Łukasz Łaniewski-Wołłk, Raymond L. Johnson Jr., Saiied M. Aminossadati, and Christopher R. Leonardi, The University of Queensland

Abstract

Screenout of micro-proppants in narrow fractures is a significant issue for this emerging stimulation technique, however the predictive tools currently used in hydraulic fracturing simulators are inadequate. This work investigates screenout using numerical simulations. Data from the numerical test cell is translated to regions of screenout, which are dependent on the proppant solid volume fraction, ø, and the ratio of fracture width to proppant diameter, w/d. The dependence on w/d which is demonstrated is commensurate with existing bridging modelling. The method of numerical simulation, however, allows further insight into the underlying mechanisms of screenout, namely collision frequency and bridge stability. Incorporation of the screenout regions into a hydraulic fracturing simulator significantly improves the current industry standard of using a threshold of $w/d = 2.5$, at similar computational cost during the hydraulic fracture simulation. The screenout regions can be readily reproduced for any desired modification of parameters, such as friction, by modifying the numerical simulations. This is done here in the presence of electrostatics, and is the first time a methodology has been presented which can incorporate electrostatic parameters into screenout predictions of hydraulic fracturing simulators. Overall, the methodology significantly improves the efficacy of screenout predictions by considering the underlying parameters.

19 Appendix H: Di Vaira, N.J., Łaniewski-Wołłk, Ł., Johnson Jr., R.L., Aminossadati, S.M. and Leonardi, C.R. (2022), Influence of particle polydispersity on bulk migration and size segregation in channel flows, Journal of Fluid Mechanics, 939, A30.

CrossMark

JFM PAPERS

Influence of particle polydispersity on bulk migration and size segregation in channel flows

Nathan J. Di Vaira[1], Łukasz Łaniewski-Wołłk[1,2], Raymond L. Johnson Jr.[3], Saiied M. Aminossadati[1] and Christopher R. Leonardi[1,3,†]

[1]School of Mechanical and Mining Engineering, The University of Queensland, Brisbane, QLD 4072, Australia

[2]Institute of Aeronautics and Applied Mechanics, Warsaw University of Technology, Warsaw 00-665, Poland

[3]Centre for Natural Gas, The University of Queensland, Brisbane, QLD 4072, Australia

The shear-induced migration of dense suspensions with continuously distributed (polydisperse) particle sizes is investigated in planar channel flows for the first time. A coupled lattice Boltzmann–discrete element method numerical framework is employed and validated against benchmark experimental results of bulk shear-induced migration and segregation by particle size. Distinct dependence on the particle size distribution is shown in the flowing (non-plugged) regime (where the bulk solid volume fraction, $\bar{\phi}$, ≤ 0.3) resulting from a dual dependence on the particle self-diffusivity and local rheology imposed by the particle pressure gradient. Close agreement between statistically equivalent bidisperse and polydisperse suspensions suggests that the bulk migration, and by extension the shear-induced diffusivity, is completely characterised by the first three statistical moments of the particle size distribution. For both bidisperse and polydisperse suspensions in the plugging regime, $\bar{\phi} \geq 0.4$, the smallest particles preferentially form the plugs, causing the largest particles to segregate to the channel walls. This effect is accentuated as $\bar{\phi}$ increases and has not been reported in the literature hitherto. It is proposed that smaller particles preferentially form the plugs due to their higher shear-rate fluctuations, which completely dominate particle motion near the plug where the mean shear rate vanishes. Finally, increasing inertia causes a greater bulk migration towards the channel walls, but increased mid-plane migration for the largest particles due to the dependence of the particle self-diffusivity on the particle Reynolds number. As $\bar{\phi}$ increases shear-induced migration dominates and these inertial effects disappear, as does dependence on the particle size distribution.

Key words: suspensions, computational methods, particle/fluid flow

† Email address for correspondence: c.leonardi@uq.edu.au

939 A30-1

20 Appendix I: Laboratory Testing Results, University of Adelaide

20.1 Benchtop Fluid/Micro proppant Testing

Prepared by   Prof. Pavel Bedrikovetsky, Dr. Alexander Badalyan, Mr. Dale Womacks, Dr. Abbas Zeinijahromi, Dr Themis Carageorgos

Organisation   Australian School of Petroleum, The University of Adelaide

Date   10.10.2019.

Content

1. Introduction

This report focuses on the effect of injection of "guar-gel+proppant+enzyme-solution" on permeability of unconsolidated sand pack. All formulations were prepared and experimental procedures were carried out according to Ray's suggestions in e-mail communications from 29.03.2019 to 26.07.2019. The obtained results will be used to study formation damage during injection of the similar formulation into a coal sample.

2. Materials and their preparation

2.1. Sand

A glass beaker with silica sand and MilliQ deionised (DI) water was placed in an ultrasonic bath for about 10 min to wash sand from solid contaminants (clays, mud, etc.). This procedure was repeated about 8 times until supernatant visually was transparent. Then, sand was dried in an atmospheric oven at 60 °C for 24 hours.

Removal of organic impurities was carried out by washing this sand initially with hexane and then by acetone. Acetone was removed from sand by washing it with DI water. Inorganic impurities were removed by washing the above sand with 0.5 M hydrochloric acid. Finally, this sand was washed with DI water until pH of supernatant DI water is equal to pH of the source DI water. Sand drying was carried out in the atmospheric oven at 60 °C for 24 hours.

Washed dry sand was sieved using 210 μm (70 US mesh) and 425 μm (40 US mesh) stainless-steel sieves. This sand (85 g) was used to prepare unconsolidated porous medium with length of 4.5 cm and diameter of 3.81 cm. Mean pore-throat half-size for this porous medium was estimated to be approximately 27 μm.

2.2. Water

Tap water was used for preparation all guar-gel formulation and enzyme solutions. This water was heated up to 70 °C and then placed in the ultrasonic bath to remove dissolved chlorine. pH of de-chlorinated tap water (later in the text referred to as "water") varied between 8.05 and 8.17.

2.3. Guar powder

Guar powder, FWG150D fracturing additive, was mixed with water in blender in the following proportion: 9.6 g of guar powder per 1000 mL of water. By using a variable *ac* voltage supply we adjusted the number of revolutions of blender blades, so no air was entrapped in gel. This eliminated the formation of the so-called "fish-eyes" (small, elongated bubbles filled with air). The presence of air-bubbles in gel will lead to their entrapment in a porous medium and consequent decrease of core permeability.

2.4. Enzyme

Enzyme concentrate, ASP®FWB605E, was used to prepare 200 mL 2% (v/v) stock solution. This stock solution was further diluted by water to 0.1% (v/v) (later in the text referred to as "enzyme-solution") to inject into unconsolidated sand core as a background solution to determine undamaged core permeability. We measured pH of this solution to be pH=7.68.

2.5. Proppant

Ceramic microspheres were used as proppant. Two sizes of proppants were suppled, namely, Deeprop® 600 and Deeprop®1000. In the current tests we used Deeprop® 600 with the median particle radius approximately 5 μm. In this case the jamming ratio (the ratio between the median particle radius and mean pore-throat half-size) $j = 0.19$. This value falls in the range of the so-called "1/7-1/3"-rule for jamming ratio. Particles falling in this range

contribute to formation damage through deep-bed-filtration when injected in a porous medium. Part of these particles may form an external filter cake at unfavourable conditions such as low pH and high salinity. However, during our tests, pH of "guar-gel" and "enzyme-solution" were equal to 7.65 and 7.68, respectively, and no salt was added to fluids resulting in their low salinity.

For particle deposition into a sand pack, this proppant was added to stabilised "guar-gel" to get 8 ppg concentration.

3. Experimental

3.1. Viscosity measurements of guar-gel formulation

Rheological behaviour of prepared "guar-gel" formulations at room temperature (22.3±0.5 °C) was carried out using Anton Paar Rheometer shown in Figure 37. Variation of "guar-gel" viscosity as a function of shear rate was studied 30 min after the completion of "guar-gel" preparation. Since guar-gel viscosity changes with time, it affects the stability of "guar-gel+proppant" suspension. In order to determine the most appropriate time for proppant addition to "guar-gel" we also studied variation of guar-gel viscosity with time.

Figure 37. Anton Paar rheometer.

3.2. Experimental setup to study formation damage

The following setup was proposed by Ray (see Figure 38). The major components of this setup are high-pressure pump, flowmeters, valves, slurry repository and sand pack (core). The following experimental procedure was proposed by Ray according to Figure 38:

a). <u>Injection 1 - Initial permeability test:</u> "Enzyme-solution" injection, pump via Flowmeter 1 Valve 1 with Valve 2 and Valve 3 closed (measure permeability);

b). <u>Injection 2 - Inject specified volume of particles:</u> Inject specified volume of particles: Close Valve 1 to desired ratio of Enzyme to slurry, pressurize repository opening Valve 2, then slowly open Valve 3 until desired ratio is achieved; after desired volume is pumped then close Valve 3 then Valve 2 and commence injection 3;

c). <u>Injection 3 - Retained permeability test:</u> "Enzyme-solution" injection, pump via Flowmeter 1 Valve 1 with Valve 2 and Valve 3 closed (measure permeability);

c). It may be desirable to repeat injections 2 and 3 with additional or differing sized particles. As such, the repository is isolated, can be reloaded and multiple injections can be

performed.
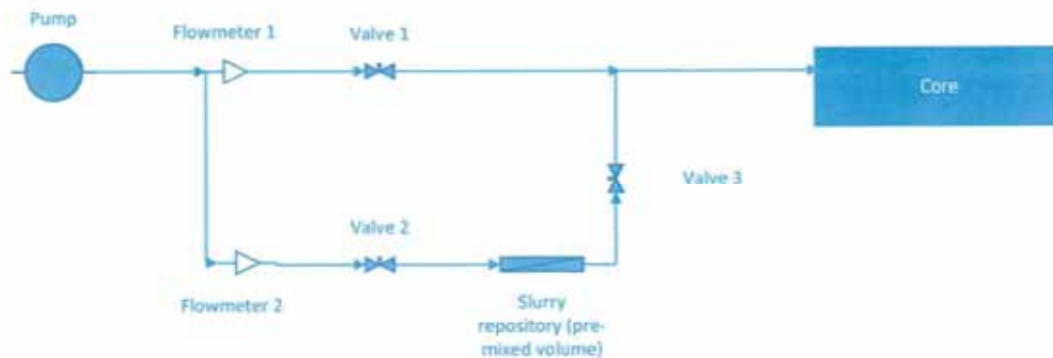
Figure 38. Schematic of the proposed setup

To make this setup and procedure feasible in laboratory and improve the accuracy and reliability of experimental data, the following improvements were implemented in an assembled setup.

Schematic of an experimental setup is shown in **Figure 39**. Compacted unconsolidated sand core *1* is placed inside a Viton sleeve *2* and fixed in its position by two stainless steel flow-distributors *3*. The entire arrangement is enclosed by a high-pressure stainless steel coreholder *4*. A manual pressure generator *5* compresses distilled water *6* and generates overburden pressure measured by an absolute pressure transmitter *7*. Enzyme solution 8 is delivered by a high-performance liquid chromatography (HPLC) pump *9* and mixes in a 3-port valve *10* with "guar-gel+proppant" suspension *12* before entering an ultrasound bath *11*. The "guar-gel+proppant" suspension" is placed inside a high-pressure stainless-steel separating vessel *13*. A Teflon piston *14* separates brine/water *15* from this suspension. The second HPLC pump *16* delivers the suspension to mix with enzyme solution. Two absolute pressure transmitters *17* and *18* measure inlet and outlet pressure for the unconsolidated core. A back-pressure regulator *19* ensures a smooth operation of the HPLC pump and maintains constant pressure of fluids in the pore network. Compressed air from the cylinder *20* develops the required pressure over the elastomeric diaphragm of the back-pressure generator. The differential pressure across the unconsolidated core is measured by four differential pressure transducers (DPTs) *21-24* with the following measuring ranges: 0-0.65 psi, 0-14.5 psi, 0-75 psi and 0-2500 psi. All DPTs are re-zeroed using equilibration three-way manual valves *25-28* prior differential pressure measurements. All information form pressure transmitters and DPTs is transmitted to a real-time data acquisition system consisted of a data acquisition module *29* signal converter *30* and a standalone personal computer *31*. Custom built software based on performed necessary calculations, and via dynamic data, exchange server delivers values of differential pressures and fluid viscosity in real-time to Microsoft Excel file which incorporates all corresponding calculations and graphs. A fraction collector *34* is used to collect effluent suspensions in centrifuge 15 mL and 50 mL plastic tubes *35*. Suspended particle concentrations (in *ppm v/v*) in effluent fluid samples were measured by a portable particle counter *36*.

| a | b |
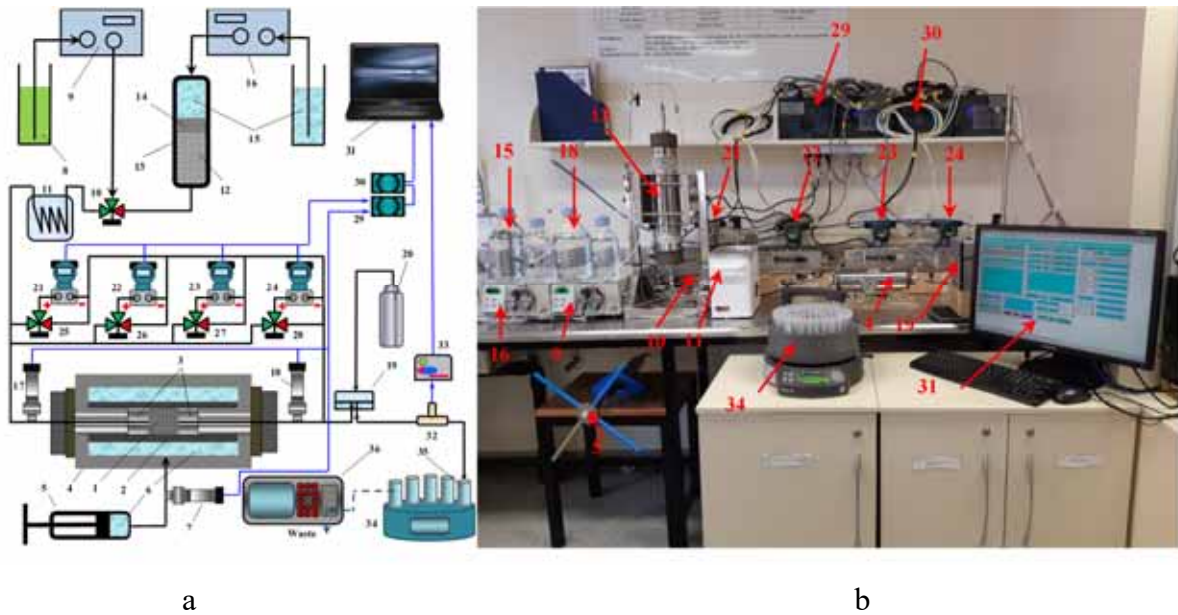
Figure 39. Schematic (a) and photo (b) of experimental setup for deposition of proppant into sand pack

4. Results and discussion

4.1. Rheological properties of "guar-gel" formulation

"Guar-gel" viscosity decreases with shear rates varying from 0.01 s^{-1} to 100 s^{-1} (see Figure 40). Variation of "guar-gel" viscosity with time started 40 min after the completion of "guar-gel" preparation. Viscosity was measured at 100 s^{-1} shear rate. Results are presented in Figure 41. As follows from this figure, 30 min after guar-gel preparation its viscosity may be regarded as stable around 0.395 Pa×s with standard deviation of 0.22%.
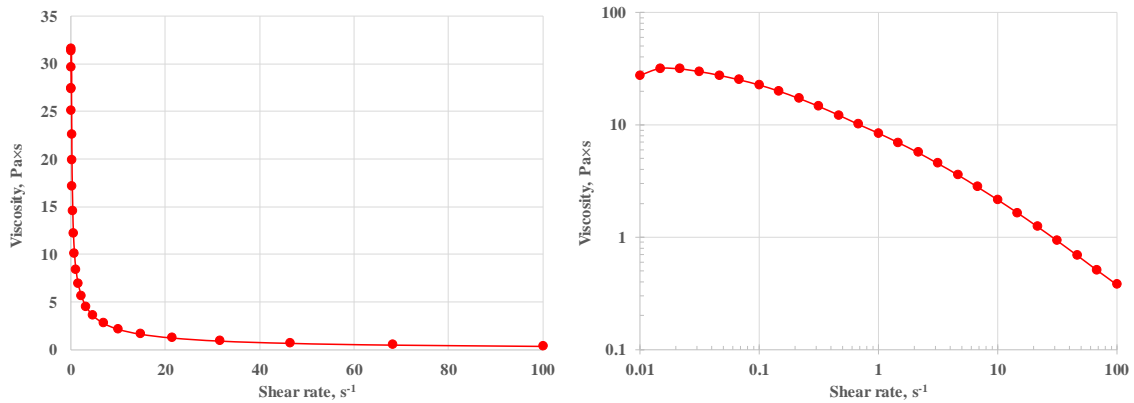
Figure 40. "Guar-gel" viscosity as function of shear rate
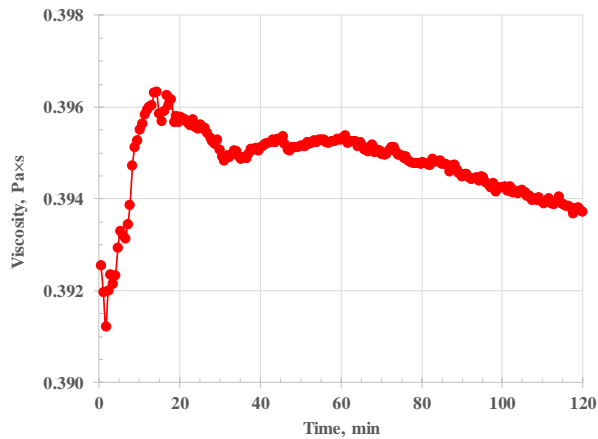
Figure 41. "Guar-gel" viscosity as function of time (at 100 s-1 shear rate) after guar-gel preparation

4.2. Mixing of "guar-gel" and "enzyme solution"

The quality of mixing "guar-gel" and "enzyme-solution" will have significant effect on sand pack core permeability damage. Therefore, full mixing must be achieved before the obtained mixture is injected into the core. Simple mixing of two streams didn't achieve the goal of full mixing as follows from Figure 42 (left measuring cylinder): we can see "guar-gel" in the bottom of the measuring cylinder, and "enzyme-solution" at the top. When coiled tube with two mixed streams was placed in ultrasonic water bath, the quality of mixing process was perfect (see Figure 42, right measuring cylinder).
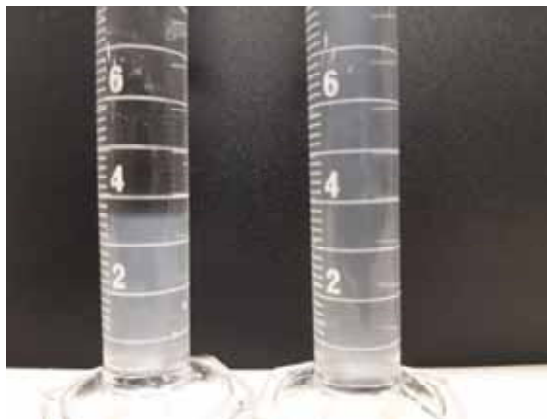
Figure 42. Mixing "guar-gel" with "enzyme-solution" without (left measuring cylinder) and with ultrasonification (right measuring cylinder).

4.3. Core saturation with water and corefloods with "enzyme-solution" and "guar-gel (25% v/v) + enzyme-solution (75% v/v)"

Sandpack was prepared according to the procedure described in details elsewhere (Russell, et al., 2017). An overburden pressure of 1600 psi was developed. Sand core was saturated by injecting about 270 pore-volumes (PVI) of water at 1 mL/min volumetric flowrate. Correlation between pressure drop across the core, ΔP, and volumetric flowrate, Q, was linear for flowrates varying between 4 mL/min and 10 mL/min. It took about 3 min for ΔP to stabilise at flowrates below 4 mL/min. At volumetric flowrates above 5 mL/min ΔP stabilises in 2-3 seconds. However, $\Delta P=f(Q)$-relationship deviates upward from linearity (lower permeability values) at volumetric flowrates above 10 mL/min. An undamaged core

permeability is equal to $k_{0,enz} = 6007 \pm 85$ mD. This corresponds to 0.0947 ± 0.0037 psi pressure drop across the core. These parameters were measured at 6 mL/min volumetric flowrate during injection of a freshly prepared "enzyme-solution" for about 10 PVI (42 min). The obtained experimental data are shown in   (a)

(b)

Figure 43. As follows from Figure 43, undamaged core permeability is stable within its experimental uncertainty of 3.2%.

(a)   (b)
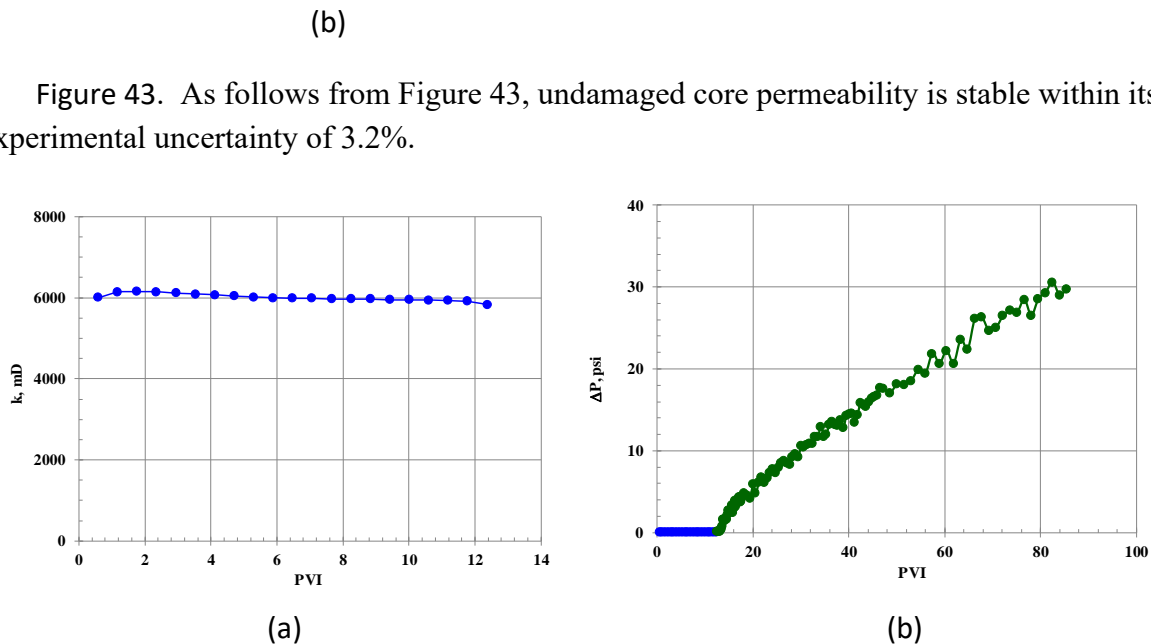
Figure 43. Permeability (a) and pressure drop (b) across the unconsolidated core: blue circles – injection of enzyme solution; green circles – injection of "guar-gel (25% v/v) + enzyme-solution (75% v/v)"

According to Figure 41, a freshly prepared "guar-gel" reaches its stability after about 30 min from its preparation. This "guar-gel" was placed into the high-pressure stainless-steel separating vessel. We started injection of guar-gel 45 min after its preparation and injected about 73 PVI of "guar-gel (25% v/v) + enzyme-solution (75% v/v)". This was achieved by injecting "guar-gel" by Prep-100 HPLC pump with 1.5 mL/min flowrate, and injecting enzyme solution by Prep-36 HPLC pump with 4.5 mL/min flowrate. It was not possible to accurately calculate core permeability during transient process of this injection due to unavailability of viscosity data for this mixture at various stages of transient process. Instead, we present variation of pressure drop across the core as a function of PVI ((a)

(b)

Figure 43b). Pressure drop across the core continues to raise even after 73 PVI. We decided to stop injection of "guar-gel (25% v/v) + enzyme-solution (75% v/v)" since during next test we will inject only 2 PVI of "guar-gel+proppant+enzyme-solution".

After this injection we injected "enzyme-solution" into the core to check if initial core permeability can be restored (see   (a)

(b)

Figure 44a). End-point permeability of the core to "enzyme-solution" is $k_{1-end,enz} = 35.0 \pm 1.2$ mD with corresponding $\Delta P_{1-end,enz} = 16.8 \pm 0.6$ psi pressure drop across the core. This

damaged core permeability is significantly lower than that for undamaged core $k_{0,enz} = 6007 \pm 85$ mD. Therefore, it is not possible to recover initial/undamaged core permeability by injection of "enzyme-solution" ONLY. This $\Delta P_{1\text{-}end,enz}$-value should be considered when injecting "guar-gel+proppant+enzyme-solution" suspension into the core.

(a)   (b)
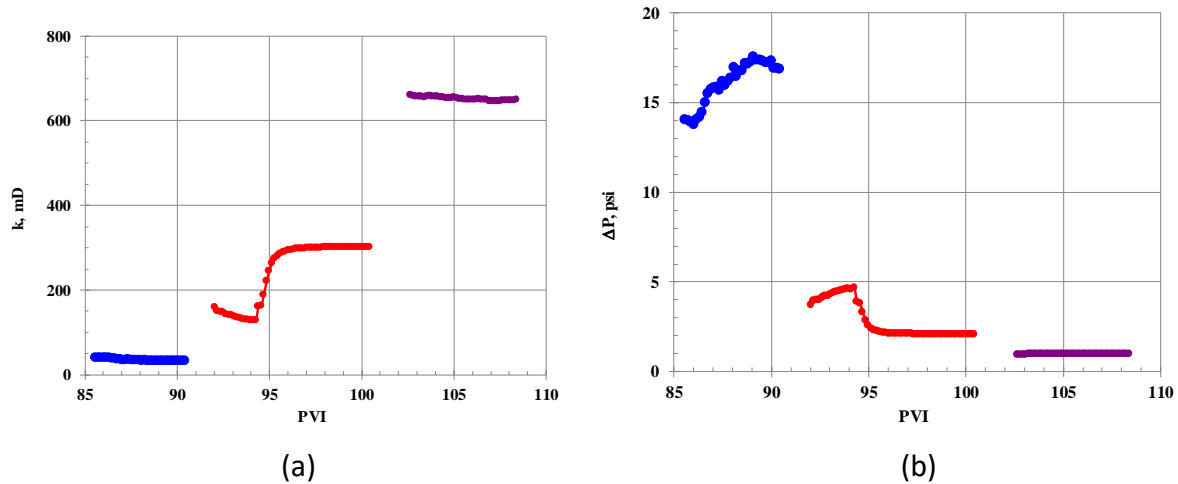
Figure 44. Permeability (a) and pressure drop (b) across the core during injection of "enzyme-solution": blue circles – after guar-gel injection; red circles – after 36 mL/min; and purple circles – after 100 mL/min (all data are for 6 mL/min volumetric flowrate)

Gradual increase of "enzyme-solution" flowrate, initially to 36 mL/min and then to 100 mL/min, resulted in increased core permeability up to 301.7 ± 0.1 mD and 649.8 ± 2.2 mD, respectively, according to   (a)

(b)

Figure 44a. This was accompanied with the decrease of pressure drop across the core (see

(a)   (b)

Figure 44b). However, it was not possible to completely restore core permeability after injection of "guar-gel (25% v/v) + enzyme-solution (75% v/v)". During injection of proppant into the next newly prepared sand pack we will compare the effect of proppant deposition into a porous medium by comparing values of pressure drop across an undamaged core and that with proppant deposited.

4.4. Injection of formulation without agitation

The previous core has been removed from the coreholder, and a new sand pack (210 μm-425 μm sand grain size) was prepared according to the previous procedure (sub-section 2.1). The core was saturated with water and then with "enzyme-solution" at 0.1 mL/min.

"Guar-gel" was prepared according to the previous procedure described in sub-section 2.3. After "guar-gel" stabilisation during 30 min, Deeprop® 600 proppant was added to "guar-gel" to get 8 ppg concentration. This suspension was placed in the high-pressure stainless-steel separating vessel.

Undamaged core permeability to "enzyme-solution" was measured to be equal to 5994 ± 42 mD after 10.3 PVI injected (see   (a)

(b)

Figure 45). Then, we started simultaneous injection of "guar-gel+proppant" at 1.5 mL/min (Prep-100 HPLC pump) and "enzyme-solution" at 4.5 mL/min (Prep-36 HPLC pump). These flowrates will achieve 25% dilution of "guar-gel+proppant". Below we present the observation during this trial:

➢ pressure over Teflon piston in the high-pressure stainless-steel separating vessel started to gradually increase up to 3000 psi without visible movement of guar-gel in connecting transparent tubing;
➢ we were not able to pump "guar-gel+proppant" suspension since this formulation started look like soft rubber (see Figure 46);
➢ we stopped test and disconnected the high-pressure stainless-steel separating vessel from the coreholder;
➢ we will try to prepare 25% diluted "guar-gel+proppant+enzyme-solution" and inject it at 6 mL/min into the core, hoping proppant will not sediment for the duration of the test.
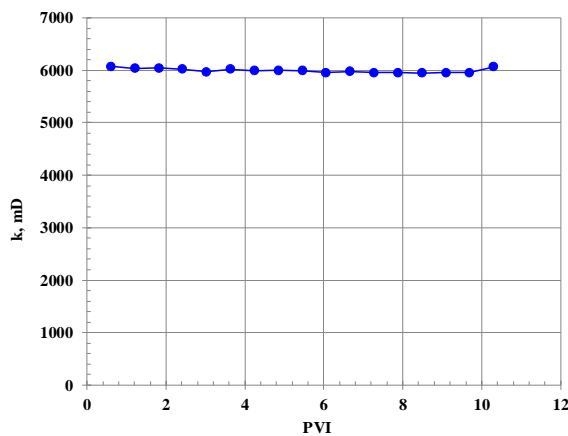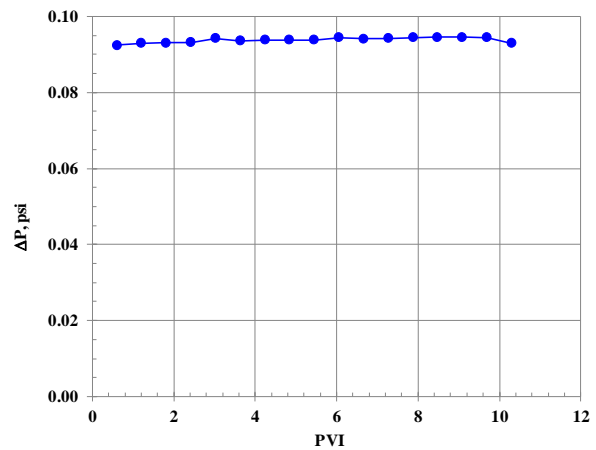
(a) (b)

Figure 45. Permeability (a) and pressure drop (b) across the core: blue circles - during injection of "enzyme-solution" at 6 mL/min

Figure 46. Formulation of "guar-gel+proppant" at 8 ppg 30 min after its preparation

4.5. Injection of pre-diluted formulation

We prepared the following formulation: water – 25 mL, guar-powder - 0.24 g, proppant – 24 g, and "enzyme-solution" 75 mL. Concentrations of this formulation correspond to that

intended to be injected into the core in section 4.4. The formulation was carefully agitated and placed in a 100 mL measuring cylinder, and the rate of proppant particle sedimentation was recorded and photographed with the results presented in (a) (b) Figure 47.

(a) (b)
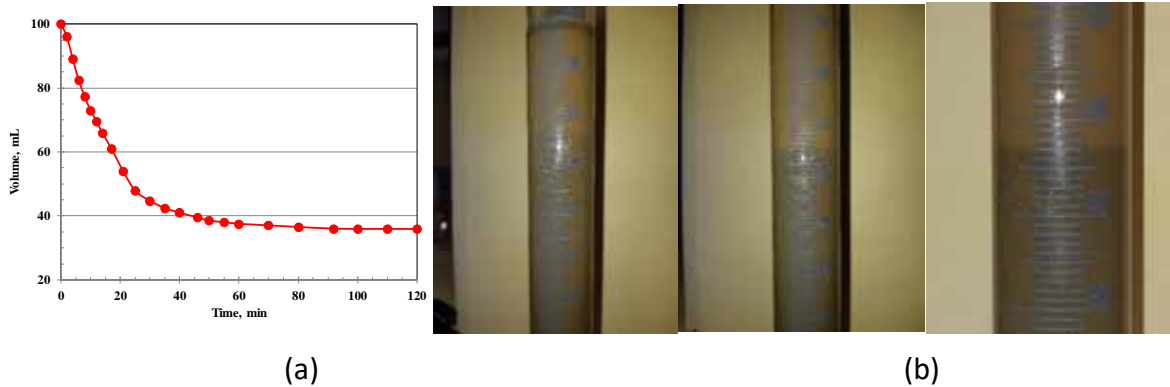
Figure 47. Results of proppant sedimentation (a) and associated photos for various stages of proppant sedimentation (b)

As follows from (a) (b)

Figure 47a,b, injection of formulation should be carried out during the first 2 min after filling the formulation into the stainless-steel separating vessel. This will achieve injection of proppant with required concentration. Otherwise, it is necessary to rotate this separating vessel. Even during such rotation, it is not possible to agitate the formulation located in the downstream tubes before the coreholder.

The amount of proppant particles approaching an inlet cross-section of the sand pack-core is about 1.37×10^6. At the same time, the number of pores in the same cross-section of the sand pack-core is about 2.22×10^5. This results in about 6 proppant particles per ONE pore in sand pack. This proppant particle concentration is too high, which will result in instantaneous formation of an external filter cake and sand pack-core damage. Such high proppant concentration when injecting into coal fractures may not be a problem, however, it is questionable in the case of the sand pack-core.

A new sand pack was prepared. Measured undamaged core permeability to "enzyme-solution" is equal to 5701 ± 173 mD (StDev=3.1 %, volumetric flowrate = 6 mL/min) after 45 PVI injected (see Figure 48).
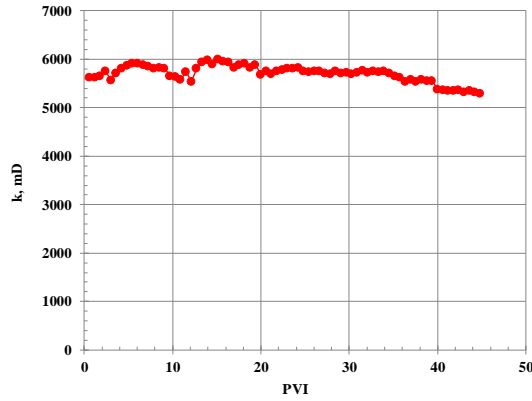
Figure 48. Undamaged permeability of sand pack (210-425 mm grain size)

The following formulation was prepared according to the previously agreed recipe: water – 25 mL, guar-powder - 0.24 g, proppant – 24 g, and enzyme solution 75 mL. This formulation was placed inside a stainless steel high-pressure separating vessel. According to the previous report, after about 2 min since preparation of the above formulation the volume of the proppant decreased by about 4%. In order to keep proppant suspended during the injection of this formulation into the sand pack, we rotated the stainless steel high-pressure separating vessel 5 times for every 30 sec.

Injection of the formulation was carried for 0.45 PVI. Pressure drop across the sand pack increased rapidly up to about 2500 psi (see   (a)

         (b)

Figure 49). Sandpack permeability dropped down to about 0.22 mD without recovery during injection of "enzyme-solution". Further injection of the "enzyme-solution" didn't improve the situation: pressure drop was maintained around 2500 psi (the limit for our high-pressure valves).

We reduced inlet pressure by opening the valve before the sand pack: some proppant dropped into the beaker. After this, we continued injection of the "enzyme-solution" with the results presented in   (a)   (b)

Figure 50. An unexplained result was obtained: final permeability of the sand pack after 1st proppant formulation injection is about 1116 mD, whereas in the previous report we obtained 35.0 mD for the sand pack exposed to proppant-free formulation. We can't explain this observation at least at this stage.
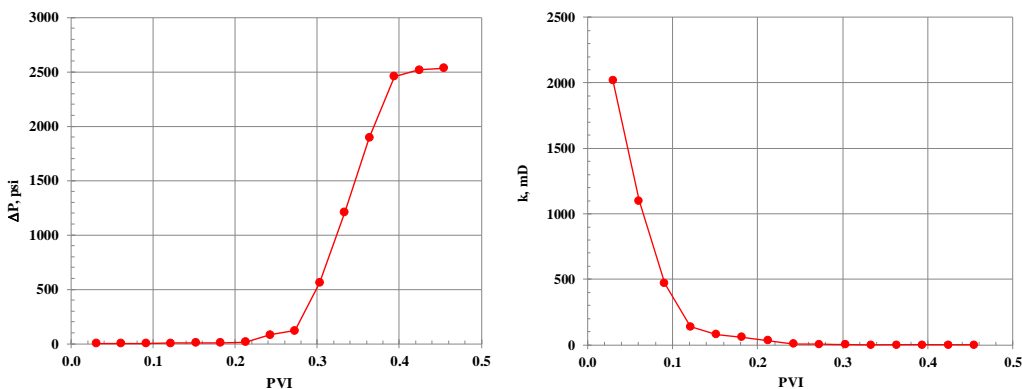
Figure 49. Injection of proppant formulation into the unconsolidated sand pack
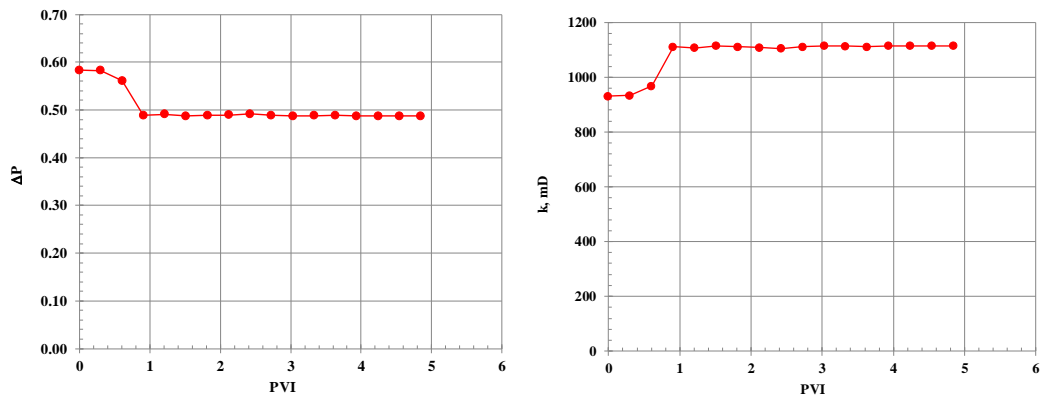
(a)   (b)

Figure 50. Injection of "enzyme-solution" into the unconsolidated sand pack: a – pressure drop across the sand pack, b - permeability of the sand pack

The second injection of the proppant formulation into the sand pack during 0.29 PVI resulted in permanent damage of the sand pack as follows from   (a)

(b)

Figure 51. Further injection of the "enzyme-solution", opening valve to reduce inlet pressure and again injection of "enzyme-solution" didn't improve the situation.
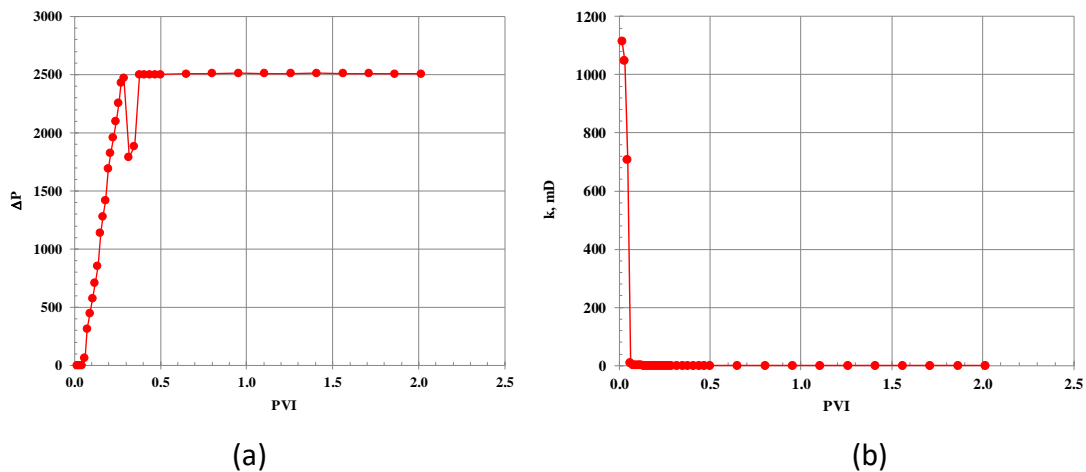
(a)   (b)

Figure 51. Injection of "enzyme-solution" into the unconsolidated sand pack: a – pressure drop across the sand pack, b – permeability of the sand pack

By rotating the stainless steel high-pressure separating vessel, we maintained proppant suspended in the formulation for the duration of two injections. However, high proppant concentration results in a very quick sand pack damage. It is not easy to operate experimental setup and perform reliable experimental data collection when pressure drop across the core changes very quickly. We propose to reduce proppant concentration in the formulation for at least 10 times. This will allow us to observe a gradual permeability damage of the sand pack, get better control over the experimental setup and better and more reliable collection of

experimental data.

Before removing the sand pack we disassembled all inlet tubing, removed small amount of proppant which remained there, re-assembled all connections, and injected enzyme solution to determine the final damaged sand pack permeability. Since the damage was significant, we were unable to inject this solution at the previous volumetric flowrate of 6 mL/min, instead injection flowrate was set at 1 mL/min. The experimental data are presented in   (a)   (b)

Figure 52. After two injections of "guar-gel+proppant+enzyme-solution"-formulation into the sand pack, its permeability dropped from 5995 mD down to 0.0567 mD.

(a)   (b)
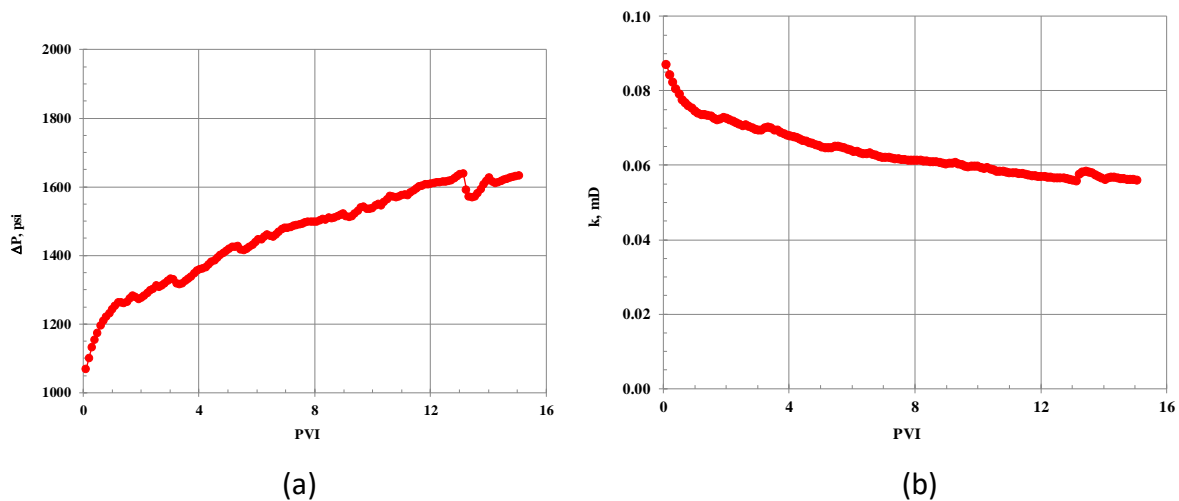
Figure 52. Pressure drop across the sand pack (a) and damaged sand pack permeability (b)

We measured mass of proppant in two effluent samples (during 1st and 2nd proppant injections) and that recovered from the sand pack. Results are presented in Figure 53. Higher amount of proppant in the effluent stream during 1st injection than during 2nd injection is an indication that the sand pack was able to pass more proppant when it is less damaged. However, damaging the sand pack resulted in almost complete filtration of proppant by the sand pack. Amount of proppant recovered from the sand pack after experiment is significantly higher than those presented in effluent streams. This is another indication of deep-bed filtration and external cake formation. The number of proppant particles in approximately 2 mm of sand pack from its inlet surface ($m_{proppant} = 0.074$ g) is equal to about 3.70×10^8. Taking into an account that mean sand grain size is about 318 μm, we have about 6 layers of sand in 2 mm sand pack length, and, consequently, 6.17×10^7 proppant particles per sand pack layer. This number of proppant particles significantly exceeds the number of pores of about 2.22×10^5 in the cross-section of the sand pack-core. *We again conclude that the proposed proppant concentration in the injected "guar-gel+proppant+enzyme-solution"-formulation is very high to properly study the effect of damage in the sand pack.* This was proved by a quick increase of the pressure drop across the sand pack with resultant severe sand pack damage. However, for coal fractures this concentration may be acceptable.
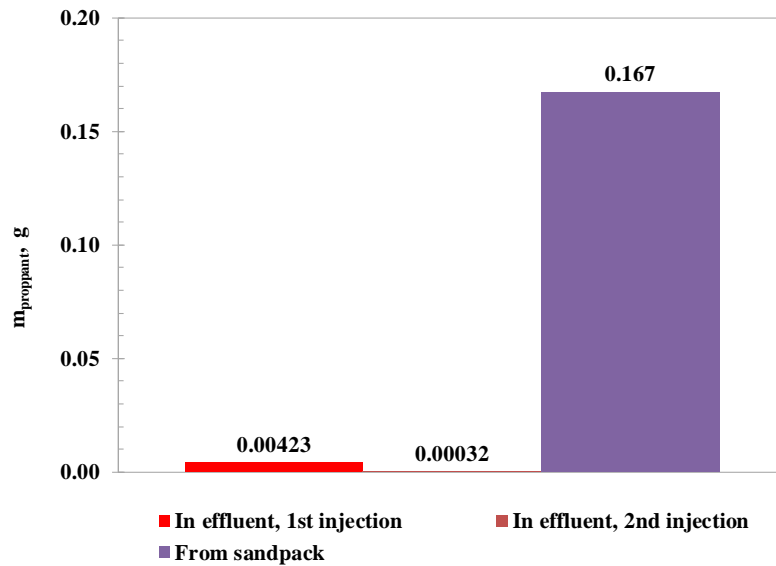
Figure 53. Proppant concentrations

We made photographs of clean sand and inlet surface of the damaged sand pack (see

(a)   (b)

Figure 54). The surface of the sand pack has greyish colour like that of proppant which proved the deposition of proppant on the inlet surface of the sand pack.

(a)   (b)
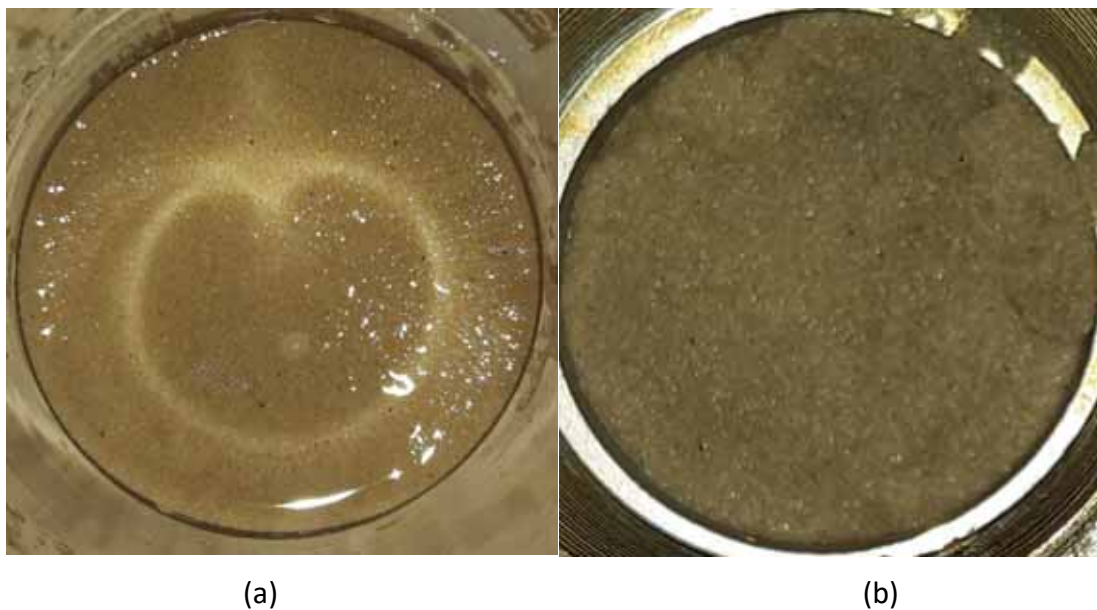
Figure 54. Photos of clean sand (a) and inlet surface of the damaged sand pack (b)

4.6. Injection of formulation with agitation

A new sand pack was prepared from washed sand (sand grain size varied from 210 μm to 425 μm which corresponds to 20/40 US mesh size). An overburden pressure of 1600 psi was developed. Undamaged core permeability to "enzyme solution" (0.1% v/v) at 6 mL/min volumetric flowrate was measured to be 4909±43 mD (see Figure 55).

(a)   (b)
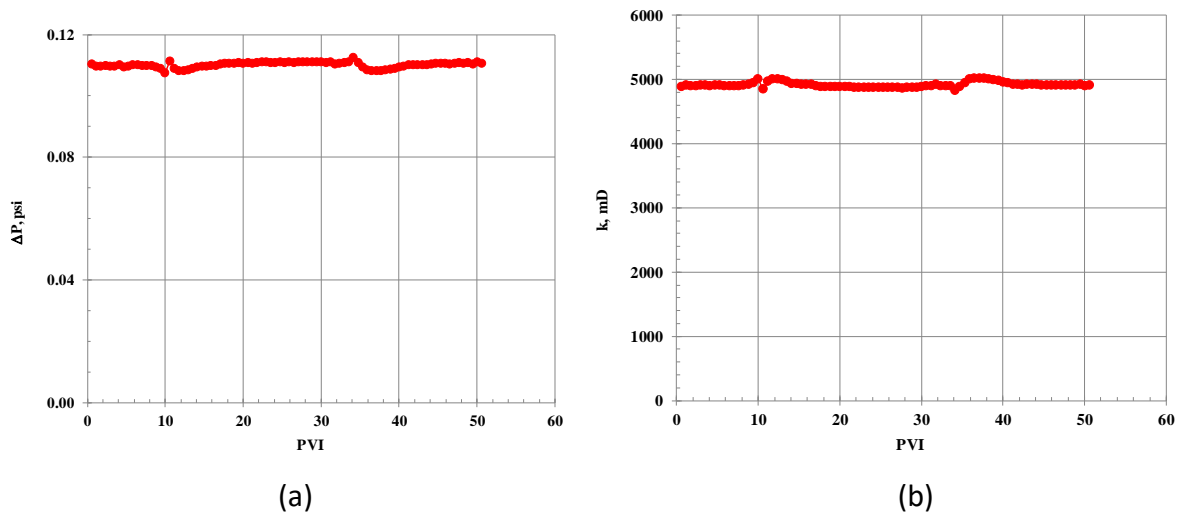
Figure 55. Pressure drop across the sand pack (a) and undamaged sand pack permeability to "enzyme solution" (b) (1st injection)

"Guar-gel" is a pseudoplastic fluid. It maintains its fluidity for some time after applying a shear stress. We freshly-prepared 10 mL of the "guar-gel+proppant" formulation (8 ppg concentration), placed it in a plastic syringe and shook it for 15 min. Then, the syringe with the formulation was left for 30 min undisturbed. After that we were able to easily dispense the formulation from the syringe. It means for at least 30 min after its agitation the "guar-gel+proppant" formulation maintains its fluidity, and we will be able to inject it from the high-pressure separating vessel into tubing to mix it with the enzyme solution" before injecting into the sand pack.

A freshly-prepared 136 mL of the "guar-gel+proppant" formulation (8 ppg concentration) was placed in 300 mL glass bottle. This formulation was shaken for 15 min. After that, it was quickly transferred to the high-pressure separating vessel. The vessel was connected by tubing to a coiled stainless-steel tube placed inside the ultrasonic bath. Flowrate of "enzyme-solution" was set at 6 mL/min. In anticipation of pressure drop across the sand pack to change very quickly during injection of "guar-gel+proppant+enzyme-solution" we set the data acquisition cycle to 1 sec. The previous trials showed us that injection of 0.45 PVI of "guar-gel+proppant+enzyme-solution" into the sand pack delivered too many proppant microspheres to the sand pack and caused significant permeability damage. For this reason, in this trial we decided to inject 0.011 PVI (0.23 mL of "guar-gel+proppant+enzyme-solution" formulation). A volume of a high-pressure transparent tube before the coreholder was measured, and thus we determined the injected volume.

The flowrate of HPLC pump *16* delivering "guar-gel+proppant" formulation was set to 1.5 mL/min and the flowrate of HPLC pump *9* delivering "enzyme-solution" (0.1% v/v) was set to 4.5 mL/min (see Figure 39). Thus, we achieved 25% dilution of the concentrated "guar-gel+proppant" formulation. The "guar-gel+proppant+enzyme-solution" formulation leaving the coiled stainless-steel tube after the ultrasonic bath was uniform due to ultrasonication. We injected 0.011 PVI, stopped HPLC pump *16*, set the flowrate of HPLC pump *9* at 6 mL/min, run the "enzyme-solution" and determined damaged sand pack permeability after the first injection. Pressure drop across the sand pack and damaged core permeability to "enzyme-solution" are shown in   (a)

(b)

Figure 56. Damaged sand pack permeability is equal to 1443±28 mD.

(a)

(b)
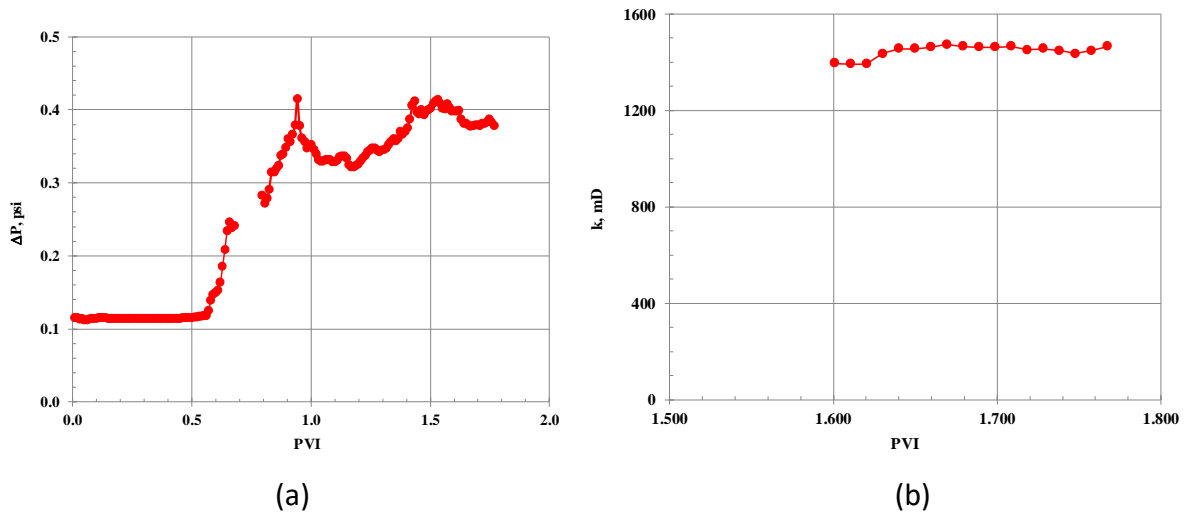
Figure 56. Pressure drop across the sand pack (a) and damaged sand pack permeability to "enzyme-solution" (b) (2nd injection)

We carried out three additional injections with the results presented in Figure 57, 22 and 23. Damaged sand pack permeabilities are 618±11 mD, 340.3±4.6 mD and 0.282±0.016 mD, respectively. As follows from   (a)

          (b)

Figure 59, the core was severely damaged after 4th injection.

(a)

(b)
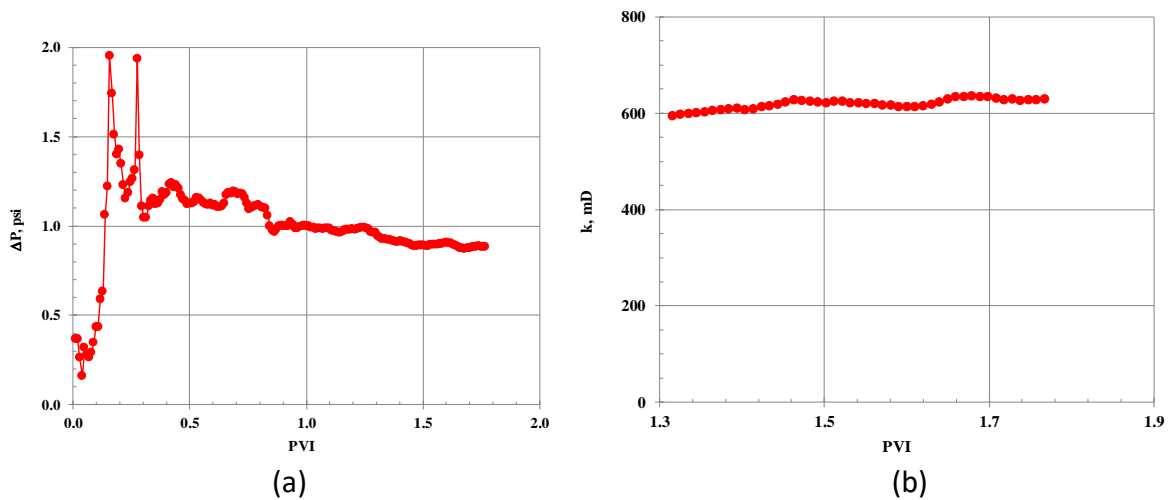
Figure 57. Pressure drop across the sand pack (a) and damaged core permeability to "enzyme-solution" (b) (3rd injection)
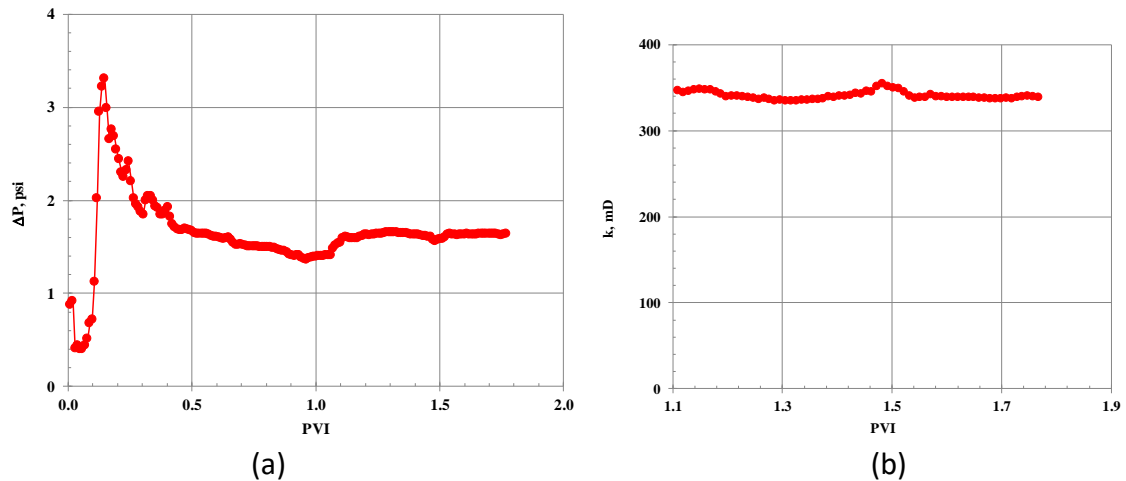
Figure 58: Pressure drop across the sand pack (a) and damaged core permeability to "enzyme-solution" (b) during the third injection
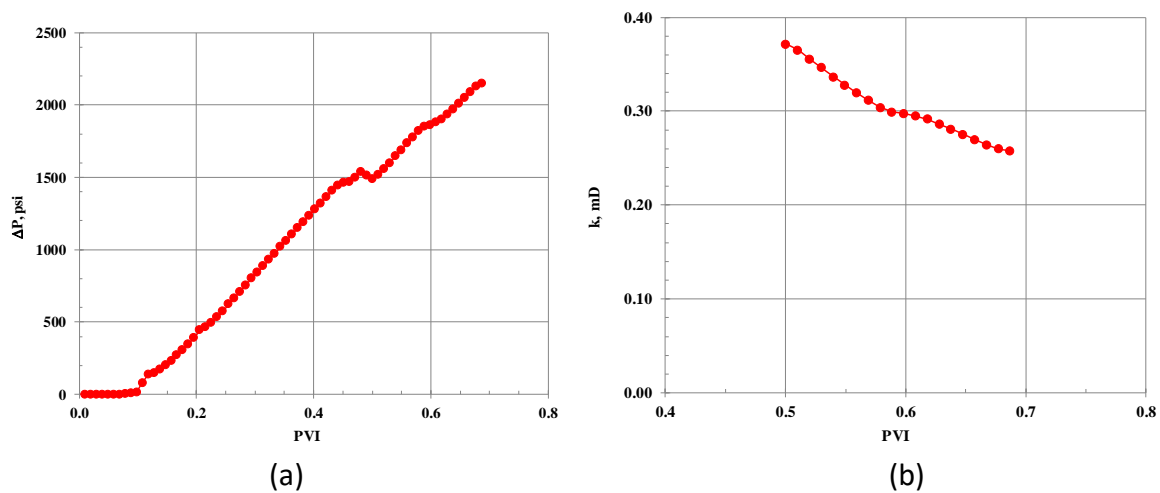
Figure 59. Pressure drop across the sand pack (a) and damaged core permeability to "enzyme-solution" (b) (4th injection)

20.2 Variation of viscosity of "guar-gel+enzyme-solutions" as a function of shear rate

Prepared by: Prof. Pavel Bedrikovetsky, Dr. Alexander Badalyan, Dr. Abbas Zeinijahromi, Dr Themis Carageorgos

Four "guar-gel+enzyme-solutions" formulations were prepared as follows:

1. Dissolve 0.96 g of guar in 100 mL of tap water.
2. For 95:5 formulation ratio remove 5 mL of "guar-gel", measure pH of the remaining, by adding 40 drops of 0.5% (v/v) acetic acid solution in distilled water pH of "guar-gel" is adjusted at around 5.5 (see Table 10).
3. Add 5 mL of 0.002% (v/v) solution in tap water.
4. Check pH of "guar-gel+enzyme-solution" and add more acetic acid if needed.

5. Repeat above steps for 90:10, 85:15 and 80:20 formulations; by removing 10, 15 and 20 mL of "guar-gel" and adding the same volumes of 0.5% (v/v) acetic acid solution in distilled water.
6. pH-values of prepared solutions are presented in Table 10.
7. Time intervals between completion of preparation of "guar-gel+enzyme-solutions" formulations and commencing viscosity measurements were always less than 5 min.

Table 10. pH of prepared formulations.

Guar-gel % (v/v)	Enzyme solution %, (v/v)	pH		
		Guar-gel	Enzyme-solution	Guar-gel+enzyme-solution
95	5	7.67		5.55
90	10	7.50	7.59	5.48
85	15	7.63		5.49
80	20	7.64		5.58

Results of viscosity measurements as function of shear rate (0.01 to 1000 s^{-1}) are presented in Figure 60.
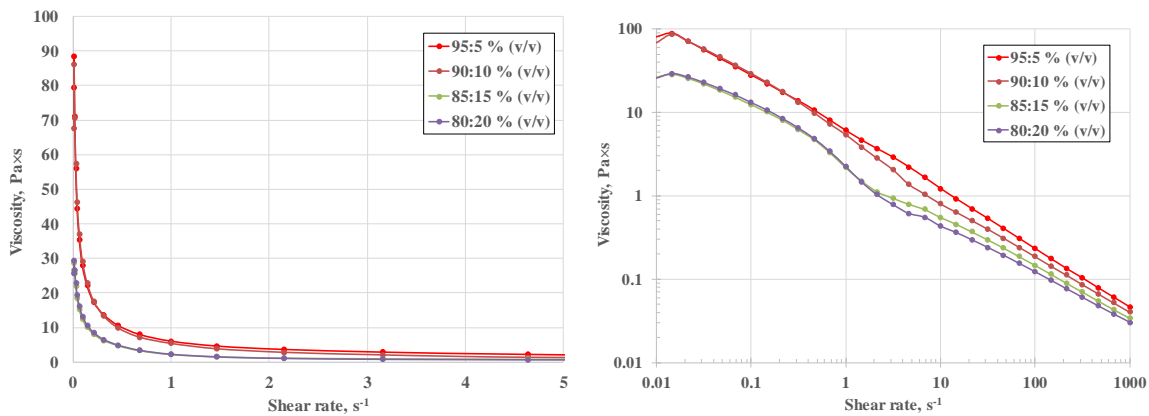
Figure 60. Viscosity of "guar-gel+enzyme-solution" formulations as function of shear rate.

Below we present experimental data for viscosity as function of shear rate for four "guar-gel+enzyme-solution" formulations (Tables 11 to 14).

Table 11. Viscosity as function of shear rate for 95:5 % (v/v) "guar-gel+enzyme-solution" formulation.

Meas. Pts.	Shear Rate	Shear Stress	Viscosity	Speed	Torque
	s^{-1}	Pa	Pa×s	1/min	μNm
1	0.00991	0.788	79.5	0.00329	25.7
2	0.0147	1.3	88.4	0.00487	42.4

3	0.0215	1.53	71	0.00715	50
4	0.0316	1.77	55.9	0.0105	57.7
5	0.0464	2.06	44.3	0.0154	67.3
6	0.0681	2.4	35.3	0.0226	78.5
7	0.1	2.79	27.9	0.0332	91.2
8	0.147	3.24	22.1	0.0487	106
9	0.215	3.74	17.3	0.0715	122
10	0.316	4.32	13.7	0.105	141
11	0.464	4.9	10.6	0.154	160
12	0.681	5.46	8.01	0.226	178
13	1	6.05	6.05	0.332	198
14	1.47	6.8	4.63	0.487	222
15	2.15	7.86	3.65	0.715	257
16	3.16	9.15	2.89	1.05	299
17	4.64	10.3	2.21	1.54	335
18	6.81	11.3	1.66	2.26	369
19	10	12.2	1.22	3.32	400
20	14.7	13.4	0.916	4.87	439
21	21.5	15.1	0.699	7.15	492
22	31.6	16.9	0.535	10.5	553
23	46.4	18.9	0.406	15.4	617
24	68.1	20.9	0.307	22.6	684
25	100	23.2	0.232	33.2	760
26	147	25.9	0.176	48.7	846
27	215	28.9	0.134	71.5	946
28	316	32.5	0.103	105	1,060
29	464	36.6	0.0788	154	1,200
30	681	41.1	0.0603	226	1,340
31	1,000	46.4	0.0464	332	1,520

Table 12. Viscosity as function of shear rate for 90:10 % (v/v) "guar-gel+enzyme-solution" formulation.

Meas. Pts.	Shear Rate	Shear Stress	Viscosity	Speed	Torque
	s⁻¹	Pa	Pa×s	1/min	µNm
1	0.0099	0.67	67.6	0.00328	21.9
2	0.0147	1.26	86.1	0.00486	41.3
3	0.0215	1.52	70.5	0.00714	49.6
4	0.0316	1.81	57.4	0.0105	59.3
5	0.0464	2.14	46.2	0.0154	70.1
6	0.0681	2.51	36.9	0.0226	82.1
7	0.1	2.92	29.2	0.0332	95.4
8	0.147	3.37	22.9	0.0487	110
9	0.215	3.8	17.6	0.0715	124
10	0.316	4.2	13.3	0.105	137
11	0.464	4.57	9.84	0.154	149
12	0.681	4.91	7.21	0.226	161
13	1	5.41	5.41	0.332	177
14	1.47	5.65	3.85	0.487	185
15	2.15	6.08	2.82	0.715	199
16	3.16	6.48	2.05	1.05	212
17	4.64	6.36	1.37	1.54	208
18	6.81	7.13	1.05	2.26	233
19	10	8.01	0.801	3.32	262
20	14.7	9.33	0.636	4.87	305
21	21.5	10.9	0.505	7.15	356
22	31.6	12.6	0.398	10.5	411
23	46.4	14.4	0.311	15.4	471
24	68.1	16.4	0.241	22.6	537
25	100	18.7	0.187	33.2	610
26	147	21.2	0.144	48.7	693
27	215	24.1	0.112	71.5	787
28	316	27.4	0.0865	105	894
29	464	31.1	0.067	154	1,020
30	681	35.4	0.0519	226	1,160
31	1,000	40.5	0.0405	332	1,320

Table 13. Viscosity as function of shear rate for 85:15 % (v/v) "guar-gel+enzyme-solution" formulation.

Meas. Pts.	Shear Rate	Shear Stress	Viscosity	Speed	Torque
	s^{-1}	Pa	Pa×s	1/min	µNm
1	0.00995	0.263	26.5	0.0033	8.61
2	0.0147	0.42	28.7	0.00486	13.7
3	0.0215	0.552	25.7	0.00714	18.1
4	0.0316	0.696	22	0.0105	22.7
5	0.0464	0.856	18.5	0.0154	28
6	0.0681	1.04	15.2	0.0226	34
7	0.1	1.24	12.4	0.0332	40.6
8	0.147	1.48	10.1	0.0487	48.4
9	0.215	1.74	8.07	0.0715	56.8
10	0.316	1.97	6.24	0.105	64.5
11	0.464	2.19	4.72	0.154	71.7
12	0.681	2.25	3.3	0.226	73.5
13	1	2.19	2.19	0.332	71.5
14	1.47	2.22	1.51	0.487	72.5
15	2.15	2.41	1.12	0.715	78.8
16	3.16	2.96	0.935	1.05	96.7
17	4.64	3.69	0.794	1.54	120
18	6.81	4.67	0.686	2.26	153
19	10	5.52	0.552	3.32	180
20	14.7	6.7	0.457	4.87	219
21	21.5	7.98	0.37	7.15	261
22	31.6	9.42	0.298	10.5	308
23	46.4	11	0.237	15.4	359
24	68.1	12.7	0.187	22.6	416
25	100	14.7	0.147	33.2	479
26	147	16.9	0.115	48.7	552
27	215	19.4	0.0898	71.5	633
28	316	22.2	0.0703	105	726
29	464	25.6	0.0551	154	837
30	681	29.5	0.0432	226	963
31	1,000	34.1	0.0341	332	1,120

Table 14. Viscosity as function of shear rate for 80:20 % (v/v) "guar-gel+enzyme-solution" formulation.

Meas. Pts.	Shear Rate	Shear Stress	Viscosity	Speed	Torque
	s^{-1}	Pa	Pa×s	1/min	μNm
1	0.00994	0.255	25.7	0.0033	8.35
2	0.0147	0.429	29.3	0.00486	14
3	0.0215	0.573	26.6	0.00715	18.7
4	0.0316	0.725	22.9	0.0105	23.7
5	0.0464	0.902	19.4	0.0154	29.5
6	0.0681	1.1	16.2	0.0226	36.1
7	0.1	1.32	13.2	0.0332	43.3
8	0.147	1.57	10.7	0.0487	51.4
9	0.215	1.83	8.48	0.0715	59.7
10	0.316	2.07	6.53	0.105	67.5
11	0.464	2.26	4.87	0.154	73.9
12	0.682	2.32	3.4	0.226	75.8
13	1	2.26	2.26	0.332	73.9
14	1.47	2.16	1.47	0.487	70.5
15	2.15	2.22	1.03	0.715	72.6
16	3.16	2.48	0.784	1.05	81
17	4.64	2.86	0.616	1.54	93.5
18	6.81	3.78	0.554	2.26	123
19	10	4.34	0.434	3.32	142
20	14.7	5.33	0.363	4.87	174
21	21.5	6.4	0.297	7.15	209
22	31.6	7.64	0.241	10.5	250
23	46.4	9.02	0.194	15.4	295
24	68.1	10.6	0.155	22.6	346
25	100	12.3	0.123	33.2	403
26	147	14.3	0.0973	48.7	467
27	215	16.6	0.0769	71.5	541
28	316	19.2	0.0607	105	627
29	464	22.3	0.048	154	728
30	681	26	0.0382	226	850
31	1,000	30.4	0.0304	332	995

Conclusions

Analysis of experimental data on the effect of "guar-gel+proppant+enzyme-solution" injection on permeability of unconsolidated sandpacks allowed us to make the following conclusions:

1. "Guar-gel" formulation maintains its viscosity for the duration of about 80 minutes from its preparation. This contributes to the stability of "guar-gel+proppant" formulation.
2. Mixing "guar-gel" and "enzyme-solution" in a coiled stainless-steel tube placed in an ultrasound bath results in their uniform mixing. This will improve the quality of proppant injection.
3. Injection of diluted "guar-gel" (25% dilution with "enzyme-solution") into the sand pack results in its un-repairable damage.
4. Non-agitated "guar-gel+proppant" formulation loses its fluidity in about 10 min thus, preventing its mixing with "enzyme-solution" and consecutive injection into the sand pack.
5. Injection of proppant-free "guar-gel+enzyme-solution" formulation (25% dilution) leads to the irreparable sand pack damage, irrespectively of the duration of the following injection of pure "enzyme-solution". It means, that even after a good mixing of "guar-gel" and "enzyme-solution" prior to injection into the sand pack, "guar-gel" still maintains its elevated viscosity for the appreciable time. As a result, after injection of pure "enzyme-solution", some of gel is removed from the sand pack, whereas part of it still remains in pores like residual crude oil in sandstones after waterflooding.
6. Injection of small volumes of pre-diluted "guar-gel+proppant+enzyme-solution" formulation into the sand pack leads in significant damage of the sand pack due to the presence of high number of proppant microspheres depositing onto the inlet cross-section of the sand pack.
7. Very small amount of proppant microspheres pass through the sand pack (about 2.7%), whereas the remaining ones are captured by sand pack.
8. Pre-agitation of "guar-gel+proppant" formulation contributed to maintaining its fluidity for the duration of the experimental program and allowed carrying several injections into the sand pack.
9. Very small volumes of injected proppant microspheres allowed performing several injections with the sand pack permeability decline after each injection.

20.3 Variation of viscosity of guar-gel and guar-gel+enzyme solution+acetic acid formulations a function of shear rate and time using bob and cup rheometer

Prepared by: Prof. Pavel Bedrikovetsky, Dr. Alexander Badalyan, Dr. Abbas Zeinijahromi, Dr Themis Carageorgos

Date: 11.07.2020.

1. Rheological properties of 100% guar-gel as a function of shear rate at various pH

Two guar-gel formulations were prepared by adding 0.24 g of guar powder to 100 mL of tap water, and they are referred to as 100% guar-gel below.

Table 15 presents the results of pH for the prepared formulations and viscosity test conditions. Experimental viscosity-*vs*-share rate data for the studied formulations are presented in Figures 52 to Figure 66. Table 16 presents a summary of the interpolated experimental viscosity data at 30 s^{-1} shear rate.

Table 15. pH of prepared formulations for viscosity-vs-shear-rate tests

Guar-gel % (v/v)	pH		
	Tap	Guar-gel	Guar-gel + Acetic acid
100	7.63	7.98/7.99*	N/A
100	7.73	7.83	5.41/5.51*

Note: * - pH after 24 hours

Rheological tests start immediately after formulation preparation:
- ➢ 5 viscosity measurements were performed at 0, 15, 30, 45 and 60 min after formulation preparation;
- ➢ experimental viscosity data were interpolated in the range of shear rates from 10.7 to 110 s^{-1} by polynomials with R^2 greater than 0.994, and viscosities were calculated at 30 s^{-1} shear rate at 0, 15, 30, 45 and 60 min after formulation preparation;
- ➢ 5 viscosity measurements were carried on the same formulation 24 hours after its preparation with calculated mean value and standard deviation.

1.1. 100% guar-gel at pH=7.98
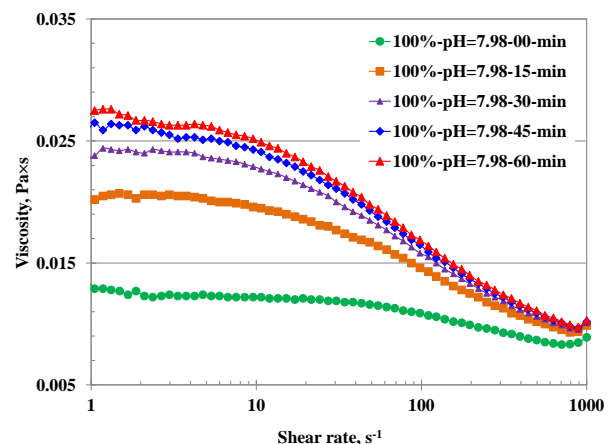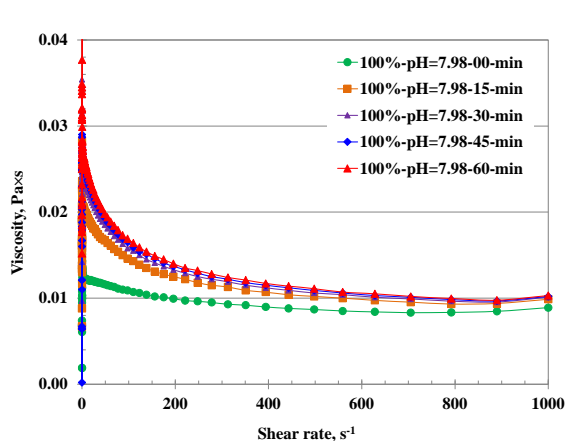
Figure 61: Viscosity-vs-shear rate for guar-gel formulation at pH=7.98: (a) linear scale, (b, c) logarithmic scale

Figure 62: Viscosity-vs-time of hydration for guar-gel formulation at pH=7.98 and at 30 s-1 shear rate (interpolated experimental viscosity data)

(c)

Figure 63: Viscosity-vs-shear rate for guar-gel formulation at pH=7.98 after 24 hours of hydration: (a) linear scale, (b, c) logarithmic scale

1.2. <u>100% guar-gel at pH=5.41</u>
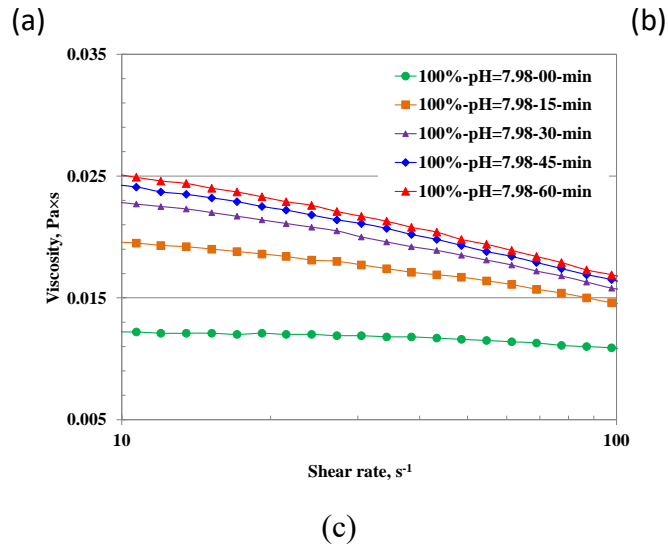

(a)

(b)

(c)

Figure 64: Viscosity-vs-shear rate for guar-gel+acetic acid formulation at pH=5.41: (a) linear scale, (b, c) logarithmic scale
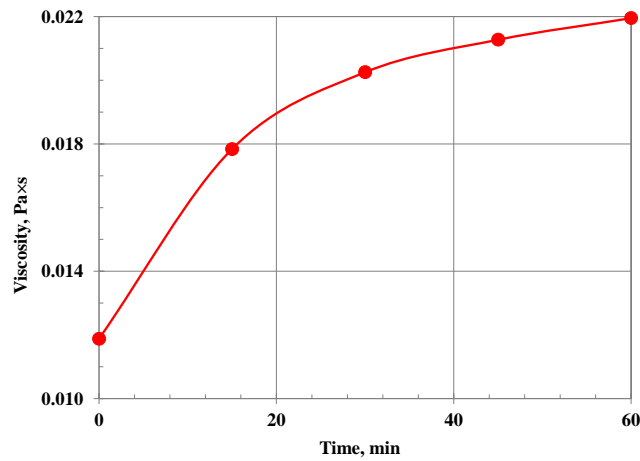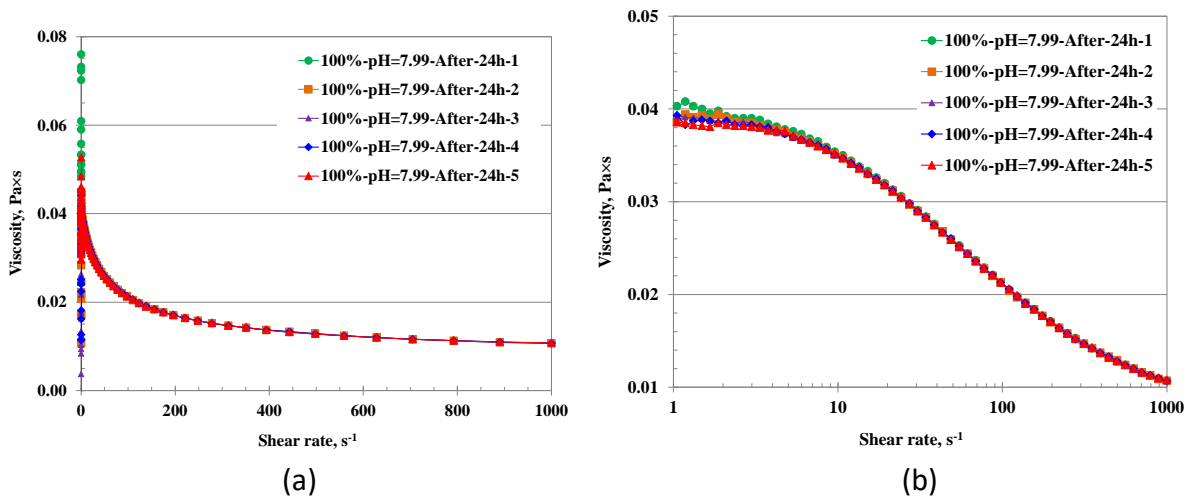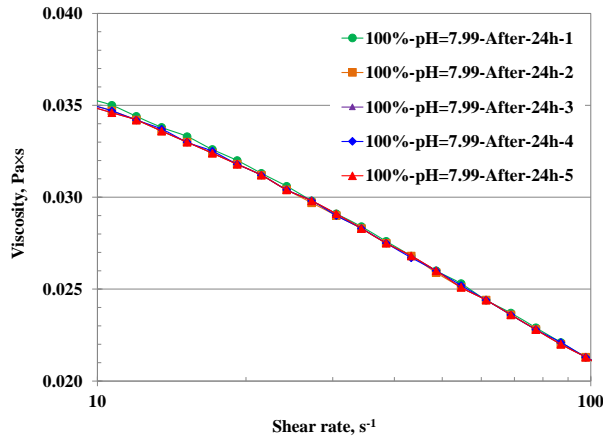
Figure 65: Viscosity-vs-time of hydration for guar-gel+acetic acid formulation at pH=5.41 and 30 s-1 shear rate (interpolated experimental viscosity data)
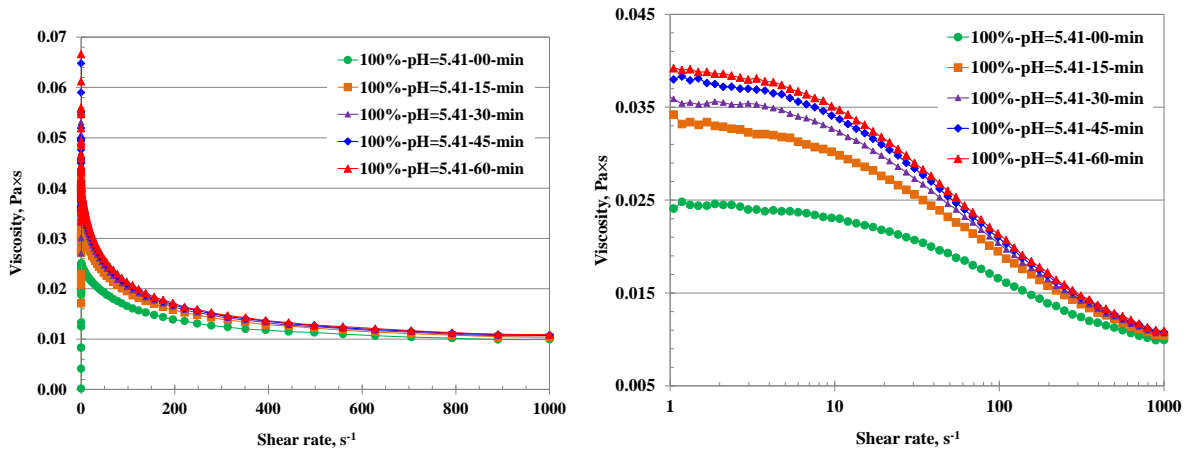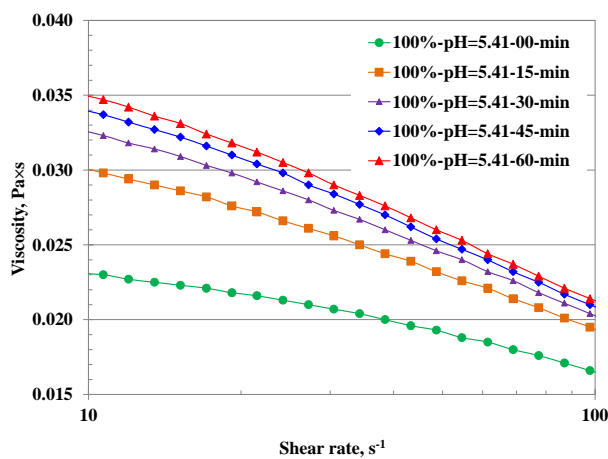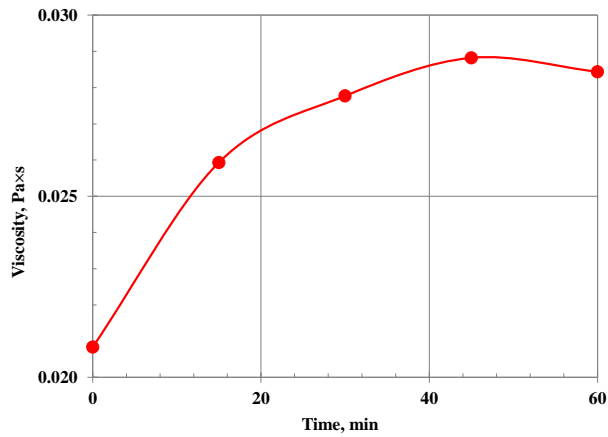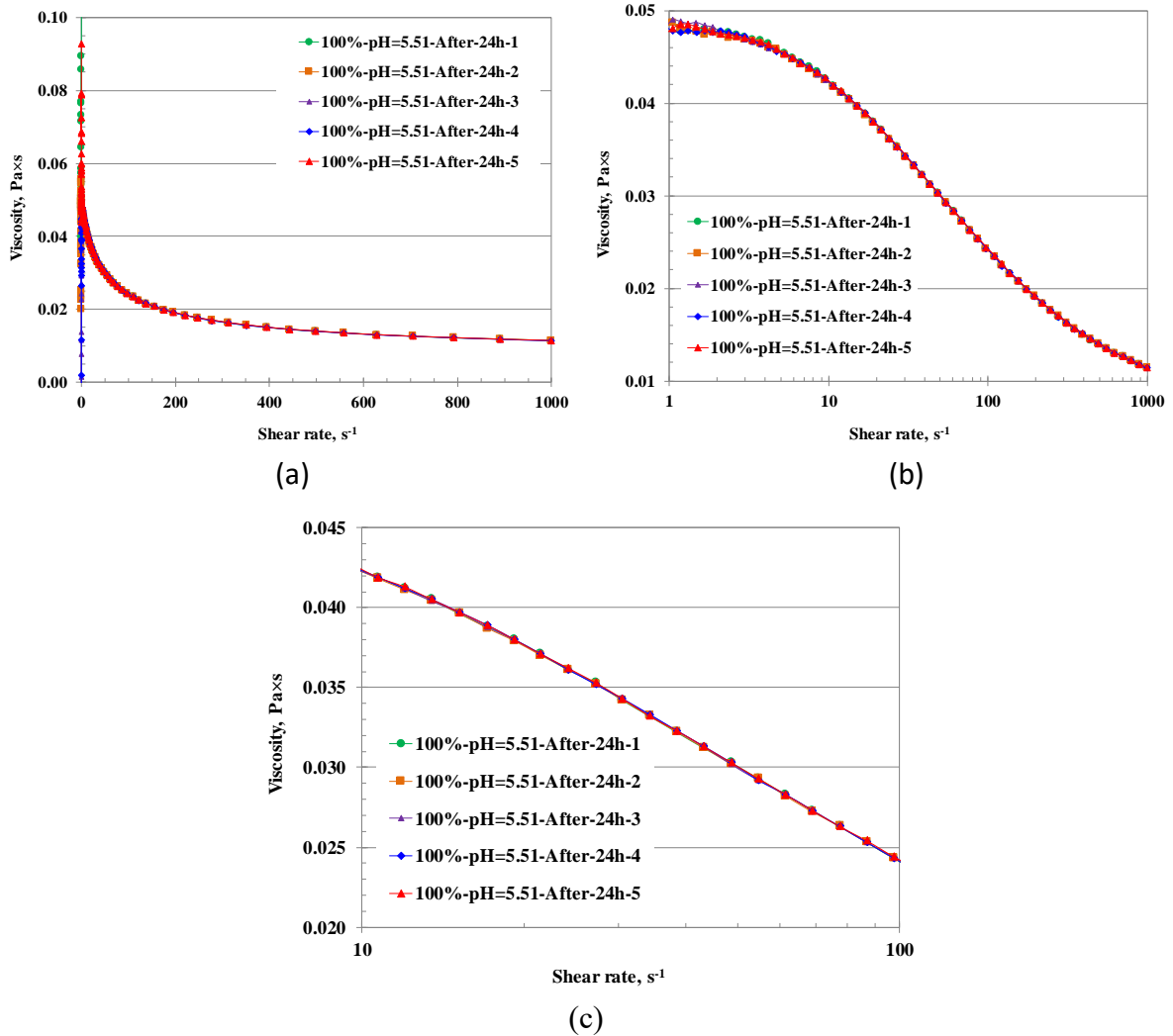

(a)

(b)

(c)

Figure 66. Viscosity-vs-shear-rate for guar-gel+acetic acid formulation at pH=5.51 after 24 hours of hydration: (a) linear scale, (b, c) logarithmic scale

Table 16. Viscosity of guar-gel formulations as function of hydration time at 30 s^{-1} shear rate

Guar-gel formulation	Hydration time	Viscosity	St. Dev.	St. Dev.
	min	Pa×s	Pa×s	%
Normal pH				
100%-pH=7.98-00-min	0	0.0119		
100%-pH=7.98-15-min	15	0.0178		
100%-pH=7.98-30-min	30	0.0203	N/A	N/A
100%-pH=7.98-45-min	45	0.0213		
100%-pH=7.98-60-min	60	0.0220		
100%-pH=7.99-After-24h-1	1440 (24 hours)	0.0293		
100%-pH=7.99-After-24h-2	1440 (24 hours)	0.0292		
100%-pH=7.99-After-24h-3	1440 (24 hours)	0.0295	0.0001	0.49
100%-pH=7.99-After-24h-4	1440 (24 hours)	0.0292		
100%-pH=7.99-After-24h-5	1440 (24 hours)	0.0292		
Low pH				
100%-pH=5.41-00-min	0	0.0208		
100%-pH=5.41-15-min	15	0.0259		
100%-pH=5.41-30-min	30	0.0278	N/A	N/A
100%-pH=5.41-45-min	45	0.0288		
100%-pH=5.41-60-min	60	0.0284		
100%-pH=5.51-After-24h-1	1440 (24 hours)	0.0345		
100%-pH=5.51-After-24h-2	1440 (24 hours)	0.0344		
100%-pH=5.51-After-24h-3	1440 (24 hours)	0.0345	0.00004	0.10
100%-pH=5.51-After-24h-4	1440 (24 hours)	0.0345		
100%-pH=5.51-After-24h-5	1440 (24 hours)	0.0345		

Comments:

➤ viscosities of guar-gel formulations with normal and low pH increase with hydration time;

➤ viscosity of guar-gel formulation increased 1.85-times (85%) after the first hour of hydration process at pH=7.98;

➤ viscosity of guar-gel formulation increased 2.47-times (147%) after 24 hours of hydration process at normal pH=7.99;

➤ viscosity of guar-gel formulation increased 1.37-times (37%) after the first hour of hydration process at pH=5.41;

➤ viscosity of guar-gel formulation increased 1.66-times (66%) after 24 hours of hydration process at normal pH=5.51;

➤ decreasing pH of guar-gel formulation from 7.99 to 5.51 increased its viscosity 2.90-times immediately after preparation, and 1.18-times after 24 hours.

2. Rheological properties of guar-gel+enzyme-solution+acetic acid as function of shear rate

Four guar-gel+enzyme-solution+acetic acid formulations were prepared by addition of 0.002% (v/v) enzyme solution to guar-gel prepared as per Section 1 above. Table 17 gives the results of pH measurement for the prepared formulations.

Table 17. pH of prepared formulations for viscosity-vs-shear rate tests

Guar-gel % (v/v)	Enzyme solution % (v/v)	pH				
		Tap water	Guar-gel	Enzyme solution	Guar-gel + Enzyme-solution	Guar-gel + Enzyme-solution + Acetic-acid
95	5	7.66	7.67	7.93	7.68	5.46/5.61*
90	10	7.73	7.74	7.89	7.75	5.45/5.60*
85	15	7.83	7.76	7.91	7.73	5.44/5.60*
80	20	7.91	7.95	7.96	7.83	5.45/5.55*

Note: * - pH after 24 hours

Rheological tests start immediately after formulation preparation:
- ➢ 5 viscosity measurements were performed at 0, 15, 30, 45 and 60 min after formulation preparation;
- ➢ experimental viscosity data were interpolated in the range of shear rates from 10.7 to 110 s^{-1} by polynomials with R^2 greater than 0.994, and viscosities were calculated at 30 s^{-1} shear rate at 0, 15, 30, 45 and 60 min after formulation preparation;
- ➢ 5 viscosity measurements were carried on the same formulation 24 hours after its preparation with calculated mean value and standard deviation.

2.1. 95% guar-gel and 5% enzyme solution at pH=5.46

Figure 67: Viscosity-vs-shear-rate for guar-gel+enzyme-solution+acetic acid formulation (95%-5%) at pH=5.46: (a) linear scale, (b, c) logarithmic scale

Figure 68. Viscosity-vs-time of hydration for guar-gel+enzyme-solution+acetic acid formulation (95%-5%) at pH=5.46 and 30 s-1 shear rate (interpolated viscosity data)

Figure 69: Viscosity-vs-shear-rate for guar-gel+enzyme-solution+acetic acid formulation (95%-5%) at pH=5.61 after 24 hours of hydration: (a) linear scale, (b, c) logarithmic scale

2.2. 90% guar-gel and 10% enzyme solution at pH=5.45

(c)

Figure 70: Viscosity-vs-shear-rate for guar-gel+enzyme-solution+acetic acid formulation (90%-10%) at pH=5.45: (a) linear scale, (b, c) logarithmic scale

Figure 71: Viscosity-vs-time of hydration for guar gel-enzyme-solution-acetic acid formulation (90%-10%) at pH=5.45 and 30 s-1 shear rate (interpolated viscosity data)

(a)

(b)

(c)

Figure 72: Viscosity-vs-shear-rate for guar-gel+enzyme-solution+acetic acid formulation (90%-10%) at pH=5.60 after 24 hours of hydration: (a) linear scale, (b, c) logarithmic scale

2.3. 85% guar-gel and 15% enzyme solution at pH=5.44
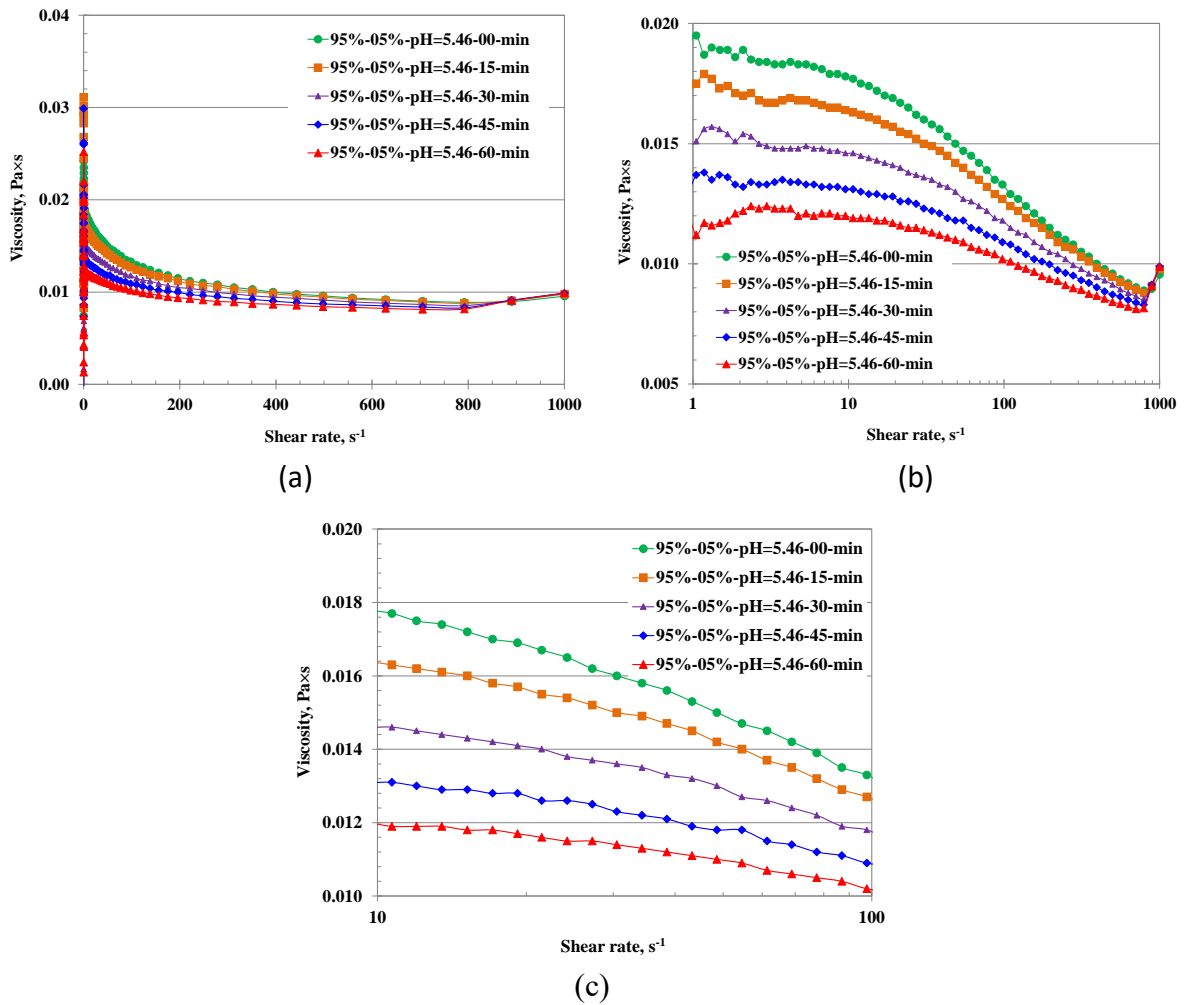

(a)

(b)

(c)
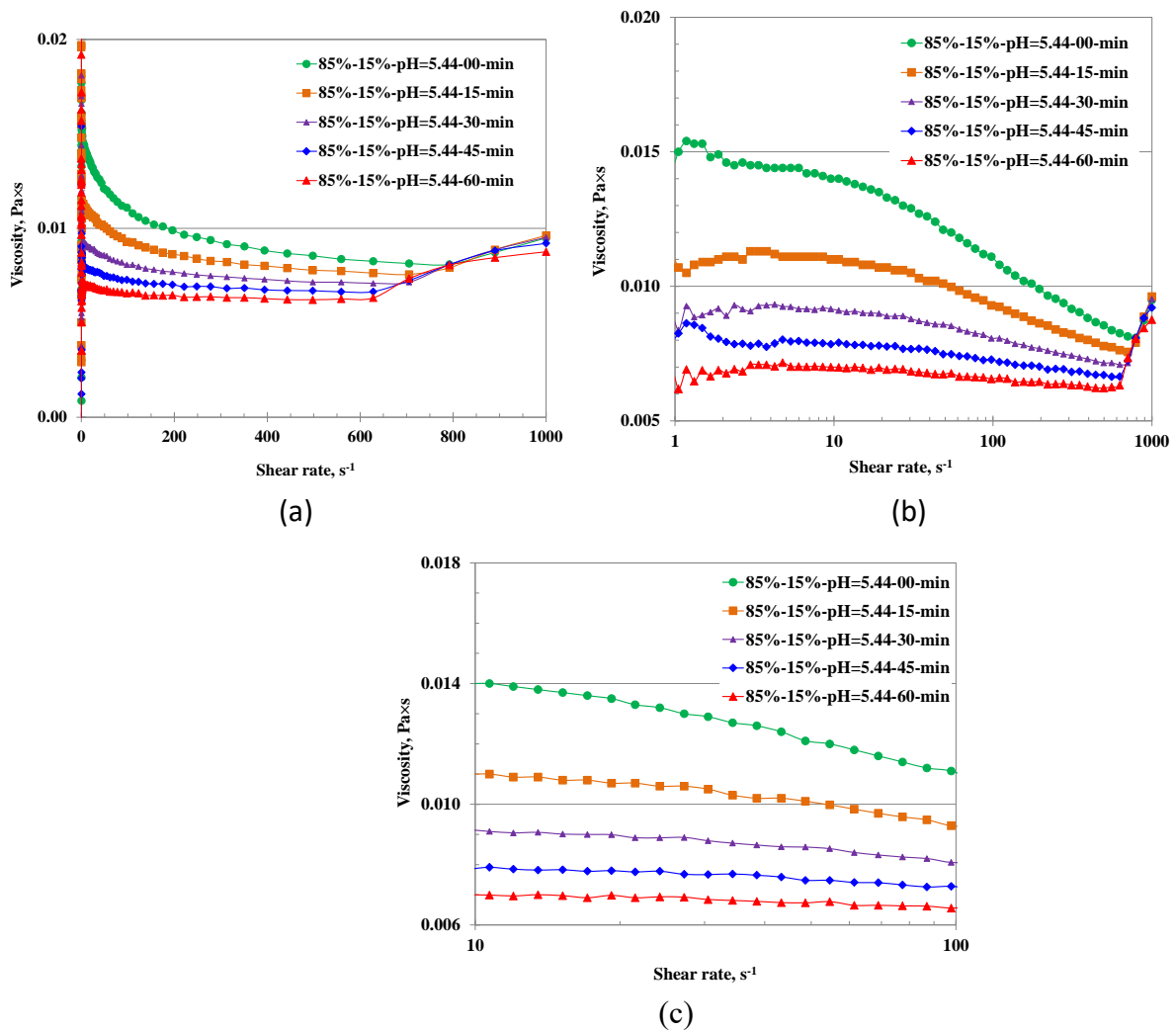
Figure 73: Viscosity-vs-shear-rate for guar-gel+enzyme-solution+acetic acid formulation (85%-15%) at pH=5.44: (a) linear scale, (b, c) logarithmic scale
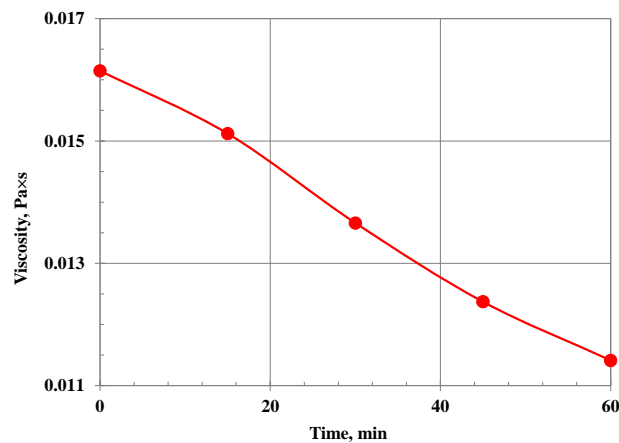

Figure 74. Viscosity-vs-time of hydration for guar-gel+enzyme-solution+acetic acid formulation (85%-15%) at pH=5.44 and 30 s-1 shear rate (interpolated viscosity data)
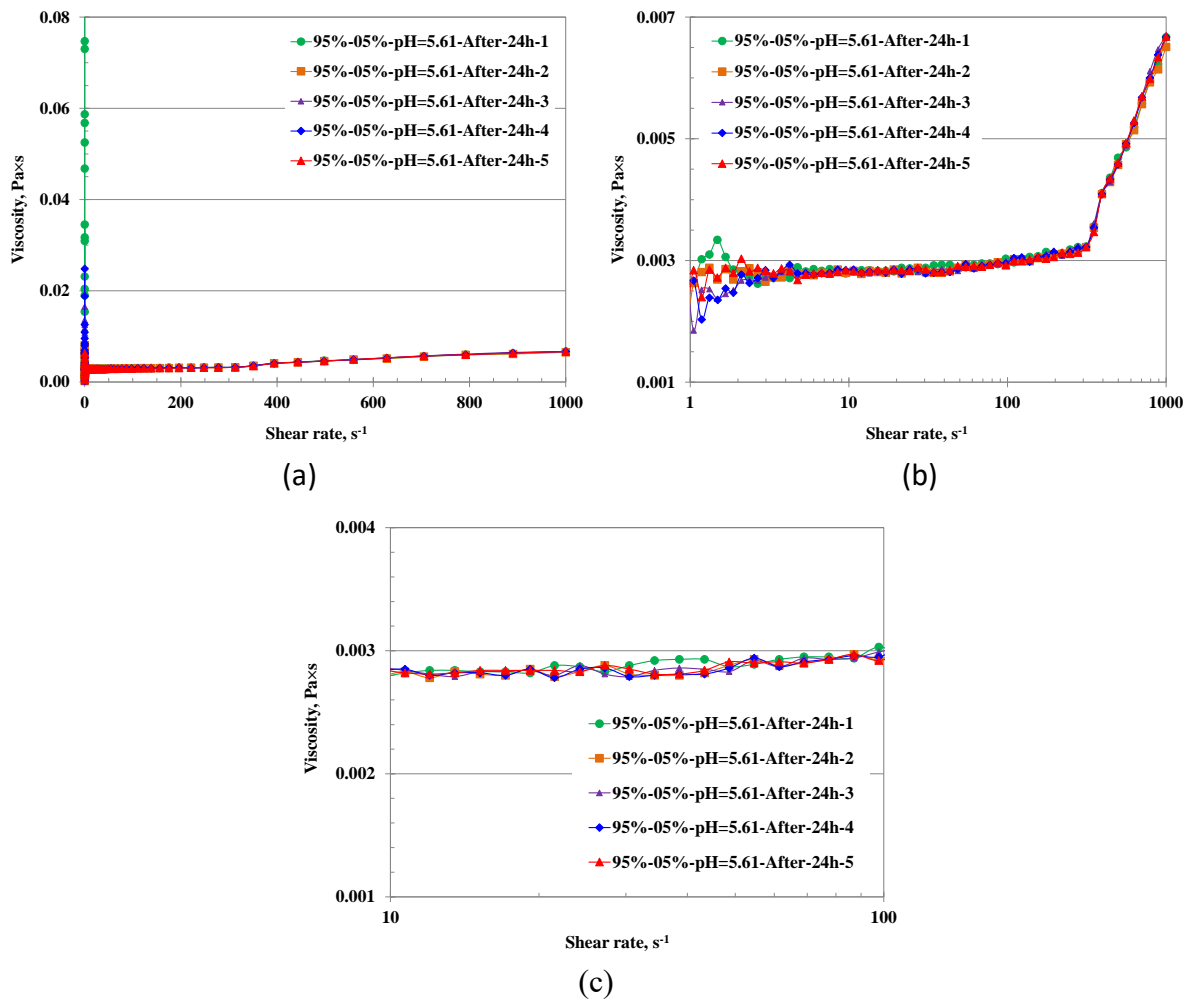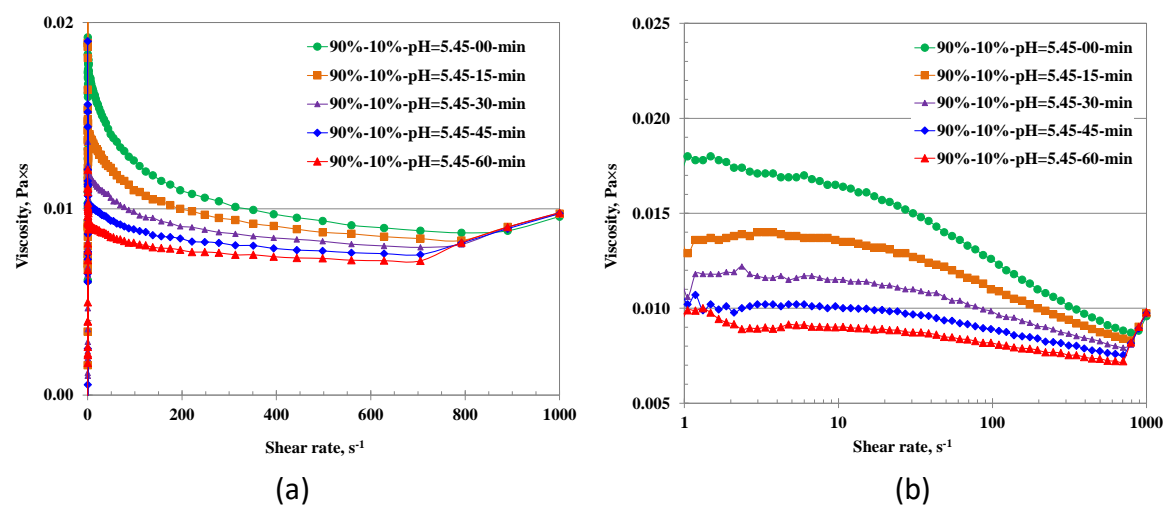
Figure 75. Viscosity-vs-shear-rate for guar-gel+enzyme-solution+acetic acid formulation (85%-15%) at pH=5.60 after 24 hours of hydration: (a) linear scale, (b, c) logarithmic scale

2.4. 80% guar-gel and 20% enzyme solution at pH=5.45

(a)

(b)

(c)

Figure 76. Viscosity-vs-shear-rate for guar-gel+enzyme-solution+acetic acid formulation (80%-20%) at pH=5.45: (a) linear scale, (b, c) logarithmic scale

Figure 77. Viscosity-vs-time of hydration for guar-gel+enzyme-solution+acetic acid formulation (80%-20%) at pH=5.45 and 30 s-1 shear rate (interpolated viscosity data)
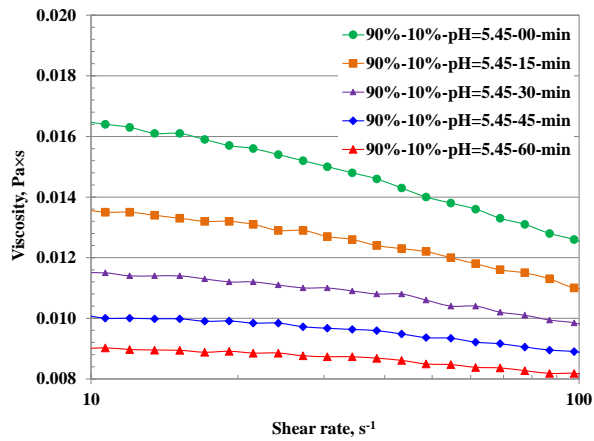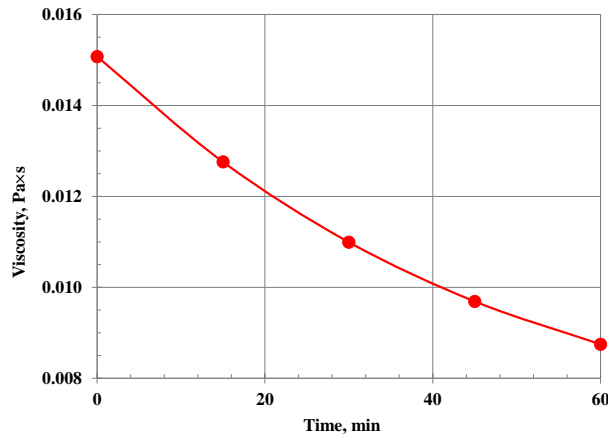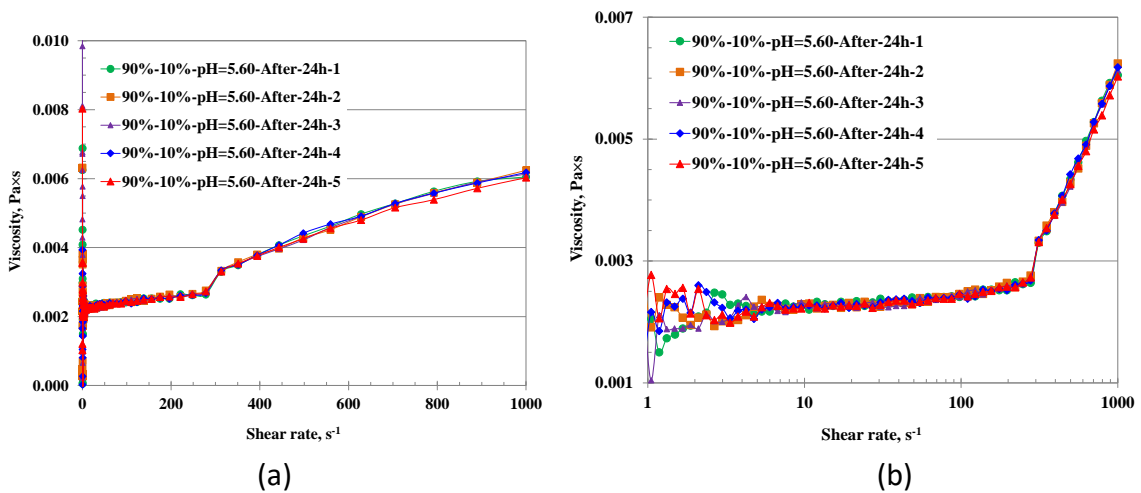
Figure 78. Viscosity-vs-shear-rate for guar-gel+enzyme-solution+acetic acid formulation (80%-20%) at pH=5.55 after 24 hours of hydration: (a) linear scale, (b, c) logarithmic scale

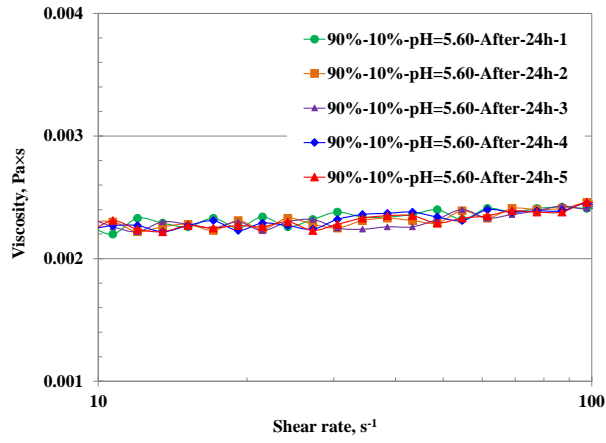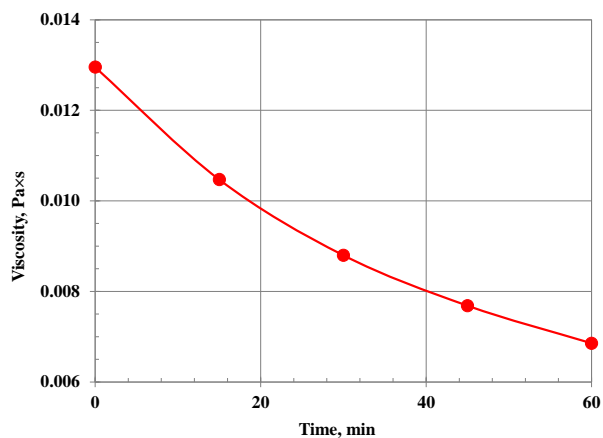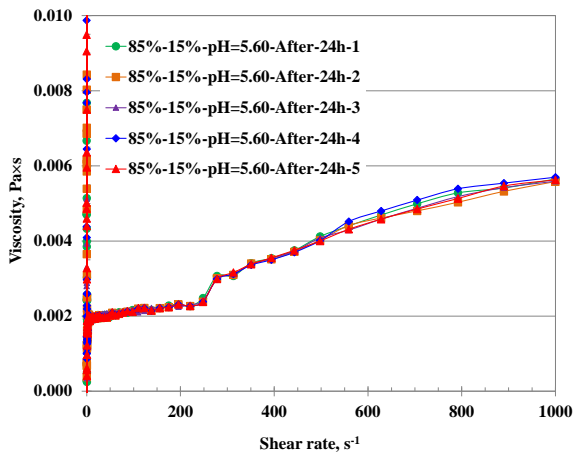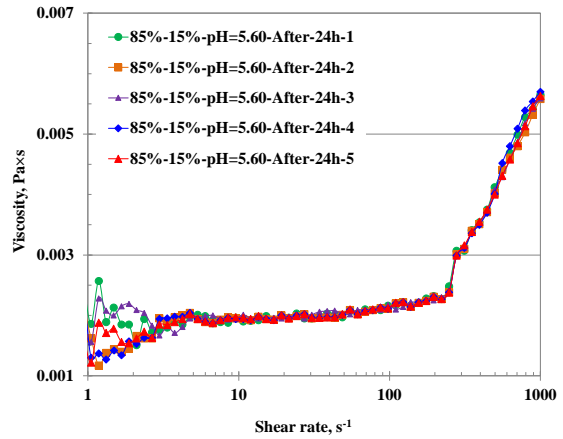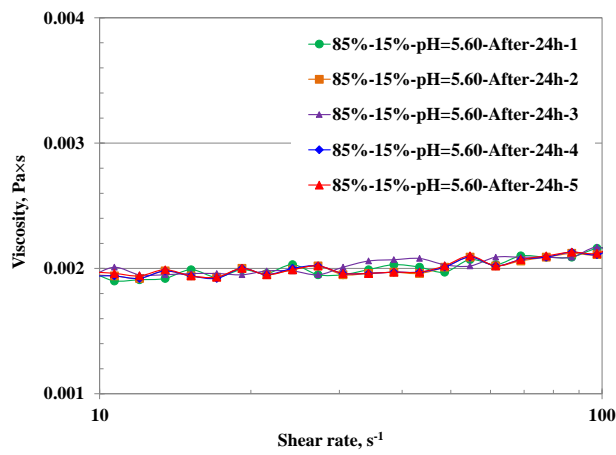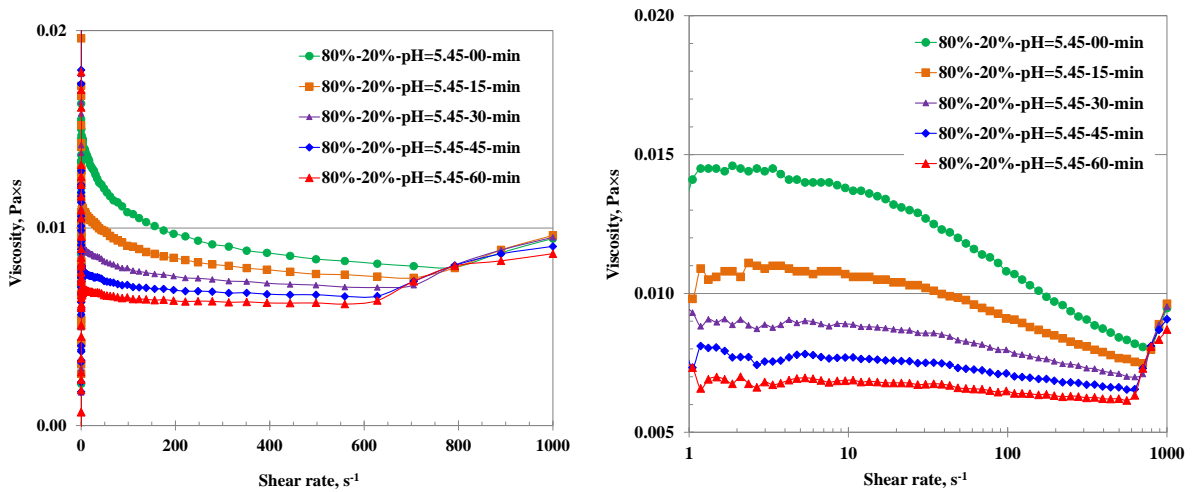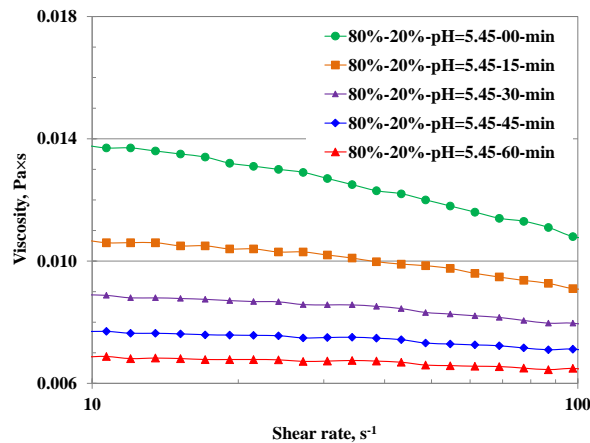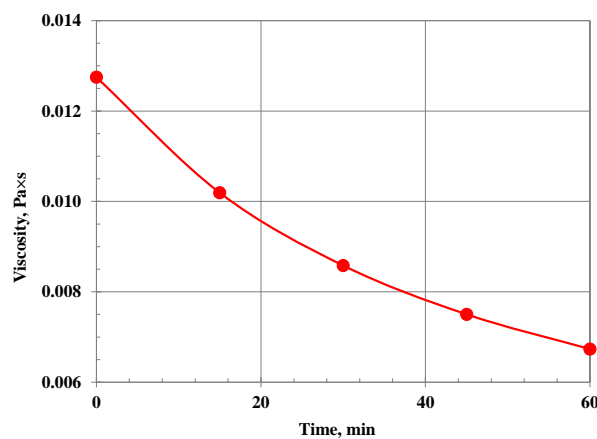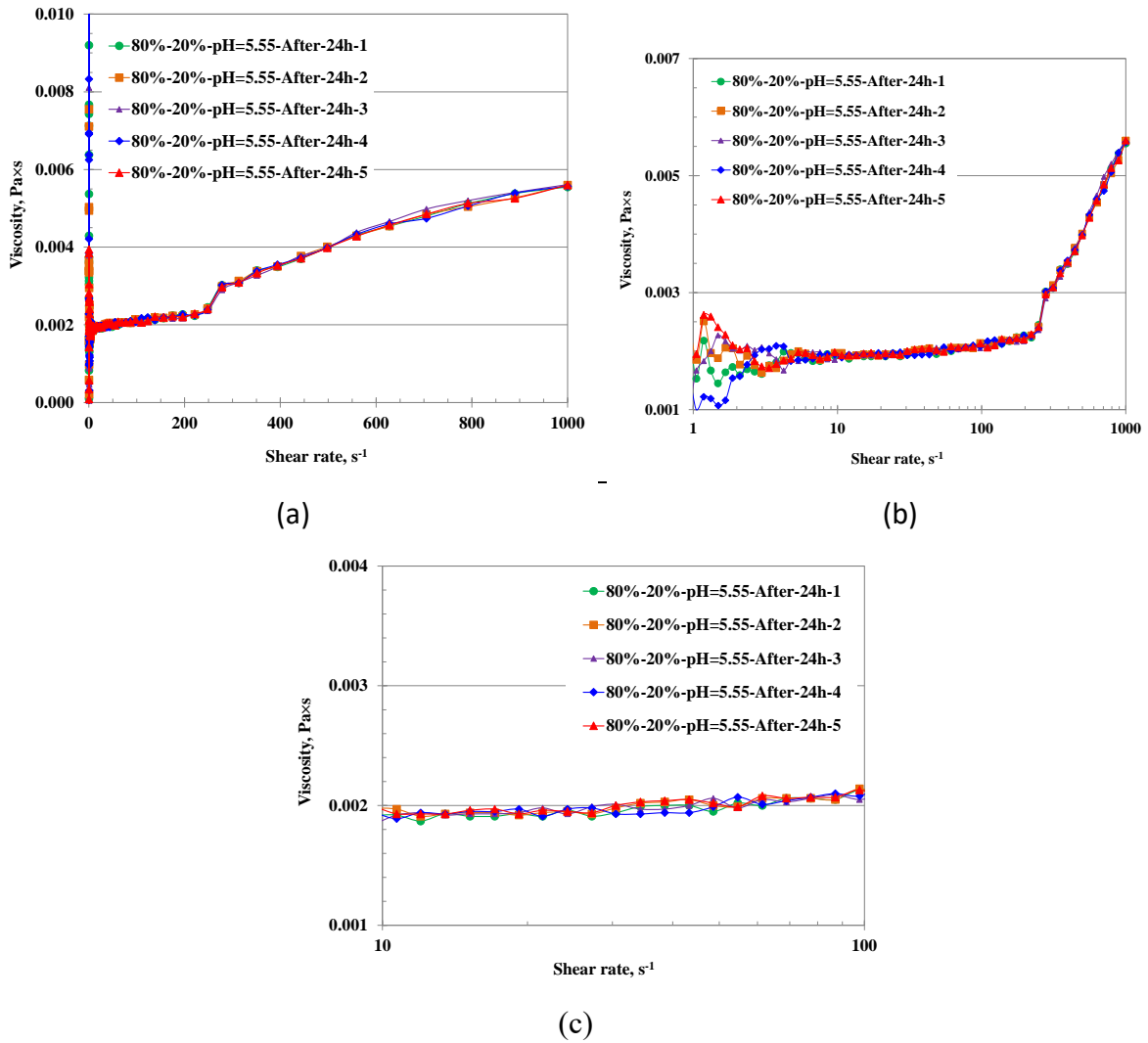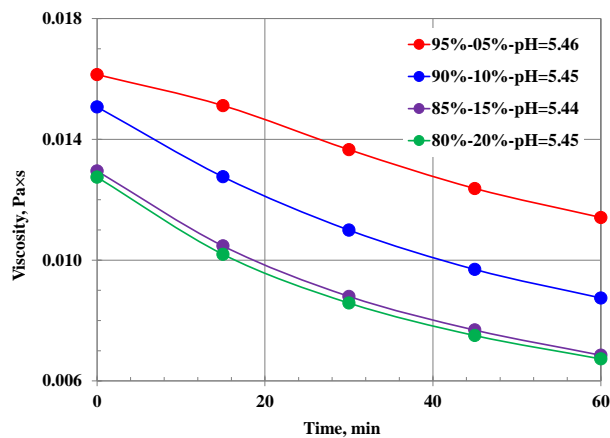*Figure 79. Summary of viscosity-vs-time of hydration for guar-gel+enzyme-solution+acetic acid formulations at low pH and 30 s-1 shear rate (interpolated viscosity data)*

Table 18. Viscosity of guar-gel+enzyme-solution+acetic acid formulations as a function of hydration time at 30 s^{-1} shear rate at low pH

Guar-gel formulation	Hydration time	Viscosity	St. Dev.	St. Dev.
	min	Pa×s	Pa×s	%
95%-05%-pH=5.46-00-min	0	0.0161		
95%-05%-pH=5.46-15-min	15	0.0151		
95%-05%-pH=5.46-30-min	30	0.0137	N/A	N/A
95%-05%-pH=5.46-45-min	45	0.0124		
95%-05%-pH=5.46-60-min	60	0.0114		
95%-05%-pH=5.61-After-24h-1	1440 (24 hours)	0.0029		
95%-05%-pH=5.61-After-24h-2	1440 (24 hours)	0.0028		
95%-05%-pH=5.61-After-24h-3	1440 (24 hours)	0.0028	0.000028	1.00
95%-05%-pH=5.61-After-24h-4	1440 (24 hours)	0.0028		
95%-05%-pH=5.61-After-24h-5	1440 (24 hours)	0.0028		
90%-10%-pH=5.45-00-min	0	0.0151		
90%-10%-pH=5.45-15-min	15	0.0128		
90%-10%-pH=5.45-30-min	30	0.0110	N/A	N/A
90%-10%-pH=5.45-45-min	45	0.00969		
90%-10%-pH=5.45-60-min	60	0.00875		
90%-10%-pH=5.60-After-24h-1	1440 (24 hours)	0.00232		
90%-10%-pH=5.60-After-24h-2	1440 (24 hours)	0.00283		
90%-10%-pH=5.60-After-24h-3	1440 (24 hours)	0.00281	0.000225	8.26
90%-10%-pH=5.60-After-24h-4	1440 (24 hours)	0.00280		
90%-10%-pH=5.60-After-24h-5	1440 (24 hours)	0.00284		
85%-15%-pH=5.44-00-min	0	0.0130		
85%-15%-pH=5.44-15-min	15	0.0105		
85%-15%-pH=5.44-30-min	30	0.00880	N/A	N/A
85%-15%-pH=5.44-45-min	45	0.00769		
85%-15%-pH=5.44-60-min	60	0.00685		
85%-15%-pH=5.60-After-24h-1	1440 (24 hours)	0.00198		
85%-15%-pH=5.60-After-24h-2	1440 (24 hours)	0.00230		
85%-15%-pH=5.60-After-24h-3	1440 (24 hours)	0.00210	0.000138	6.73
85%-15%-pH=5.60-After-24h-4	1440 (24 hours)	0.00198		
85%-15%-pH=5.60-After-24h-5	1440 (24 hours)	0.00199		
80%-20%-pH=5.45-00-min	0	0.0128		
80%-20%-pH=5.45-15-min	15	0.0102		
80%-20%-pH=5.45-30-min	30	0.00858	N/A	N/A
80%-20%-pH=5.45-45-min	45	0.00750		
80%-20%-pH=5.45-60-min	60	0.00673		
80%-20%-pH=5.55-After-24h-1	1440 (24 hours)	0.00195		
80%-20%-pH=5.55-After-24h-2	1440 (24 hours)	0.00230		
80%-20%-pH=5.55-After-24h-3	1440 (24 hours)	0.00200	0.000142	6.97
80%-20%-pH=5.55-After-24h-4	1440 (24 hours)	0.00198		
80%-20%-pH=5.55-After-24h-5	1440 (24 hours)	0.00199		

Comments:

- viscosity of all studied guar-gel+enzyme-solution+acetic acid formulations decrease with hydration time;

- the higher is enzyme solution concentration the lower is viscosity of the guar-gel+enzyme-solution+acetic acid formulation;

- the rate of viscosity decrease with hydration time is almost similar for all studied formulations (with added enzyme solution) at least for the first hour of hydration (see Figure 79);

- repeatability of viscosity data after 24-hour hydration period is good.

3. Rheological properties of guar-gel+enzyme solution+acetic acid as a function of time at fixed share rate

Six guar-gel+enzyme solution+acetic acid formulations were prepared as per Sections 1 and 2. Table 19 presents results of pH for the prepared formulations. Variation of viscosity-*vs*-time for the studied formulations are presented in Figure 80.

Table 19. pH of prepared formulations for "viscosity-vs-time" tests at fixed shear rate 30 s^{-1}

Guar-gel % (v/v)	Enzyme solution %, (v/v)	pH				
		Tap water	Guar-gel	Enzyme solution	Guar-gel + Enzyme-solution	Guar-gel + Enzyme-solution + Acetic-acid
100	0	7.84	7.83	N/A	N/A	N/A
100	0	7.88	7.91	N/A	N/A	5.45 (no enzyme solution)
95	5	7.92	7.74	7.86	7.74	5.40/5.43*
90	10	8.11	7.96	7.91	7.88	5.40/5.44*
85	15	8.13	7.94	7.87	7.85	5.42/5.48*
80	20	7.79	7.91	7.78	7.83	5.44/5.43*

Note: * - pH after 24 hours
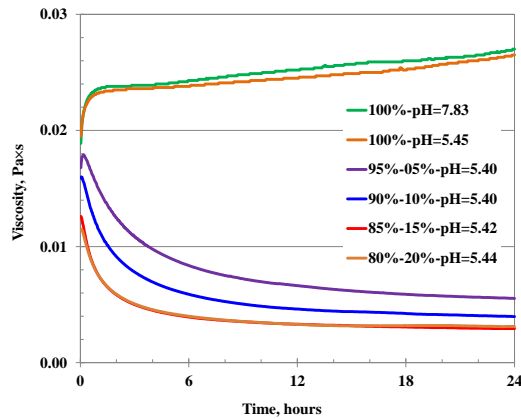
Figure 80. Viscosity-vs-time for guar-gel+enzyme solution+acetic acid at various pH and fixed shear rate 30 s-1 during 24-hour tests
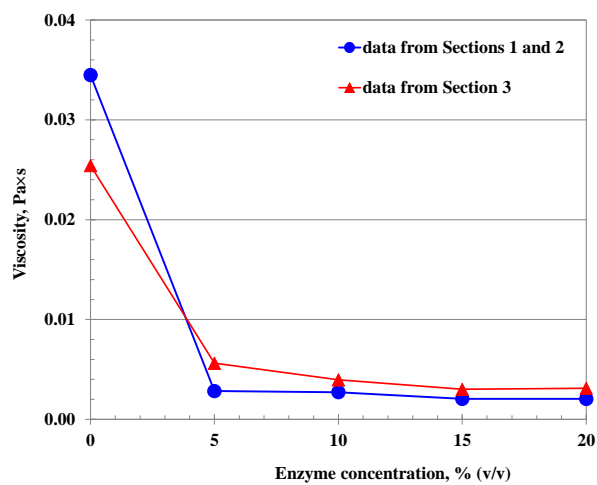
Figure 81. Viscosity-vs-enzyme solution concentration at low pH and fixed shear rate 30 s-1 at the completion of 24-hour tests

Comments:
- hydration of guar-gel formulation (without added enzyme solution) results in the increase of its viscosity without stabilisation after 24-hour tests;
- the higher is enzyme-solution concentration the lower is viscosity of guar-gel+enzyme solution+acetic acid formulation;
- viscosities of guar-gel formulations with added enzyme solution stabilise after about 20-22 hours from their preparation;
- the higher is enzyme concentration the quicker viscosity of guar-gel+enzyme solution+acetic acid formulation stabilises.

20.4 Variation of sand pack (40/70) permeability during injection of 'guar-gel+enzyme-solution+acetic-acid' formulation

Prepared by: Prof. Pavel Bedrikovetsky, Dr. Alexander Badalyan, Dr. Abbas Zeinijahromi,

Dr Themis Carageorgos

Date: 25.12.2020.

1. <u>**Injection of tap water (1st fluid) into undamaged sand pack**</u>
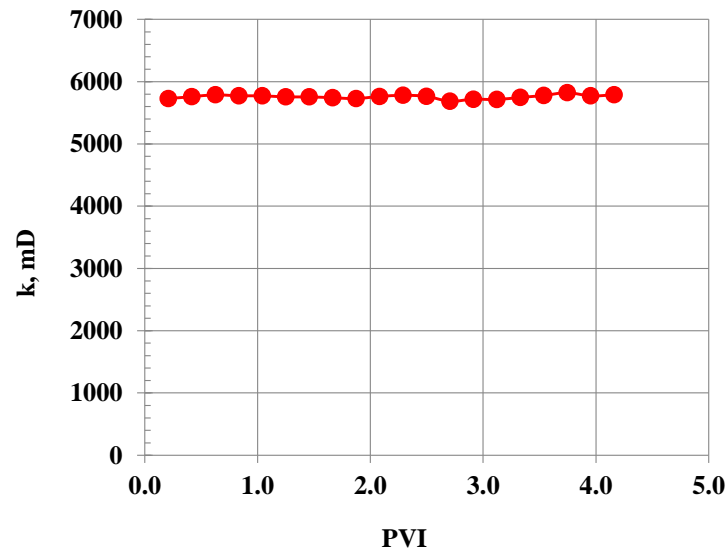
Figure 82. Undamaged sand pack permeability to tap water at 4 mL/min

The following mean permeability to tap water was calculated from the experimental data: $k_0^w = 5758 \pm 31$mD.

2. <u>**Injection of 0.002 % (v/v) enzyme-solution (pH = 5.50) (2nd fluid) into undamaged sand pack**</u>
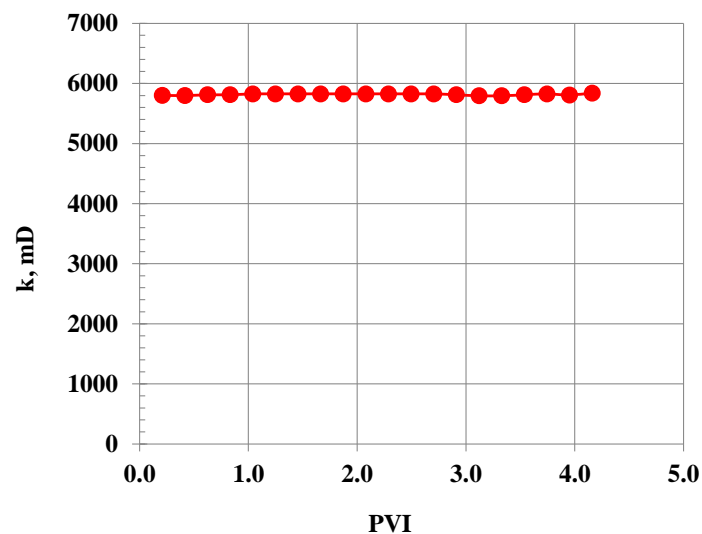
Figure 83. Undamaged sand pack permeability to 0.002 % (v/v) enzyme-solution (pH = 5.50)

at 4 mL/min

The following mean permeability to 0.002 % (v/v) enzyme-solution (pH = 5.50) was calculated from the experimental data: $k_0^e = 5817 \pm 12$ mD.

Agreement between k_0^w and k_0^e is 1.0 % which is within 3.2 % of experimental uncertainty for liquid permeability data. Therefore, we can accept that $k_0^e \approx k_0^w$.

3. Injection of 10 % (v/v) of 0.002 % (v/v) enzyme-solution (pH = 5.50) and 90% of 24-hour-old guar-gel-solution (3rd fluid) into undamaged sand pack

It took nearly 50 PVI to achieve stability of pressure drop across the sand pack. We showed only $\Delta P = f(PVI)$-relationship for this injection in After pressure drop stabilisation during injection of 0.002 % (v/v) enzyme-solution, we moved to injection of guar-gel-proppant formulation using the following concentrations:

➤ 2 ppg of proppant in guar-gel (2.4 g of guar-gel in 1000 mL of tap water) with pH=5.47;
➤ guar-gel solution was persistently agitated in the mixer for 60 min for hydration - this includes 30 min after initial guar-gel preparation, and 30 min after pH adjustment at around 5.5 and quick proppant mixing;
➤ 0.002 % (v/v) enzyme-solution (pH = 5.53);
➤ final injected formulation consists of 90% of guar-gel-proppant suspension *plus* 10% of enzyme solution.

With the arrival of proppant to the face of the sand pack pressure drop across it increased very quickly by about 21.4 times (from 0.059 psi up to 1.262 psi) after only about 2.36 PVI (see *Figure 91*, RED symbols). We showed only $\Delta P = f(PVI)$-relationship for this injection since it was not possible to calculate sand pack permeability during transition from 0.002 % (v/v) enzyme-solution to injected final formulation. The final pressure drop across the sand pack was 1.262 psi. The setup was sealed for 24 hours for enzyme solution to break down guar-gel. In parallel, we prepared the following formulation: 90% of guar-gel (2 ppg of proppant in guar-gel, pH=5.47) plus 10% of 0.002 % (v/v) enzyme-solution (pH = 5.53) for the next day injection.

, since it was not possible to calculate sand pack permeability during transition from 2nd to 3rd fluid.
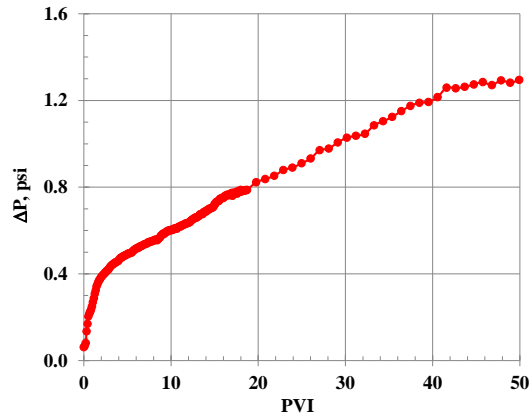
Figure 84. Pressure drop across the sand pack during injection of 10 % (v/v) of 0.002 % (v/v) enzyme-solution (pH = 5.50) and 90% of 24-hour-old guar-gel-solution (pH = 5.51) into the undamaged sand pack (flowrates are equal to 0.4 mL/min and 3.6 mL/min, respectively)

The final pressure drop across the sand pack was 1.2945 psi. Permeability of the sand pack at the completion of 3rd fluid injection was calculated using Darcy's equation. Since freshly-mixed 3rd liquid was injected into the sand pack, we assume that NO enzyme-driven guar-gel degradation occurs inside the sand pack for the duration of this injection. Therefore, in the Darcy's equation we use the following value of dynamic viscosity of 3rd fluid $\mu_{9:1}^{g,e}$ = 0.015076 (Section 20.3, Table 18) resulting in the final sand pack permeability at the completion of 3rd fluid injection $k_1^{g,e}$ = 4595 ± 85 mD. Please note that this is not an absolute sandpack permeability, by the 'so-called' end-point permeability similar to that usually calculated during non-steady-state two-phase corefloods.

4. Injection 0.002 % (v/v) enzyme-solution (pH = 5.50)

Injection of 2nd fluid started straight after injection of 3rd fluid and determining $k_1^{g,e}$-value above. Permeability of the sandpack during transition from 3rd to 2nd fluid was not determined, only pressure drop variation across the sand pack as a function of PVI (see Figure 85).
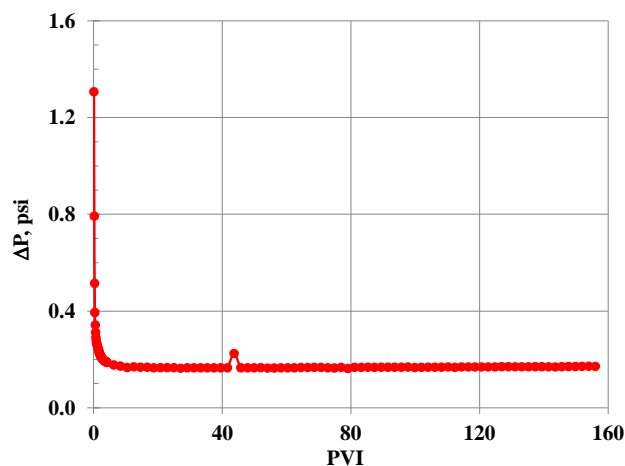
Figure 85. Pressure drop across the sand pack during injection of 0.002 % (v/v) enzyme-solution (pH = 5.50) into damaged sand pack at 4 mL/min

Stabilisation of pressure drop across the core started from about 20 PVI. We continued

injection of 2nd fluid for the duration of about 156 PVI. The final sand pack permeability was $k_2^{g,e} = 2207 \pm 49$ mD.

5. Injection of tap water

Injection of tap water started straight after injection of 2nd fluid and determining $k_2^{g,e}$-value above. Permeability of the sandpack during transition from 3rd to 2nd fluid was not determined, only pressure drop variation across the sand pack as a function of PVI was recorded (see *Figure 85* and Figure 86).

Figure 86. Pressure drop across the sand pack during injection of tap water into the sand pack at 4 mL/min

Permeability of the sand pack was stabilised at $k_3^w = 2011 \pm 14$ mD. We think that the reasons for the sandpack permeability damage are as follows: fingering during flow of less viscous tap water through a more viscous 3rd fluid which fills the sand pack, and guar-gel (non-broken by enzyme) remaining in the pore network of the sand pack and not-accessible by tap water.

This was the end of the proposed test program. However, we decided to do some more injections.

6. Injection of tap water at higher flowrate

We decided injection of tap water at higher flowrate hoping to further restore sand pack permeability, since we think that some of guar-gel not broken by enzyme is responsible for the residual sand pack damage. The flowrate of tap water during injection was equal to 50 mL/min, and this injection lasted for about 13 PVI. After that, we reduced tap water flowrate down to 4 mL/min.
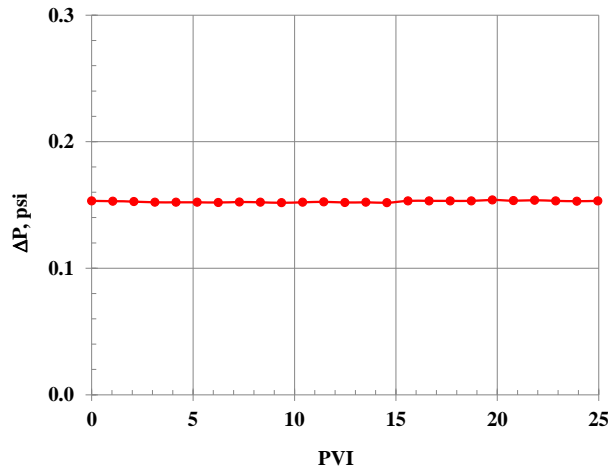
Figure 87. Pressure drop across the sand pack during injection of tap water into the sand pack at 4 mL/min

Permeability of the sand pack was stabilised at $k_4^w = 2338 \pm 17$ mD. Thus, permeability increased by 18.7 % after sandpack exposure to high velocity tap water: it means that some of the above-mentioned non-accessible guar-gel was removed by high-velocity tap water.

7. <u>Injection 0.002 % (v/v) enzyme-solution (pH = 5.50)</u>

We again injected 2nd fluid for the duration of about 21 PVI (Figure 88a) and left it overnight for 16 hours, hoping that injected enzyme solution will reach the remaining non-accessible guar-gel and break it. In the morning we continued injection for the duration of about 21 PVI (see Figure 88b).

(a)

(b)

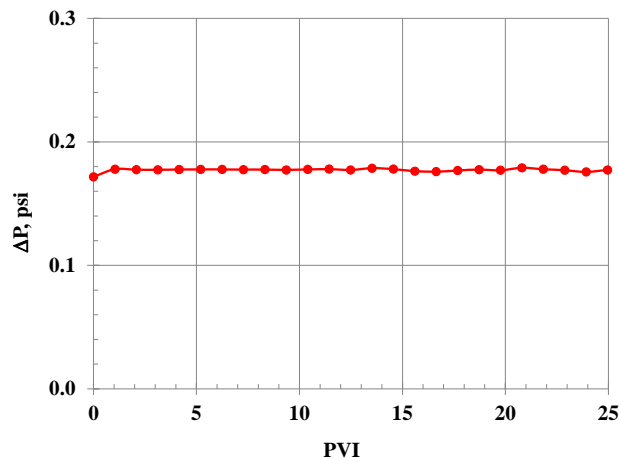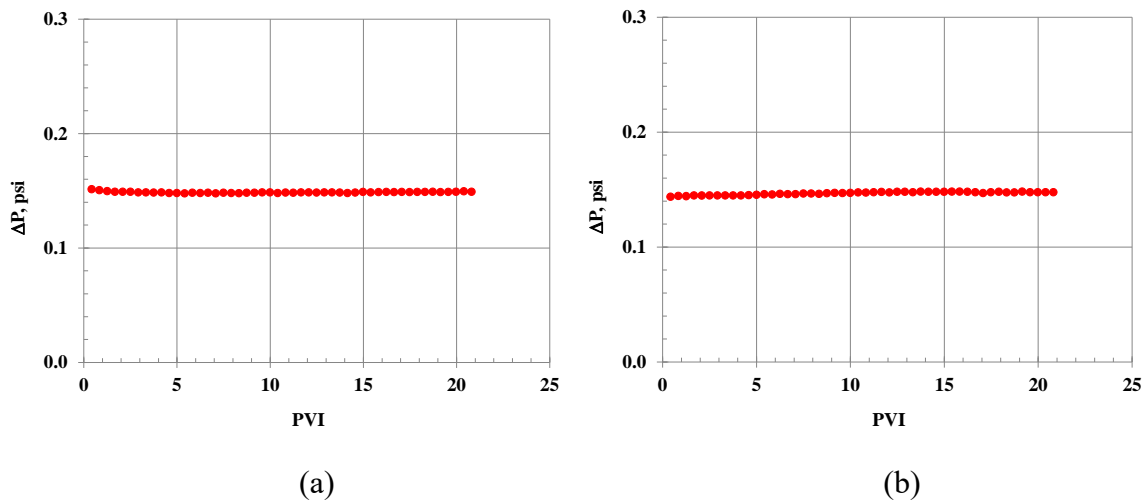*Figure 88. Pressure drop across the sand pack during injection of 2nd fluid into the sand pack at 4 mL/min*

Stabilised sand pack permeabilities for these two injections are as follows: $k_5^e = 2554 \pm 8$ mD and $k_6^e = 2576 \pm 66$ mD. Agreement between these two values is about 0.89 % (experimental uncertainty for permeability is about 3.2 %), which indicates that non-accessible guar-gel spread in the porous network of the sand pack is not accessible to the injected enzyme solution.

Compared to undamaged sand pack permeability of $k_0^e = 5817 \pm 12$ mD, we obtained about 2.3-time permeability damage ONLY due to injection of 3rd fluid into the sand pack. Either of the above k_5^e or k_5^e values can be used as the baseline sandpack permeability in evaluation of sandpack damage during injection of formulation with proppant during future tests.

20.5 Variation of sand pack (20/40) permeability during injection of 'guar-gel+proppant+enzyme-solution+acetic-acid' formulation

Prepared by: Prof. Pavel Bedrikovetsky, Dr. Alexander Badalyan, Dr. Abbas Zeinijahromi, Dr Themis Carageorgos

Date: 14.02.2021.

We have finished studies on injection of proppant (Zeeospheres Ceramic Microspheres N600, concentration is 2 ppg) into a sand pack (20/40 mesh, 420 to 710 μm, note that we used sieve 710 μm instead of 841 μm).

8. Injection of tap water (1st fluid) into undamaged sand pack

Figure 89. Undamaged sand pack permeability to tap water at 4 mL/min

The following mean permeability to tap water was calculated from the experimental data: $k_0^w = 6014 \pm 37$ mD.

9. Injection of 0.002 % (v/v) enzyme-solution (pH = 5.53) (2nd fluid) into undamaged sand pack

Figure 90. Undamaged sand pack permeability to 0.002 % (v/v) enzyme-solution (pH = 5.53) at 4 mL/min
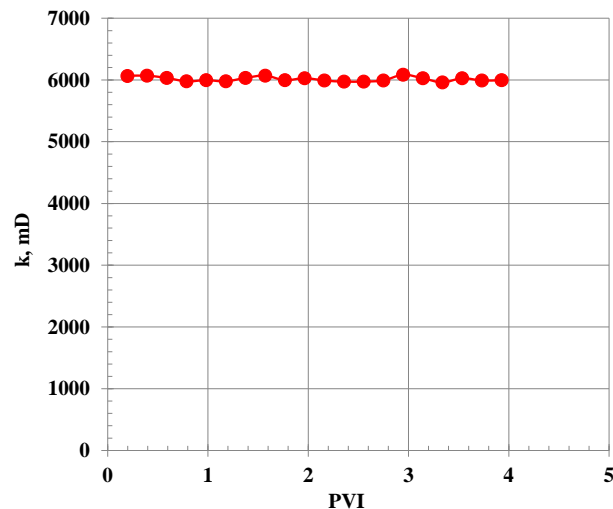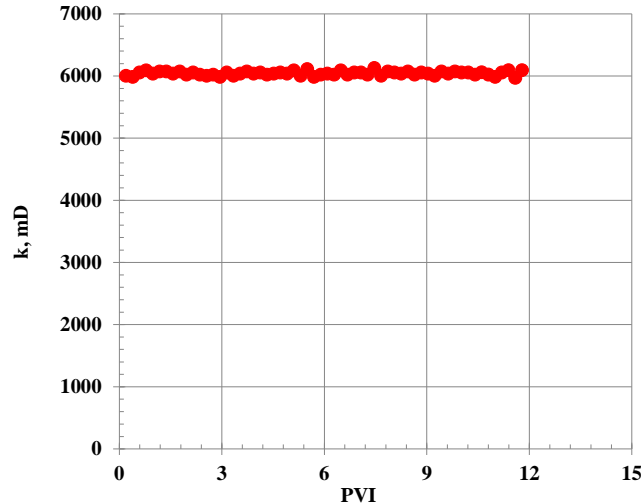
The following mean permeability to 0.002 % (v/v) enzyme-solution (pH = 5.53) was calculated from the experimental data: $k_0^e = 6045 \pm 33$ mD.

Agreement between k_0^w and k_0^e is 1.0 % which is within 0.15 % of experimental uncertainty for liquid permeability data. Therefore, we can accept that $k_0^e \approx k_0^w$.

10. 1st injection of guar-gel-proppant and enzyme solution into undamaged sand pack

After pressure drop stabilisation during injection of 0.002 % (v/v) enzyme-solution, we moved to injection of guar-gel-proppant formulation using the following concentrations:
  - 2 ppg of proppant in guar-gel (2.4 g of guar-gel in 1000 mL of tap water) with pH=5.47;
  - guar-gel solution was persistently agitated in the mixer for 60 min for hydration - this includes 30 min after initial guar-gel preparation, and 30 min after pH adjustment at around 5.5 and quick proppant mixing;
  - 0.002 % (v/v) enzyme-solution (pH = 5.53);
  - final injected formulation consists of 90% of guar-gel-proppant suspension *plus* 10% of enzyme solution.

With the arrival of proppant to the face of the sand pack pressure drop across it increased very quickly by about 21.4 times (from 0.059 psi up to 1.262 psi) after only about 2.36 PVI (see *Figure 91*, RED symbols). We showed only $\Delta P = f(PVI)$-relationship for this injection since it was not possible to calculate sand pack permeability during transition from 0.002 % (v/v) enzyme-solution to injected final formulation. The final pressure drop across the sand pack was 1.262 psi. The setup was sealed for 24 hours for enzyme solution to break down guar-gel. In parallel, we prepared the following formulation: 90% of guar-gel (2 ppg of proppant in guar-gel, pH=5.47) plus 10% of 0.002 % (v/v) enzyme-solution (pH = 5.53) for the next day injection.

Figure 91. Pressure drop across the sand pack during 1st injection of formulation

Results of injection of 24-hour old guar-gel/enzyme-solution (pH=5.54) are shown in (Figure 91, BLUE symbols). Initial very quick 14.6-time decline of pressure drop across the core (from 1.26 psi down to 0.087 psi) was followed by its increase up to 0.389 psi, which can be explained by re-distribution of proppant inside pores of the sand pack. Followed injection of 0.002 % (v/v) enzyme-solution (pH=5.57) did not appreciably change pressure drop across the sand pack as shown in Figure 91 (PURPLE symbols). Stabilisation of sand pack permeability occurred at about $k_1^{g,p,e} = 928$ mD ± 3 mD. Calculated impedance value is $J_2 = \frac{k_0^e}{k_1^{g,p,e}} = 6.5$. Very low standard deviation of sand pack permeability (± 3 mD) points to a very good stability of sand pack permeability, meaning that proppant is securely fixed inside the porous network of the sand pack.

11. **2nd injection of guar-gel-proppant and enzyme solution into partially-damaged sand pack**

We carried out the 2nd injection using freshly prepared guar-gel-proppant and enzyme solution into the partially-damaged sand pack. The following formulations were prepared:

> ➢ 2 ppg of proppant in guar-gel (2.4 g of guar-gel in 1000 mL of tap water) with pH=5.56;
> ➢ guar-gel solution was persistently agitated in the mixer for 60 min for hydration - this includes 30 min after initial guar-gel preparation, and 30 min after pH adjustment at around 5.5 and quick proppant mixing;
> ➢ 0.002 % (v/v) enzyme-solution (pH = 5.46);
> ➢ final injected formulation consists of 90% of guar-gel-proppant suspension *plus* 10% of enzyme solution.

Initially, sand pack permeability was stabilised at about 900 ± 24 mD by injecting a freshly-prepared 0.002 % (v/v) enzyme-solution (see *Figure 92*, BROWN symbols). Injection of the final formulation significantly increased pressure drop across the sand pack by about 25.7 times (from 0.347 psi up to 8.921 psi) as shown in *Figure 92* (RED symbols). The setup was sealed for 24 hours for enzyme solution to break down guar-gel. In parallel, we prepared the following formulation: 90% of guar-gel (2 ppg of proppant in guar-gel, pH=5.56) plus 10%

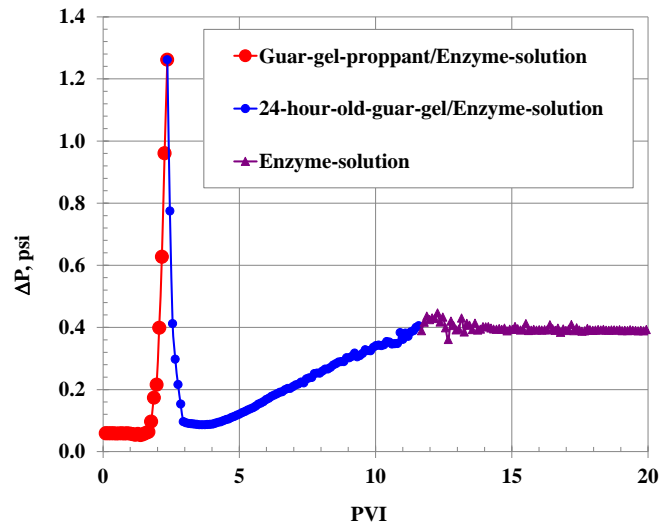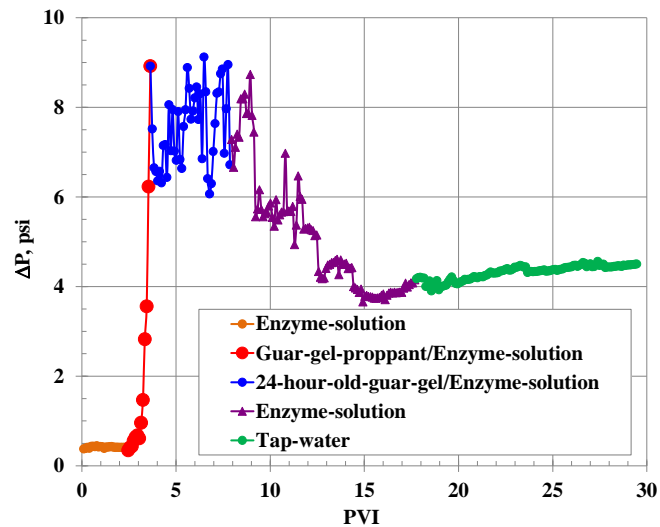of 0.002 % (v/v) enzyme-solution (pH = 5.46) for the next day injection.

Figure 92. Pressure drop across the sand pack during 2nd injection of formulation

Results of injection of 24-hour old guar-gel/enzyme-solution (pH=5.59) are shown in (see Figure 92, BLUE symbols). Pressure drop across the sand pack fluctuated around the mean value of 7.51 psi ± 0.84 psi. Such fluctuation can be explained by the re-distribution (maybe 'cake erosion') of proppant on the surface of the external cake and that some of proppant is carried away into the porous network of the sand pack. This pressure drop fluctuation continued for about 4 PVI. The final permeability of the sand pack at the end of injection of enzyme-solution (pH=5.52) is equal to $k_2^{g,p,e} = 96.8$ mD ± 3 mD (see Figure 92, PURPLE symbols). Calculated impedance values are as follows: $J_2 = \frac{k_0^e}{k_2^{g,p,e}} = 62.5$ (compared to initial undamaged sandpack permeability) and $J_3 = \frac{k_1^{g,p,e}}{k_2^{g,p,e}} = 9.6$ (compared to partially-damaged sandpack permeability). It took about 2.36 PVI to damage sandpack permeability by about 6.5 times during 1st injection of proppant formulation, and about 1.28 PVI to achieve almost 9.6-time sand pack permeability damage during 2nd injection of proppant formulation. Injection of tap water at the completion of these tests resulted in stabilised sand pack permeability of $k_2^{g,p,e,w} = 84.2$ mD ± 0.7 mD (see Figure 92, GREEN symbols).

This was the end of the proposed test program. However, we carried out one more injection.

12. **Injection of tap water at higher flowrate**

We decided to inject tap water at higher flowrate to check how sand pack permeability reacts to high-velocity flow. Tap water was injected at 50 mL/min for the duration of 1 min corresponding to about 2.5 PVI. After that, permeability was stabilized at about 335 mD ± 2 mD (at 4 mL/min) according to Figure 93.
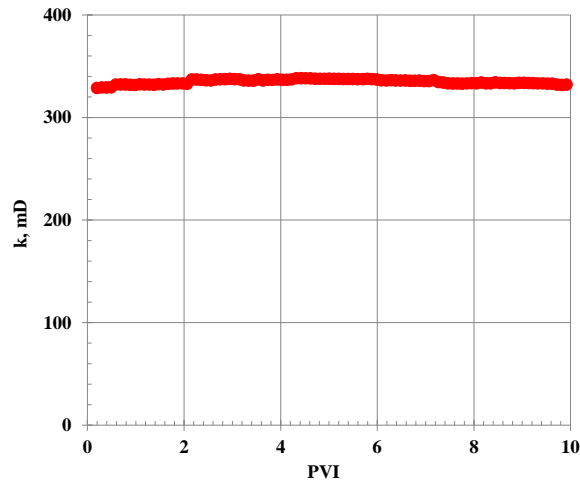
Figure 93. Sandpack permeability after high-velocity flow

Increase of sand pack permeability from 84.2 mD up to 335 mD was accompanied by removal of proppant from sand pack porous network which was observed by the appearance of proppant in effluent stream and its sedimentation in the effluent bottle. Although proppant is to some extent securely fixed at unchanged hydrodynamic conditions (fixed fluid flowrate), its position inside the sand pack porous network is not stable when exposed to fluctuations of fluid flowrate.

20.6 Micro-CT Scans of coal samples

Analysis of two coal samples was carried out using SkyScan-1279 Micro-CT. Although the instrument can magnify images down to 2.8 mm pixel size, Micro-CT scans were done at 20 mm but the images and analysis were done at 80 mm as the data size was large when generating 3D images and performing 3D analysis of fractures/pores. 3D images of the analysed coal samples are presented in Figures 82 and 83. As follows from these images, coal core-3 has more developed pore network (white colour). This observation is supported by calculation of pore volumes for coal core-1 and core-3 (Table 20).

(a)   (b)
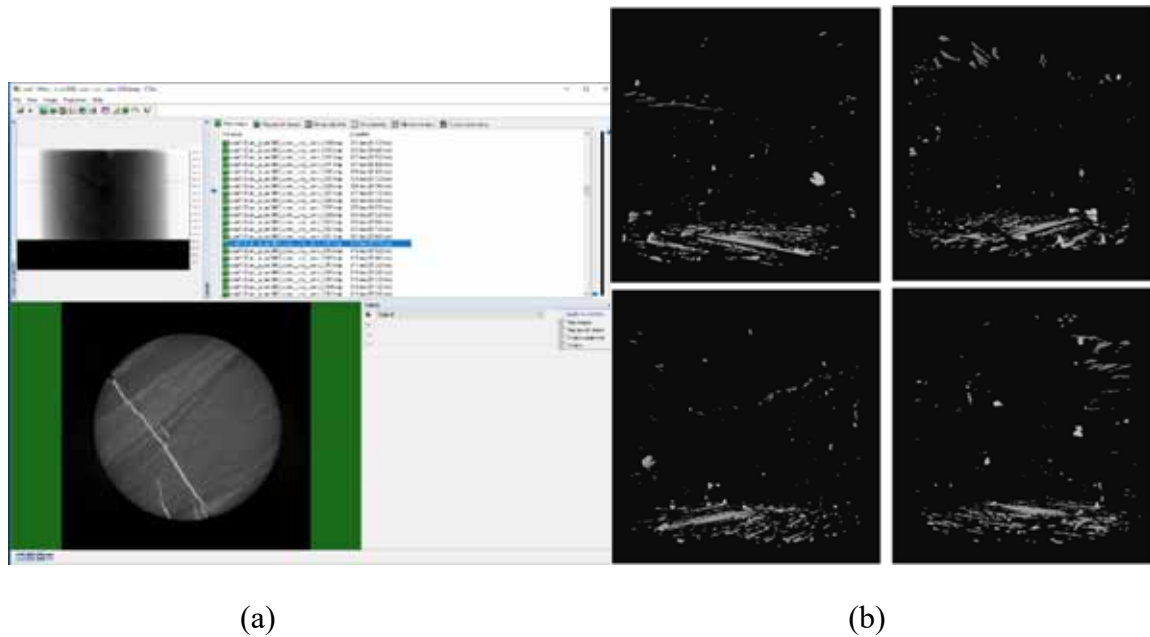
Figure 94. 2D image of core inlet cross-section (a) and 3D images of pore spaces rotated by 90° coal core-1.

(a)   (b)
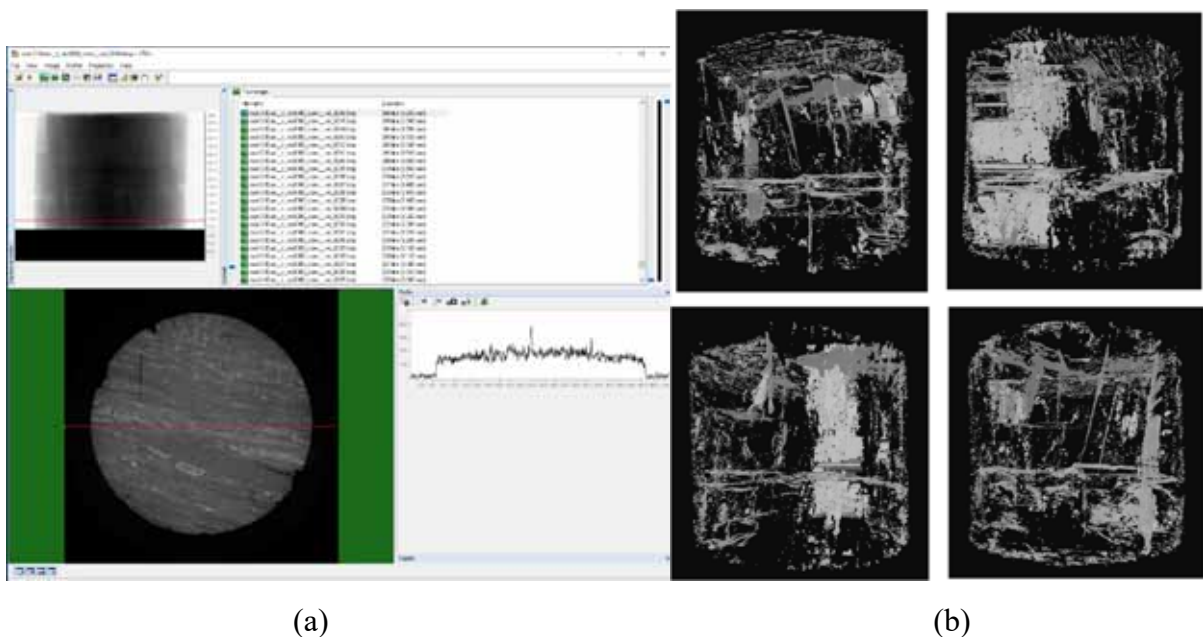
Figure 95. 2D image of core inlet cross-section (a) and 3D images of pore spaces rotated by 90° coal core-3.

Table 20. Results of pore volume calculation from Micro-CT scan data

Parameter	Coal core-1	Coal core-2
Total volume, mm^3	28100	31400
Pore volume, mm^3	15.6	166
%-ge of pore volume	0.056	0.53

Values of coal core porosities presented in (Table 20) agree with those reported in [1] being less than 1%.

This Micro-CT instrument can distinguish between textures which have different densities. In the case of ceramic proppant in coal fractures we most likely will be able to locate the depth of proppant penetration into coal fractures due to appreciable differences in densities of coal, ceramic proppant, and air: $\rho_{coal} \approx 1300\text{-}1500$ kg/m^3, $\rho_{proppant} \approx 2100\text{-}2700$ kg/m^3, and $\rho_{air} \approx 1.200$ kg/m^3.

20.7 Testing of Guar-Gel/Enzyme-Solution/Proppant In Coal Core

Report: Milestone-3-Contingent laboratory studies

Title: Injection of guar-gel/enzyme-solution/proppant into coal core

Prepared by: Prof. Pavel Bedrikovetsky, Dr. Alexander Badalyan, Dr. Abbas Zeinijahromi, and Dr Themis Carageorgos

Date: 14.01.2022.

1. Development of an experimental procedure

In this section we determine the degree of coal core damage during injection of guar-gel. This information is required to estimate coal core damage due to placement of proppant in core fractures. Coal core-4 was chosen for these studies.

1.1. Characterisation of materials

Coal core images are shown in Figure 96. The current choice the inlet face was since it was less damaged than the opposite cross-section, although it has less fractures.

a   b   c
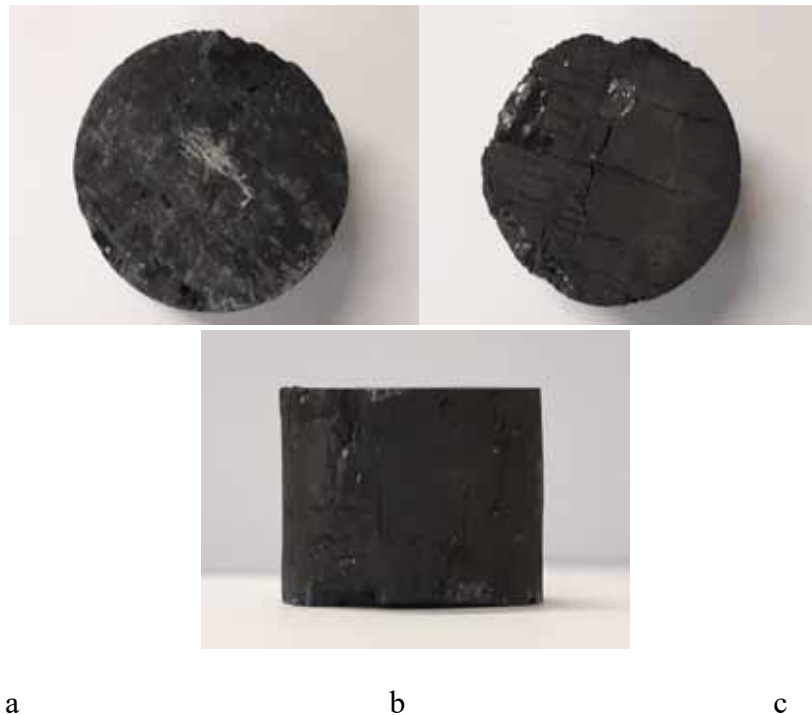
Figure 96. Coal core-4 images: a – inlet, b – outlet, c – side

Below we present information characterising coal core-4 and tap water used for injection:

- coal-core length 3.18 cm, core-core diameter 3.78 cm;
- tap water properties: pH = 7.87, electrolytic conductivity = 493 µS/cm (equivalent to 0.005 M NaCl);
- tap water volumetric flowrates were equal to 1, 2, 4, 6, 8, 10 mL/min, and were developed by two Prep-100 HPLC (high performance liquid chromatography)

pumps: Pump-1 (the so-called enzyme-solution pump) and Pump-2 (the so-called guar-gel/proppant pump).

1.2. Experimental setup

Photo of an experimental setup is shown in Figure 97. Pump-1 *1* is used to pump enzyme-solution and Pump-2 *2* injects distilled water into the upper part of the transfer vessel 3 to push through a Teflon piston guar-gel/proppant formulation through the coal core located in the high-pressure coreholder *4*. Overburden pressure is developed by manual pressure generator *5*. Back pressure is developed in back-pressure regulator *6* using compressed air from cylinder *7*. Differential pressure is measured by differential pressure transmitters *8*. Inlet and outlet pressures are measured by pressure transmitters *9* and *10*, respectively. Signals from differential pressure and pressure transmitters via data acquisition system *11* are delivered to standalone computer *12* which records experimental parameters in real-time mode. Effluent samples are collected in the sampling carousel 13.
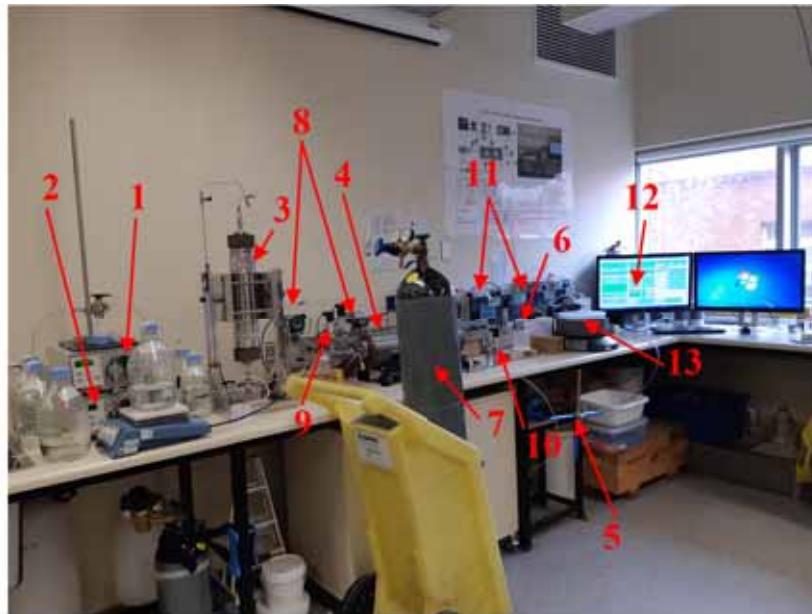

Figure 97. Photo of the experimental setup used for proppant deposition.

1.3. Coal core-4: conditioning with tap water

We carried coal core conditioning, checked HPLC pump operation, and determined linear relationship between fluid volumetric flowrate and pressure drop across the core during injection of tap water. Results of the above corefloods are presented in Figure 98.
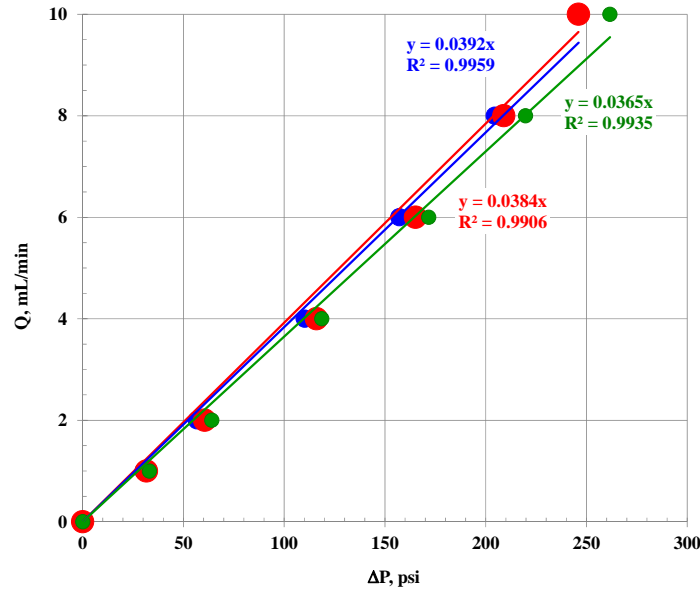
Figure 98. Results of corefloods in coal-core-4: BLUE' symbols - Pump-1 with increasing flowrate, 'RED' symbols - Pump-2 with decreasing flowrate, and 'GREEN' symbols - Pump-1 and Pump-2 operating simultaneously at equal increasing volumetric flowrates.

Comments:

- ➢ operation of pumps is sufficiently accurate with standard deviation between values of slopes of linear trendlines $Q = f(\Delta P)$ being equal to 3.64% and with coefficient of determination R^2 being greater than 0.99 which is acceptable for engineering purposes;

- ➢ the above also indicates the absence of hysteresis in coal behaviour at increased and decreased volumetric flowrates;

- ➢ $Q = f(\Delta P)$-data are linear at volumetric flowrates of up to 4 mL/min, with slight deviation at higher volumetric flowrates;

- ➢ our previous tests on sandpacks (40/70 mesh) were carried out volumetric flowrates of 4 mL/min with pressure drop across the undamaged sand pack being around 0.062 psi corresponding to permeability of 5817 mD;

- ➢ as follows from Figure 98, in the case of coal core-4 pressure drop across the core is around 115 psi at 4 mL/min volumetric flowrate;

- ➢ the limit of the experimental coreflood setup is 2800 psi;

- ➢ 1st injection of 'guar-gel'-plus-'enzyme-solution' (90%:10% vol/vol) into the previous sand pack resulted in pressure drop across the sand pack increasing from 0.062 psi up to about 1.262 psi (20.3 times increase);

- ➢ 2nd injection of 'guar-gel'-plus-'enzyme-solution' (90%:10% vol/vol) into the already damaged sand pack resulted in pressured drop across the sand pack increasing from 0.347 psi up to about 8.921 psi (25.8 times increase);

- ➢ translating these numbers to coal core-4 we may anticipate values of pressure drop across the coal-core being around 2334 psi and 2966 psi which near to pressure limit of our experimental setup; and

> pressure drop will be much higher in the case when we inject 'guar-gel'-plus-'proppant'-plus-'enzyme-solution'.

Conclusion

To be able to reliably perform experiments we decided to do corefloods at the overall flowrate of 1 mL/min.

1.4. Coal core-4: 1st injection of 'guar-gel'-plus-'enzyme-solution' into coal core-4

The experimental procedure is as follows:

> coal-core-4 was 'conditioned' by flooding with 0.002 % (v/v) enzyme solution with pH = 5.47;

> stabilised pressure drop across the core was 40.602 psi ± 0.125 psi (0.39%); and

> the following formulation was injected at 1 mL/min volumetric flowrate: 90% (v/v) of guar-gel (pH = 5.51) and 10% (v/v) of 0.002% (v/v) enzyme-solution (pH = 5.50).

Comments:

> injection lasted about 122 min (35.3 PVI);

> pressure drop continuously increased reaching 2750 psi according to Figure 99, which is the upper pressure limit of the setup;

> we were unable to continuing injection of the above formulation, due to significant coal-core damage and inlet pressure increase;
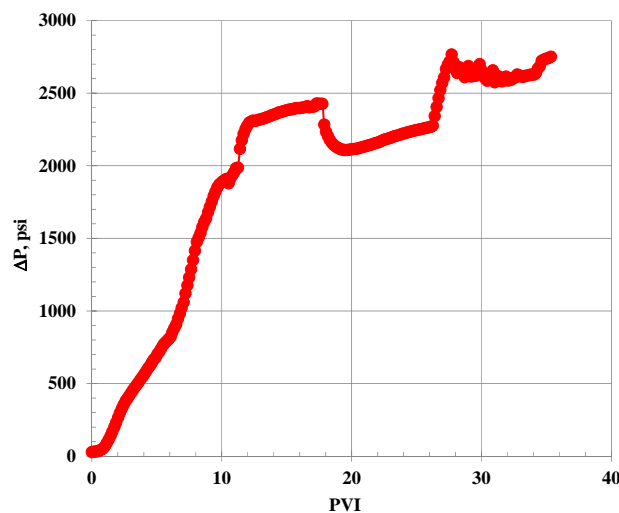

Figure 99. Results of 1st injection of 'guar-gel'-plus-'enzyme-solution'

> we stopped guar-gel injection, and started backward injection of enzyme-solution at 1 mL/min volumetric flowrate trying to restore the coal-core permeability;

> followed forward injection of enzyme-solution at 0.1 mL/min gave results shown in Figure 100;
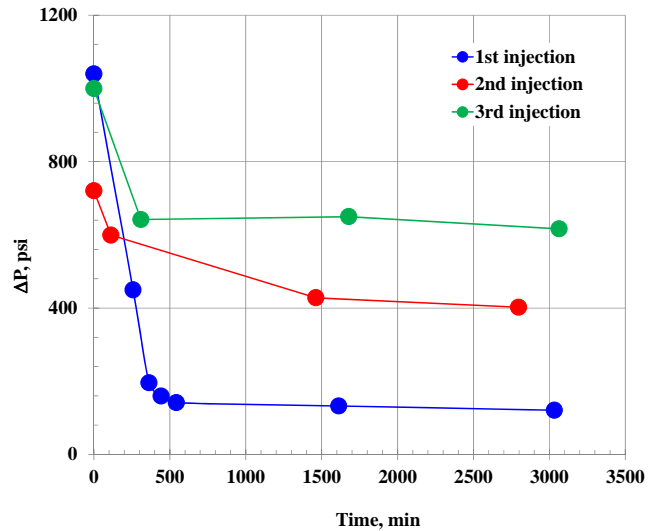
Figure 100. Results after 1st, 2nd and 3rd injections of 'guar-gel'-plus-'enzyme-solution': stabilised pressure drops across the coal-core

> experimental points 6 and 7 with respective pressure drops of 132 psi and 121 psi during the 1st injection correspond to overnight soaking the coal-core in enzyme-solution;

> as follows from Figure 100, the coal-core has not restored its initial hydrodynamic properties: pressure drop across the core is 121 psi compared to 40.602 psi.

1.5. Coal core-4: 2nd injection of 'guar-gel'-plus-'enzyme-solution' into coal core-3

We decided to change experimental procedure as follows:

> pressure drop the coal-core reached stabilisation at 120.7 psi ± 0.747 psi during injection of enzyme-solution;

> the following formulation was injected at 1 mL/min volumetric flowrate: 50% (v/v) of guar-gel (pH = 5.51) and 50% (v/v) of 0.002% (v/v) enzyme-solution (pH = 5.50).

Comments:

> injection lasted about 33 min (9.52 PVI);

> pressure drop continuously increased reaching 2354 psi according to Figure 101, which is nearly the upper pressure limit of the setup;

> overburden pressure has also gradually increased;

> we stopped guar-gel injection, and continued (forward) injection of enzyme-solution at 1 mL/min volumetric flowrate;
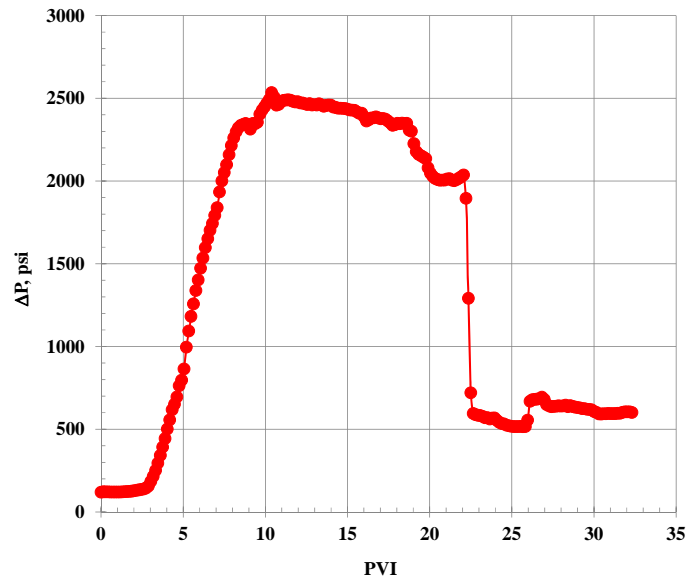
Figure 101. Results of 2nd injection of 'guar-gel'-plus-'enzyme-solution'

- ➢ pressure drop across the coal-core continued increasing up to 2534 psi at 10.39 PVI (36 min cumulative time);

- ➢ then, we slowly started reducing the overburden pressure down to its initial value of 1000 psi;

- ➢ we thus, arrived at stabilised pressured drop of 721 psi after 78 min (22.5 PVI);

- ➢ continued injection and soaking in enzyme-solution resulted in pressure drops across the coal-core shown in Figure 100 with the final value of 402 psi;

- ➢ as follows from Figure 100, the coal-core has not restored its previous hydrodynamic properties: pressure drop across the coal-core is 402 psi compared to 121 psi.

1.6. Coal core-4: 3rd injection of 'guar-gel'-plus-'enzyme-solution' into coal core-3

The following procedure was used during 3rd injection of 'guar-gel'-plus-'enzyme-solution' into coal-core:

- ➢ pressure drop the coal-core reached stabilisation at 402.2 psi ± 6.04 psi during injection of enzyme-solution;
- ➢ the following formulation was injected at 1 mL/min volumetric flowrate: 20% (v/v) of guar-gel (pH = 5.51) and 80% (v/v) of 0.002% (v/v) enzyme-solution (pH = 5.50).

Comments:

- ➢ injection lasted about 119.5 min (34.48 PVI);

- ➢ according to Figure 102, pressure drop increased reaching stabilisation at 1259 psi ± 48 psi which is below the upper pressure limit of the setup;

- ➢ overburden pressure has also gradually increased up to 1526 at 119.5 min of injection;

- ➢ we stopped guar-gel injection, and continued (forward) injection of enzyme-solution at 1 mL/min volumetric flowrate;
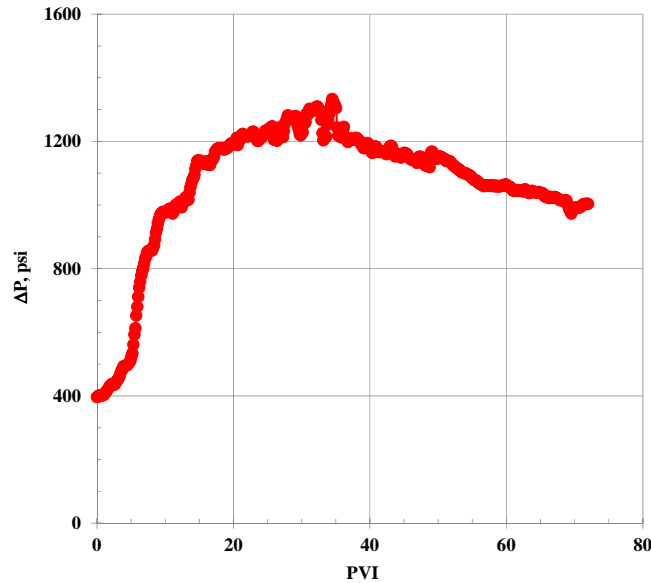
Figure 102. Results after 3rd injection of 'guar-gel'-plus-'enzyme-solution': stabilised pressure drops across the coal-core

➢ after that, we slowly started reducing the overburden pressure down to 1200 psi;

➢ we thus, arrived at stabilised pressured drop of 1000 psi after 249.5 min (72.0 PVI);

➢ continued injection and soaking in enzyme-solution resulted in pressure drops across the coal-core shown in Figure 100 with the final value of 616 psi;

➢ as follows from Figure 100, the coal-core has not restored its previous hydrodynamic properties: pressure drop across the coal-core is 616 psi compared to 402 psi.

Overall conclusions

1. As follows from Figure 100, consecutive injection of 'guar-gel'-plus-'enzyme-solution' results in gradual irreversible coal-core damage. We think that this is due to accumulation of guar-gel (not completely degraded by enzyme solution) in fractures of the coal-core.

2. Our previous results on rheological properties of the formulation made of 90% (v/v) of guar-gel and 10% (v/v) of 0.002% (v/v) enzyme-solution (pH = 5.60) (Section 20.3, Table 18) show that viscosity of this formulation drops by about 5.3 times from 0.0151 Pa×s down to 0.00284 Pa×s during 24-hour period. As follows from Figure 100, pressure drop across the coal-core during 1st injection of the above formulation decreased about 7.9 times from 1040 psi down to 132 psi during 27-hour period. This shows that partial restoration of coal-core hydrodynamic properties is due to reduction of viscosity of the above formulation as the result of guar-gel degradation by enzyme solution.

3. In our final test we will injected 10% of 'guar-gel-plus-proppant' and 90% of 'enzyme solution' formulation at pH = 5.5 into coal core-3 which has undergone micro-CT-scanning. This formulation will be injected at 1 mL/min volumetric flowrate.

4. Prior to formulation injection we will condition this coal-core by injection of tap water at 1 mL/min with increasing and decreasing effective stress to remove hysteresis. This will be followed by coal-core conditioning with enzyme solution (pH = 5.5) at 50 °C.

2. Micro-CT scans of coal samples before proppant deposition

Analysis of two coal samples was carried out using SkyScan-1279 Micro-CT. Although the instrument can magnify images down to 2.8 μm pixel size, Micro-CT scans were done at 20 μm but the images and analysis were done at 80 μm as the data size was large when generating 3D images and performing 3D analysis of fractures/pores.

3D images of the analysed coal samples are presented in Figure 103 and Figure 104. As follows from these images, coal core-3 has more developed pore network (white colour). This observation is supported by calculation of pore volumes for coal core-1 and core-3 (see Table 21).
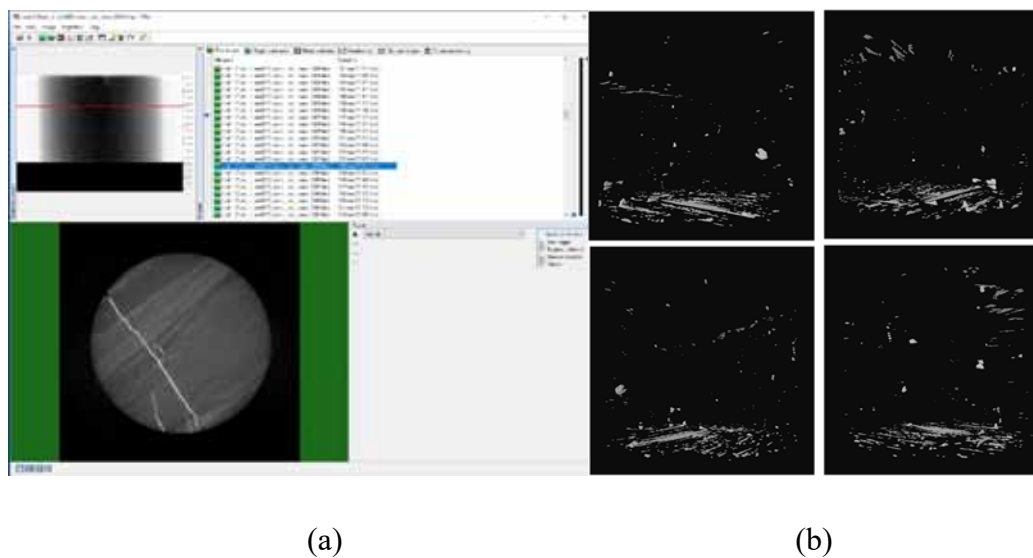

(a)   (b)

Figure 103. Coal core-1: 2D image of coal core-1 inlet cross-section (a) and 3D images of pore spaces rotated by 90°

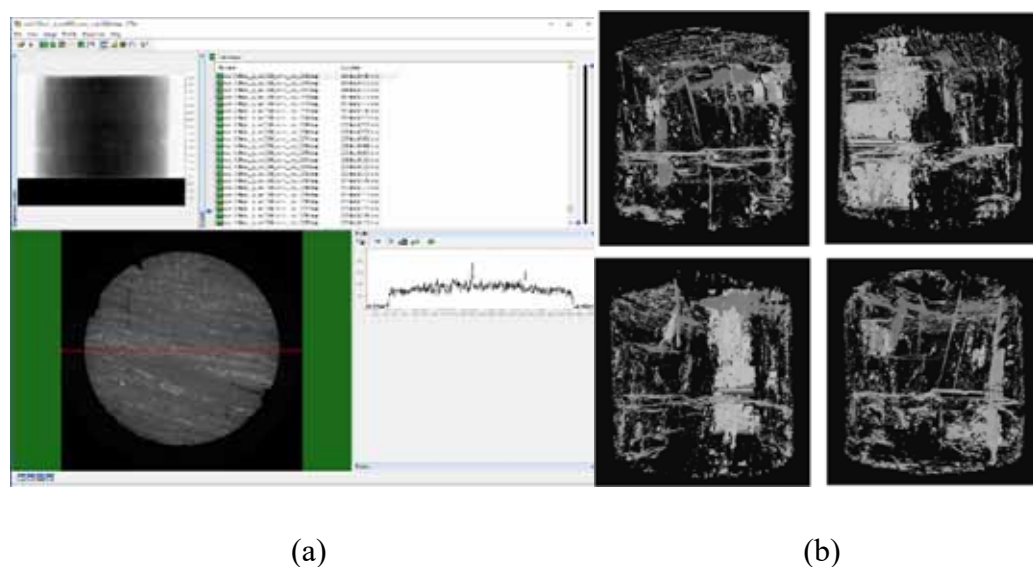(a)   (b)

Figure 104. Coal core-3: (a) 2D image of inlet cross-section, and (b) 3D images of pore spaces rotated by 90°

Values of coal porosities less than 1% were reported in [Reiss, 1980]. As follows from 1, values of coal core porosities estimated in the present study agree with those reported in [Reiss, 1980].

Table 21. Results of pore volume calculation from micro-CT scan data

Parameter	Coal core-1	Coal core-3
Total volume, mm^3	28100	31400
Pore volume, mm^3	15.6	166
%-ge of pore volume	0.056	0.53

This micro-CT scan instrument can distinguish between textures which have different densities. In the case of ceramic proppant in coal fractures we most likely will be able to locate the depth of proppant penetration into coal fractures due to appreciable differences in densities of coal, ceramic proppant, and air: $\rho_{coal} \approx$ 1300-1500 kg/m^3, $\rho_{proppant} \approx$ 2100-2700 kg/m^3, and $\rho_{air} \approx$ 1.200 kg/m^3.

Coal core-3 was chosen for proppant deposition due to a more developed fracture network compared to coal core-1.

3.   Deposition of proppant in coal core-3

3.1. Experimental program

We adopted the following experimental program:

1.   Place coal core-3 into the coreholder. Develop overburden pressure of 1000 psi. Develop backup pressure of about 30 psi.

2.   Increase and decrease the effective stress by increasing backup pressure during injection of tap water for hysteresis removal.

3.   After hysteresis has been removed within experimental uncertainty (about 3.2% for liquid permeability) during tap water injection, start injection of 0.002% (v/v) enzyme-solution (pH $\approx$ 5.50) for a single increase and decrease of the effective stress - one additional cycle for core conditioning: enzyme solution should penetrate as more fractures as possible.

4.   Preheat coreholder and maintain it at 50 °C throughout the entire experiment.

5.   Inject 0.002% (v/v) enzyme-solution (pH $\approx$ 5.50) for a single increase and decrease of the effective stress.

6.   Inject enzyme solution until effective stress of about 200 psi has been reached.

7.   Inject guar-gel-proppant (10% v/v) and enzyme solution (90% v/v) until pressure drop increases by about 40-50%.

8.   Stop guar-gel-proppant injection, continue injection of enzyme solution.

9.   Gradually increase effective stress to its maximum value which was used during hysteresis removal cycles.

10.   Continue injection of enzyme solution until pressure drop stabilises.

11.   Stop injection of enzyme solution.

12.   Leave the entire system overnight at 50 °C.

13.   Next day, inject enzyme solution at the last maximum effective stress until pressure drop stabilises.

14. As an option, stop injection of enzyme solution, leave the system overnight, and next day repeat step 9.

15. Perform backflush with enzyme solution at various volumetric flowrates to remove possible external cake formed by deposited proppant.

3.2. Characterisation of materials

Coal core-3 images are shown in Figure 105. The current choice of the inlet face was since it was less damaged and has sufficient fractures.

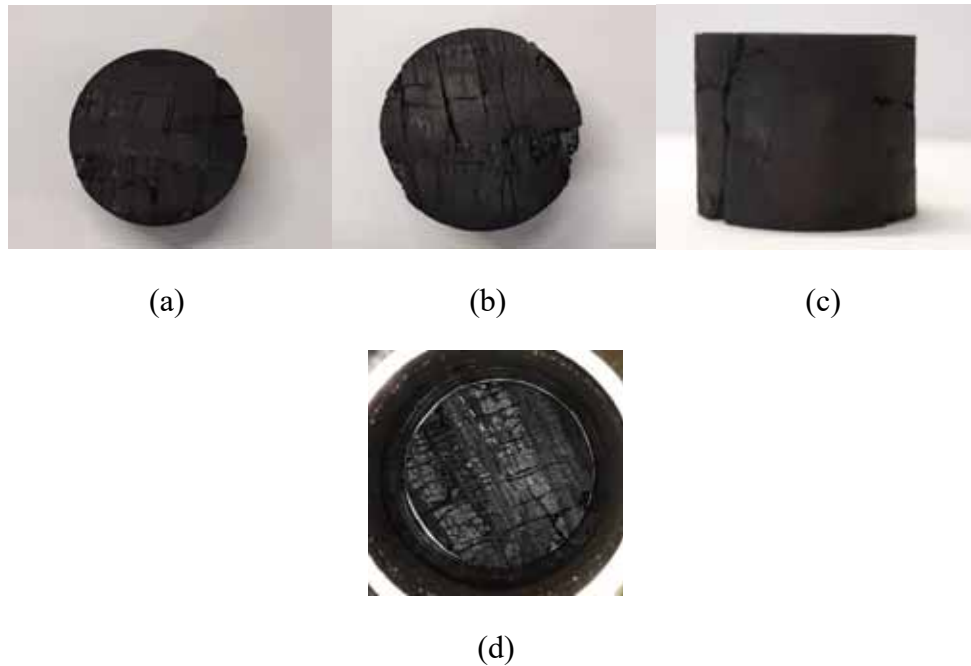(a)   (b)   (c)

(d)

Figure 105. Coal core-3 images before proppant deposition test: a – inlet cross-section, b – outlet cross-section, c – side, d – core in the coreholder (inlet cross-section).

Below we present information characterising coal core-3 and liquids used in proppant deposition tests:

➢ coal-core length 3.07 cm, core-core diameter 3.79 cm;

➢ tap water properties: pH = 7.64, electrolytic conductivity = 514 μS/cm (equivalent to 0.005 M NaCl);

➢ enzyme solution pH = 5.49, guar-gel pH = 5.53;

➢ liquid volumetric flowrate is equal to 1 mL/min.

3.3. Experimental setup

We have modified the experimental setup used in Section 1.2 by addition of a heating mantle *1* and a process controller *2* to carry out experiments at 50 °C (see Figure 106). It took about 4 hours to stabilise overburden pressure at 1000 psi when coreholder temperature increased from 22 °C to 50 °C.
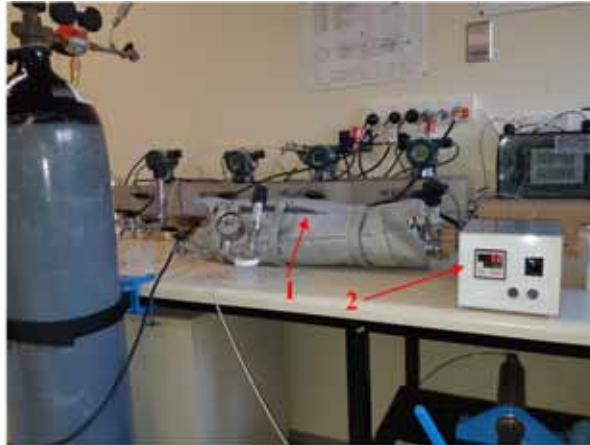
Figure 106. Photo of the coreholder covered by a heating mantle for proppant deposition at 50 °C.

3.4. Hysteresis removal

By increasing and decreasing fracture pressure during injection of tap water we gradually removed hysteresis in reduced core permeability as function of the effective stress. Five cycles of increased and decreased fracture pressure at 22 °C are shown in Figure 107.
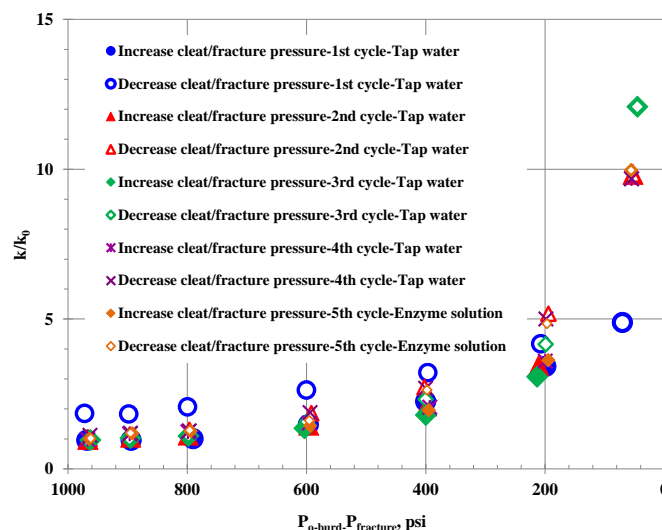

Figure 107. Graphs showing removal of hysteresis in reduced core permeability as function of effective stress at 22 °C.

Comments:

➢ we made four cycles with tap water and one cycle with enzyme solution. For 4th cycle, at the effective stress of about 800 psi hysteresis can be already regarded as negligible (hysteresis is 3.17%), at about 600 psi effective stress hysteresis increases up to 23%;

➢ during 5th cycle we injected enzyme solution to saturate this core with enzyme before injecting guar-gel-proppant formulation;

➢ for proppant injection Zeeospheres Ceramic Microspheres N600 (particle size 25 mm with 90% percentile) with concentration 2 ppg in guar-gel will be used;

- in our previous project, 10 μm proppant was injected into coal core at effective stress of about 250 psi resulting in successful proppant deposition in coal fractures;

- Figure 108 presents a graph correlating fracture opening (h in μm) and effective stress and jamming ratio (ratio between proppant size and fracture opening) plotted using our presents experimental data. Horizontal RED line corresponds to particle size 25 mm (90% percentile) and BLUE line corresponds to the upper and lower limits of deep-bed-filtration '1/7-1/3'-rule ($0.14 < j < 0.33$). As follows from this graph, it is possible to inject our proppant at about 200 psi effective stress, so particles will be deposited inside fractures.
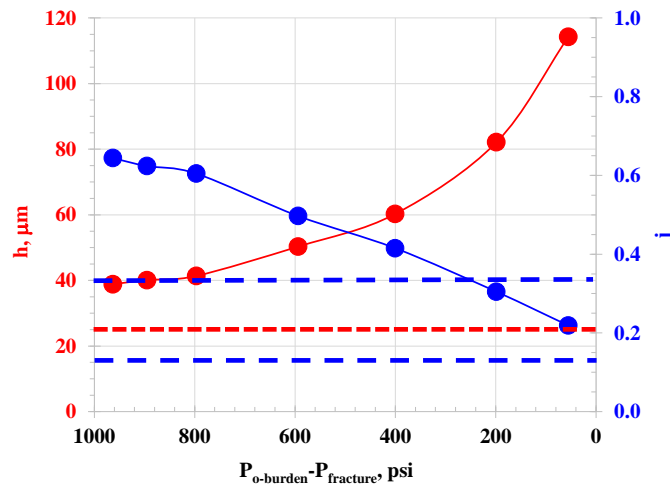

Figure 108. Graphs showing determination of effective stress suitable for proppant deposition.

3.5. Proppant deposition

The last increase and decrease fracture pressure cycle before proppant injection was carried out with enzyme-solution at 50 °C (see Figure 109).
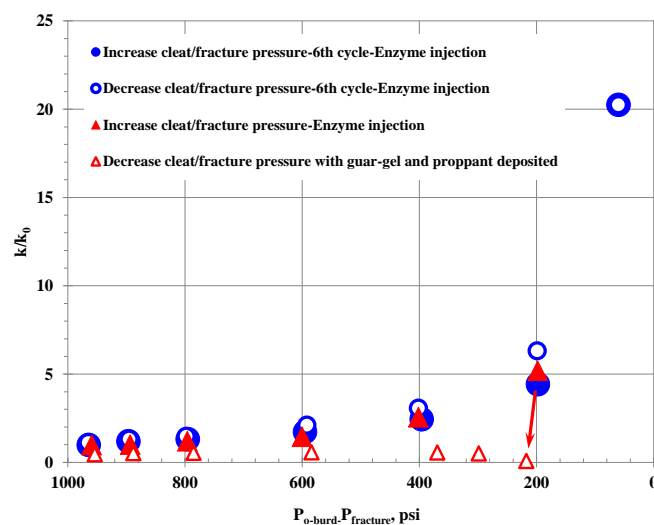

Figure 109. Increase and decrease fracture pressure during enzyme solution injection and proppant deposition at 50 ℃ (proppant injection is shown by RED arrow).

Injection of guar-gel-proppant and enzyme solution formulation (10% and 90%,

respectively) started when the effective stress has reached the value of 217.6 psi (see Figure 109). Reduced core permeability during proppant deposition, k/k_0, dropped from 5.141 down to 0.023.

Variation of pressure drop across the coal core from the beginning of proppant injection, and during increasing the effective stress and stabilisation of pressure drop at maximum effective stress is shown in Figure 110 and summary of results for proppant deposition is presented in Table 22.
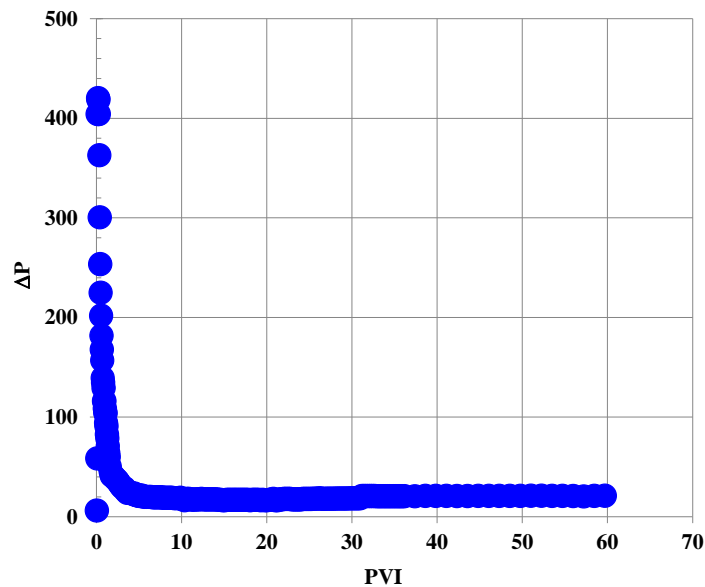

Figure 110. Variation of pressure drop across the coal core during and after proppant injection.

Table 22. Summary of results for proppant deposition

Various stages of test	k, mD	k/k₀
Before proppant injection at 195.4 psi effective stress	18.558	5.141
When stopped proppant injection at 217.6 psi effective stress	0.083	0.023
Injection of Enzyme solution at 1 mL/min and maximum effective stress of ≈ 950 psi		
After proppant injection stopped and ΔP across the coal-core has stabilised	1.659	0.460
Next morning	0.949	0.263
Same morning	1.005	0.281
Next morning	0.736	0.206
After 20 mL/min backflush	2.063	0.577
After 40 mL/min backflush	2.026	0.566
After 60 mL/min backflush	1.777	0.497
After 80 mL/min backflush	1.207	0.337
After 100 mL/min backflush	0.898	0.251

After completion of the proppant injection test, the coal-core-3 has been removed from the coreholder. Photos of inlet and outlet cross-sections of the core, and outer cross-section of the inlet flow-distributor are presented in Figure 111. As follows from this figure, backflush with enzyme solution did not remove all proppant from the inlet cross-section the core. However, backflush did remove proppant from fractures located in the inlet cross-section of the core - we can't see any appreciable amount of proppant in these fractures. At the same time, the outlet cross-section of the core remains almost proppant-free. This may suggest that these are the so-called dead-end fractures. Some residual proppant is visible on the outer cross-section of the flow-distributor.

(a)   *(b)*   *(c)*
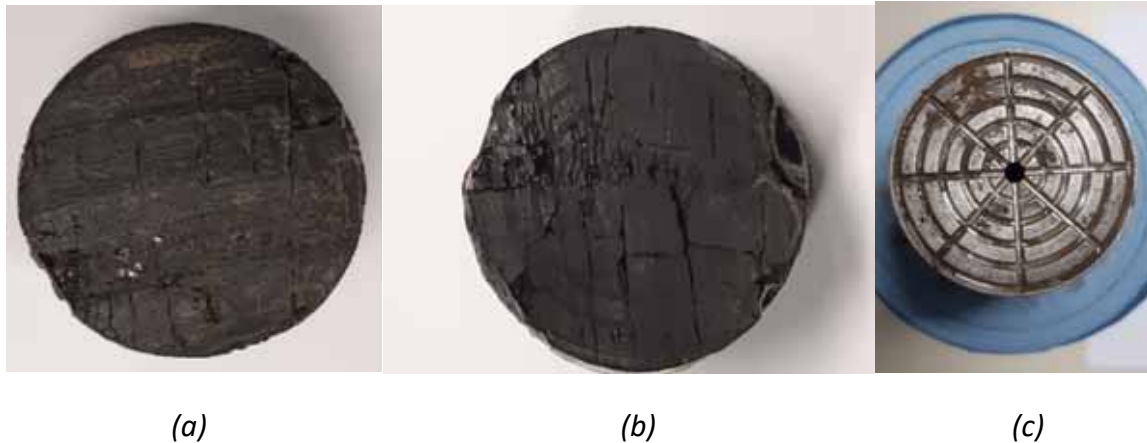
Figure 111. Coal core-3 images after proppant deposition test: (a) - inlet cross-section, (b) - outlet cross-section, and (c) outer cross-section of the inlet flow-distributor.
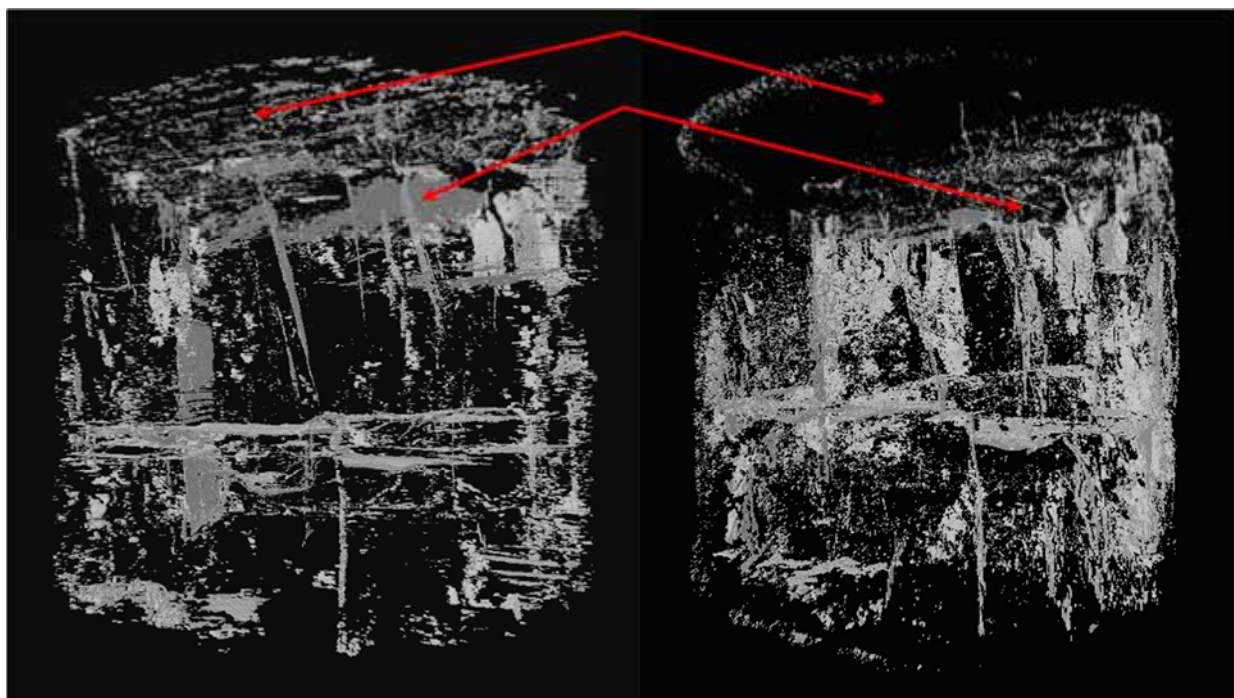
Comments:

➢ as follows from Figure 108 and Figure 109, we have almost removed hysteresis at high values of effective stress;

➢ injection of proppant has significantly increased pressure drop from about 1.871 psi at effective stress of 197.7 psi to about 420.319 psi at effective stress of about 217.6 psi;

➢ the above resulted in decrease of coal-core permeability from 18.558 mD down to 0.083 mD (although, strictly speaking, we can't use the term permeability here, since the composition of fluid was continuously changing inside the coal-core);

➢ injection of enzyme solution after stopping proppant injection resulted in a gradual decrease of ΔP across the coal-core with the stabilised permeability of 1.659 mD;

➢ next morning, we obtained lower permeability values which fluctuated as follows: 0.949 mD, 1.005 mD, and 0.736 mD;

➢ we carried backflush with enzyme solution at the following volumetric flowrates: 1 mL/min, 5 mL/min, 20 mL/min, 40 mL/min, 60 mL/min, 80 mL/min, and 100 mL/min;

➢ results of backflush were the most promising after 20 mL/min backflush volumetric flowrate: we observed maximum increase in coal-core permeability from 1.659 mD up to 2.063 mD; this is an indication that there is some maximum backflush flowrate

above which deposited proppant can be removed, thus increasing hydraulic resistance of the core (or reducing core permeability).

➢ backflush at higher flowrates was not effective, probably, due to the removal of proppant located in the close vicinity to fracture inlet, thus causing partial closure/collapse of a part the fracture wall in the close vicinity to the fracture inlet at maximum effective stress;

➢ to support the above statement, we carefully examined the inlet cross-section of the core before and after proppant deposition as shown in Figure 105a and Figure 111a, respectively. We did observe that some inlet fractures have reduced their widths, and some fractures have disappeared/collapsed.
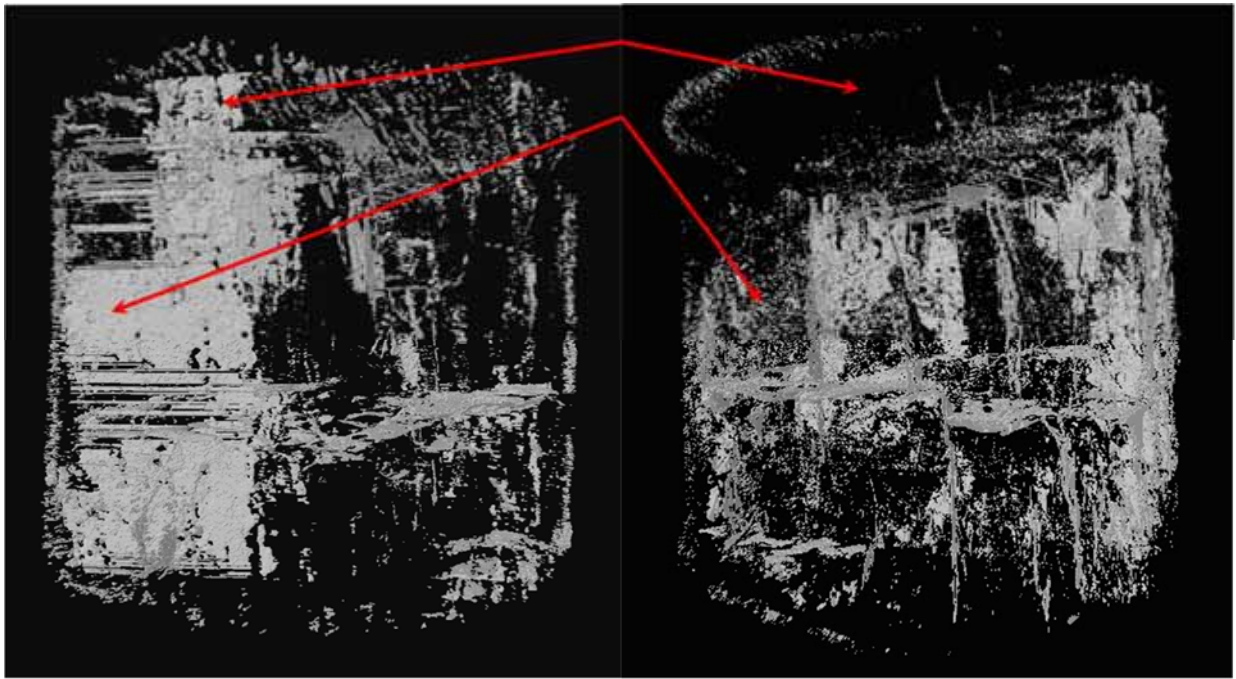
4. Micro-CT scans of coal sample after proppant deposition

After removal of coal core-3 from the core holder, this sample has undergone micro-CT scan at conditions similar to those described in Section 2. The obtained results together with those for this sample before proppant deposition are shown in Figure 112.
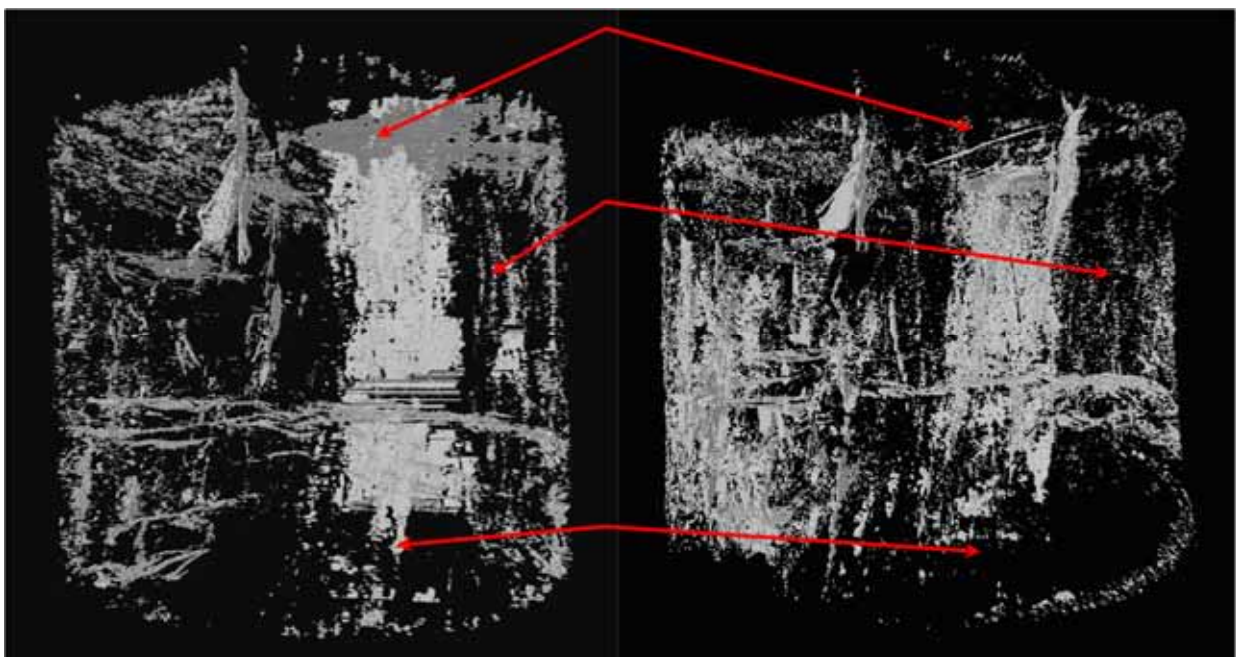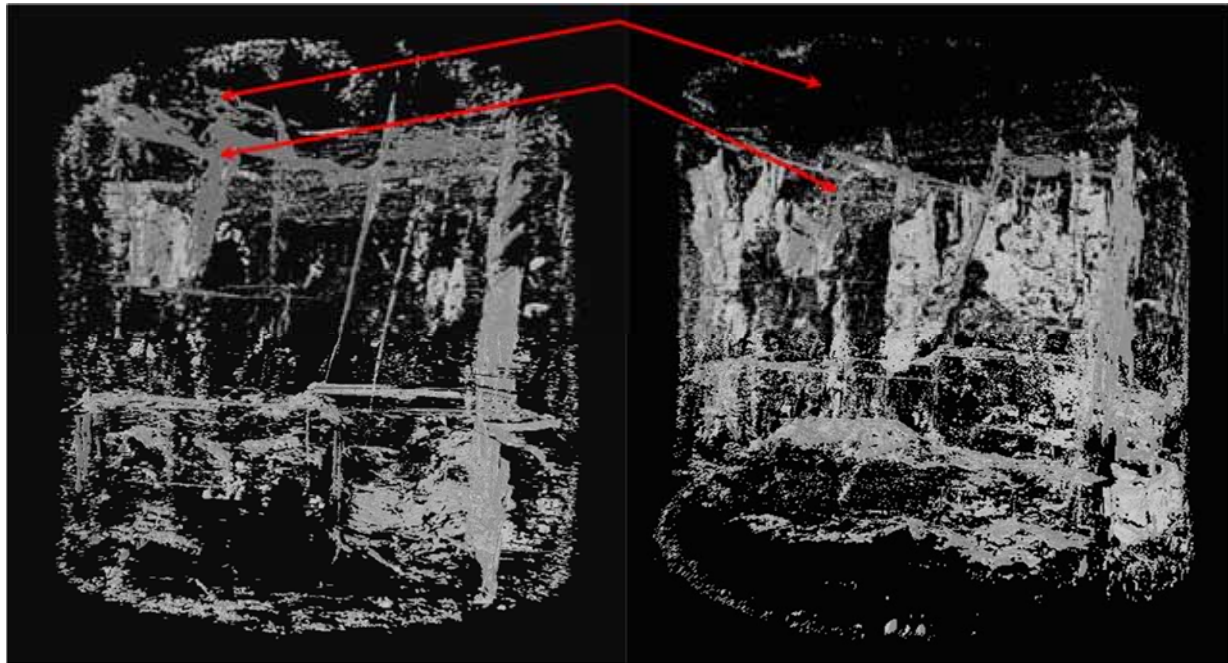

Before   After

Before   After

Before   After

Before   After

Figure 112. 3D images of pore spaces rotated by 90° for coal core-3 before after proppant deposition. (Red arrows show some parts of the coal core with deposited proppant).

Comments:

➢ as follows from Figure 112, it is obvious that new fractures were generated in this coal core during hysteresis removal procedure;

➢ fractures on the inlet cross-section of the core are filled with proppant;

➢ some fractures in the middle of the core are also filled with proppant, suggesting that backflush with enzyme solution hasn't removed all deposited proppant;

➢ outlet cross-section of the core has also fractures filled with proppant.

21 Appendix J: University of Alberta, Graded Particle Injection Studies
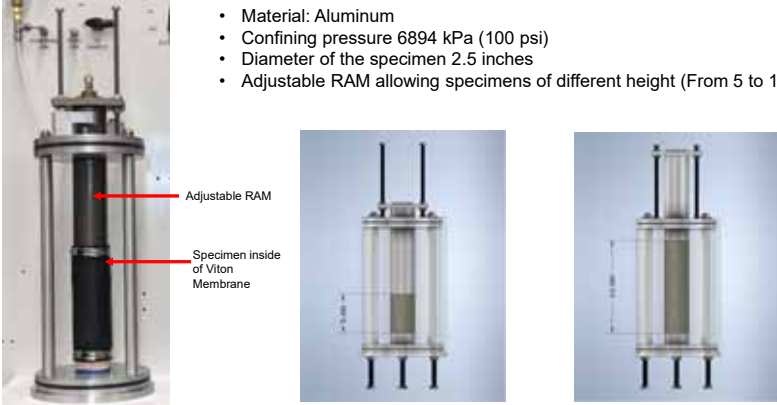
Hassler Cell Specifications
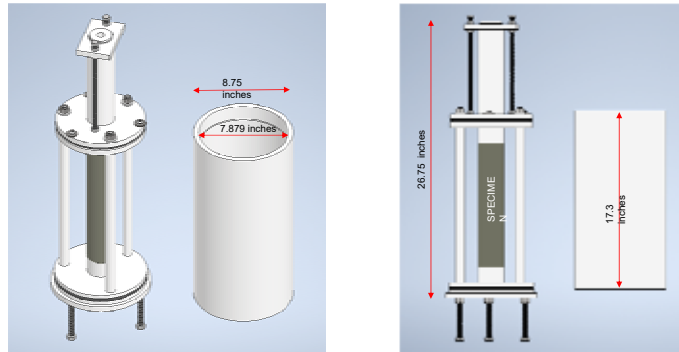
Flow Diagram
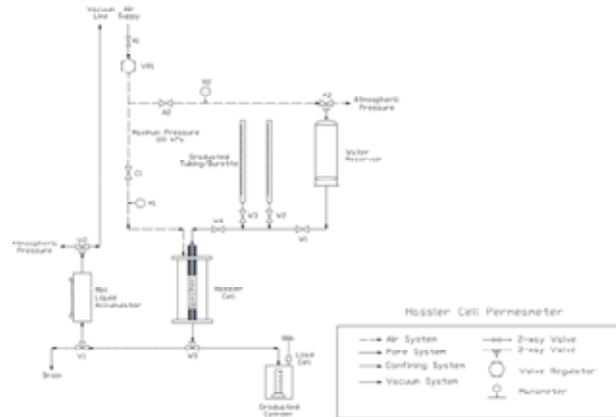
Permeability and Proppant Injection Setup
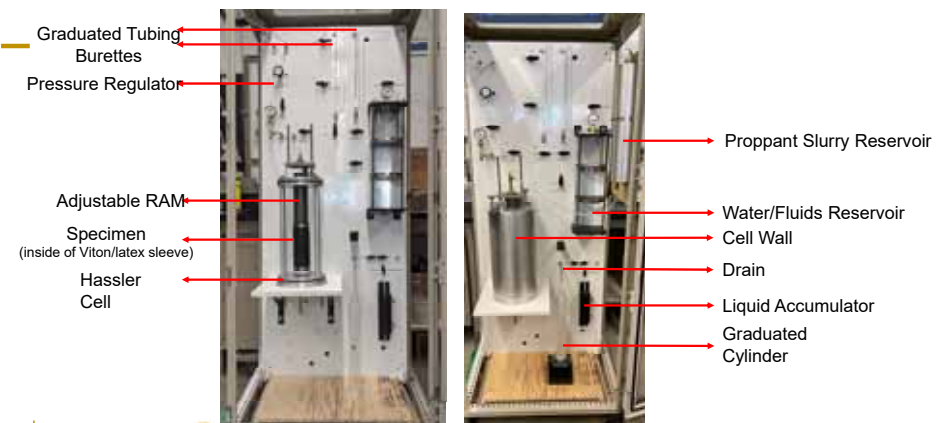
Experimental results

Proppant Injection Testing – 3D-Printed Fractured Porous Media

- Feasibility test for graded proppant injection into 3D-printed synthetic coal using guar-gel, proppants, and enzyme breakers.

Experimental results

Proppant Injection Testing – 3D-Printed Fractured Porous Media
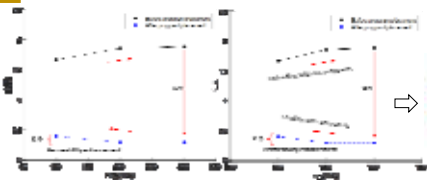
Figure 1 - Permeability evolution before and after proppant placement. Permeability versus injection pressure – left, and permeability versus effective stress – right.

σ confining (KPa)	Pressure injection (kPa)	Pressure out (kPa)	Pressure pore (kPa)	σ' (KPa)	K (D)	K/Ko (D)
350	100	0	50	300	1.66	1.00
350	200	0	100	250	1.85	1.11
350	300	0	150	200	1.88	1.13
350	300	0	150	200	0.29	0.17
350	200	0	100	250	0.29	0.17
350	100	0	50	300	0.39	0.24

Figure 2. Proppant penetration in matrix and fractures at the inlet face of the 3D-printed rock. Two fronts with different saturations were observed. The first front (higher concentration) is outlined with the thicker dash line. The second front shows a lower concentration of particles (thinner dash line).

Experimental results

Proppant Injection Testing – 3D-Printed Fractured Porous Media

Conclusions:

1. After the particle injection, an irreparably damaged permeability was measured. Although it was not possible to obtain a higher than the initial permeability, it is observed a slight permeability enhancement. This can be attributed to proppants placed inside the fractures avoiding complete fracture closure (fracture stimulation).

2. The drastic permeability reduction may be attributed to pore plugging by the micro-particles. Even though the rock has two fractures, and should behave as a fractured-dominated flow, the size of the proppant is not appropriate for the matrix pore throats. Therefore, the jamming radius is disproportionate.

3. The efficiency of the particle injection technique depends on whether rock conductivity is provided by fractures or pores. In porous rocks with a pore-dominated hydraulic conductivity, the graded proppant injection causes pore plugging by the particle straining with the consequent permeability reduction.

Recommendations:

A synthetic rock with zero matrix porosity and multiple fractures may be more suited to use with the small proppant sizes.

Experimental results

Proppant Injection Testing – 3D-Printed Fractured Media

Design of synthetic rock proposed for a fractured-dominated flow.

Layer A
Layer B
Layer A

Front
Side
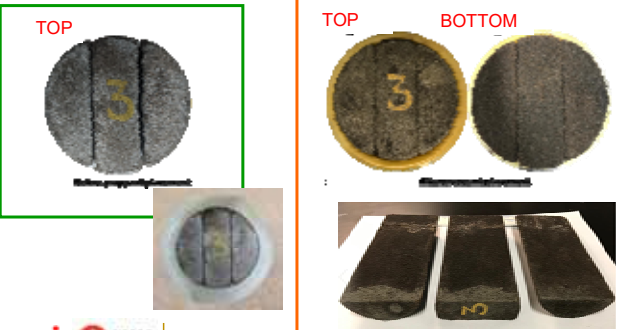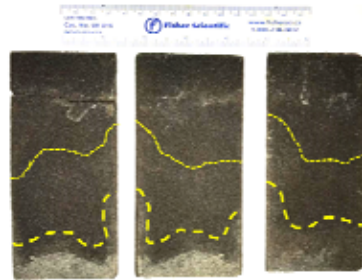
Length: 5 inches
Diameter: 2.5 inches

[RG]² — NSERC/Energi Simulation Industrial Research Consortium on Reservoir Geomechanics — 9

Experimental results

Proppant Injection Testing – 3D-Printed Fractured Media

Layer A

Top
Side
Front

Layer B

Top
Side
Front

[RG]² — NSERC/Energi Simulation Industrial Research Consortium on Reservoir Geomechanics — 10

Experimental results
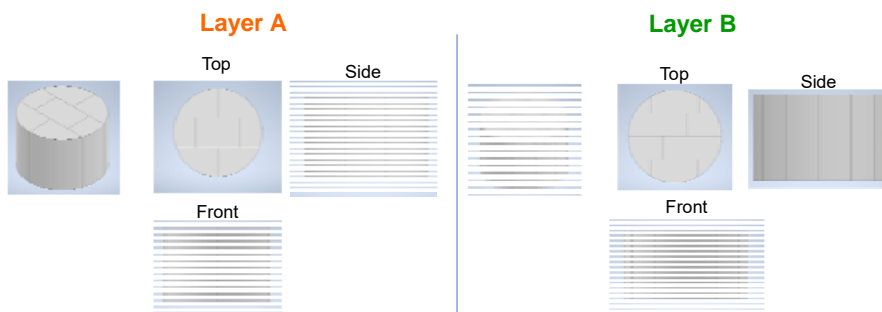
Proppant Injection Testing – 3D-Printed Fractured Media

Layer A

Top
Side
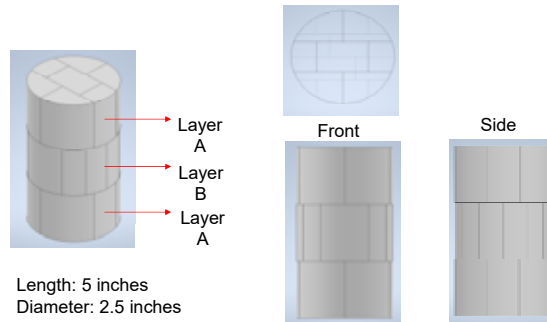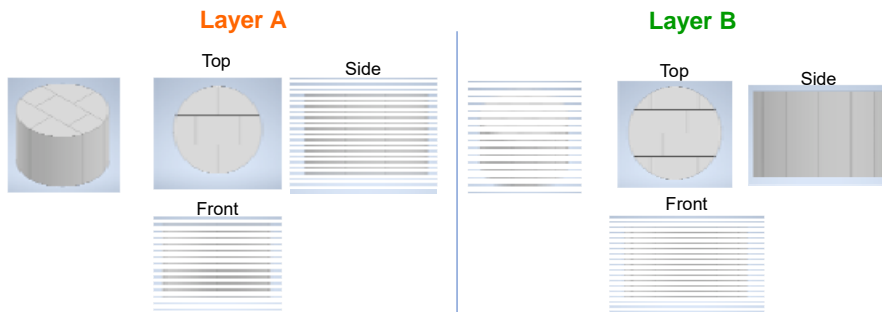Front

Layer B

Top
Side
Front

[RG]² — NSERC/Energi Simulation Industrial Research Consortium on Reservoir Geomechanics — 11

Experimental results

Proppant Injection Testing – 3D-Printed Fractured Media

3D-Printed rock (synthetic coal) with a fractured-dominated flow design.

Layer A   **Layer B**

Material: VeroClear
(transparent PolyJet
Photopolymer)

Experimental results

Proppant slurry preparation
200ml distilled water + 1.92g of guargum powder + 9.6g of proppants + 50ºC heat and constant stirring

Prepared slurry (initial state)   **Prepared slurry (1 day after: no separation)**

Experimental results

Placement of the proppant slurry in second reservoir

Shows high viscosity

Experimental results

Injection of the proppant slurry to sample

Experimental results

Injection of the proppant slurry to synthetic coal
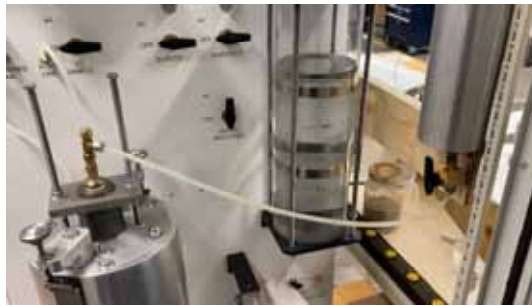
Experimental results

Proppant Injection Test 1

The proppant injection generated a filter cake and clogged the entry.
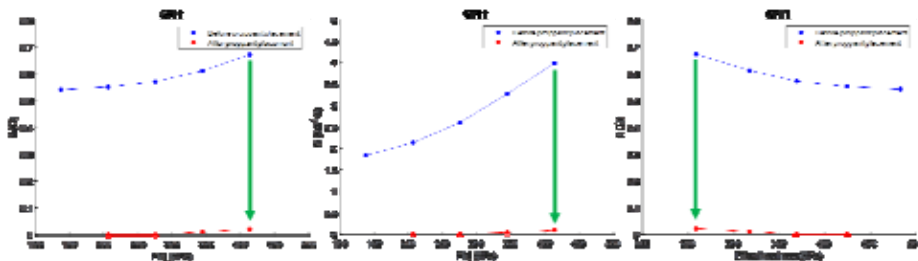
Disclaimer: The permeability values were calculated with measurements taken from pressure gauges and mechanical devices. It is possible that the differential pressure across the specimen is not entirely accurate.

Experimental results

Proppant Injection Test 2

Proppants were injected sequentially in three steps to find the proper slurry volume.
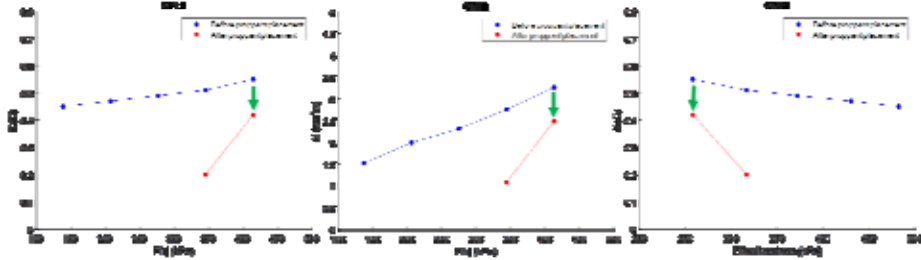
Disclaimer: The permeability values were calculated with measurements taken from pressure gauges and mechanical devices. It is possible that the differential pressure across the specimen is not entirely accurate.

Experimental results

Proppant Injection Test 3

Permeability was damaged after the proppant injection but shut down completely during fracture closure.
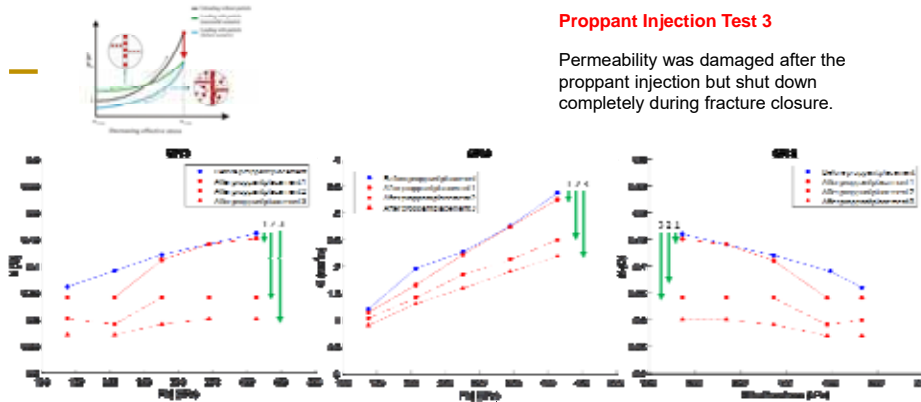
Disclaimer: The permeability values were calculated with measurements taken from pressure gauges and mechanical devices. It is possible that the differential pressure across the specimen is not entirely accurate.

Experimental results

Proppant Injection Test 4

The right proppant volume was injected and permeability was damaged. However, the permeability almost remained as initial

Disclaimer: The permeability values were calculated with measurements taken from pressure gauges and mechanical devices. It is possible that the differential pressure across the specimen is not entirely accurate.
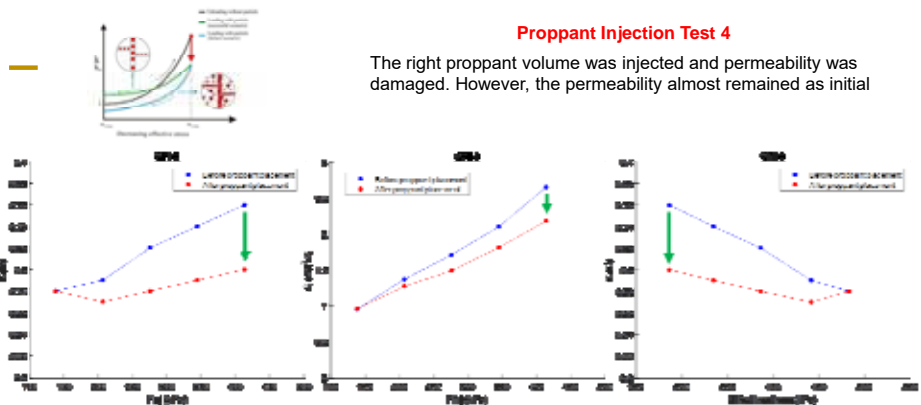
Experimental results

Observation of residual proppants inside the synthetic coal after the test

Layer 1 (A)

Layer 2 (B)

Layer 3 (A)

Top of the first sample layer

Top of the second sample layer

Top of the third sample layer

Experimental results

Observation of residual proppants inside the synthetic coal after the test

Between the fractures

In the drained water
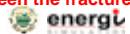
Experimental results

Proppant Injection Testing – 3D-Printed Fractured Media

Conclusions:

- The experimental results showed that after the particle injection, the permeability was immediately damaged. The consecutive tests showed the required amount of particles needed for proper placement.

- After the proppant placement, a slight permeability enhancement was observed. This was attributed to proppants placed inside the fractures avoiding complete fracture closure, which was observed when the specimen was open.

- The size and type of proppant may not be appropriate for the type of 3D-printed material. However, the experiment showed that proppant placement can be successfully placed.

Recommendations:

- A secondary assessment of proppant-material compatibility must be performed. In addition, the design of the 3D-printed specimen must be improved to capture more realistic behaviours of coal fractures and cleats.

- The proppant-injection permeameter system must be improved to allow accurate measurements and higher confining and pore pressures.
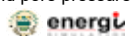
22 References

Aghighi, M. A., Johnson Jr., R. L., & Leonardi, C. R. (2019). Challenges in modelling of hydraulic fracturing in low-permeability coal seams with complex cleat networks and stress regime. *The APPEA Journal, 59*(1), 12.

Badri, M., Dare, D., Rodda, J., Thiesfield, G., & Blauch, M. (2000). *Keys to the Successful Application of Hydraulic Fracturing in an Emerging Coalbed Methane Prospect - An Example from the Peat Coals of Australia*. Paper presented at the SPE Asia Pacific Oil and Gas Conference and Exhibition, Brisbane, Australia. https://doi.org/10.2118/64493-MS

Barree, R. D., & Winterfeld, P. H. (1998). *Effects of Shear Planes and Interfacial Slippage on Fracture Growth and Treating Pressures*. Paper presented at the SPE Annual Technical Conference and Exhibition, New Orleans, Louisiana. https://doi.org/10.2118/48926-MS

Bedrikovetsky, P. G., Nguyen, T., Hage, A., Ciccarelli, J., ab Wahab, M., Chang, G., . . . Furtado, C. (2011). Taking advantage of injectivity decline for improved recovery during waterflood with horizontal wells. *Journal of Petroleum Science and Engineering, 78*, 5.

Brannon, H. D., & Tjon-Joe-Pin, R. M. (1995). *Application of Damage Removal Treatment Results in Multi-Fold Well Productivity Improvement: A Case Study, Paper SPE-29677-MS*. Paper presented at the SPE Western Regional Meeting, Bakersfield, California. https://doi.org/10.2118/29677-MS

Brannon, H. D., & Tjon-Joe-Pin, R. M. (1995). *Characterization of Breaker Efficiency Based upon Size Distribution of Polymeric Fragments, Paper SPE-30492-MS*. Paper presented at the SPE Annual Technical Conference and Exhibition, Dallas, Texas. https://doi.org/10.2118/30492-MS

Brannon, H. D., Tjon-Joe-Pin, R. M., Carman, P. S., & Wood, W. D. (2003). *Enzyme Breaker Technologies: A Decade of Improved Well Stimulation, Paper SPE-84213-MS*. Paper presented at the SPE Annual Technical Conference and Exhibition, Denver, Colorado. https://doi.org/10.2118/84213-MS

Camac, B. A., Benson, J., Chan, V., & Goedecke, A. (2018). *Cooper Basin Deep Coal – the New Unconventional Paradigm: Deepest Producing Coals in Australia*. Paper presented at the AEGC 2018: First Australian Exploration Geoscience Conference, Sydney, Australia.

Conway, M. W., Barree, R. D., Hollingshead, J., Willis, C., & Farrens, M. (1997). *Characterization and Performance of Coalbed Methane Wells in Drunkards Wash, Carbon County, Utah*. Paper presented at the 1997 International Coalbed Methane Symposium, Tuscaloosa, Alabama.

Di Vaira, N. J., Laniewski-Wollk, L., Johnson Jr, R. L., Aminossadati, S. M., & Leonardi, C. R. (2021). *A Novel Methodology for Predicting Micro-Proppant Screenout in Hydraulic Fracturing Treatments, Paper AP-URTEC-2021-208342*. Paper presented at the SPE/AAPG/SEG Asia Pacific Unconventional Resources Technology Conference. https://doi.org/10.15530/AP-URTEC-2021-208342

Di Vaira, N. J., Łaniewski-Wołłk, Ł., Johnson Jr, R. L., Aminossadati, S. M., & Leonardi, C. R. (2022). Influence of particle polydispersity on bulk migration and size segregation in channel flows. *Journal of Fluid Mechanics, 939*(A30).

Diamond, W. P. (1987). Underground Observations of Mined-Through Stimulation Treatments of Coalbeds. *Quarterly Review of Methane from Coal Seams Technology, 7*(3), 19-29.

Flottman, T., Brooke-Barnett, S., Naidu, S. K., Paul, P. K., Kirk-Burnnand, E., Busetti, S., . . . Trubshaw, R. L. (2013). *Influence of in Situ Stresses on Fracture Stimulation in the Surat Basin, Southeast Queensland, SPE 167064*. Paper presented at the SPE Unconventional Resources Conference and Exhibition-Asia Pacific, Brisbane, Australia.

Flottman, T., Brooke-Barnett, S., Trubshaw, R., Naidu, S.-K., Kirk-Burnnand, E., Paul, P., . . . Hennings, P. (2013). *Influence of in Situ Stresses on Fracture Stimulation in the Surat Basin, Southeast Queensland*. Paper presented at the SPE Unconventional Resources Conference and

Exhibition-Asia Pacific, Brisbane, Australia. https://doi.org/10.2118/167064-MS

Fraser, S. A., & Johnson Jr, R. L. (2018). *Impact of Laboratory Testing Variability in Fracture Conductivity for Stimulation Effectiveness in Permian Deep Coal Source Rocks, Cooper Basin, South Australia, paper SPE-191883-MS*. Paper presented at the SPE Asia Pacific Oil and Gas Conference and Exhibition, Brisbane, Australia. https://doi.org/10.2118/191883-MS

Gu, H., & Siebrits, E. (2006). *Effect of Formation Modulus Contrast on Hydraulic Fracture Height Containment*. Paper presented at the International Oil & Gas Conference and Exhibition in China, Beijing, China. https://doi.org/10.2118/103822-MS

Jeffrey, R. G., Brynes, R. P., Lynch, P. J., & Ling, D. J. (1992). *An Analysis of Hydraulic Fracture and Mineback Data for a Treatment in the German Creek Coal Seam*. Paper presented at the SPE Rocky Mountain Regional Meeting, Casper, Wyoming. https://doi.org/10.2118/24362-MS

Jeffrey, R. G., & Settari, A. (1995). *A Comparison of Hydraulic Fracture Field Experiments, Including Mineback Geometry Data, with Numerical Fracture Model Simulations*. Paper presented at the SPE Annual Technical Conference and Exhibition, Dallas, Texas. https://doi.org/10.2118/30508-MS

Jeffrey, R. G., & Settari, A. (1998). *An Instrumented Hydraulic Fracture Experiment in Coal*. Paper presented at the SPE Rocky Mountain Regional/Low-Permeability Reservoirs Symposium, Denver, Colorado. https://doi.org/10.2118/39908-MS

Jeffrey, R. G., Vlahovic, W., Doyle, R. P., & Wood, J. H. (1998). *Propped Fracture Geometry of Three Hydraulic Fractures in Sydney Basin Coal Seams*. Paper presented at the SPE Asia Pacific Oil and Gas Conference and Exhibition, Perth, Australia. https://doi.org/10.2118/50061-MS

Johnson Jr., R. L., You, Z., Ribeiro, A., Mukherjee, S., Salomao de Santiago, V., & Leonardi, C. R. (2020). *Integrating Reservoir Characterisation, Diagnostic Fracture Injection Testing, Hydraulic Fracturing and Post-Frac Well Production Data to Define Pressure Dependent Permeability Behavior in Coal, paper SPE-202330-MS.* Paper presented at the SPE Asia Pacific Oil & Gas Conference and Exhibition.

Johnson Jr, R. L. (1995). *Fracture Treatment Modifications And Bottomhole Treating Pressure Analysis In The Pictured Cliffs Formation, Rio Arriba County, New Mexico*. Paper presented at the SPE Production Operations Symposium, Oklahoma City, Oklahoma. https://doi.org/10.2118/29448-MS

Johnson Jr, R. L., Flottman, T., & Campagna, D. J. (2002). *Improving Results of Coalbed Methane Development Strategies by Integrating Geomechanics and Hydraulic Fracturing Technologies*. Paper presented at the SPE Asia Pacific Oil and Gas Conference and Exhibition, Melbourne, Australia. https://doi.org/10.2118/77824-MS

Johnson Jr, R. L., Glassborow, B., Scott, M. P., Pallikathekathil, Z. J., Datey, A., & Meyer, J. (2010). *Utilizing Current Technologies to Understand Permeability, Stress Azimuths and Magnitudes and their Impact on Hydraulic Fracturing Success in a Coal Seam Gas Reservoir*. Paper presented at the SPE Asia Pacific Oil and Gas Conference and Exhibition, Brisbane, Queensland, Australia. https://doi.org/10.2118/133066-MS

Johnson Jr, R. L., Scott, M. P., Jeffrey, R. G., Chen, Z., Bennett, L., Vandenborn, C. B., & Tcherkashnev, S. (2010). *Evaluating Hydraulic Fracture Effectiveness in a Coal Seam Gas Reservoir from Surface Tiltmeter and Microseismic Monitoring*. Paper presented at the SPE Annual Technical Conference and Exhibition, Florence, Italy. https://doi.org/10.2118/133063-MS

Johnson Jr, R. L., & Woodroof, R. A. (1996). *The Application of Hydraulic Fracturing Models in Conjunction with Tracer Surveys to Characterize and Optimize Fracture Treatments in the Brushy Canyon Formation, Southeastern New Mexico*. Paper presented at the SPE Annual Technical Conference and Exhibition, Denver, Colorado. https://doi.org/10.2118/36470-MS

Johnson Jr., R. L., & Mazumder, S. (2014). *Key Factors Differentiate the Success Rate of Coalbed Methane Pilots Outside of North America - Some Australian Experiences, IPTC-18108-MS*.

Johnson, R. L., Jr., Flottman, T., & Campagna, D. J. (2002). *Improving Results of Coalbed Methane Development Strategies by Integrating Geomechanics and Hydraulic Fracturing Technologies,*

SPE 77824-MS. Paper presented at the SPE Asia Pacific Oil and Gas Conference and Exhibition, Melbourne, Australia.

Johnson, R. L., Ramanandraibe, H. M., Ribeiro, A., Ramsay, M., Kaa, T., & Corbett, W. (2021). *Applications of Indirect Hydraulic Fracturing to Improve Coal Seam Gas Drainage for the Surat and Bowen Basins, Australia, Paper AP-URTEC-2021-208375*. Paper presented at the SPE/AAPG/SEG Asia Pacific Unconventional Resources Technology Conference. November 2021 retrieved from https://doi.org/10.15530/AP-URTEC-2021-208375

Keshavarz, A., Badalyan, A., Carageorgos, T., Bedrikovetsky, P., & Johnson, R. (2015). Stimulation of coal seam permeability by micro-sized graded proppant placement using selective fluid properties. *Fuel, 144*, 228-236. doi:10.1016/j.fuel.2014.12.054

Keshavarz, A., Badalyan, A., Carageorgos, T., Bedrikovetsky, P., & Johnson, R. L., Jr. (2014). Enhancement of CBM well fracturing through stimulation of cleat permeability by ultra-fine particle injection. *APPEA Journal 2014*, 12.

Keshavarz, A., Badalyan, A., Johnson, R., & Bedrikovetsky, P. (2016). Productivity enhancement by stimulation of natural fractures around a hydraulic fracture using micro-sized proppant placement. *Journal of Natural Gas Science and Engineering, 33*, 1010-1024. doi:10.1016/j.jngse.2016.03.065

Keshavarz, A., Yang, Y., Badalyan, A., Johnson, R., & Bedrikovetsky, P. (2014). Laboratory-based mathematical modelling of graded proppant injection in CBM reservoirs. *International Journal of Coal Geology, 136*, 1-16. doi:10.1016/j.coal.2014.10.005

Keshavarz, A., Yang, Y., Badalyan, A., Johnson, R. L., Jr., & Bedrikovetsky, P. (2014). Laboratory-based mathematical modelling of graded proppant injection in CBM reservoirs. *International Journal of Coal Geology, 136*, 1-16. doi:10.1016/j.coal.2014.10.005

Khanna, A., Keshavarz, A., Mobbs, K., Davis, M., & Bedrikovetsky, P. (2013). Stimulation of the natural fracture system by graded proppant injection. *Journal of Petroleum Science and Engineering, 111*, 71-77. doi:http://dx.doi.org/10.1016/j.petrol.2013.07.004

Leonardi, C. R., Flottman, T., Pandey, V. J., & Johnson Jr., R. L. (2019). *Quantifying the Influence of Three Dimensionality on Hydraulic Fracturing in Coal Seam Gas Wells, Paper SPE-198203-MS*. Paper presented at the Asia Pacific Unconventional Resources Technology Conference, Brisbane, Australia.

Lyon, M. K., & Leal, L. G. (1998). An experimental study of the motion of concentrated suspensions in two-dimensional channel flow. Part 2. Bidisperse systems. *Journal of Fluid Mechanics, 363*, 20.

Megorden, M. P., Jiang, H., & Bentley, P. J. D. (2013). *Improving Hydraulic Fracture Geometry by Directional Drilling in Coal Seam Gas Formation*. Paper presented at the SPE Unconventional Resources Conference and Exhibition-Asia Pacific, Brisbane, Australia. https://doi.org/10.2118/167053-MS

Morales, R. H., & Davidson, S. C. (1993). *Analysis of the Hydraulic Fracturing Behavior in the Bowen Basin*. Paper presented at the Low Permeability Reservoirs Symposium, Denver, Colorado. https://doi.org/10.2118/25862-MS

Ness, C., & Sun, J. (2015). Flow regime transitions in dense non-Brownian suspensions: Rheology, microstructural characterization, and constitutive modeling. *Physical Review E, 91*.

Pandey, V. J., & Flottmann, T. (2015). *Applications of Geomechanics to Hydraulic Fracturing: Case Studies From Coal Stimulations, SPE-173378-MS*. Paper presented at the SPE Hydraulic Fracturing Technology Conference, The Woodlands, TX.

Pandey, V. J., Flottmann, T., & Zwarich, N. R. (2017). Applications of Geomechanics to Hydraulic Fracturing: Case Studies From Coal Stimulations. *SPE Production & Operations, 32*(04), 404-422. doi:10.2118/173378-PA

Penny, G. S., & Conway, M. W. (1995). *Coordinated Studies in Support of Hydraulic Fracturing of Coalbed Methane, GRI-95/0283*. Retrieved from Chicago, Illinois:

Ramanandraibe, H. M., Ribeiro, A. S., Johnson, R., & You, Z. (2021). Improved modelling of pressure-

dependent permeability behaviour in coal based on a new workflow of petrophysics, hydraulic fracturing and reservoir simulation. *APPEA Journal, 61*, 11. doi:https://doi.org/10.1071/AJ20157

Ribeiro, A., Santiago, V., You, Z., Johnson Jr., R. L., & Hurter, S. (2019). *Evaluating Performance of Graded Proppant Injection Into CSG Reservoir: A Reservoir Simulation Study, Paper SPE-198324-MS*. Paper presented at the Asia Pacific Unconventional Resources Technology Conference (URTeC 2019), Brisbane Australia.

Russell, T., Pham, D., Neishaboor, M. T., Badalyan, A., Behr, A., Genolet, L., . . . Bedrikovetsky Pavel. (2017). Effects of kaolinite in rocks on fines migration. *Journal of Natural Gas Science and Engineering, 45*, 243-255. doi:http://dx.doi.org/10.1016/j.jngse.2017.05.020

Saini, R. K., Todd, B. L., Weaver, J. D., Ogle, J. W., Loveless, D. M., & Nguyen, P. (2015). US8985213B2. Halliburton Energy Services, Inc.

Santiago, V., Ribeiro, A., Johnson Jr, R. L., Hurter, S., & You, Z. (2021). *Modelling and Economic Analyses of Graded Particle Injections in Conjunction with Hydraulically Fracturing of Coal Seam Gas Reservoirs, paper SPE-208404-MS*. Paper presented at the Asia Pacific Unconventional Resources Technology Conference 2021, Brisbane, Australia.

Santiago, V., Ribeiro, A., Johnson Jr, R. L., Hurter, S., & You, Z. (2022). Modeling and Economic Analyses of Graded Particle Injections in Conjunction with Hydraulic Fracturing of Coal Seam Gas Reservoirs. *SPE Journal*, 1-16. doi:10.2118/208404-PA

Scott, M. P., Johnson Jr, R. L., Datey, A., Vandenborn, C. B., & Woodroof, R. A. (2010). *Evaluating Hydraulic Fracture Geometry from Sonic Anisotropy and Radioactive Tracer Logs*. Paper presented at the SPE Asia Pacific Oil and Gas Conference and Exhibition, Brisbane, Queensland, Australia. https://doi.org/10.2118/133059-MS

Tavener, E., Flottmann, T., & Brooke-Barnett, S. (2017). In situ stress distribution and mechanical stratigraphy in the Bowen and Surat basins, Queensland, Australia. *Geological Society, London, Special Publications, 458*(1), 31. doi:10.1144/SP458.4

Trulsson, M., Andreotti, B., & Claudin, P. (2012). Transition from the Viscous to Inertial Regime in Dense Suspensions. *Physical Review Letters, 109*(11).

Warpinski, N. R., Moschovidis, Z. A., Parker, C. D., & Abou-Sayed, I. S. (1994). Comparison Study of Hydraulic Fracturing Models—Test Case: GRI Staged Field Experiment No. 3 (includes associated paper 28158). *SPE Production & Facilities, 9*(01), 7-16. doi:10.2118/25890-PA

You, Z., Wang, D., Leonardi, C. R., Johnson Jr, R., & Bedrikovetsky, P. (2019). Influence of elastoplastic embedment on CSG production enhancement using graded particle injection. *APPEA Journal, 59*, 9. doi:https://doi.org/10.1071/AJ18086